Durham E-Theses

Enriched and Isogeometric Boundary Element Methods for Acoustic Wave Scattering

PEAKE, MICHAEL,JOHN

How to cite:

PEAKE, MICHAEL,JOHN (2014) *Enriched and Isogeometric Boundary Element Methods for Acoustic Wave Scattering*, Durham theses, Durham University. Available at Durham E-Theses Online: http://etheses.dur.ac.uk/10655/

Use policy

Durham University

Enriched and Isogeometric Boundary Element Methods for Acoustic Wave Scattering

Michael John Peake

Thesis submitted for consideration towards
the degree of Doctor of Philosophy

Durham University

School of Engineering
and Computing Sciences

School of Engineering & Computing Sciences

Durham University

United Kingdom

May 2014

Preface

This thesis concerns numerical acoustic wave scattering analysis. Such problems have been solved with computational procedures for decades, with the boundary element method being established as a popular choice of approach. However, such problems become more computationally expensive as the wavelength of an incident wave decreases; this is because capturing the oscillatory nature of the incident wave and its scattered field requires increasing numbers of nodal variables.

Authors from mathematical and engineering backgrounds have attempted to overcome this problem using a wide variety of procedures. One such approach, and the approach which is further developed in this thesis, is to include the fundamental character of wave propagation in the element formulation. This concept, known as the Partition of Unity Boundary Element Method (PU-BEM), has been shown to significantly reduce the computational burden of wave scattering problems.

This thesis furthers this work by considering the different interpolation functions that are used in boundary elements. Initially, shape functions based on trigonometric functions are developed to increase continuity between elements. Following that, non-uniform rational B-splines, ubiquitous in Computer Aided Design (CAD) software, are used in developing an isogeometric approach to wave scattering analysis of medium-wave problems. The enriched isogeometric approach is named the eXtended Isogeometric Boundary Element Method (XIBEM).

In addition to the work above, a novel algorithm for finding a uniform placement of points on a unit sphere is presented. The algorithm allows an arbitrary number of points to be chosen; it also allows a fixed point or a bias towards a fixed point to be used. This algorithm is used for the three-dimensional acoustic analyses in this thesis.

The new techniques developed within this thesis significantly reduce the number of degrees of freedom required to solve a problem to a certain accuracy—this reduction is more than 70% in some cases. This reduces the number of equations that have to be solved and reduces the amount of integration required to evaluate these equations.

Declaration

This thesis contains research carried out within the Mechanics Group of the School of Engineering and Computing Sciences, Durham University. No part of this report has been submitted elsewhere for any other degree or qualification and it is all the authors' own work unless it is referenced otherwise in the text.

Some parts of the material contained herein have been previously published in the following peer-reviewed journal papers:

- M.J. Peake, J. Trevelyan and G. Coates
  Novel basis functions for the partition of unity boundary element method for Helmholtz problems
  International Journal for Numerical Methods in Engineering, **93**(9): 905-918, 2013

- M.J. Peake, J. Trevelyan and G. Coates
  Extended isogeometric boundary element method (XIBEM) for two-dimensional Helmholtz problems
  Computer Methods in Applied Mechanics and Engineering, **259**: 93-102, 2013

- M.J. Peake, J. Trevelyan and G. Coates
  The equal spacing of N points on a sphere with application to partition-of-unity wave diffraction problems
  Engineering Analysis with Boundary Elements, **40**: 114-122, 2014

Acknowledgements

Coming to end my PhD, it is easy to start feeling as though writing a thesis is the work of one exhausted individual. Of course this is nonsense: when I speak of *my work*, I am speaking of the output of many individuals which has my name on it.

I would like to extend my most heartfelt thanks to Jon and Graham, for giving me the opportunity and for supporting and advising me throughout this research. I feel blessed to have been part of such a exemplary team. Thank you both for your patience through months of debugging and *"shapes function"*-gate.

Outside of Durham, I would like to thank Rob Simpson for many helpful discussions over the last couple of years. Rob's presentation at ACME 2011 was the inspiration for XIBEM and so, unbeknownst to him, he is quite responsible for the direction of my work. Also in this group, I would like to thank Joel Phillips for demonstrating the delights of the Python programming language to me. It has been an invaluable tool.

Thank you to the guys in the office and wider department for the conversation (work and non-work), crosswords and lunchtime film chats. I have loved our fantasy F1 league, not least as it gave me the excuse to programme Heikki Robolainen!

Now I'd like to thank the "Michael's Friends and Family" group. I am a strong believer that variety and balance are the most important ingredients to happiness and being productive; my friends and family have provided me with this. Sadly, there's not enough space to mention everyone; you know who you are and I am truly grateful for everything. That said, there are three people I would like to mention ...

Thank you to my parents: for everything. I've never been able to put into words how grateful I am for your love, support and belief ... and I still can't.

And finally, Zoe: the most inspirational of all. Thank you for doing all of this with me, through every up and down, success and failure. Thank you for your support and love. These three and half years would simply not have been the same without you there; I cherish every minute.

Michael Peake
Durham, March 2014

Contents

List of Figures

List of Tables

Acronyms & nomenclature

Acronyms

BEM	Boundary Element Method
BIE	Boundary Integral Equation
BIEM	Boundary Integral Equation Method
CAD	Computer Aided Design
CBIE	Conventional Boundary Integral Equation
FEM	Finite Element Method
FMM	Fast Multipole Method
HBIE	Hypersingular Boundary Integral Equation
IGABEM	IsoGeometric (Analysis) Boundary Element Method
PU	Partition of Unity
PU-BEM	Partition of Unity Boundary Element Method
RBIE	Regularised Boundary Integral Equation
SPL	Sound Pressure Level [dB]
SVD	Singular Value Decomposition
XIBEM	eXtended Isogeometric Boundary Element Method

English

$\mathbf{A}$	vector of unknown amplitudes
$\mathbf{B}$	magnetic induction vector [T]
$\mathbf{C}$	matrix populated with c jump terms
$\mathbf{d}$	plane wave direction of propagation
$\mathbf{E}$	electric field vector [V·m^{-1}]
$\mathbf{F}$	mapping between local coordinate and global coordinates
$\mathbf{H}$	matrix populated with H integrals
$\mathbf{P}$	control point
$\mathbf{q}$	vector populated with q integrals
A	wave amplitude

A_Γ	surface area of boundary Γ
$B_{j,p}$	jth Bernstein polynomial of degree p
c	speed of a wave in a medium $[\text{m·s}^{-1}]$
$c(\mathbf{p})$	jump term at $\mathbf{p}$
E	number of elements in a scatterer's boundary
e	element index
f	cyclic frequency [Hz]
$G(\mathbf{p}, \mathbf{q})$	Green's function representing response at $\mathbf{q}$ from unit source at $\mathbf{p}$
H_j^e	integral relating to jth basis function on eth element
$h_n(\cdot)$	Legendre function of the first kind
$H_n^{(1)}(\cdot)$	Hankel function of the first kind, order n
J	number of shape functions (or J-1 NURBS functions)
$J_n(\cdot)$	Bessel function of the first kind, order n
$j_n(\cdot)$	spherical Bessel function of the first kind, order n
k	wavenumber $[\text{m}^{-1}]$
M	number of plane wave in expansion
$n(\mathbf{q})$	unit normal at $\mathbf{q}$ pointing outward from the solution domain
N_j	shape function associated with the jth node of an element
N_{dof}	number of degrees of freedom
p	degree of approximation
P_Γ	perimeter of boundary Γ
Q^e	integral relating to eth element
r	Euclidean distance between two points
$R_{j,p}$	jth rational basis function of degree p
s	number of knots in Ξ minus one
t	time [s]
u	acoustic potential in time domain [m]
w_j	jth control point weight

Greek

α	impedance property of a scatterer
β	active boundary condition property
$\delta(\cdot)$	Dirac delta
ϵ_0	electric permittivity of free space $[\approx 8.85 \times 10^{-12}\,\text{C}^2\,\text{N}^{-1}\,\text{m}^{-2}]$
ϵ_n	Neumann symbol
Γ	domain boundary / boundary of scatterer
Γ	domain boundary
Γ_e	an element with index e

κ	matrix condition number
λ	wavelength [m]
μ_o	magnetic permeability of free space $[4\pi \times 10^{-7} \text{ H} \cdot \text{m}^{-1}]$
Ω	acoustic domain
ω	angular frequency [rad$\cdot$s^{-1}]
ϕ	acoustic potential in frequency domain [m]
ϕ^{inc}	incident wave
ρ	acoustic domain density [kg$\cdot$m^{-n} in $\mathbb{R}^n$]
ρ	minimum angle between two points on a sphere
τ	effeciency measure: number of degrees of freedom per wavelength in problem
θ	an angle [rads]
Ξ	knot vector
ξ	local coordinate

Other symbols

$\mathcal{E}$	error
$\nabla^2(\cdot)$	Laplace operator

1

Introduction

Nevertheless, there are some areas where our present techniques of formulation and solution prove inadequate and where important developments are yet to take place [. . .] a completely new method of approximation is needed to deal with the very short-wave solution.

OC Zienkiewicz (2000) [134]

Olgierd Zienkiewicz was a celebrated engineer and one of the pioneers of the finite element method (FEM). The words above come from a paper in which he presented two "unsolved" problems facing current numerical methods: shortwave scattering and boundary layer/turbulence modelling in fluids. This thesis concerns problems of the former type.

When an acoustic, electromagnetic or other type of propagating wave encounters an obstacle, a scattered field is created. The question of the nature of this field is known as the *wave scattering problem*. The problem is of interest to academics and industrialists alike, in a wide variety of fields from hydrodynamics to wireless communications and power.

Engineers working in a number of disciplines rely on having solutions to wave equations. In civil engineering, for example, waves are of interest in earthquake prediction and sonar mapping; lasers are studied in electronic and optical engineering; a large branch of mechanical engineering is dedicated to the study of waves in the form of vibrations and noise. Research in these areas has led to significant advances in the understanding of waves. In turn, this has led to the development of technologies that have shaped today's world; e.g. the Global Positioning System, wireless communications (mobile phones and Wi-Fi), wireless energy transmission, to name just a few.

Numerical analysis of wave phenomena requires a modelling technique capable of reproducing oscillations. A heuristic rule suggests that, for low order approximations (linear or quadratic), 10 nodal variables per wavelength in each coordinate direction are required in order to effectively capture wave oscillations. As such, numerical

analysis of wave problems is strongly dependent on the wavelength, λ, of such waves: for a three dimensional problem, the number of FEM nodes required is proportional to λ^{-3}. The Boundary Element Method (BEM), a popular tool for wave scattering analysis, utilises a reduced number of dimensions for its analyses; thus, the number of BEM nodes required is proportional to λ^{-2}. This may appear a modest requirement at first but the limitations of this rule will soon be apparent. This is the problem that concerned Zienkiewicz.

Consider a 10 GHz radar wave being scattered by an aircraft—the wave has a wavelength of 0.03 metres (relatively large for radar). A finite element simulation is to approximate the solution within a cube region of sides 100 metres in length. The volume of the cube is 1×10^6 cubic metres, equivalent to 37×10^9 cubic wavelengths, which requires 37×10^{12} nodal variables to be modelled. A boundary element simulation of the same problem only requires the potential on the surface of the aircraft to be approximated. Say the aircraft is crudely approximated as a sphere with a 20 metre diameter; this surface area is 1.4×10^6 square wavelengths, or 140×10^6 nodal variables.

The requirements above would push even the most powerful computers today to their limits. Even then, the wavelength being considered is not especially short and the FEM mesh does not cover a considerable area. The BEM simulation, using a reduced dimensional requirement, is sufficient to find a solution anywhere in space but the 140×10^6 nodal variables lead to a matrix system with 19×10^{15} entries. Clearly, it is imperative to find a way to reduce the nodal spacing requirement of these simulations.

While other techniques, such as the Fast Multipole Method (FMM) have shown promise, enriched methods may also offer a solution. Including knowledge of the nature of waves in the basis of approximation has been shown to reduce the number of degrees of freedom required in simulations of the Helmholtz equation using finite and boundary element methods. Boundary element approaches are more suitable to wave scattering problems, however, because they inherently deal with infinite domains with no need for domain truncation or non-reflecting boundary conditions. Finite elements always require the domain to be truncated and artificial boundary conditions to be set which inevitably invoke errors into the approximate solution.

1.1   Thesis statement

This thesis concerns partition of unity enriched, boundary element method simulations of wave scattering problems governed by the Helmholtz equation. In particular, the work within these chapters will introduce different interpolation functions to be used with an existing partition of unity enrichment boundary element method [97–99]. The interpolation functions are either entirely original or have not been used within a enriched boundary element context before.

The motivation for exploring such numerical methods is to reduce the number of degrees of freedom required to model acoustic wave scattering problems. There is an added motivation that the use of some of these functions may lay the foundation for a fully integrated CAD/numerical analysis approach.

All the numerical results in this thesis come from simulations run using Python. The code was developed entirely by the author, using libraries such as NumPy and SciPy for various matrix operations.

1.2   Overview of thesis

This thesis is structured into two halves to separate previous work (by others) from the new work of the author. The first four chapters can be considered background material. Chapters 5 and onwards all contain original work with the exception of Chapter 7 which introduces more background material at a convenient point within the thesis. Unlike more traditional outlines for a thesis, the existing literature is reviewed at the beginning of relevant chapters. The content of each chapter is outlined below.

Chapter 2: Waves includes basic theory on the nature of waves together with some analytical solutions of wave scattering problems.

Chapter 3: BEM for acoustic wave problems reviews the literature of the boundary element method and derives the conventional boundary element method for acoustic wave scattering problems in two dimensions.

Chapter 4: Enriched methods for medium-wavelength problems reviews recent literature that focuses on mediumwave and shortwave problems. It then introduces the existing partition of unity boundary element method formulation.

Chapter 5: Trigonometric shape functions is the first chapter containing new work: novel two-dimensional boundary element shape functions are developed with the aim of reducing errors at the end of wave enriched boundary elements.

Chapter 6: PU-BEM for three-dimensional problems considers the move from two-dimensional simulations to three-dimensional. Considerations specific to 3D simulations are noted and a new algorithm is presented for finding a uniform spacing of points on a sphere.

Chapter 7: Isogeometric analysis and NURBS introduces a field of research that is rapidly expanding in both FEM and BEM. Non-uniform rational B-splines are introduced, the interpolation functions used in Chapters 8 and 9.

Chapter 8: 2D IGABEM and XIBEM includes original work pioneering the use of functions used in CAD software and combining that with the partition of unity enrichment described in earlier chapters.

Chapter 9: 3D IGABEM and XIBEM continues the work of Chapter 8 in three-dimensions with early numerical results provided.

Chapter 10: Conclusions and future work concludes the thesis with reflections on what has been achieved and questions that could still be answered.

2

Waves

2.1 Acoustic waves

2.1.1 The wave equation

The propagation of acoustic waves through an isotropic, homogeneous medium, Ω, is governed by the scalar wave equation,

$$\nabla^2 u - \frac{1}{c^2}\frac{\partial^2 u}{\partial t^2} = 0, \tag{2.1}$$

in which $\nabla^2(\cdot)$ is the Laplace operator*, the complex variable $u = u(\mathbf{p}, t)$ denotes the acoustic potential at $\mathbf{p} \in \Omega$ and time t, and c is the speed of sound in the medium. The acoustic domain, Ω, may be an finite interior domain or an infinite exterior domain.

2.1.2 Harmonic waves and the Helmholtz equation

In order to look for time harmonic solutions to (2.1). One can assume that u can be expressed as

$$u(\mathbf{p}, t) = \phi(\mathbf{p})e^{-i\omega t}, \tag{2.2}$$

where $\phi \in \mathbb{C}$ is the acoustic potential in the frequency domain, and ω is the angular frequency (or pulsation) of the wave. It should be noted that while the above is more common, $e^{i\omega t}$ is an alternative sign convention used in some texts. By substituting (2.2) into (2.1), one obtains

$$\nabla^2 \phi(\mathbf{p}) + \frac{\omega^2}{c^2}\phi(\mathbf{p}) = 0, \quad \forall \mathbf{p} \in \Omega. \tag{2.3}$$

Now the *wavenumber*, $k = \omega/c$, is introduced. It should be noted that the wavenumber is also related to the cyclic frequency, f, and the wavelength, λ, by the following equation:

$$k = \frac{2\pi f}{c} = \frac{2\pi}{\lambda}. \tag{2.4}$$

---

*$\nabla^2 u = \frac{\partial^2 u}{\partial x^2} + \frac{\partial^2 u}{\partial y^2}$ in 2D, and $\nabla^2 u = \frac{\partial^2 u}{\partial x^2} + \frac{\partial^2 u}{\partial y^2} + \frac{\partial^2 u}{\partial z^2}$ in 3D

Substituting k into (2.3) yields the governing equation for acoustic waves in the frequency domain:

$$\nabla^2\phi(\mathbf{p}) + k^2\phi(\mathbf{p}) = 0, \quad \forall \mathbf{p} \in \Omega. \tag{2.5}$$

This equation is known as the *homogeneous Helmholtz equation* and it is this equation that is solved using the BEM in this work.

2.1.3 Acoustic pressure

The human ear responds to acoustic pressure and so it is this which is often of interest to engineers. ϕ is a function of position only; it is related to acoustic pressure by the equation,

$$p = -i\omega\rho\phi, \tag{2.6}$$

in which p denotes pressure and ρ is the density of the acoustic medium. As the ear responds to these pressures in an almost logarithmic way, p is often measured on a logarithmic scale. The most common of these is Sound Pressure Level (SPL), with units of decibels, which is expressed as

$$\text{SPL} = 10\log_{10}\left|\frac{p^2}{p_{\text{ref}}^2}\right| = 20\log_{10}\left|\frac{p}{p_{\text{ref}}}\right|. \tag{2.7}$$

The reference pressure, $p_{\text{ref}} = 2.0 \times 10^{-5}$ Pa (rms), is considered to be the threshold of human hearing.

2.1.4 Fundamental solutions

Initially, it is assumed that the acoustic medium Ω is an infinite domain with no boundary—it is said that Ω occupies the full space. If a unit source or disturbance is placed at $\mathbf{p}$, the (acoustic pressure) response to this source at another point $\mathbf{q}$ is called the full-space Green's function or fundamental solution for acoustic problems. The Green's function is denoted as $G(\mathbf{p}, \mathbf{q})$ and must satisfy the inhomogeneous Helmholtz equation,

$$\nabla^2 G(\mathbf{p}, \mathbf{q}) + k^2 G(\mathbf{p}, \mathbf{q}) = -\delta(\mathbf{p}, \mathbf{q}), \quad \forall \mathbf{p}, \mathbf{q} \in \Omega, \tag{2.8}$$

where the derivatives are taken at $\mathbf{q}$ and $\delta(\mathbf{p}, \mathbf{q})$, representing the unit source, is the Dirac delta distribution:

$$\delta(\mathbf{p}, \mathbf{q}) = \begin{cases} +\infty, & \mathbf{q} = \mathbf{p} \\ 0, & \mathbf{q} \neq \mathbf{p}, \end{cases} \tag{2.9}$$

and

$$\int_{-\infty}^{\infty} \delta(\mathbf{p}, \mathbf{q}) \mathrm{d}\mathbf{q} = 1. \tag{2.10}$$

For 2D acoustic wave problems, the Green's function is

$$G(\mathbf{p}, \mathbf{q}) = \frac{i}{4} H_0^{(1)}(kr), \tag{2.11}$$

and its normal derivative is

$$\frac{\partial G(\mathbf{p}, \mathbf{q})}{\partial n(\mathbf{q})} = -\frac{ik}{4} H_1^{(1)}(kr) \frac{\partial r}{\partial n}, \tag{2.12}$$

in which $H_j^{(1)}(\cdot)$ denotes the Hankel function of the first kind and order j, r is the Euclidean distance between $\mathbf{p}$ and $\mathbf{q}$, and $n(\mathbf{q})$ is the unit normal at $\mathbf{q}$ pointing outward from the solution domain.

For 3D acoustic wave problems, the Green's function is

$$G(\mathbf{p}, \mathbf{q}) = \frac{e^{ikr}}{4\pi r}, \tag{2.13}$$

and its normal derivative is

$$\frac{\partial G(\mathbf{p}, \mathbf{q})}{\partial n(\mathbf{q})} = \frac{e^{ikr}}{4\pi r} \left(ik - \frac{1}{r} \right) \frac{\partial r}{\partial n}. \tag{2.14}$$

2.2 Electromagnetic waves

2.2.1 Wave equation

Maxwell's equations are to classical electromagnetism what Newton's laws are to classical mechanics. They relate the *electric field* $\mathbf{E}$, the *magnetic field* $\mathbf{B}$, and their sources. The homogeneous form of the electromagnetic wave equation can be written either in terms of the electric field,

$$\nabla^2 \mathbf{E} = \mu_0 \epsilon_0 \frac{\partial^2 \mathbf{E}}{\partial t^2}, \tag{2.15}$$

or in terms of the magnetic field,

$$\nabla^2 \mathbf{B} = \mu_0 \epsilon_0 \frac{\partial^2 \mathbf{B}}{\partial t^2}, \tag{2.16}$$

where μ_0 is the magnetic permeability of free space and ϵ_0 is the electric permittivity of free space.

(2.15) and (2.16) are of the same form as the general wave equation (2.1) and, in 1862, Maxwell showed that these equations predicted the speed of electromagnetic waves in free space to be

$$c = \frac{1}{\sqrt{\mu_0 \epsilon_0}}. \tag{2.17}$$

It was noted that this was equal to the speed of light and, thus, Maxwell surmised

that light was also an electromagnetic wave.

2.2.2   TE and TM waves

Because there are two vector wave equations governing the problem, the formulation of the boundary integral equation for electromagnetic wave problems differs from that of acoustic problems. However, for two-dimensional problems, TE or TM waves are sometimes considered. A TE wave has a **B**-field in the z direction alone (i.e. out of the plane of interest); similarly, a TM wave has a **E** field in the z direction only. In these cases, one can consider either (2.15) or (2.16) alone rather than coupling them; thus, both cases simply result in the Helmholtz equation again. Therefore, for TE and TM wave problems, the same methods can be used for solving acoustic and electromagnetic wave scattering problems.

2.3   Numerical analysis

Until the 20th century, there was principally one method for finding solutions to wave equations and other partial differential equations: find a closed-form (or analytical) solution. Such an approach finds functions that are only valid for a small set of simple, idealised geometries and homogeneous domains. The books [14,65,91] contain such solutions, some of which are shown in the following section. The resulting functions are often complicated but it is the small, finite number of cases that can be solved for which ultimately limits this approach.

Instead of finding a complicated, closed-form solution, one can search for an approximate solution based a combination of more simple functions. Such an approach is often reliant on a significant number of calculations being made and so, though numerical approximations have existed for many centuries, it has only been with the advent of computers that the method has been truly realised.

There is an assortment of approaches than can be used to solve partial differential equations. These include: the well-known FEM; the finite difference method, in which functions are represented by grid points and the derivatives between them are approximated through differences; spectral methods, in which the solution is expressed as the sum of some global basis functions. This thesis, however, only focuses on the BEM.

2.4   Analytical solutions

Three of the Helmholtz problems analysed in this thesis have analytical solutions. Those closed-form solutions are included here, along with the rest of the acoustic wave theory, in order to make them easier to find.

2.4.1   Scattering by a circular cylinder

Consider a two-dimensional domain Ω and a perfectly reflecting cylindrical scatterer Γ of radius a, centred at the origin $(0,0)$. The scatterer is impinged by a unit-amplitude, incident plane wave propagating in the direction $\mathbf{d} = (1,0)$. The incident wave potential at $\mathbf{p} = r(\cos\theta, \sin\theta)$ is expressed $\phi^{\text{inc}}(\mathbf{p}) = e^{ik\mathbf{d}\cdot\mathbf{p}}$. The scatterered potential is expressed by [65]

$$\phi^{\text{scat}}(\mathbf{p}) = \frac{J_0'(ka)}{H_0'(ka)} H_0(kr) - 2 \sum_{n=1}^{\infty} i^n \frac{J_n'(ka)}{H_n'(ka)} H_n(kr) \cos(n\theta), \quad \mathbf{p} \in \Omega, \qquad (2.18)$$

where $J_n(\cdot)$ represents a Bessel function of the first kind order n, the Hankel functions are of the first kind, and a prime denotes the derivative of a Bessel or Hankel function with respect to ka. The total wave potential at $\mathbf{p}$ is the sum of the incident potential and scattered potential:

$$\phi(\mathbf{p}) = \phi^{\text{inc}}(\mathbf{p}) + \phi^{\text{scat}}(\mathbf{p}). \qquad (2.19)$$

In the case where $r = a$, i.e. the point being evaluated is on the surface of the cylinder, the total potential can be expressed as

$$\phi(\mathbf{p}) = \frac{2}{\pi ka} \sum_{n=0}^{\infty} \epsilon_n \frac{i^{n+1}}{H_n'(ka)} \cos(n\theta), \quad \mathbf{p} \in \Gamma, \qquad (2.20)$$

where ϵ_n denotes the Neumann symbol:

$$\epsilon_n = \begin{cases} 1 & \text{for } n = 0, \\ 2 & \text{for } n \in \mathbb{Z}^+. \end{cases} \qquad (2.21)$$

2.4.2   Scattering by multiple cylinders

For the more complicated problem of scattering by multiple perfectly scattering cylinders, the solution is given by Linton and Evans [79]. Provided no cylinders touch or overlap, the solution is valid for any number of cylinders, cylinder radii and centre locations. The geometry of the problem is defined in Figure 2.1.

For a set of N cylinders, the total acoustic potential on the surface of the vth cylinder can be expressed as

$$\phi(a_v, \theta_v) = -\frac{2i}{\pi ka_v} \sum_{n=-\infty}^{\infty} \frac{A_n^v}{H_n'(ka_v)} e^{in\theta_v}, \qquad (2.22)$$
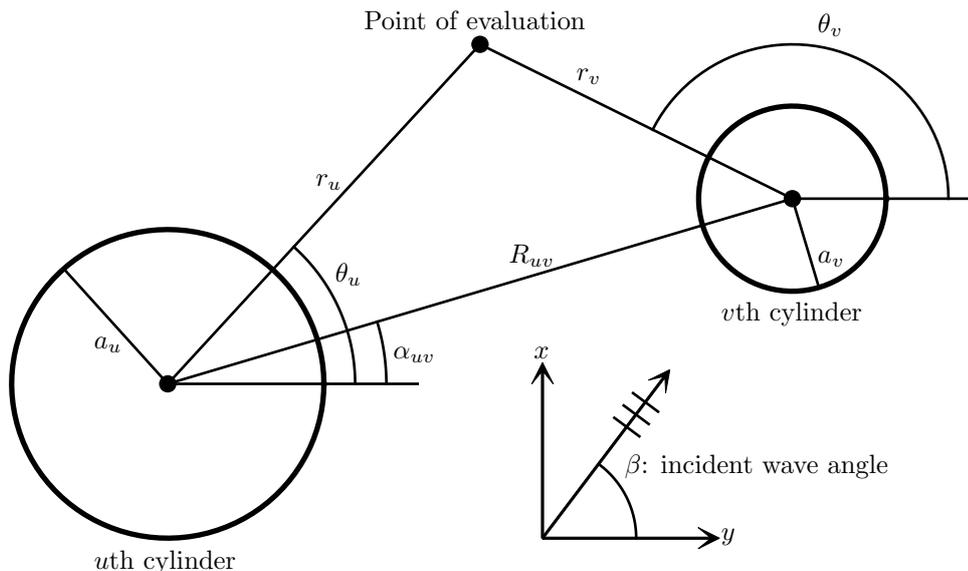
Figure 2.1: Geometry for the Linton and Evans series solution.

where A_n^v are constants that are found by using the equation

$$A_m^v + \sum_{\substack{u=1 \\ \neq v}}^{N} \sum_{n=-\infty}^{\infty} A_n^u Z_n^u e^{i(n-m)\alpha_{uv}} H_{n-m}(kR_{uv}) = -I_v e^{im(\pi/2 - \theta^{\mathrm{inc}})},$$

$$v = 1, \ldots, N, \quad m = -\infty, \ldots, \infty, \qquad (2.23)$$

where α_{uv} and R_{uv} are the angle and distance between the centres of the uth and vth cylinder; I_v is a phase factor associated with the vth cylinder, θ^{inc} is the angle of incidence of the incident plane wave, and

$$Z_n^u (\equiv Z_{-n}^u) = H_n(kr_u), \qquad (2.24)$$

where r_u is the distances between the origin and the centre of the uth cylinder. (2.23) is truncated:

$$A_m^v + \sum_{\substack{u=1 \\ \neq v}}^{N} \sum_{n=-M}^{M} A_n^u Z_n^u e^{i(n-m)\alpha_{uv}} H_{n-m}(kR_{uv}) = -I_v e^{im(\pi/2 - \theta^{\mathrm{inc}})},$$

$$v = 1, \ldots, N, \quad m = -M, \ldots, M. \qquad (2.25)$$

Now a square system of $N(2M+1)$ can be solved to find the constants A_m^v. Increasing M improves the accuracy of the constants at the expense of computing time.

2.4.3 Scattering by a sphere

Consider a plane wave impinging a perfectly scattering sphere. Assuming the incident wave (of wavenumber K) is propagating in the direction $\mathbf{d}^{\mathrm{inc}} = (0, 0, 1)$, the scattered acoustic potential at any point $z(r, \theta) = r\cos(\theta)$ can be found with the

analytical scattered solution [91]:

$$\phi^{\text{scat}}(r, \theta) = \sum_{n=0}^{\infty} -\frac{i^n(2n+1)j_n'(ka)}{h_n'(ka)}P_n(\cos\theta)h_n(kr) \qquad (2.26)$$

where j_n is the spherical Bessel function of the first kind, h_n is the spherical Hankel function of the first kind, P_n is the Legendre function of the first kind and a is the radius of the sphere.

Again, the total wave potential at $z(r, \theta)$ is the sum of the incident potential and scattered potential:

$$\phi(z(r, \theta)) = e^{ikz} + \phi^{\text{scat}}(r, \theta). \qquad (2.27)$$

3

BEM for acoustic wave problems

3.1 Introduction

The *boundary element method* is a term that encompasses many different "flavours" of boundary integral approach for a wide range of engineering (and purely mathematical) problems. To attempt a discussion of the entire field within these pages would be both naive and futile: a keyword search on Web of Knowledge shows that there are more than 12,500 journal papers containing "boundary element" or "boundary integral" in the title alone.* Instead, this chapter contains a brief review of the history of the BEM with a focus on acoustic analysis, followed by the derivation of the conventional BEM for acoustic wave scattering problems. Subsequent chapters will discuss more recent research and the work carried out by the author.

3.2 Background of the BEM

3.2.1 Early development

Despite existing for many centuries, numerical analysis did not truly prosper until the advent of the digital computer. The history of many of these methods lies in the eminent scientists and mathematicians of the 18th century: Euler, Lagrange, Laplace and Fourier, amongst others, all experimented with numerical techniques and, subsequently, their names are to be found in the titles of many of the numerical methods still used today. From the 19th century, the works of Gauss and Green[†] are also significant: Green's second identity is central to the formulation of many boundary integral equations.

---

*Web of Knowledge. `http://apps.webofknowledge.com/`. Accessed 7 January 2014

[†]Green was virtually unknown in his lifetime, despite his 1828 work *An essay on the application of mathematical analysis to the theories of electricity and magnetism* being one of the most significant texts in numerical analysis, particularly for the BEM. The work was self-published before Green had any formal adult education. Before joining Cambridge University, Green received only one year of education starting when he was eight years of age [24].

The founder of boundary integral approaches is commonly cited as Fredholm [46] who, in 1903, was the first to prove the existence and uniqueness of solutions to the fundamental, boundary-value problems of potential, using integral equations. Fredholm suggested that a discretisation procedure could be used to find these solutions; though, with no digital computers, solving the resulting system of linear equations was infeasible. So, despite Fredholm's insights, it was only in the 1960s, with the actualisation of widely available digital computers, that numerical methods for solving partial differential equations started to develop rapidly towards the forms they are today. Techniques such as the Finite Element Method (FEM), the Finite Difference Method (FDM) and the Boundary Integral Equation Method (BIEM)—which later became the BEM— were all developed during this decade.

With a number of independent studies starting in 1962, many applications and discretisation procedures to solve boundary integral equations were published throughout the 1960s. The work of Jaswon, Ponter and Symm [60, 61, 122] at the Department of Mathematics at Imperial College, London, particularly should not go unnoted. These authors found two-dimensional solutions for Laplace's equations. They adopted what is now called the *direct formulation*: the function to be evaluated and the fundamental solution—Green's function for an infinite domain—are substituted into Green's second identity to find a boundary integral equation. Their work was the start of the development of the BEM for problems of potential.

Rizzo's landmark paper of 1967, *An integral equation approach to boundary value problems of classical elastostatics* [104], marked an increased interest in the BIEM. Until then, the BIEM had been largely neglected in favour of the FEM which was, and possibly still is, relatively easier for most engineers to understand. Rizzo formally laid out the direct formulation of the BIEM and presented numerical results of stress analysis problems.

In 1975, the first conference featuring the method, organised by Rizzo and Cruse, was held at Rensselaer Polytechnic Institute. This was followed by the publication of Lachat and Watson [73] a year later in which isoparametric elements were used for the first time in the BIEM; Seybert *at al.* [114] later showed that this type of element could significantly improve the accuracy of a BEM solution. Isoparametric elements were first presented for the FEM back in 1966 [59]. The BIEM's late adoption of the tool, now almost ubiquitous in both FEM and BEM, demonstrates how rapidly the FEM had advanced ahead of the BEM before Rizzo's work.

In 1977, the first book discussing various boundary integral equation methods was published, written by Jaswon and Symm [62]. The same year was marked with an article published by Brebbia and Dominguez [16] in which the method was first referred to as the BEM; since 1977, the method has almost exclusively been referred to as the BEM. The following year, Brebbia organised a conference in Southampton, UK, which was devoted entirely to the method; this was followed by the first teaching text on the BEM, also published by Brebbia [15].

Since the early 1990s, a number of books have been published concerning the BEM. Some are introductory and focus on the fundamentals with potential and elasticity problems (e.g. Brebbia and Dominguez [17]); some concentrate on the computational and programming aspects of the BEM (e.g. Kirkup [68]); a few books provide a thorough examination of a number of applications of the method (e.g. Becker [7], Trevelyan [127], and Wrobel [132]).

In electromagnetic wave research, a method with considerable similarity to the BEM exists under the name the method of moments (MoM). A generalised MoM has been developed for vector Helmholtz equation problems [94] and Maxwell's equations problems [93].

3.2.2   Boundary element methods in acoustics

Once the boundary integral equation for infinite domain, acoustic problems had been derived, a significant amount of interest developed. In particular, the U.S. Navy offered significant amounts of funding for research into BEM applications for underwater scattering and radiation problems [33].

In 1962, Friedman and Shaw [47] presented a solution to the time-domain, scalar wave equation for a pulse scattered by a cylindrical obstacle. The direct formulation was used to produce a boundary integral equation for the scattered wave field; this could be differentiated to find the acoustic pressure. The boundary equation was discretised in space and a time-stepping scheme used to evaluate the solution. Numerical results were given for the case of a box-shaped rigid cylinder.

In 1963, Banaugh and Goldsmith [4] solved the two-dimensional, Helmholtz equation. Derived using Green's second identity, they presented an integral representation of the Helmholtz equation called "Weber's equation":

$$\phi = \frac{i}{4} \int_\Gamma \left[\frac{\partial \phi}{\partial n} H_0^{(1)}(kr) - \phi \frac{\partial H_0^{(1)}(kr)}{\partial n} \right] \mathrm{d}\Gamma. \tag{3.1}$$

Here Γ represents the boundary of a scatterer and $H_0^{(1)}(\cdot)$ is the Hankel function of the first kind, order zero. The use of constant elements—assuming constant variation of potential and its derivative over the subinterval—made the integration simple. Results were demonstrated for the problems of a steady-state wave scattered from the surface of hard and soft circular cylinders. Results at low wave numbers were precise; however, it was notable that the accuracy diminished as the wave number increased.

Also in 1963, Chen and Schweikert [30] published a solution for the problem of sound radiating from a body in an infinite fluid medium. This was the first paper in which a boundary integral equation method was used to solve a three-dimensional acoustic problem. The Neumann problem—in which the derivative of potential is defined on the boundary—was solved in the frequency domain using a Fredholm

integral equation of the second kind:

$$\frac{\partial\phi(\mathbf{p})}{\partial n} = -2\pi\sigma(\mathbf{p}) + \int_\Gamma \sigma(\mathbf{q})\frac{\partial}{\partial n}\left(\frac{e^{ikr}}{r}\right)\mathrm{d}\Gamma(\mathbf{q}), \quad \mathbf{p}, \mathbf{q} \in \Gamma, \qquad (3.2)$$

where $\mathbf{q}$ is a general field point, $\mathbf{p}$ is point of source and σ is the source strength. Pressures of the fluid were expressed in terms of monopoles on the surface of the radiating surface. Numerical examples included a piston-shaped scatterer set in a rigid sphere and a vibrating, cylindrical shell in water. Chen and Schweikert noted that the capacity of computers at the time was a limiting factor but also that there was a relationship between the wavelength of a problem and the required size of elements. It was later found that Chen and Schweikert's method suffered from nonexistence of solutions at discrete eigenfrequencies associated with the interior Dirichlet problem (potential defined on boundary) [9].

Work on vibrating surfaces was continued by Chertock [32]. In his 1964 paper, Chertock returned to Banaugh and Goldsmith's integral representation, (3.1), and presented it in its three-dimensional form:

$$\phi(\mathbf{p}) = \frac{1}{4\pi}\int_\Gamma \left[\frac{\partial\phi(\mathbf{q})}{\partial n}\frac{e^{ikr}}{r} - \phi(\mathbf{q})\frac{\partial}{\partial n}\left(\frac{e^{ikr}}{r}\right)\right]\mathrm{d}\Gamma(\mathbf{q}). \qquad (3.3)$$

Chertock gave numerical examples of spheroids and spheroid-like, axisymmetric bodies in fluids. This work was continued by Copley [35] who suggested using an interior Helmholtz equation where the $\phi(\mathbf{p})$ part of (3.3) is null as all the sources are placed inside the scatterer. He showed that a unique solution could be found if the integral relation is satisfied at all these points.

In 1991, Ciskowski and Brebbia [33] published the first book entirely devoted to the use of boundary elements in acoustics. They gave a mathematical derivation for the BEM in a form to solve the Helmholtz equation. Ciskowski and Brebbia covered technical aspects such as acoustic radiation, acoustic scattering, and structural-acoustic coupling. They suggested a wide number of applications, including numerical examples for some. These applications included the automotive industry, architectural acoustics and environmental noise.

3.2.3 Nonuniqueness

In 1968, Copley [36] published an article that reported the integral equation formulation failed for exterior acoustic problems at discrete eigenfrequencies associated with the interior Dirichlet problem. Copley showed that a unique solution could be obtained by using an integral equation evaluated at only interior points—like in the author's previous work [35]; however, the relation had to be satisfied at all interior points and, because it was formulated as an integral equation of the first kind rather than second, it was less numerically stable than the boundary only formulation [9].

A method to overcome nonuniqueness was devised, by Schenck [111], coined

the *Combined Helmholtz Integral Equation Formulation* (CHIEF). The method collocates the Helmholtz equation at some arbitrary points inside the body (outside the solution domain) as well as on the boundary—this utilises an interior Helmholtz equation such as Copley's. These constraint equations, which remove nonuniqueness and overdetermine the system matrix, have come to be known as CHIEF equations. A noted issue with this method is in choosing the CHIEF points at which to collocate: if the points chosen are on, or very close to, nodal points of the interior eigenmode, the equations will not solve nonuniqueness. Techniques to effectively choose points have been the focus of research since. Examples of this include Seybert and Rengarajan [113] who, in 1987, demonstrated that it takes only one "good" point to establish a unique solution.

In 1971, Burton and Miller [20] published a paper discussing the use of the BEM for the Laplace equation and the Helmholtz equation, noting the difficulties of nonuniqueness associated with the latter. Burton and Miller demonstrated a method of deriving an integral equation by combining the integral equation used in CHIEF with its derivative. They showed that the formulation guaranteed existence and uniqueness, at all wavenumbers. Burton and Miller called the equation the *Combined Field Integral Equation* (CFIE). There is, however, a major drawback to the method: an artefact of the formulation is the creation of some hypersingular integrals that must be evaluated. More recently, it has been shown that these integrals can be regularised to present a BIE containing only weakly singular integrals [78, 82].

In 1989, Koopmann *et al.* [70] devised a wave superposition method using an array of points sources. Rather than the monopoles being placed on the surface of the radiator, like Chen and Schweikert, this array of monopoles was placed on the surface of a "fictitious" surface that fitted inside the boundary of the radiator. Numerical results were good, showing better performance at high wavenumbers compared to other boundary element techniques. One reason for this was the lack of singularities in the integration as $r \not\to 0$ over the integral limits. Also, as the basis of the formulation was monopoles, rather than elements, Gaussian integration could be dropped in favour of one-point integration schemes; this reduced the time it took to produce the system matrix. Despite Koopmann *et al.*'s claim that the formulation did not suffer from nonuniqueness, Jeans and Mathews [63] later found that it did. Then, in 1993, Wilton *et al.* [131] showed that it also suffers from a nonexistence similar to Chen and Schweikert's formulation. Again, this was at eigenfrequencies associated with the interior Dirichlet problem; however, it was for the interior of the monopoles' fictitious surface, rather than the radiating surface that was the focus of the problem to be solved.

In 1997, Benthien and Schenck [9] produced a review of the techniques that had been developed to overcome the nonuniqueness problem associated with the BEM in acoustics. In their conclusions, Benthien and Schenck said that wave superposition methods had "an accuracy advantage" but admitted that their efficacy for surfaces

with discontinuities was not comparable to that of CHIEF. The classic Burton and Miller formulation was mentioned; however, they felt that the hypersingularities that accompanied the formulation incurred too much of a computational penalty. They noted that, for methods such as CHIEF and wave superposition, the selection of interior points to use became inherently more difficult as the wavenumber rose. Despite this, Benthien and Schenck said that CHIEF was still the most "viable and efficient approach" and that choosing the right interior points was "not difficult".

In 2001, Chen *et al.* [29] produced an analytical study of using the CHIEF method in two-dimensional problems. They showed how the irregular frequencies could be found for any problem and that, if carefully chosen, only two CHIEF points are needed to eradicate them; however, the choice of these points requires knowledge of the eigenfrequencies which are time-consuming to find for complex geometries. Indeed, the process is potentially as long as solving the original problem. Three numerical examples were given: a radiating infinite cylinder, a plane wave scattered by an infinite cylinder and a plane wave scattered by an infinite square rod. The results aligned with the analytical solutions and the Burton and Miller formulation.

In 2006, Mohsen and Hesham [89] suggested sampling a few "regularly spaced" interior points and choosing those where the field deviates most from zero; this guarantees that they do not lie on nodes. LU decomposition was used for two reasons: firstly, the system matrix could be decomposed in such a way that resonance could be detected in the U matrix; secondly, by modifying one column and row in L and U respectively, for each interior point used, a square system could be kept allowing an efficient solver to be used.

In 2013, Diwan *et al.* compared the CHIEF method and Burton and Miller formulation for overcoming nonuniqueness for the partition of unity enriched BEM (discussed in Chapter 4). They concluded that the accuracy obtained using the CHIEF formulation surpassed that of using the Burton and Miller formulation. It was also noted that the likelihood of CHIEF failing was very small and the complicated integration involved in solving a problem with the Burton and Miller formulation was undesirable.

3.2.4   Evaluation of integrals

By the 1980s, the BEM had been widely accepted as an effective method for solving acoustics problems; however, the issue of the efficiency of numerical evaluations had rarely been discussed. In 1987, Telles [125] published a seminal paper discussing the evaluation of singular integrals that were required to populate influence matrices. Telles noted that Gaussian quadrature was not accurate enough for integration over elements with these singularities and suggested a third-degree polynomial transformation. This transformation assumes the integral is between -1 and $+1$ and requires only knowledge of where the singularity lies in the region; it then clusters quadrature points near to the singularity. The Jacobian of the transformation approaches zero
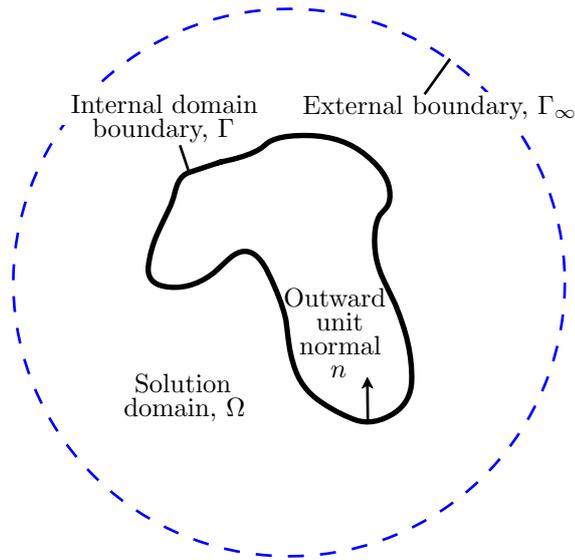
Figure 3.1: Two-dimensional problem domain.

at the singularity, reducing its effect.

In 1994, Telles and Oliveira [126] suggested some improvements to the 1987 scheme. In particular, the use of an optimisation parameter was discussed so that more strongly singular integrals could be evaluated with it.

A series of papers, culminating in Guiggiani *et al.* [51], proposed a general approach for the evaluation of integrals of arbitrary order of singularity. This is done by subtracting the singularity, leaving a regular integral that can be evaluated using simple quadrature; the singularity term is then integrated analytically and added to the regular part.

3.3   Analytical formulation

The remaining sections of this chapter present the direct collocation BEM for acoustic wave scattering problems.

3.3.1   Boundary integral equation

Figure 3.1 shows an infinite, homogeneous solution domain Ω, exterior to a scattering body with arbitrary boundary Γ. The dashed line represents an artificial boundary at infinity, Γ_∞. In the frequency-domain, such a problem is governed by the Helmholtz equation (2.5).

To obtain a boundary integral equation for this problem, *Green's second identity* is required:

$$\int_\Omega \left[u\nabla^2 v - v\nabla^2 u \right] \mathrm{d}\Omega = \int_{\Gamma \cup \Gamma_\infty} \left[u\frac{\partial v}{\partial n} - v\frac{\partial u}{\partial n} \right] \mathrm{d}\Gamma. \tag{3.4}$$

Here, u and v are arbitrary functions with continuous first and second derivatives

within Ω. Let u be an acoustic potential $\phi(\mathbf{q})$, and v be the fundamental solution $G(\mathbf{p}, \mathbf{q})$ as defined in (2.11) or (2.13). These can be substituted into (3.4) to obtain

$$\int_\Omega \left[\phi(\mathbf{q})\nabla^2 G(\mathbf{p}, \mathbf{q}) - G(\mathbf{p}, \mathbf{q})\nabla^2 \phi(\mathbf{q}) \right] \mathrm{d}\Omega$$
$$= \int_{\Gamma \cup \Gamma_\infty} \left[\phi(\mathbf{q})\frac{\partial G(\mathbf{p}, \mathbf{q})}{\partial n(\mathbf{q})} - G(\mathbf{p}, \mathbf{q})\frac{\partial \phi(\mathbf{q})}{\partial n(\mathbf{q})} \right] \mathrm{d}\Gamma(\mathbf{q}), \quad \mathbf{p} \in \Omega. \quad (3.5)$$

Here, $\mathrm{d}\Gamma(\mathbf{q})$ is used to show that the integration is over the points $\mathbf{q}$ that are seen as part of Γ.

Using the Helmholtz equation (2.5) to substitute for $\nabla^2 \phi(\mathbf{q})$, one obtains

$$\int_\Omega \left[\nabla^2 G(\mathbf{p}, \mathbf{q}) + k^2 G(\mathbf{p}, \mathbf{q}) \right] \phi(\mathbf{q}) \, \mathrm{d}\Omega$$
$$= \int_{\Gamma \cup \Gamma_\infty} \left[\phi(\mathbf{q})\frac{\partial G(\mathbf{p}, \mathbf{q})}{\partial n(\mathbf{q})} - G(\mathbf{p}, \mathbf{q})\frac{\partial \phi(\mathbf{q})}{\partial n(\mathbf{q})} \right] \mathrm{d}\Gamma(\mathbf{q}), \quad \mathbf{p} \in \Omega. \quad (3.6)$$

Now, substituting (2.8) into (3.6) and using the knowledge of (2.10), one obtains

$$\phi(\mathbf{p}) = \int_{\Gamma \cup \Gamma_\infty} \left[G(\mathbf{p}, \mathbf{q})\frac{\partial \phi(\mathbf{q})}{\partial n(\mathbf{q})} - \frac{\partial G(\mathbf{p}, \mathbf{q})}{\partial n(\mathbf{q})}\phi(\mathbf{q}) \right] \mathrm{d}\Gamma(\mathbf{q}), \quad \mathbf{p} \in \Omega. \quad (3.7)$$

This is an equation that expresses the nature of the acoustic potential at any point $\mathbf{p}$ in the domain, using only information on the boundaries of that domain.

3.3.2 Infinite regions

For interior problems, the boundary Γ_∞ does not exist and only the integral on Γ is considered. However, it will now be shown that the integral on Γ_∞ can be ignored for external problems also. To guarantee that the mathematical solution is of a wave propagating from source to infinity—and not *vice versa*—a far-field boundary condition is required. For acoustic waves, this is the *Sommerfeld radiation condition*:

$$\lim_{r \to \infty} \left[r^{\frac{1}{2}} \left(\frac{\partial \phi}{\partial r} - ik\phi \right) \right] = 0, \quad \text{in 2D}, \quad (3.8)$$

$$\lim_{r \to \infty} \left[r \left(\frac{\partial \phi}{\partial r} - ik\phi \right) \right] = 0, \quad \text{in 3D}. \quad (3.9)$$

The fictitious boundary Γ_∞ can be considered to be circular in two dimensions or spherical in three dimensions. Then, substituting the Sommerfeld condition $\partial\phi/\partial r = \partial\phi/\partial n = ik\phi$ into the integral over Γ_∞ in (3.7) gives

$$\int_{\Gamma_\infty} \left[G(\mathbf{p}, \mathbf{q})\frac{\partial \phi(\mathbf{q})}{\partial n(\mathbf{q})} - \frac{\partial G(\mathbf{p}, \mathbf{q})}{\partial n(\mathbf{q})}\phi(\mathbf{q}) \right] \mathrm{d}\Gamma_\infty(\mathbf{q})$$
$$= \int_{\Gamma_\infty} \left[ikG(\mathbf{p}, \mathbf{q}) - \frac{\partial G(\mathbf{p}, \mathbf{q})}{\partial n(\mathbf{q})} \right] \phi(\mathbf{q}) \, \mathrm{d}\Gamma_\infty(\mathbf{q}) \quad (3.10)$$

Now consider the kernel of the integral in (3.10) at infinity. In two-dimensional problems, the asymptotic forms of the Hankel functions are required:

$$H_0^{(1)}(kr) \sim \sqrt{\frac{2}{\pi kr}} e^{i(kr-\pi/4)}, \tag{3.11}$$

and, given $e^{i(kr-\pi/2)} = ie^{ikr}$,

$$H_1^{(1)}(kr) \sim \sqrt{\frac{2}{\pi kr}} e^{i(kr-3\pi/4)} = -i\sqrt{\frac{2}{\pi kr}} e^{i(kr-\pi/4)} = -iH_0^{(1)}(kr). \tag{3.12}$$

Substituting these asymptotic forms into (2.11) and (2.12) and, given that Γ_∞ is circular, $\partial r/\partial n \to 1$ as $r \to \infty$, the following kernel is obtained:

$$\frac{\partial G(\mathbf{p},\mathbf{q})}{\partial n(\mathbf{q})} - ikG(\mathbf{p},\mathbf{q}) = -\frac{k}{4}H_0^{(1)}(kr) + \frac{k}{4}H_0^{(1)}(kr) = 0. \tag{3.13}$$

As this integral kernel satisfies the Sommerfeld condition at infinity, the integral on Γ_∞ reduces to zero. It can, therefore, be removed from (3.7) making the equation valid for both finite and infinite regions.

For three-dimensional problems, the proof is simpler. Given that Γ_∞ is spherical, $1/r \to 0$ and $\partial r/\partial n \to 1$ as $r \to \infty$. Now, substituting this information into (2.13) and (2.14), the integral kernel is

$$\frac{\partial G(\mathbf{p},\mathbf{q})}{\partial n(\mathbf{q})} - ikG(\mathbf{p},\mathbf{q}) = ik\frac{e^{ikr}}{4\pi r} - ik\frac{e^{ikr}}{4\pi r} = 0. \tag{3.14}$$

The same logic as used in the two-dimensional case is applied making (3.7) valid for both finite and infinite regions.

3.3.3   Boundary integral equation for BEM

It is now possible to rewrite (3.7) as

$$\phi(\mathbf{p}) = \int_\Gamma \left[G(\mathbf{p},\mathbf{q})\frac{\partial \phi(\mathbf{q})}{\partial n(\mathbf{q})} - \frac{\partial G(\mathbf{p},\mathbf{q})}{\partial n(\mathbf{q})}\phi(\mathbf{q}) \right] d\Gamma(\mathbf{q}), \quad \mathbf{p} \in \Omega. \tag{3.15}$$

This is the representation integral for the solution ϕ inside Ω for a radiation problem. If the values of ϕ and $\partial\phi/\partial n$ are known on Γ, (3.15) can be used to calculate ϕ anywhere in Ω.

To use the BEM to find unknown values of ϕ and $\partial\phi/\partial n$ on Γ, (3.15) is made a 'boundary-only' equation. To do this, let $\mathbf{p}$ tend to Γ. This gives the following boundary integral equation:

$$c(\mathbf{p})\phi(\mathbf{p}) = \int_\Gamma \left[G(\mathbf{p},\mathbf{q})\frac{\partial \phi(\mathbf{q})}{\partial n(\mathbf{q})} - \frac{\partial G(\mathbf{p},\mathbf{q})}{\partial n(\mathbf{q})}\phi(\mathbf{q}) \right] d\Gamma(\mathbf{q}), \quad \mathbf{p},\mathbf{q} \in \Gamma, \tag{3.16}$$

where the value $c(\mathbf{p})$ is calculated by surrounding the point $\mathbf{p}$ by a small semi-circle

of radius ϵ and evaluating, in a Cauchy principal value sense, each term of (3.16) in the limit $\epsilon \to 0$. If Γ is smooth around $\mathbf{p}$, then $c(\mathbf{p}) = \frac{1}{2}$.

3.3.4   Incident waves

Equation (3.16) is a BIE for radiation problems that can be solved for using the BEM. For scattering problems, an incident wave $\phi^{\text{inc}}(\mathbf{p})$ must be included:

$$c(\mathbf{p})\phi(\mathbf{p}) = \int_{\Gamma} \left[G(\mathbf{p},\mathbf{q})\frac{\partial\phi(\mathbf{q})}{\partial n(\mathbf{q})} - \frac{\partial G(\mathbf{p},\mathbf{q})}{\partial n(\mathbf{q})}\phi(\mathbf{q}) \right] \mathrm{d}\Gamma(\mathbf{q}) + \phi^{\text{inc}}(\mathbf{p}). \qquad (3.17)$$

This equation is the representation integral for the solution ϕ inside Ω for a scattering problem. The incident wave is often taken to be a plane wave or spherical wave, that is:

$$\phi^{\text{inc}}(\mathbf{p}) = A^{\text{inc}} \exp\left(ik\mathbf{d}^{\text{inc}} \cdot \mathbf{p}\right), \quad \left|\mathbf{d}^{\text{inc}}\right| = 1, \qquad (3.18)$$

or

$$\phi^{\text{inc}}(\mathbf{p}) = A^{\text{inc}} \frac{\exp\left(ikr^{\text{inc}}\right)}{4\pi r^{\text{inc}}}, \qquad (3.19)$$

where $A^{\text{inc}} \in \mathbb{C}$ is the wave amplitude, $\mathbf{d}^{\text{inc}}$ is a unit vector pointing in the direction of propagation of the plane wave, and r^{inc} is the Euclidean distance between $\mathbf{p}$ and the position of the spherical source.

3.4   Numerical implementation

The BIE in (3.17) can only be solved analytically for a very small set of geometries.[‡] For more complex problems, a numerical approach is required to obtain approximate solutions. The BEM procedure can be divided up into stages:

1. application of boundary conditions;

2. discretisation of the boundary;

3. numerical integration;

4. solution of system;

5. calculation of variables at desired field points.

The following sections will discuss these steps, assuming a two-dimensional problem. Three-dimensional considerations are discussed in §6.1. There is also a brief discussion of the nonuniqueness problem in §3.4.6.

[‡]Becker [7] suggests that, though tedious, an analytical solution may be possible for any closed boundary that can be represented by a simple equation.

3.4.1   Application of the boundary conditions

In some texts, the boundary conditions are only introduced after the numerical integration. This is because the computational process of applying boundary conditions sometimes happens just before solving the matrix system. However, it can be beneficial to introduce boundary conditions earlier in the derivation, particularly for problems that use the Robin condition which fundamentally changes the BIE.

There are three common types of boundary condition:

- *Dirichlet condition* (fixed potential): the acoustic potential takes a known value over a portion of the boundary:

$$\phi(\mathbf{q}) = \bar{\phi}(\mathbf{q}) \tag{3.20}$$

- *Neumann condition* (fixed velocity): the acoustic velocity takes a known value over a portion of the boundary:

$$\frac{\partial \phi(\mathbf{q})}{\partial n(\mathbf{q})} = \frac{\partial \bar{\phi}(\mathbf{q})}{\partial n(\mathbf{q})} \tag{3.21}$$

- *Robin condition* (mixed): the derivative of the potential is expressed as a linear function of the potential:

$$\frac{\partial \phi(\mathbf{q})}{\partial n(\mathbf{q})} = \alpha(\mathbf{q})\phi(\mathbf{q}) + \beta(\mathbf{q}) \tag{3.22}$$

For wave scattering problems, the Robin condition is of most interest: $\alpha(\mathbf{q}) \in \mathbb{C}$ is an impedance property of the scatterer; $\beta(\mathbf{q}) \in \mathbb{C}$ is non-zero for active boundary conditions (radiation problems) and zero otherwise. Clearly, when $\alpha(\mathbf{q}) = 0$, the Robin condition degenerates into a Neumann boundary condition.

Substituting (3.22) into (3.17) and a small rearrangement produces a different formulation of the BIE:

$$c(\mathbf{p})\phi(\mathbf{p}) + \int_{\Gamma} \left[\frac{\partial G(\mathbf{p},\mathbf{q})}{\partial n(\mathbf{q})} - \alpha(\mathbf{q})G(\mathbf{p},\mathbf{q}) \right] \phi(\mathbf{q})\mathrm{d}\Gamma(\mathbf{q}) =$$
$$\int_{\Gamma} \beta(\mathbf{q})G(\mathbf{p},\mathbf{q})\mathrm{d}\Gamma(\mathbf{q}) + \phi^{\mathrm{inc}}(\mathbf{p}). \tag{3.23}$$

3.4.2   Discretisation of the boundary

As with many numerical approaches, the BEM is based on a discretisation procedure. Two types of approximation are made: geometrical and functional. In the FEM, approximations are made by discretising the entire solution domain into segments; in the BEM, only the boundary has to be discretised.

The first step of the BEM is to divide the entire geometrical boundary, Γ, into

E segments called *boundary elements*, such that the boundary can be expressed as

$$\Gamma = \bigcup_{e=1}^{E} \Gamma_e, \tag{3.24}$$

where none of the elements overlap, i.e.

$$\Gamma_e \bigcap \Gamma_j = \emptyset, \quad e \neq j. \tag{3.25}$$

The elements provide the geometry through the mapping

$$\Gamma_e = \{\mathbf{F}_e(\xi) : \xi \in [-1, 1]\}. \tag{3.26}$$

Now, (3.23) is written

$$c(\mathbf{p})\phi(\mathbf{p}) + \sum_{e=1}^{E} \int_{\Gamma_e} \left[\frac{\partial G(\mathbf{p}, \mathbf{q})}{\partial n(\mathbf{q})} - \alpha(\mathbf{q})G(\mathbf{p}, \mathbf{q}) \right] \phi(\mathbf{q}) d\Gamma_e(\mathbf{q}) =$$

$$\sum_{e=1}^{E} \int_{\Gamma_e} \beta(\mathbf{q})G(\mathbf{p}, \mathbf{q}) d\Gamma_e(\mathbf{q}) + \phi^{\text{inc}}(\mathbf{p}). \tag{3.27}$$

At first, it may seem that the global direction in which each element's local coordinate increases is arbitrary. However, it is conventional for the elements to "travel" clockwise for external problems and anti-clockwise for internal problems—an alternative way to consider this is to imagine walking along the elements, from the lowest value local coordinate to the highest; as one walks along the elements, the solution domain should be on one's left-hand side. The reason for this convention is to ensure than the normals, n, point out of the solution domain rather than into the domain.

Inside each element, the geometry is approximated by a constant value or by interpolation functions of some kind. Boundary elements come in a wide variety of forms, too many to list here. However, the most common types of element used, to date, in the BEM are Lagrangian elements. These have been used since the earliest BEM publications of Jaswon [60] and Symm [122]. This section will demonstrate two-dimensional quadratic Lagrange curves. Chapter 5 onwards will introduce new types of element and interpolation functions.

Figure 3.2 shows a continuous quadratic Lagrangian element. It consists of three nodes: two end nodes and a midpoint node. The two-dimensional geometry is approximated by a one-dimensional interpolation functions:

$$x(\xi) = \sum_{j=1}^{J} N_j(\xi)x_j = N_1(\xi)x_1 + N_2(\xi)x_2 + N_3(\xi)x_3, \tag{3.28}$$

$$y(\xi) = \sum_{j=1}^{J} N_j(\xi)y_j = N_1(\xi)y_1 + N_2(\xi)y_2 + N_3(\xi)y_3, \tag{3.29}$$
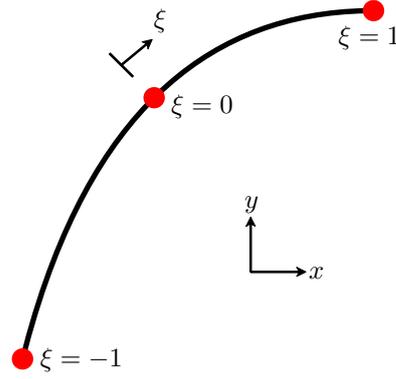
Figure 3.2: Quadratic continuous Lagrangian element.

where J is the number of shape functions on the element (3 in this case), N_j are the shape functions for the element, x_j and y_j are the global (x, y) coordinates defining the locations of the nodes, and $\xi \in [-1, 1]$ is the *local coordinate*. The shape functions are expressed as

$$N_1(\xi) = \frac{1}{2}\xi(\xi - 1), \tag{3.30}$$

$$N_2(\xi) = (1 - \xi)(1 + \xi), \tag{3.31}$$

$$N_3(\xi) = \frac{1}{2}\xi(\xi + 1). \tag{3.32}$$

Elements with these shape functions are described as continuous because each end node is shared by the two adjacent elements; it is quadratic because the shape functions are of quadratic degree; it is a Lagrangian element because the shape functions are derived from the Lagrange polynomials.

Depending on the boundary conditions applied, the variation of ϕ or its derivative is unknown; therefore a functional approximation is required. It is common to use the same interpolation functions for the approximation of the geometry and the field variables. This practise is known as *isoparametric representation* and the corresponding elements known as *isoparametric elements* (a term first used in [38]). Using this approach, the variation of ϕ over each element is defined as

$$\phi(\xi) = \sum_{j=1}^{J} N_j(\xi)\phi_j = N_1(\xi)\phi_1 + N_2(\xi)\phi_2 + N_3(\xi)\phi_3, \tag{3.33}$$

where ϕ_j are nodal values of acoustic potential ϕ. The acoustic velocity $\partial\phi/\partial n$ can be calculated similarly.

Examining (3.23), $G(\mathbf{p}, \mathbf{q})$ can be easily calculated as r, for any $\mathbf{p}$ and $\mathbf{q}$, is simply the global Euclidean distance between those two points. In order to calculate $\partial G(\mathbf{p}, \mathbf{q})/\partial n(\mathbf{q})$, the normals n need to be calculated. The starting point for this is

to calculate the tangential vector, $\mathbf{m}$:

$$\mathbf{m} = m_x \hat{\mathbf{x}} + m_y \hat{\mathbf{y}} = \frac{\mathrm{d}x(\xi)}{\mathrm{d}\xi} \hat{\mathbf{x}} + \frac{\mathrm{d}y(\xi)}{\mathrm{d}\xi} \hat{\mathbf{y}}, \tag{3.34}$$

where m_x and m_y are the vector components of $\mathbf{m}$, and, respectively, $\hat{\mathbf{x}}$ and $\hat{\mathbf{y}}$ are the unit vectors in the x and y directions. The derivatives of $x(\xi)$ and $y(\xi)$ with respect to ξ are calculated with the derivatives of the shape functions, i.e.:

$$\frac{\mathrm{d}x(\xi)}{\mathrm{d}\xi} = \sum_{j=1}^{J} \frac{\mathrm{d}N_j(\xi)}{\mathrm{d}\xi} x_j, \tag{3.35}$$

$$\frac{\mathrm{d}y(\xi)}{\mathrm{d}\xi} = \sum_{j=1}^{J} \frac{\mathrm{d}N_j(\xi)}{\mathrm{d}\xi} y_j. \tag{3.36}$$

The normal vector, $\mathbf{n}$, is related to $\mathbf{m}$ through the expression

$$\mathbf{n} = \begin{vmatrix} \hat{\mathbf{x}} & \hat{\mathbf{y}} \\ m_x & m_y \end{vmatrix} = m_y \hat{\mathbf{x}} - m_x \hat{\mathbf{y}} = \frac{\mathrm{d}y(\xi)}{\mathrm{d}\xi} \hat{\mathbf{x}} - \frac{\mathrm{d}y(\xi)}{\mathrm{d}\xi} \hat{\mathbf{x}}. \tag{3.37}$$

Thus, the vector components of $\mathbf{n}$ are

$$\begin{aligned} n_x &= \frac{\mathrm{d}y(\xi)}{\mathrm{d}\xi}, \\ n_y &= -\frac{\mathrm{d}x(\xi)}{\mathrm{d}\xi}, \end{aligned} \tag{3.38}$$

and, in order to obtain the unit normal vector components, (3.38) is divided by the magnitude of the normal vector,

$$|\mathbf{n}| = \sqrt{(n_x)^2 + (n_y)^2}. \tag{3.39}$$

3.4.3 Numerical integration of the kernels

Using the isoparametric, Lagrangian elements described in the previous section, (3.27) may be rewritten as

$$c(\mathbf{p})\phi(\mathbf{p}) + \sum_{e=1}^{E} \sum_{j=1}^{J} \int_{-1}^{1} \left[\frac{\partial G(\mathbf{p}, \mathbf{q}_\xi)}{\partial n(\mathbf{q}_\xi)} - \alpha(\mathbf{q}_\xi) G(\mathbf{p}, \mathbf{q}_\xi) \right] N_j(\xi) \phi_j^e |J_{\mathbf{F}_e}| \mathrm{d}\xi =$$

$$\sum_{e=1}^{E} \int_{-1}^{1} \beta(\mathbf{q}_\xi) G(\mathbf{p}, \mathbf{q}_\xi) |J_{\mathbf{F}_e}| \mathrm{d}\xi + \phi^{\mathrm{inc}}(\mathbf{p}). \tag{3.40}$$

where $\mathbf{q}_\xi \equiv \mathbf{q}^e(\xi)$, ϕ_j^e are the nodal values of acoustic potential on element e. Also, the integral is now written in terms of the local coordinate ξ instead of Γ_e. To make this change, the Jacobian of transformation from the mapping (3.26) is introduced. A Jacobian is used when transforming the variables of integration from one set to

another. For two-dimensional boundary elements, the Jacobian is defined as

$$|J_{\mathbf{F}_e}| = \frac{\mathrm{d}\Gamma}{\mathrm{d}\xi} = \sqrt{\left(\frac{\mathrm{d}x(\xi)}{\mathrm{d}\xi}\right)^2 + \left(\frac{\mathrm{d}y(\xi)}{\mathrm{d}\xi}\right)^2}. \tag{3.41}$$

which is the same value as the magnitude of normal vector $\mathbf{n}$.[§]

The reader may note that, in (3.40), $\phi(\mathbf{q})$ has been discretised but $\phi(\mathbf{p})$ has not. This is standard practice in BEM derivations as, for conventional implementations with Lagrangian polynomials and collocation at nodal points, this discretisation is trivial. For non-conventional implementations, such as the methods developed in this thesis, the discretisation of $\phi(\mathbf{p})$ is non-trivial. The author chooses to continue with the convention of leaving $\phi(\mathbf{p})$ unexpanded in BIEs and, instead, discretises them in a separate equation where it is relevant to do so.

At this point, (3.40) may be evaluated using suitable quadrature. The quadrature being used depends on both the boundary conditions applied and proximity of $\mathbf{p}$ to $\mathbf{q}$.

The boundary condition $\alpha(\mathbf{q}) = \beta(\mathbf{q}) = 0$ is the case of a perfectly reflecting scatterer (sometimes called the sound-hard case). If this is the boundary condition everywhere, only the derivative Green's function $\partial G(\mathbf{p}, \mathbf{q})/\partial n$ has to be calculated. Although $\partial G/\partial r$ is $\mathcal{O}(1/r)$, $\partial r/\partial n$ is $\mathcal{O}(r)$ and so the derivative Green's function is regular. Standard quadrature can be used to evaluate the entire simulation for cases like this; e.g. Gauss quadrature.

Any other boundary condition requires the evaluation of integrals containing $G(\mathbf{p}, \mathbf{q})$. These integrals are $\mathcal{O}(\log r)$ and referred to as weakly singular. The real parts of these kernels approach infinity as $r \to 0$. If $\mathbf{p}$ lies on a different element to Γ_e—and not on an element adjacent to Γ_e—then $\mathbf{p}$ and $\mathbf{q}$ are sufficiently far apart that the integrals can be evaluated using standard quadrature. For the other cases, a special integration scheme must be used. Two examples of coordinate transformation schemes follow.

Telles Transformation

In the BEM, the evaluation of singular integrals is often improved using non-linear coordinate transformations. Possibly the best known of these is the third-degree coordinate transformation of Telles [125]. The Jacobian of the transformation smoothes out the singularity of the integral.

Consider the integral

$$I = \int_{-1}^{1} f(\xi)\mathrm{d}\xi, \tag{3.42}$$

[§]N.B. this is not the same as the unit normal which obviously has a unit magnitude.

where $f(\xi)$ is singular at the point $\bar{\xi}$. Choosing a third-degree relation

$$\xi(\gamma) = a\gamma^3 + b\gamma^2 + c\gamma + d, \tag{3.43}$$

such that the following requirements are met:

$$\begin{aligned}
\left.\frac{\mathrm{d}\xi}{\mathrm{d}\gamma}\right|_{\bar{\xi}} &= 0, \\
\left.\frac{\mathrm{d}^2\xi}{\mathrm{d}\gamma^2}\right|_{\bar{\xi}} &= 0, \\
\xi(1) &= 1, \\
\xi(-1) &= -1.
\end{aligned} \tag{3.44}$$

Then a solution can be found, given by

$$\begin{aligned}
a &= 1/Q, \\
b &= -3\bar{\gamma}/Q, \\
c &= 3\bar{\gamma}^2/Q, \\
d &= -b, \\
Q &= 1 + 3\bar{\gamma}^2,
\end{aligned} \tag{3.45}$$

where $\bar{\gamma}$ is the value of γ that satisfies $\xi(\bar{\gamma}) = \bar{\xi}$. This value can be calculated by

$$\bar{\gamma} = \sqrt[3]{\bar{\xi}\xi^* + |\xi^*|} + \sqrt[3]{\bar{\xi}\xi^* - |\xi^*|} + \bar{\xi}, \tag{3.46}$$

where $\xi^* = \bar{\xi}^2 - 1$. Using this solution, (3.42) becomes

$$I = \int_{-1}^{1} \underbrace{f\left(\frac{(\gamma - \bar{\gamma})^3 + \bar{\gamma}(\bar{\gamma}^2 + 3)}{1 + 3\bar{\gamma}^2}\right)}_{f\left(\xi(\gamma)\right)} \underbrace{\frac{3(\gamma - \bar{\gamma})^2}{1 + 3\bar{\gamma}^2}}_{\mathrm{d}\xi/\mathrm{d}\gamma} \,\mathrm{d}\gamma. \tag{3.47}$$

$\mathrm{d}\xi/\mathrm{d}\gamma$ is the Jacobian which is required to use the change of variable.

The Telles transformation improves the accuracy of integration over singularities from a very small number of Gauss points; however, beyond 10 Gauss points, the accuracy of integration improves at approximately the same rate at standard Gauss-Legendre.

Sato Transformation

For two-dimensional problems, a transformation proposed by Sato [110] is more effective than the Telles transformation [119]. The Sato transformation of order $\sigma \geq 2$ is given by

$$\xi(\gamma) = \bar{\xi} - \frac{\bar{\xi}}{2^{\sigma-1}}\left(1 - \bar{\xi}\gamma\right)^\sigma. \tag{3.48}$$

As before, γ is the original Gauss point, ξ is the remapped point and the singularity lies at $\bar{\xi}$. For (3.48) to work, $\bar{\xi}$ must be ± 1. For interior singularities (i.e. $\bar{\xi} \neq \pm 1$) the interval must be partitioned at the singularity and the transformation is applied to both partitions. This makes the general transformation

$$
I = \frac{1+\bar{\xi}}{2} \int_{-1}^{1} f\left(\frac{1}{2}\left[(1+\bar{\xi})\left(1 - \frac{(1-\gamma)^\sigma}{2^{\sigma-1}}\right) + \bar{\xi} - 1\right]\right) \frac{\sigma(1-\gamma)^{\sigma-1}}{2^{\sigma-1}} \, \mathrm{d}\gamma
$$
$$
+ \frac{1-\bar{\xi}}{2} \int_{-1}^{1} f\left(\frac{1}{2}\left[(1-\bar{\xi})\left(\frac{(1+\gamma)^\sigma}{2^{\sigma-1}} - 1\right) + \bar{\xi} + 1\right]\right) \frac{\sigma(1+\gamma)^{\sigma-1}}{2^{\sigma-1}} \, \mathrm{d}\gamma. \quad (3.49)
$$

3.4.4 Solving the system of linear equations

The BIE (3.40) may be written in the compact form:

$$
c(\mathbf{p})\phi(\mathbf{p}) + \sum_{e=1}^{E} \sum_{j=1}^{J} H_j^e \phi_j^e = \sum_{e=1}^{E} Q^e + \phi^{\mathrm{inc}}(\mathbf{p}), \qquad (3.50)
$$

where H_j^e and Q^e are defined as

$$
H_j^e = \int_{-1}^{1} \left[\frac{\partial G(\mathbf{p}, \mathbf{q}_\xi)}{\partial n(\mathbf{q}_\xi)} - \alpha(\mathbf{q}_\xi) G(\mathbf{p}, \mathbf{q}_\xi)\right] N_j(\xi) |J_{\mathbf{F}_e}| \, \mathrm{d}\xi, \qquad (3.51)
$$

$$
Q^e = \int_{-1}^{1} \beta(\mathbf{q}_\xi) G(\mathbf{p}, \mathbf{q}_\xi) |J_{\mathbf{F}_e}| \, \mathrm{d}\xi. \qquad (3.52)
$$

The total number of unknown values ϕ_j^e is dependent on the number of elements that describe the scatterer and the degree of those elements. There may also be multiple scatterers. The total number of unknowns, or degrees of freedom, is denoted N_{dof}. (3.50) is then a linear equation with N_{dof} unknowns values.

To find the values of ϕ_j^e at all the element nodes, a collocation approach is used. (3.50) is evaluated with N_{dof} different locations of $\mathbf{p}$. The simplest, and most effective, way of doing this is to collocate at each node successively. This produces a system of linear equations that can be expressed in the matrix form

$$
\left[\mathbf{C} + \mathbf{H}\right] \left\{\phi\right\} = \left\{\mathbf{q} + \phi^{\mathrm{inc}}\right\}, \qquad (3.53)
$$

where the $\mathbf{C}$ matrix results in interpolations of $c(\mathbf{p})\phi(\mathbf{p})$ using (3.33); the $\mathbf{H}$ matrix is fully populated with integrals from (3.51); ϕ is a vector of the unknown potentials ϕ_j^e; the vector $\mathbf{q}$ is full of integrals from (3.52); and ϕ^{inc} is a vector containing the incident wave potentials of (3.18) or (3.19).

In the conventional BEM, like this, the $\mathbf{C}$ matrix is actually a diagonal matrix containing the value of $c(\mathbf{p})$ for each collocation point. For a smooth boundary, this is $\frac{1}{2}$. In the formulations in later chapters, where collocation points do not all lie on nodal points, the $c(\mathbf{p})\phi(\mathbf{p})$ terms have to be evaluated more explicitly and so this matrix becomes more complicated.

The system in (3.53) is of the form $\mathbf{Ax} = \mathbf{b}$. The columns of $\mathbf{A}$ are associated with the coefficients of each degree of freedom (ϕ_j^e in this case); the rows are associated with each collocation point $\mathbf{p}$. This square system can be solved to find the unknowns values using a direct technique such as Gaussian elimination.

3.4.5 Calculation of internal field variables

After solving the system of linear equations, all the unknown values of potential are known. It is then a straightforward procedure to determine the potential at any point in Ω. For points on the surface of the scatterer, the values of potential can be approximated using (3.33). For $\mathbf{p} \notin \Gamma$, the BIE in (3.50) can be used where $c(\mathbf{p}) = 1$. As $\mathbf{p}$ and $\mathbf{q}$ will not be coincident, no special integration schemes need to be considered unless $\mathbf{p}$ lies very close to Γ. Figure 3.3 shows some examples of external values calculated during acoustic analysis of the geometry in Figure 3.1.

It is well-known that the accuracy of approximations of field variables inside the solution domain are more accurate those on the boundary of any given domain [7].

3.4.6 Nonuniqueness

As discussed in §3.2.3, the conventional BEM formulation suffers from a nonuniqueness problem at eigenfrequencies of the interior Dirichlet problem of the same geometry. This is a purely mathematical artefact and is not connected to the physical problem. Many different schemes to overcome this problem have been developed but the most commonly cited are the CHIEF method [111] and the Burton-Miller formulation [20]. The CHIEF method is used throughout the work in this thesis.

CHIEF

The CHIEF method adds extra equations to the matrix system. These new rows are calculated using collocation points placed inside the scatterer; these new points are referred to as *CHIEF points*. The matrix coefficients are calculated using (3.50); the value of $c(\mathbf{p})$ for all CHIEF points is zero and no special integration schemes need to be used.

This creates a new system of linear equations that is rectangular, or overdetermined. A suitable solver must be chosen in order to solve this system. It is possible to create a square system again: one can add the CHIEF equations into existing rows of the system or existing rows can be removed and replaced by some CHIEF rows. Both of these approaches create a square system and both provide unique solutions at all frequencies. However, both approaches also reduce the accuracy of the BEM: at regular frequencies not associated with eigenfrequencies of the interior problem, a higher accuracy is always obtained with a square system of conventional BEM equations compared to either including CHIEF equations in existing rows or replacing conventional BIE equations with CHIEF ones.
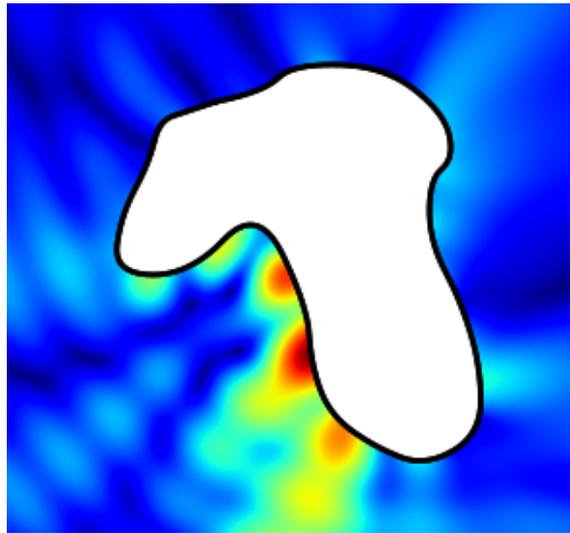
(a) $k = 1$
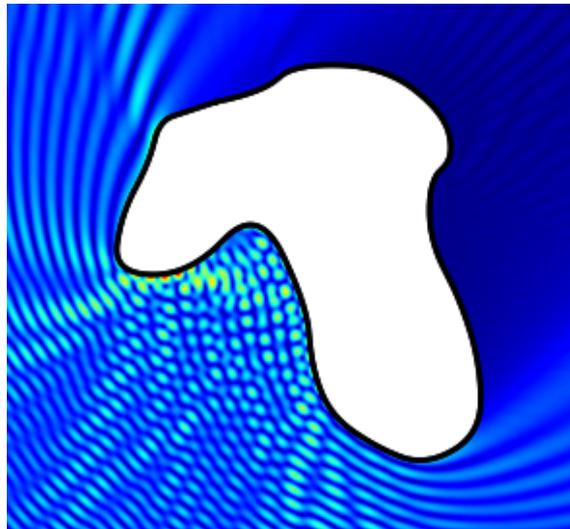
(b) $k = 5$
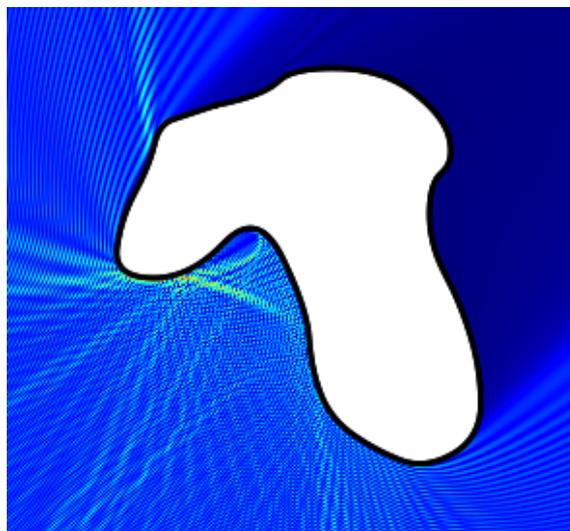
(c) $k = 20$

Figure 3.3: Examples of acoustic waves, of different wavelengths, impinging the scatterer from Figure 3.1; absolute total potential is shown.

One criticism of this method is that if all of the CHIEF points lie on nodal lines associated with the interior Dirichlet problem, the method does not work. It is suggested that for problems of higher frequencies, where these nodal lines are closer, the task of placing these points gets harder. However, throughout the work in this thesis, and the work of other authors [9, 41], this situation has not occurred.

Burton-Miller formulation

The Burton-Miller formulation invokes the use of the *hypersingular boundary integral equation* (HBIE). This is obtained by taking the derivative of (3.23) with respect to the normal at $\mathbf{p}$, giving

$$\tilde{c}(\mathbf{p})\frac{\partial\phi(\mathbf{p})}{\partial n(\mathbf{p})} + \int_\Gamma \left[\frac{\partial G^2(\mathbf{p},\mathbf{q})}{\partial n(\mathbf{p})\partial n(\mathbf{q})} - \alpha(\mathbf{q})\frac{\partial G(\mathbf{p},\mathbf{q})}{\partial n(\mathbf{p})}\right]\phi(\mathbf{q})\mathrm{d}\Gamma(\mathbf{q}) =$$
$$\int_\Gamma \beta(\mathbf{q})\frac{\partial G(\mathbf{p},\mathbf{q})}{\partial n(\mathbf{p})}\mathrm{d}\Gamma(\mathbf{q}) + \frac{\partial\phi^{\mathrm{inc}}(\mathbf{p})}{\partial n(\mathbf{p})}. \quad (3.54)$$

Here, $\tilde{c}(\mathbf{p})$ is $\frac{1}{2}$ if Γ is smooth; $n(\mathbf{p})$ represents the normal at $\mathbf{p}$; and the second derivative Green's function is expressed as, for two-dimensional problems,

$$\frac{\partial G^2(\mathbf{p},\mathbf{q})}{\partial n(\mathbf{p})\partial n(\mathbf{q})} = \frac{ik}{4r}H_1^{(1)}(kr)n(\mathbf{p})n(\mathbf{q}) - \frac{ik^2}{4}H_2^{(1)}(kr)\frac{\partial r}{\partial n(\mathbf{p})}\frac{\partial r}{\partial n(\mathbf{q})}, \quad (3.55)$$

and for three-dimensional problems,

$$\frac{\partial G^2(\mathbf{p},\mathbf{q})}{\partial n(\mathbf{p})\partial n(\mathbf{q})} = \frac{e^{ikr}}{4\pi r^3}\left[(k^2r^2 + 3ikr - 3)\frac{\partial r}{\partial n(\mathbf{p})}\frac{\partial r}{\partial n(\mathbf{q})} + (1 - ikr)n(\mathbf{p})n(\mathbf{q})\right]. \quad (3.56)$$

The hypersingular BIE is so-called because the second derivative Green's function is hypersingular. Use of (3.54) requires either a regularisation or special integration scheme.

The HBIE can be used to solve BEM problems on its own; however, the HBIE also suffers from a nonuniqueness—now associated with the interior Neumann problem. The Burton-Miller formulation uses the combination of the CBIE (3.23) and HBIE (3.54), in the form:

$$\mathrm{CBIE} + \gamma_{\mathrm{BM}}\mathrm{HBIE} = 0, \quad (3.57)$$

where $\gamma_{\mathrm{BM}} \in \mathbb{C}$ is a coupling parameter, found to be optimal when $\gamma = i/k$. This combined BIE yields unique solutions at all frequencies; however, the complexity of the regularisation schemes in the current literature can make the formulation unappealing.

4

Enriched methods for medium-wavelength problems

The previous chapter introduced the conventional BEM that has been well-established for a number of years. Contemporary BEM approaches have been developed for efficient and fast analysis of *mediumwave* and *shortwave* problems. Such problems are those in which the wavelength being considered is smaller or much smaller than the other parameters of the problem; e.g. the size of the scatterer or domain. The following section draws attention to a variety of methods that have been developed for these problems, not just those that can be called boundary element methods. §4.2 then introduces the type of enrichment used in the work of this thesis.

4.1 Mediumwave and shortwave problems

Conventional BEM schemes require meshes to be refined as the wavelength, λ, of a problem decreases. Using a conventional, low-order, piecewise polynomial basis, there exists a heuristic rule that prescribes a minimum of 10 degrees of freedom per wavelength in each local coordinate direction in order to obtain an 'engineering accuracy' ($\sim 1\%$). This is not unique to the BEM and similar restrictions exist when using finite element and meshless methods. Finite element approximations at large k may, moreover, require a finer discretisation still in order to avoid excessive pollution errors [58]. In effect, this places an upper limit on the frequency that may be considered for a problem given a specific computational resource. Much research since the 1990s has been focused on increasing this limit so that problems with a short wavelength may be solved even with a modest computational resource.

In 1995, Abboud *et al.* [1] showed that, for a convex scatterer of size much greater than λ, the scattered potential may be approximated as the product of a slowly varying function and the incident wave impinging the scatterer. This varying function can be obtained by approximating it over the boundary of the scatterer using a boundary element scheme. Bruno *et al.* [18] restricted the interval over which the boundary integrals were performed to small regions in the immediate vicinity of stationary points; it was shown that the complexity of this approach is

independent of the wavenumber. Results for scatterers of dimension $10^6\lambda$ were given. Langdon and Chandler-Wilde [77] showed that this same approach is suitable for polygonal scatterers. In 2007, Domínguez *et al.* [42] demonstrated that, to maintain a fixed error bound for problems of asymptotically large wavenumbers, the required number of degrees of freedom increases only with $\mathcal{O}(k^{1/9})$. Anand *et al.* [2] have extended the approach for problems of multiple scatterers.

An extension of these ideas was to consider a basis using multiple plane waves. Such a method, the partition of unity method (PUM), was first implemented for an integral equation approach in 1994 by de la Bourdonnaye [39]. However, it was presented under the name "microlocal discretization". It was introduced for finite element analysis by Melenk and Babuška between 1996 and 1997 [3, 87]. It was developed for use with FEM to solve localised problems in models where mesh refinement was unsuccessful. Melenk and Babuška presented a generalised approach of using approximation spaces enriched by a set of functions known to populate the solution space of the differential equation under consideration; for wave problems, sets of plane waves were proposed [88]. Work on this approach was extended for 2D acoustics by Laghrouche *et al.* [75, 76] and for 3D acoustics by Perrey-Debain *et al.* [97]. The partition of unity finite element method (PUFEM) allowed the use of *a priori* knowledge of behaviour in element space and made these spaces 'meshless'.

The PUFEM falls into a group of methods known collectively as Trefftz methods or hybrid Trefftz methods. A Trefftz method uses *a priori* knowledge of the nature of a problem directly in the approximation space; a hybrid Trefftz method (such as PUFEM) uses such functions in conjunction with other functions (such as FEM shape functions). Other FEM- or Galerkin-based Trefftz methods that have been developed for shortwave scattering problems include: the ultra-weak variational formulation (UWVF), the discontinuous enrichment method (DEM), the variational theory of complex rays (VTCR), and the discontinuous Galerkin method.

The UWVF was first implemented in 2D by Cessenat and Després [25, 26], the UWVF is similar to the FEM except the trial functions are based on the Green's function of the problem. Extra boundary conditions are applied on element interfaces that weakly enforce continuity. Huttunen *et al.* [57] later compared the UWVF to the PUFEM with the former achieving more accurate results for higher wavenumbers. Luostari *et al.* implemented the UVWF in 3D [84] and developed a UVWF using Bessel functions of the first kind instead of plane waves [83];

The DEM was proposed by Farhat *et al.* [44, 45]. The approach is similar to PUFEM except the plane wave enrichment is added to the shape functions rather than multiplied by them. The approach was implemented in 3D by Massimi *et al.* [86].

The VTCR was proposed by Ladevèze *et al.* [74]. In it, the solution is approximated through an integral superposition of plane waves. Boundary conditions are enforced in a weak sense. The approach was applied to 3D acoustic problems by

Kovalesky *et al.* [71] and and Riou *et al.* [103].

In was only in 2002 that the first BEM implementation was made, referring to the PUM. A collocation partition of unity BEM (PU-BEM) for wave simulations was developed by Perrey-Debain *et al.*; this was done first for 2D simulations [98] and later for 3D simulations [97]. It was proposed that, like [76], solving short wave problems would be easier if the waves were modelled as linear combinations of plane waves and a new type of boundary element was used which incorporated wave shapes into the element shape function. Using this technique significantly reduced the number of nodes required; it actually meant that there could be more than one wavelength between nodes. The method was derived and numerical examples were given, solved using singular value decomposition (SVD). It was concluded that, through the use of the plane wave basis boundary elements, the supported frequency range could be extended by a factor of 3–4 [99]. The PUM has also been applied to the Galerkin BEM by Chandler-Wilde and Langdon [27] and Bériot *et al.* [10].

In 2004, a theme issue of *Philosophical Transactions A* titled 'Short-Wave Scattering' was edited by Bettess *et al.* [12]. Bettess wrote an article [11] reviewing the problem of shortwaves and techniques that had been developed to address these. Bettess covered a range of approaches for the FEM, finite difference (FD) methods and the BEM. On the subject of the PU-BEM, Bettess took note of the large error reductions of the method but said that error indicators were needed for an adaptive scheme to choose wave directions; if this was accomplished, Bettess said, the PU-BEM would be "one of the most powerful" methods available.

In 2010, Trevelyan and Coates [128] published an article effectively answering Bettess' call for an adaptive scheme for the choice of number of waves in the PU-BEM. They noted that, when looking at the errors of a solution along single elements, the most significant errors appear only near the ends. They suggested that a solution with very few waves—or a low estimate—could be calculated and then the error near the end of each element could be evaluated. If the error was above a prescribed error tolerance, more waves would be added to this element to improve the solution. Then, for each new wave, a new collocation point would be prescribed and a row of the influence matrix evaluated. It was said that this method could be quicker than simply choosing more waves before running a simulation. Two numerical examples were given involving scattering by two-dimensional cylinders and the authors concluded by saying that they expected greater advantages to be gained in three-dimensional scattering problems.

4.2   Partition of unity BEM

In this section, the partition of unity BEM (PU-BEM) for two-dimensional acoustic problems will be derived. The advance to three dimensions is considered in Chapter 6.

The PU-BEM involves enriching the approximation space of a BEM simulation with linear expansions of plane waves. In the conventional BEM, the potential on Γ_e is expressed as the sum of the nodal potentials multiplied by their respective shape functions. In PU-BEM simulations, the nodal potentials ϕ_j^e are expressed as a summation of plane waves, such that (3.33) is reformulated as

$$\phi^e(\mathbf{q}(\xi)) = \sum_{j=1}^{J} N_j^e(\xi) \sum_{m=1}^{M} A_{jm}^e \exp\left(ik\mathbf{d}_{jm}^e \cdot \mathbf{q}\right), \tag{4.1}$$

where there are M plane waves in each expansion with prescribed directions of propagation $\mathbf{d}_{jm}^e \in \mathbb{R}^2$ and unknown amplitudes, $A_{jm}^e \in \mathbb{C}$.

Substitution of (4.1) into (3.40) or (3.50) yields

$$c(\mathbf{p})\phi(\mathbf{p}) + \sum_{e=1}^{E}\sum_{j=1}^{J}\sum_{m=1}^{M} H_{jm}^e A_{jm}^e = \sum_{e=1}^{E} Q^e + \phi^{\mathrm{inc}}(\mathbf{p}), \tag{4.2}$$

where Q^e is the same as in (3.52) and H_{jm}^e is defined as

$$H_{jm}^e = \int_{-1}^{1}\left[\frac{\partial G(\mathbf{p},\mathbf{q}_\xi)}{\partial n(\mathbf{q}_\xi)} - \alpha(\mathbf{q}_\xi)G(\mathbf{p},\mathbf{q}_\xi)\right] N_j^e(\xi)\exp\left(ik\mathbf{d}_{jm}^e \cdot \mathbf{q}\right)|J_{\mathbf{F}_e}|\mathrm{d}\xi, \tag{4.3}$$

where $\mathbf{q}_\xi \equiv \mathbf{q}(\xi)$. This is the discretised form of the BIE for PU-BEM which can be collocated to solve the Helmholtz equation. The resulting system takes a similar form to (3.53):

$$\left[\mathbf{C} + \mathbf{H}\right]\left\{\mathbf{A}\right\} = \left\{\mathbf{q} + \phi^{\mathrm{inc}}\right\}. \tag{4.4}$$

The vector $\mathbf{A}$ replaces the vector ϕ and contains the unknown A_{jm}^e. The $\mathbf{C}$ matrix is no longer a diagonal matrix and the entries of each row must be evaluated as

$$c(\mathbf{p})\phi(\mathbf{p}(\xi)) = \underbrace{c(\mathbf{p})\sum_{j=1}^{J} N_j^{\bar{e}}(\xi)\sum_{m=1}^{M}\exp\left(ik\mathbf{d}_{jm}^{\bar{e}} \cdot \mathbf{p}\right)\ A_{jm}^{\bar{e}},}_{\mathbf{C}\text{ matrix term that multiplies unknown } A_{jm}^e} \tag{4.5}$$

where $c(\mathbf{p}) = \frac{1}{2}$ for a smooth scatterer and $\bar{e}$ is the element on which $\mathbf{p}$ lies; i.e. the equation is only evaluated on the single element on which the collocation point $\mathbf{p}$ lies and is evaluated as zero elsewhere.

In addition to the change in the BIE, the partition of unity expansions introduce other implementation concerns:

- the choice of M;

- the choice of $\mathbf{d}_{jm}^e$;

- the requirement of additional collocation points;

- the new type of function to be integrated.

4.2.1 M and $\mathbf{d}^e_{jm}$

The parameter τ is introduced as a measure of computational efficiency. It is defined as the number of total degrees of freedom, N_{dof}, divided by the number of wavelengths that describe the boundary, Γ; i.e.

$$\tau = \frac{N_{\text{dof}}}{P_\Gamma/\lambda} = \frac{N_{\text{dof}}\Gamma_\ell}{\lambda}, \tag{4.6}$$

where P_Γ is the perimeter of Γ. The more degrees of freedom used to solve a problem, the larger τ becomes and the less efficient that method is considered to be. Similarly, if N_{dof} is fixed but the wavelength of a problem increases (which is considered computationally less complicated), τ increases too. It is desirable to develop algorithms and approaches that require the lowest τ for a given accuracy.

As mentioned in Chapter 1, a heuristic rule states that (to obtain a approximation with an error of approximately 1%) conventional numerical simulations (using linear or quadratic polynomial elements) require 10 degrees of freedom per wavelength. Another way of stating this is that simulations require $\tau \approx 10$ for an error of 1%. Work concerning two-dimensional problems has suggested that PU-BEM simulations of mediumwave problems require only $\tau \approx 3$ to obtain an error of $\leq 1\%$. This requirement drops further as problems approach the shortwave region, with $\tau \approx 2$ being possible [99].

In conventional BEM simulations, N_{dof} is typically increased though h- of p-refinement: using more elements of smaller size or increasing the order of approximation on elements. It should be noted, however, that hp-adaptive refinement and high order elements have recently been shown to produce promising results for electromagnetic scattering [105, 121].

In PU-BEM, one is free to increase τ simply by increasing M (a process referred to in this work as m-refinement). This includes more plane waves in the basis but leaves the geometry mesh unchanged. M can also be set globally or locally (in effect, having M^e_j). In [99], it was found that m-refinement and using fewer, larger elements provides a greater accuracy than the other two types of refinement.

The plane wave directions $\mathbf{d}^e_{jm}$ are defined to be equally distributed around the unit circle, explicitly for M^e_j plane waves in an expansion:

$$\mathbf{d}^e_{jm} = \left(\cos\theta^e_{jm}, \sin\theta^e_{jm}\right), \quad \theta^e_{jm} = \frac{2m\pi}{M^e_j + 1} + \theta^{\text{inc}}, \tag{4.7}$$

where θ^{inc} is the angle of incidence of the incident plane wave. Including the θ^{inc} term guarantees the inclusion of the incident wave direction in the basis. This direction is included because, for asymptotically large k, the potential in the illuminated zone takes a value of $2\phi^{\text{inc}}$. It should be noted that θ^{inc} does not have to be included in (4.7) and highly accurate results are still obtained if it is omitted. For problems of multiple incident waves, each incident wave could be included in the basis; however,

if incident angles are very similar, this could lead to poor conditioning of the system matrices.

4.2.2   Collocation

The inclusion of multiple plane waves—and thus degrees of freedom—on each element means that collocation at nodes no longer provides a sufficient number of collocation points. To find the potential on Γ, (4.2) is collocated at a set of N_{dof} collocation points to produce the matrix system (4.4).

In early PU-BEM work [98, 99], collocation points were equally spaced on the scatterer. This choice was arbitrary and an investigation of collocation schemes is carried out in §5.9.

4.2.3   Integration

It should be noted that for wave problems the Green's function is oscillatory and that all integrals need to be evaluated using a sufficient number of points to capture that oscillation, even in the far field. This is true for a conventional BEM as well as a plane wave enriched BEM. Thus, the fact that plane wave enriched BEM approximations involve elements that can span many wavelengths does not, in itself, necessarily increase the total number of integration points required to assemble the system of equations. However, the inclusion of the plane wave enrichment does have some implications on the required number of integration points required on a single element: elements that span many wavelengths require more integration points than those that do not span many wavelengths.

The enrichment may also change the apparent wavelength of the oscillatory integrand to $\bar{\lambda}$, where $\bar{\lambda} \in (0, 2\lambda)$. For this reason, although some authors have presented novel integration schemes that offer promise for rapid evaluation of these boundary integrals [28, 55, 67], it was not possible to implement them in the work presented in this thesis. The work was, instead, aimed at demonstrating novel formulations for the first time and showing that it was possible to reduce the number of degrees of freedom required for simulations.

4.3   Further notes on PU-BEM

The literature on the PU-BEM obviously highlights many of the positive aspects of the method in comparison to conventional BEM schemes. However, like all computational methods, there are limiting factors or drawbacks. The lack of efficient integration schemes has been been mentioned already (§4.2.3); however, there are two further concerns.

4.3.1   Conditioning

Mathematically speaking, the *condition number* of a matrix **A** is the ratio of its maximal and minimal singular values, σ, or absolute value of the ratio of its maximal and minimal eigenvalues, λ:

$$\kappa(\mathbf{A}) = \frac{\sigma_{\max}(\mathbf{A})}{\sigma_{\min}(\mathbf{A})} = \frac{\lambda_{\max}(\mathbf{A})}{\lambda_{\min}(\mathbf{A})}. \tag{4.8}$$

From a more engineering perspective, the condition number of a matrix in an $\mathbf{Ax} = \mathbf{b}$ system describes the amount by which a small change in the coefficients of **b** causes a change in **x**. In other words, it is a measure of how much the result can change given errors in the calculation of the coefficients.

A matrix with a small condition number is considered to be *well-conditioned*, while a matrix with a large condition number is considered *ill-conditioned*. According to Cheney and Kincaid [31], a general rule of thumb is: for a condition number of 10^k, one may lose k digits of accuracy in addition to any numerical loses due to the precision used in a computational implementation. Despite this, throughout the work in this thesis, it was found that even with condition numbers in excess of 10^{16} it was still possible to obtain some solutions accurate up to the 7th and 8th decimal place.

Conventional BEM matrices are generally well-conditioned. This means that fast, direct solvers can be used to solve the resulting systems. Conversely, PU-BEM matrices are generally ill-conditioned and require a robust solver. *Singular value decomposition* (SVD) is used throughout the work in this thesis. This is a very robust least-squares solver. It is, however, slower than solvers that can be used with conventional BEM simulations. Nevertheless, integration was still found to be the longest operation in most simulations and so this work does not focus on ways to reduce κ.

4.3.2   Analytical geometry

In conventional BEM simulations, integration points are located using local coordinate systems and shape function interpolation. In earliest acoustic PU-BEM research [98], it was discovered that it was highly desirable to use an analytical geometry for collocation and integration points. If either was placed using shape function interpolation on elements, the accuracy of resulting approximations was not significantly better than those of conventional BEM simulations—if large elements were used, the approximations often had errors of $> 100\%$.

The reason for this sensitivity likely lies in the high condition numbers of the resulting matrix systems. Interpreting Cheney and Kincaid's rule, if a matrix system has a condition number of 10^{16}, then coefficients should be calculated accurately in excess of 15 decimal places; this is only really possible with an analytical geometry or very small elements.

While an analytical geometry can be provided in some cases (some of which appear in this thesis), the requirement for such a geometry is a significant limitation on PU-BEM. The major aim of this thesis was to remove this constraint and to allow any geometry to be analysed. This is the subject of Chapters 8 and 9.

5

Trigonometric shape functions

5.1 Motivation

In 2010, Trevelyan and Coates [128] presented an adaptive basis for the collocation PU-BEM. During this work, they made observations of the error in potential along PU-BEM elements. A figure from their paper–a plot of the residual error over an element—can be seen in Figure 5.1. Trevelyan and Coates noted that the residual errors were largest at the ends of elements. They suggested that this was due to the lack of continuity in the C^0 Lagrangian quadratic shape functions they used.

The trigonometric shape functions in §5.3 were developed to provide improved continuity in the piecewise functions used in the PU-BEM. In addition to this work, a number of novel collocation schemes were trialled, the results of which are presented in §5.9.

5.2 Existing alternative elements

Before creating a new class of element, it is prudent to consider the existing alternatives. Two common alternatives are Overhauser elements and Hermite elements. They are briefly discussed in this section. B-spline elements have also been used but are discussed in Chapter 7.
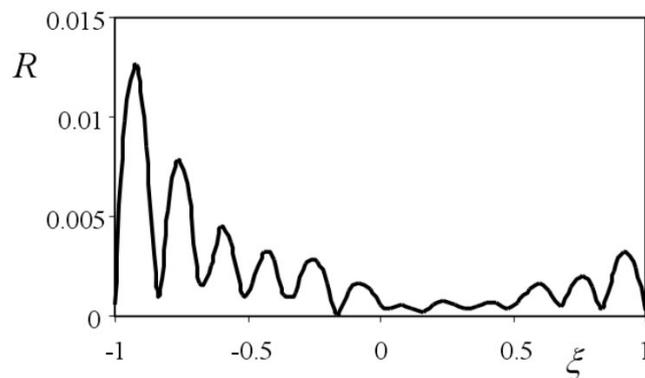
Figure 5.1: Plot of residual error over an element, taken directly from [128].
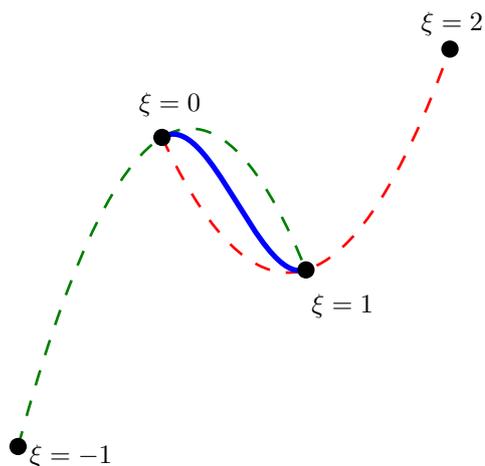
Figure 5.2: Typical cubic Overhauser element.
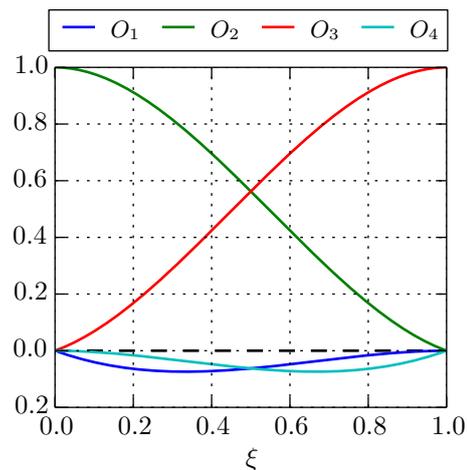
Figure 5.3: Cubic Overhauser element shape functions.

5.2.1 Overhauser elements

Overhauser elements have C^1 continuity. They were first used in BEM simulations by Ortiz *et al.* [95] for a two dimensional Poisson problem. Liu and Rizzo [81] have reported successful results when using them for three-dimensional acoustic wave problems. Their use in boundary element analysis was investigated more generally by Camp and Gipson [23].

Overhauser elements (shown in Figure 5.2) are blended cubic curves formed from the linear combination of two overlapping parabolas. The first parabola is defined on the local coordinate $\xi \in [-1, 1]$ and the second on $\xi \in [0, 2]$. The blended curve is defined for $\xi \in [0, 1]$ and expressed as

$$\psi(\xi) = \sum_{i=1}^{4} O_i(\xi)\psi_i = O_1(\xi)\psi_1 + O_2(\xi)\psi_2 + O_3(\xi)\psi_3 + O_4(\xi)\psi_4 \qquad (5.1)$$

where ψ is the field variable, ψ_i are nodal values of the field variable, and O_i are the Overhauser shape functions given by

$$O_1(\xi) = -\frac{1}{2}(\xi - 2\xi^2 + \xi^3), \qquad (5.2)$$

$$O_2(\xi) = \frac{1}{2}(2 - 5\xi^2 + 3\xi^3), \qquad (5.3)$$

$$O_3(\xi) = \frac{1}{2}(\xi + 4\xi^2 - 3\xi^3), \qquad (5.4)$$

$$O_4(\xi) = -\frac{1}{2}(\xi^2 - \xi^3). \qquad (5.5)$$

These shape functions are shown in Figure 5.3.

Continuous derivatives are ensured at the end-nodes shared by adjacent elements. However, if the relative distance between nodes varies, spurious perturbations can appear in the geometry or field variable. Also, the curves are designed for geome-

tries of continuous gradients; without modification, the functions are unsuitable for geometries with corners. The overlapping nature of Overhauser elements also makes them inherently more difficult to construct meshes from compared to conventional types of continuous element.

5.2.2 Hermite elements

Hermite elements (Figure 5.4) were first used in the BEM by Watson [130]. There are no published accounts of applying these elements to problems of acoustics in two or three dimensions.

Hermite elements use Hermite polynomials and require nodes with values of the field variable and its tangential derivative. A two-dimensional Hermite curve has local coordinate $\xi \in [-1, 1]$ and is expressed as

$$\psi(\xi) = \sum_i \left[H_{1,i}(\xi)\psi_i + H_{2,i}(\xi)\frac{\partial \psi_i}{\partial s} \right] \tag{5.6}$$

where $H_{1,i}$ and $H_{2,i}$ are the shape functions associated with the ith node, ψ_i is the field variable, and s represents the tangential component at the nodal point.

Hermite elements are usually cubic (two nodes; four variables). A continuous cubic Hermite element has nodes at $\xi = -1$ and $\xi = 1$. The shape functions are defined by

$$H_{1,1}(\xi) = \frac{1}{4}(1 - \xi)(1 - \xi)(2 + \xi), \tag{5.7}$$

$$H_{2,1}(\xi) = \frac{1}{4}(1 - \xi)(1 - \xi)(1 + \xi)\frac{\partial S}{\partial \xi}\bigg|_1, \tag{5.8}$$

$$H_{1,2}(\xi) = \frac{1}{4}(1 + \xi)(1 + \xi)(2 - \xi), \tag{5.9}$$

$$H_{2,2}(\xi) = -\frac{1}{4}(1 + \xi)(1 + \xi)(1 - \xi)\frac{\partial S}{\partial \xi}\bigg|_2. \tag{5.10}$$

These shape functions are shown in Figure 5.5.

Hermite elements are rarely used as isoparametric elements as their complex form does not improve geometry approximations. Also, because Hermite elements are approximating both ψ and $\partial\psi/\partial s$, two integral equations are required to collocate. In addition to the conventional BIE (CBIE), a tangent derivative BIE (TDBIE) is used. In addition to the TDBIE, an added complication is corners: at these points, the tangential derivatives are not continuous and so a mix of continuous, partially discontinuous and fully discontinuous elements is required; there are more variations in 3D.

Though there has been some success for crack problems and with hypersingular boundary integrals [49], the complications of using Hermite interpolation appear to outweigh the potential benefits of modelling the scalar field variable of an acoustic problem.
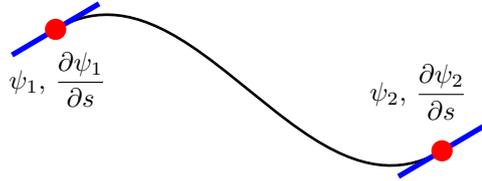
Figure 5.4: Typical 2-noded Hermite element.
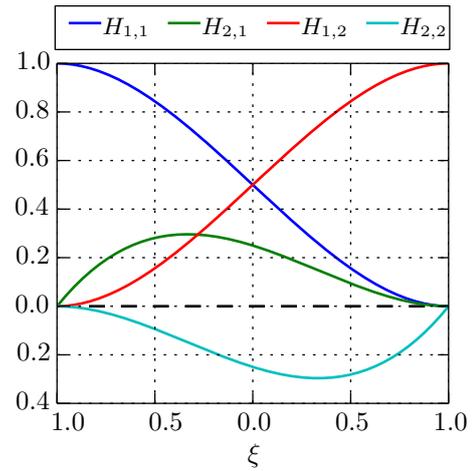
Figure 5.5: Hermite element shape functions.

5.3   Designing trigonometric shape functions

A likely source of the errors observed in [128] is the C^0 nature of Lagrangian quadratic shape functions. Figure 5.6 shows the classical quadratic shape functions expressed in (3.30)- (3.32), repeated here for convenience:

$$N_1(\xi) = \frac{1}{2}\xi(\xi - 1), \tag{3.30}$$

$$N_2(\xi) = (1 - \xi)(1 + \xi), \tag{3.31}$$

$$N_3(\xi) = \frac{1}{2}\xi(\xi + 1). \tag{3.32}$$

Each of the shape functions has non-zero gradient at the element ends; this produces a discontinuity, in the first derivative, between adjoining elements. Increasing the continuity between elements, in order to reduce these errors, is the principal aim of developing the new shape functions.

To design some shape functions with the Kronecker delta and partition of unity properties, the following rules must be obeyed:

- $N_j(\xi) = 1$ at the node j,
- $N_j(\xi) = 0$ at all other nodes, \hfill (5.11)
- $\sum N_j(\xi) = 1 \quad \forall\, \xi$.

Trigonometric functions have been chosen because they have well known smooth-
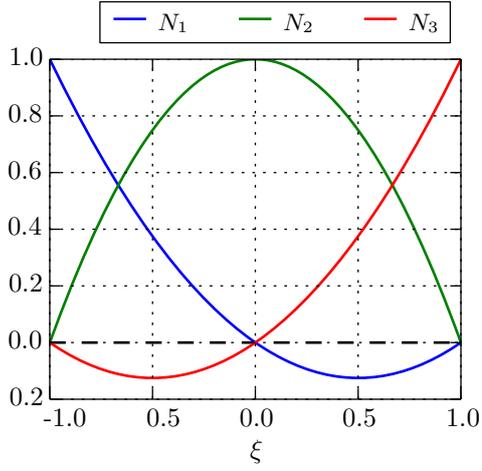
Figure 5.6: Continuous Lagrangian quadratic shape functions.
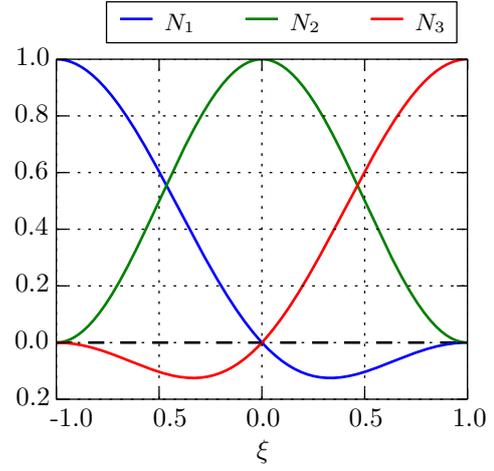
Figure 5.7: Continuous trigonometric shape functions.

ness and C^∞ continuity. Assume there is a set of shape functions of the form:

$$N_1(\xi) = \alpha_1 \cos(\pi\xi) + \alpha_2 \sin\left(\frac{\pi}{2}\xi\right) + \alpha_3, \tag{5.12}$$

$$N_2(\xi) = \alpha_4 \cos(\pi\xi) + \alpha_5 \sin\left(\frac{\pi}{2}\xi\right) + \alpha_6, \tag{5.13}$$

$$N_3(\xi) = \alpha_7 \cos(\pi\xi) + \alpha_8 \sin\left(\frac{\pi}{2}\xi\right) + \alpha_9. \tag{5.14}$$

The choice of $\cos(\pi\xi)$ and $\sin(\frac{\pi}{2}\xi)$ is somewhat arbitrary. Other combinations can (but do not always) produce unique and viable shape functions.

Taking (5.12)–(5.14), using the rules in (5.11), and assuming continuous elements with nodes at $\xi = -1, 0, 1$, three sets of three simultaneous equations are obtained. At $\xi = -1$:

$$N_1(-1) = -\alpha_1 - \alpha_2 + \alpha_3 = 1, \tag{5.15}$$

$$N_2(-1) = -\alpha_4 - \alpha_5 + \alpha_6 = 0, \tag{5.16}$$

$$N_3(-1) = -\alpha_7 - \alpha_8 + \alpha_9 = 0. \tag{5.17}$$

At $\xi = 0$:

$$N_1(0) = \alpha_1 + \alpha_3 = 0, \tag{5.18}$$

$$N_2(0) = \alpha_4 + \alpha_6 = 1, \tag{5.19}$$

$$N_3(0) = \alpha_7 + \alpha_9 = 0. \tag{5.20}$$

At $\xi = 1$:

$$N_1(1) = -\alpha_1 + \alpha_2 + \alpha_3 = 0, \tag{5.21}$$

$$N_2(1) = -\alpha_4 + \alpha_5 + \alpha_6 = 0, \tag{5.22}$$

$$N_3(1) = -\alpha_7 + \alpha_8 + \alpha_9 = 1. \tag{5.23}$$

Equations (5.15)–(5.23) can be solved to find that the shape functions are

$$N_1(\xi) = -\frac{1}{4}\cos(\pi\xi) - \frac{1}{2}\sin\left(\frac{\pi}{2}\xi\right) + \frac{1}{4}, \tag{5.24}$$

$$N_2(\xi) = \frac{1}{2}\cos(\pi\xi) + \frac{1}{2}, \tag{5.25}$$

$$N_3(\xi) = -\frac{1}{4}\cos(\pi\xi) + \frac{1}{2}\sin\left(\frac{\pi}{2}\xi\right) + \frac{1}{4}. \tag{5.26}$$

These shape functions can be seen in Figure 5.7. They have zero gradient at the element ends; partition of unity can be easily proved by taking the sum of the three shape functions; they are also C^∞ continuous in parametric space, i.e. $N_1^{(n)}(-1) = N_3^{(n)}(1) \; \forall n$.

5.4   Integration

It was briefly discussed in §4.2.3 that PU-BEM elements require care when considering the integration. This is because PU-BEM elements can be much longer than conventional BEM elements and contain many wavelengths. As a demonstration of this, Figure 5.8 shows an example of a typical integrand to be evaluated over an element in a conventional BEM simulation. The function is smooth and can be easily integrated using a conventional quadrature. Conversely, Figure 5.9 shows an example of a typical integrand to be evaluated over a PU-BEM element. Clearly a small number of quadrature points will not capture the oscillations of the integrand over the element. Indeed, using a large number of quadrature points could also be ineffective as they will cluster towards the element ends.

Instead, for the simulations in this chapter, large elements are split into N_{cells} "integration cells" that are no larger than $\lambda/4$; the length is chosen to prevent aliasing. Each cell is integrated using a 6-point Gauss quadrature on the new local coordinate system $\eta \in [-1, 1]$. The evaluated integrals in the cells can be summed over the element taking care to include both Jacobians for the mapping from the element to the ξ coordinate system, and from the ξ coordinates system to the η coordinate system.

Explaining this more generally, Figure 5.10 shows a typical element on which the function $f(x)$ is to be integrated. The integral I can be expressed

$$I = \int_{-1}^{1} f\big(x(\xi)\big) J(\xi)\,\mathrm{d}\xi \tag{5.27}$$
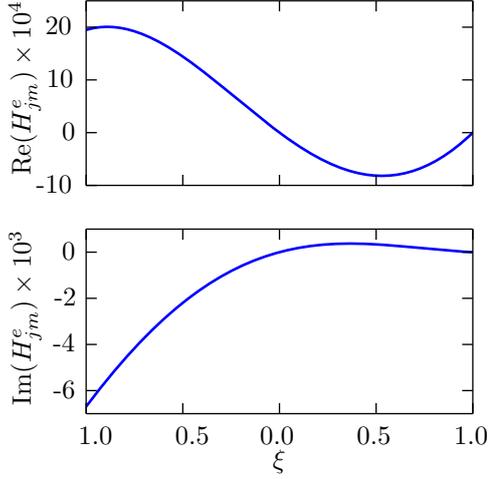
Figure 5.8: Example of H_{jm}^e over an element in a conventional BEM simulation; $k = 50$.
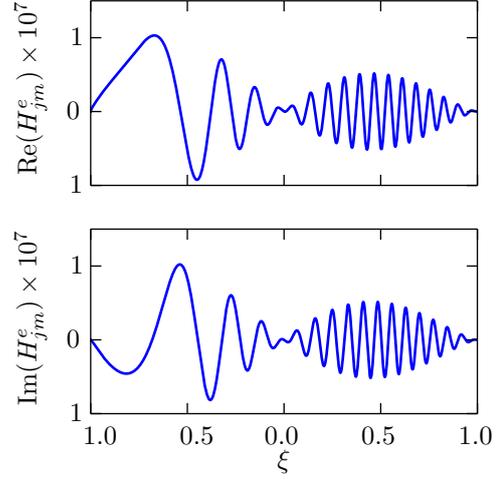
Figure 5.9: Example of H_{jm}^e over an enriched element in a PU-BEM simulation; $k = 50$.
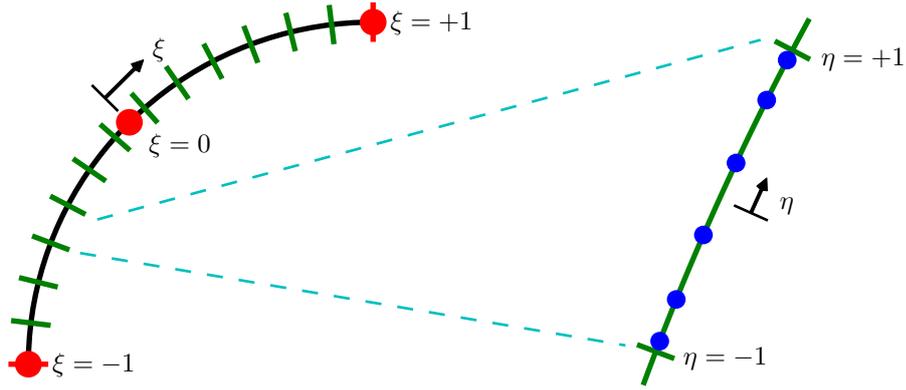
Figure 5.10: Representation of a PU-BEM element divided into integration cells. Red dots represent element nodes; green dashes represent integration cells ends; blue dots represent quadrature points.

where $J(\xi)$ is the Jacobian of transformation from the global coordinate system to local ξ system. Splitting the element into N_{cells} cells, (5.27) can now be expressed

$$I = \sum_{n=1}^{N_{\text{cells}}} \int_{-1}^{1} f\Big(x\big(\xi(\eta)\big)\Big) J(\xi) J(\eta) \, \mathrm{d}\eta \qquad (5.28)$$

where $J(\eta)$ is the Jacobian of transformation from the ξ coordinate system to the η coordinate system. $J(\eta) = 1/N_{\text{cells}}$ if the cells are of equal length in the ξ coordinate system.
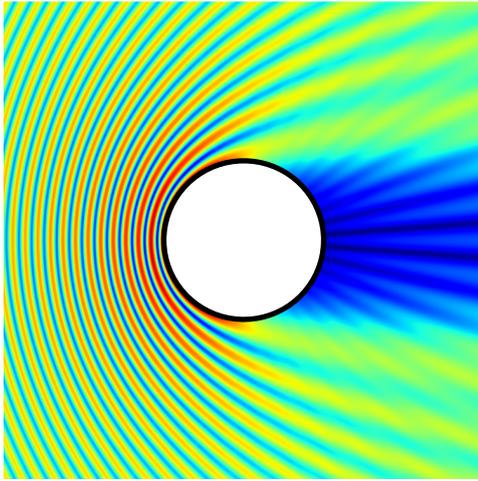
Figure 5.11: Absolute total potential, $|\phi|$, about the cylinder; $k = 20$.
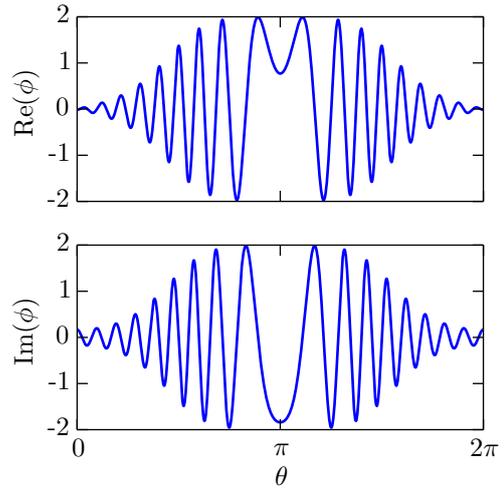
Figure 5.12: Total potential over the boundary of the cylinder; $k = 20$.
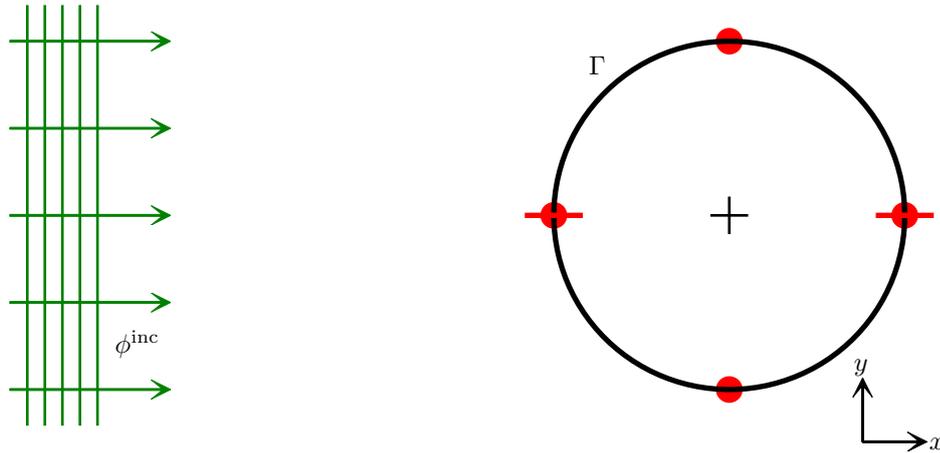
Figure 5.13: Cylinder meshed with two elements. Red lines: element ends; red dots: element nodes.

5.5 Scattering by a circular cylinder

Consider a sound-hard (Robin condition with $\alpha = \beta = 0$ or Neumann condition with $\partial\phi/\partial n = 0$) cylindrical scatterer of unit-radius ($a = 1$), centred at the origin $(0, 0)$. The scatterer is impinged by a unit-amplitude, incident plane wave that propagates in the direction $\mathbf{d} = (1, 0)$. The analytical solution for the potential on Γ is given in (2.20). An illustration of a solution in a portion of Ω can be seen in Figure 5.11. The potential over the boundary can be seen in Figure 5.12.

A high accuracy solution can be obtained by modelling this problem using just two elements and approximating the potential using PU-BEM. A representation of the problem and mesh, using continuous quadratic elements, can be seen in Figure 5.13.

Figures 5.14 - 5.16 show the absolute difference in total potential over the surface

of the cylinder evaluated by PU-BEM simulations and by analytical solution. This is displayed for PU-BEM simulations using quadratic Langrangian shape functions and for the new trigonometric shape functions of (5.24)–(5.26). The number of plane waves used in the enrichment on each shape function is noted in the caption of each figure; note that these equate to approximately 3 degrees of freedom per wavelength (τ=3). The effect of using trigonometric shape functions is clear. Using quadratic Lagrangian shape functions, the errors peak at the end of each element. Using the trigonometric shape functions, these peaks are significantly reduced in magnitude.

The total errors are also reduced: Figure 5.17 shows the L^2 errors, $\mathcal{E}$, of conventional BEM and PU-BEM simulations using Lagrangian and trigonometric shape functions. The errors are evaluated as described in (B.1), taking 10,000 equally spaced points about the cylinder surface. The conventional BEM simulations have been included to demonstrate the relative performance of PU-BEM simulations. Figure 5.17 shows conventional BEM simulations using 10 degrees of freedom per wavelength ($\tau = 10$) while the PU-BEM simulations are using 3 degrees of freedom per wavelength ($\tau = 3$). Using a third of the number of degrees of freedom means that the resulting PU-BEM system matrix is a ninth of the size of the BEM system matrix. Despite this, the PU-BEM simulations consistently give approximations of greater accuracy than the conventional BEM simulations: the errors of PU-BEM simulations are more than two orders of magnitude smaller than errors of conventional BEM simulations for $ka \geq 40$; for $ka \geq 100$, errors of PU-BEM simulations with trigonometric shape functions are approximate three orders of magnitude smaller. It should be noted that the conventional BEM meshes are not like that in Figure 5.13; many elements have to be used in order to obtain enough degrees of freedom.

In order to show that the mesh used is not a special case, Figure 5.18 shows errors similar to Figure 5.17 but using four elements. The same trends can be noted with trigonometric shape functions providing a better basis for the PU enrichment.

5.6   Scattering by five cylinders

Some schemes for high wavenumber scattering only allow for convex scatterers. This is because these methods do not always capture internal reflections well. There are some promising schemes to navigate around this problem; however, they are mathematically complicated. Conversely, the PU-BEM is very capable in such situations.

Consider a set of five sound-hard cylindrical scatters of unit radius, with centres at the polar coordinates $(3, 2n\pi/5)$ for $n = 0, 1, 2, 3, 4$; i.e. the centres are equally spaced on an imaginary circle with a radius of 3. The cylinders are impinged by a incident plane wave of unit amplitude and propagating in the direction $\mathbf{d}^{\text{inc}} = (\sqrt{2}/2, \sqrt{2}, 2)$. This geometry creates internal reflections between the cylinders; an example of this can be seen in Figure 5.19.

(a) Quadratic shape functions   **(b)** Trigonometric shape functions
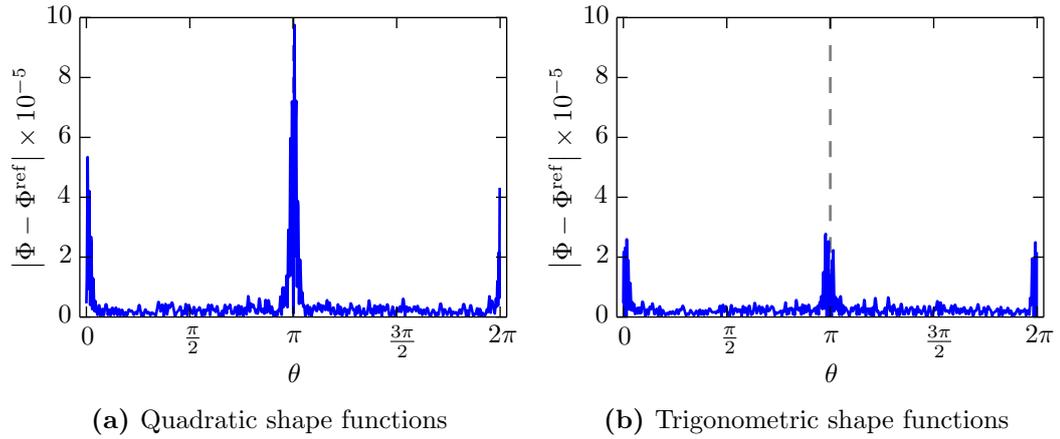
Figure 5.14: Plots of absolute difference between PU-BEM simulations against analytical solution of circular cylinder problem; dashed line represents element ends. $ka = 70$; $M = 53$; $\tau = 3.03$.

(a) Quadratic shape functions   **(b)** Trigonometric shape functions
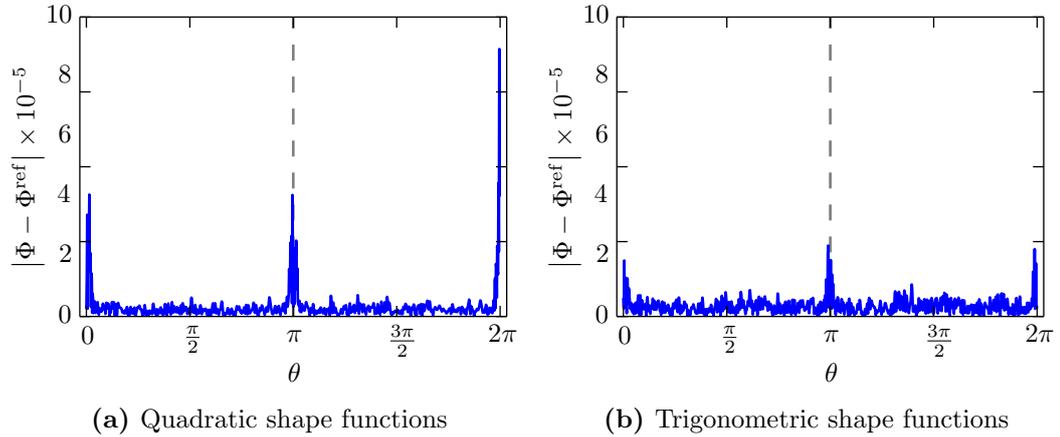
Figure 5.15: Plots of absolute difference between PU-BEM simulations against analytical solution of circular cylinder problem; dashed line represents element ends. $ka = 120$; $M = 90$; $\tau = 3.00$.

(a) Quadratic shape functions   **(b)** Trigonometric shape functions
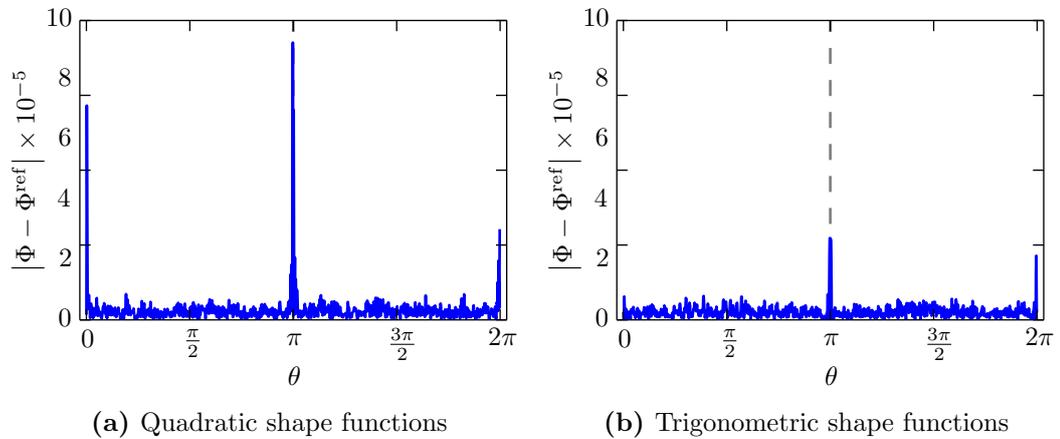
Figure 5.16: Plots of absolute difference between PU-BEM simulations against analytical solution of circular cylinder problem; dashed line represents element ends. $ka = 200$; $M = 150$; $\tau = 3.00$.
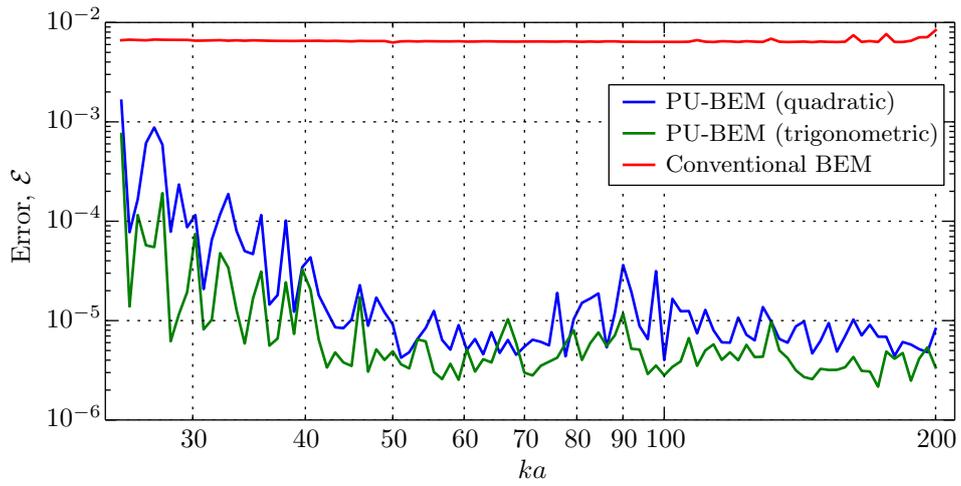
Figure 5.17: L^2 errors of simulations of cylinder problem over a spectrum; two elements per cylinder and $\tau \approx 3$ for PU-BEM; $\tau \approx 10$ for conventional BEM.
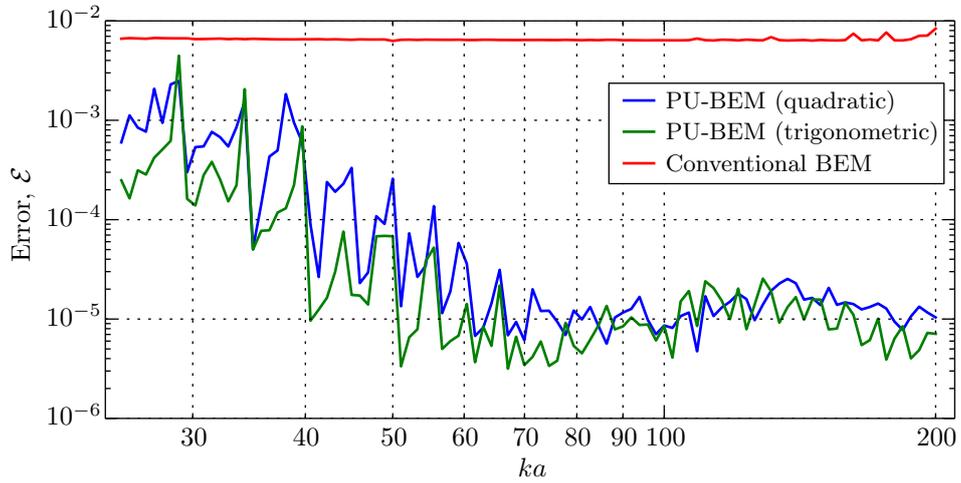
Figure 5.18: L^2 errors of simulations of cylinder problem over a spectrum; four elements per cylinder and $\tau \approx 3$ for PU-BEM; $\tau \approx 10$ for conventional BEM.
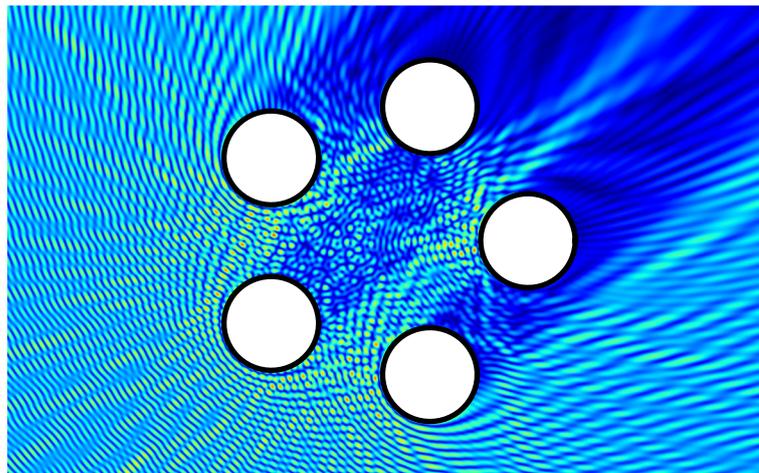
Figure 5.19: Illustration of the internal reflections caused by the five-cylinder geometry. $|\phi|$ for $k = 8\pi$ is plotted.
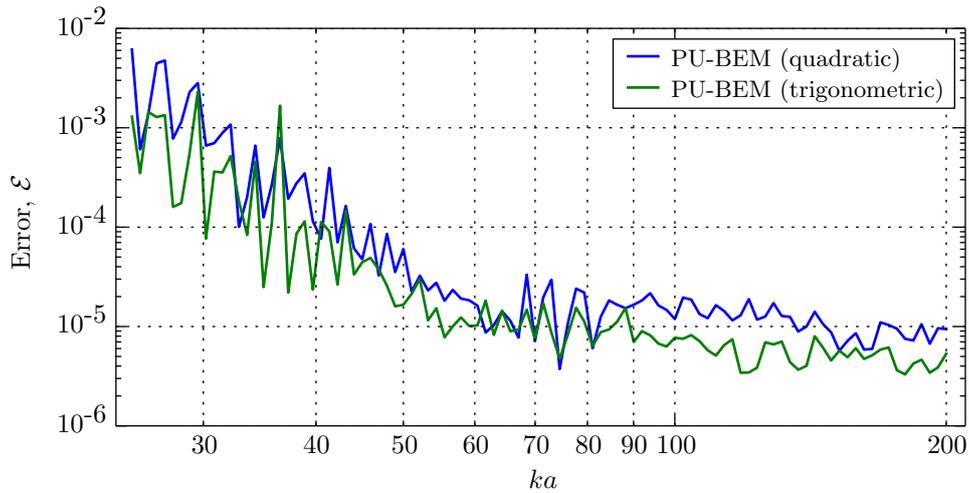
(a) Two elements per cylinder
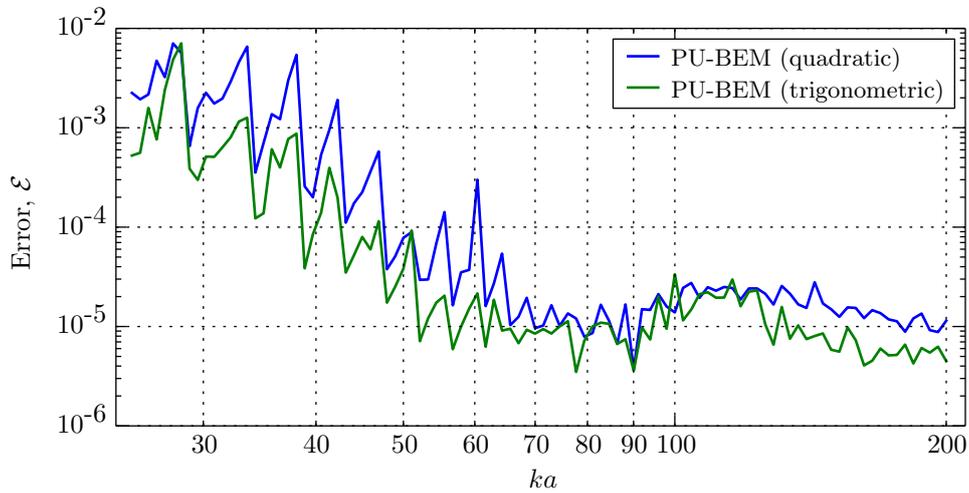
(b) Four elements per cylinder

Figure 5.20: L^2 errors of simulations of five-cylinder problem over a spectrum using (a) two element and (b) four elements per cylinder; $\tau \approx 3$.

Similar to the example in §5.5, PU-BEM simulations were run using quadratic Lagrangian and trigonometric elements. Two different meshes were used: boundary representation with two elements per cylinder and boundary representation with four elements per cylinder. The number of plane waves, M, enriching each shape function was changed in order to have approximately three degrees of freedom per wavelength ($\tau \approx 3$). The results of these simulations are displayed in Figures 5.20.

It is clear, again, that the trigonometric shape functions provide an accuracy benefit for the majority of the simulations. This is due to the increased continuity between elements.
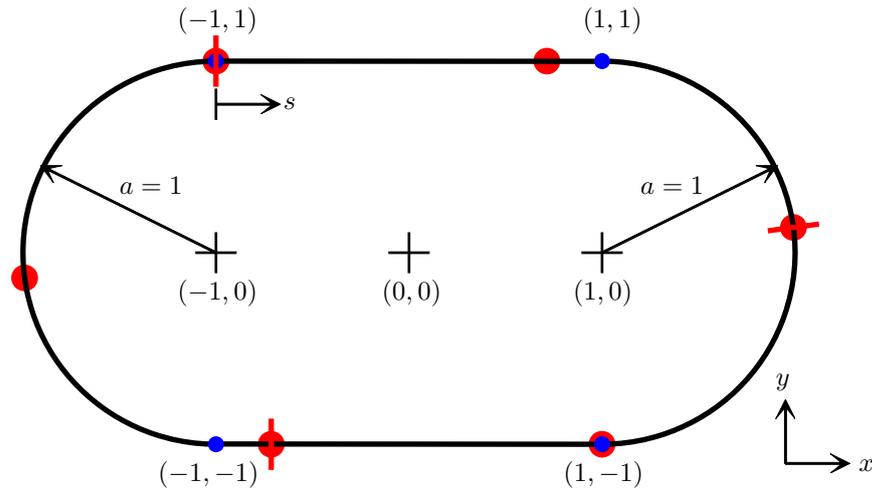
Figure 5.21: Capsule geometry discretised by three equal-length elements. Red lines: element ends; red dots: element nodes; blue dots: geometry blend points.

5.7   Scattering by a capsule

Thus far, the only numerical examples shown have had circular arcs for elements. An area of interest in other geometries is the blending points between different types of geometry component; for example, a line and an arc. This is interesting because the geometry has only C^1 continuity and the nature of the solution changes in these regions also. These regions may be susceptible to errors.

To investigate the ability of trigonometric shape functions to help capture the solution over C^1 boundaries, a capsule shape was designed consisting of two semi-circular arcs and two connecting straight sections. The capsule design can be seen in Figure 5.21

The figure shows the capsule discretised by three elements of equal length: elements of equal length provide the best approximation accuracy. As the geometry points for PU-BEM are located analytically, these elements have no impact on the evaluation of the integral kernels: collocation and integration points lie on the exact geometry.

The capsule is impinged by a unit-amplitude incident plane wave propagating in the direction $\mathbf{d}^{\text{inc}} = (1/2, \sqrt{3}/2)$. An example plot of the scattering caused by the capsule can be seen in Figure 5.22 and the potential over Γ can be seen in Figure 5.23.

Similar to the examples in §5.5 and §5.6, PU-BEM simulations were run, using quadratic and trigonometric shape functions. The parameter, τ, was kept to be approximately 3 for all simulations. There is no analytical solution for this problem and so a converged solution was used to evaluate the accuracy. Instead of comparing a boundary element solution against a boundary element solution, the *method of fundamental solutions* (MFS) [69] was used to obtain the converged solution. A short explanation of MFS is included in Appendix D.
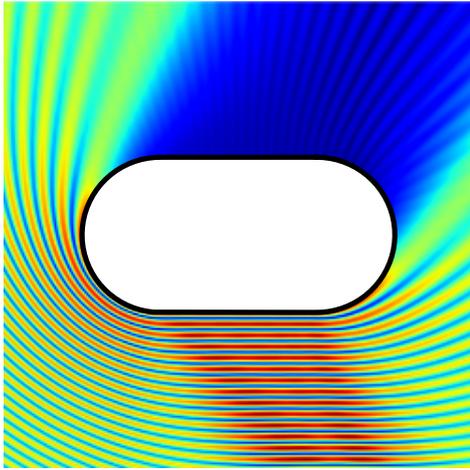
Figure 5.22: Absolute total potential; $ka = 30$.
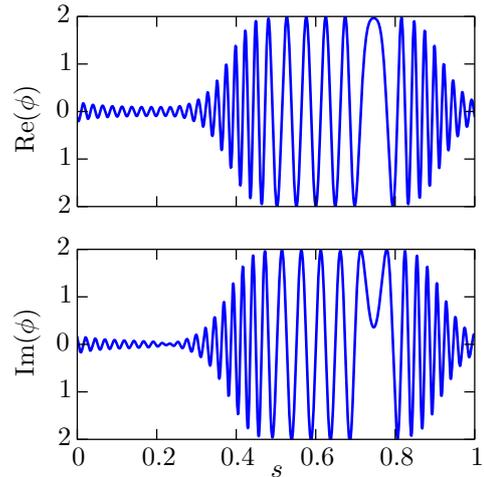
Figure 5.23: Potential over the boundary; $ka = 30$.
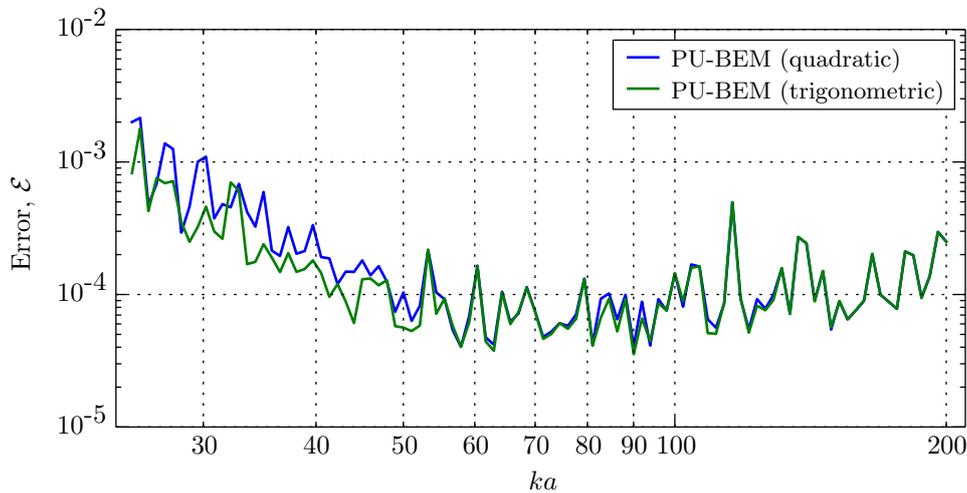
Figure 5.24: Errors of PU-BEM simulations of the capsule problem.

Figure 5.24 shows the errors, $\mathcal{E}$, of PU-BEM simulations of the capsule problem over a range of wavenumbers. The trigonometric shape functions produce accuracy benefits at lower wavenumbers; however, at higher wavenumbers, the benefits appear reduced. This is because, at high wavenumbers, there are a large number of plane waves in the expansion which become the most dominant part of the basis. For example, consider the capsule problem and unit-cylinder problem for $ka = 100$. Assuming $\tau = 3$, the potential on each node in the unit-cylinder problem (discretised with two elements) is expanded as a linear combination of $M = 63$ plane waves; for the capsule problem, the potential at each node is expanded as a linear combination of $M = 82$ plane waves. With 30% more plane waves in each expansion, these dominate the enrichment for the capsule problem and reduce the observable effect of using trigonometric shape functions.

Figure 5.25 shows the absolute difference, along the surface of the scatterer, between the PU-BEM solution and the converged MFS solution. As before, there

(a) Quadratic shape functions   **(b)** Trigonometric shape functions
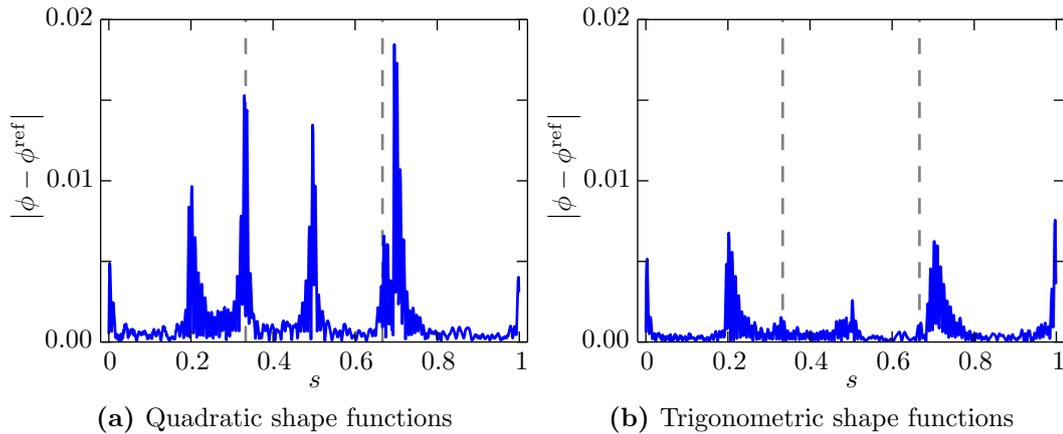
Figure 5.25: Plots of absolute difference between PU-BEM simulation against converged MFS solution for the capsule problem, $ka = 25$. (a) Quadratic and (b) trigonometric shape functions.

are significant errors at the element ends that are reduced by the trigonometric shape functions; the maximum error in the example given is reduced by 60%. There are also increased errors at the blend points between the lines and arcs; these errors have been reduced but are still large in comparison to the errors over the rest of the boundary. Clearly, the trigonometric shape functions and plane wave expansion, though continuous through these points, are not sufficient to capture the geometry's effect on the potential to a high accuracy in those areas. Nevertheless, the accuracy of the approximations is still good.

Figure 5.26 displays the errors, $\mathcal{E}$, of PU-BEM simulations for a varying number of plane waves in the PU expansion on the basis. As M increases, so does the total number of degrees of freedom and, therefore, τ; this leads to a reduction in the approximation error. Figure 5.26 shows two things. Firstly, for lower M, trigonometric shape functions provide a better accuracy of approximation; for higher M, the plane wave expansion in the basis dominates the approximation reducing the impact the choice of the shape functions has on the overall error. Secondly, there is a point at which increasing the total number of degrees of freedom, N_{dof}, does not increase the accuracy of the simulations. Assuming the accuracy of the converged MFS solution is greater than the PU-BEM solutions, we can attribute this to the high condition numbers of the PU-BEM system matrices.

MFS was chosen to provide the converged solution so that one type of BEM simulation was not simply compared against another type of BEM simulation. When calibrated effectively, the MFS is an accurate method with efficiency (in terms of degrees of freedom) comparable to PU-BEM. However, the positioning of the internal source points (see Appendix D) is a trial-and-error process. Though the method was effective in finding a converged solution in this instance, the method is hard to generalise for non-standard geometries and frequently becomes unstable.
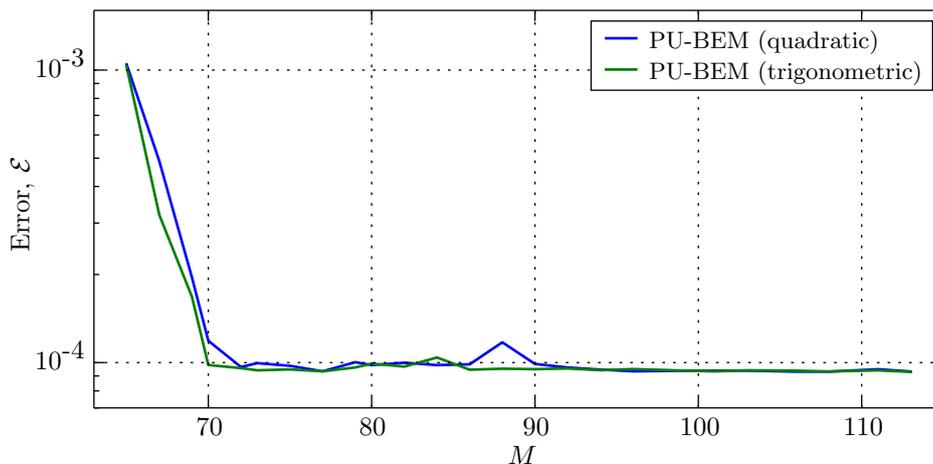
Figure 5.26: Errors of PU-BEM simulations of the capsule problem, $ka = 100$, with varying numbers of plane waves in enriched basis.

Table 5.1: Comparison of normalised simulation times of PU-BEM simulations of the capsule problem using quadratic and trigonometric shape functions.

	System build ($s/8.675$)	System solve ($s/7.429$)
$ka = 30$, quadratic	0.042	0.015
$ka = 30$, trigonometric	0.041	0.015
$ka = 70$, quadratic	0.206	0.135
$ka = 70$, trigonometric	0.206	0.133
$ka = 150$, quadratic	1.000	1.000
$ka = 150$, trigonometric	0.988	0.997

5.8   Simulation runtimes

It may be expected that the computational resources required to evaluate the trigonometric shape functions would exceed those required to compute the corresponding quadratic shape functions. Modern processors and programming packages, however, have significantly reduced this computational burden. Also, the time required to evaluate the boundary integrals in the PU-BEM is dominated by the calculation of the Hankel functions rather than shape functions. Table 5.1 compares some normalised times of simulations run for the capsule problem for a selection of wavenumbers. The trigonometric shape functions clearly do not increase the time taken to run a simulation; indeed, they appear to slightly reduce the time. It is evident, therefore, that the introduction of trigonometric shape functions does not induce any additional computational burden.

The system build and system solve times in Table 5.1 are not normalised with the same value, making it difficult to compare these columns to each other. This is intentional as it would be unfair to make comparisons of the author's integration

and matrix building Python code against the optimised libraries used to solving the resulting matrix systems.

5.9 Collocation strategies

In previous research [97–99], the choice of collocation strategy with the PU-BEM has been somewhat arbitrary and has not been formally investigated. For a polynomial basis BEM, it is sufficient to collocate the boundary integral equation at each element node; for the PU-BEM, the boundary integral equation has, generally, been collocated at a sufficient number of equally spaced points on the boundary. In adaptive basis schemes, such as [128], additional collocation points are added between existing collocation points; however, the simulations run for this chapter, only an initial array of collocation points is required.

The motivation for this part of the work is to investigate and reduce errors that may be associated with the collocation strategy. In view of the fact that the work considers frequency domain wave scattering, where waves can be modelled as sinusoids, uniformly spaced collocation points have the potential to act like a digital filter.

Three alternative approaches to the choice of collocation points are suggested here: collocating using the roots of polynomials, Fock domain clustering, and randomly perturbed collocation. In all cases, the sound-hard cylinder problem (§5.5) is used as the test case; the results for trigonometric shape functions are displayed.

5.9.1 Collocating using roots of polynomials

When examining Figures 5.14 - 5.16 and Figure 5.25, it can be seen that the absolute errors approach zero at a number of points along each element; these points correspond with the collocation points on each element. If collocation points are clustered towards an area on an element, this reduces the absolute errors in that region. Applying this approach, clustering collocation points towards the ends of elements is one way to reduce errors at the element ends; however, this will, consequently, increase errors in regions of less clustered collocation points.

One way in which to produce a regular 'clustered' collocation scheme is to use the roots of classical orthogonal polynomials. Here, results are provided for three, well-known polynomials: Chebyshev and Legendre (both special types of Jacobi polynomial), and Hermite polynomial. In each case, a number of roots can be found which can then be mapped onto the local coordinate $\xi \in [-1, 1]$; collocation can be guaranteed at $\xi = \pm 1$. Figure 5.27 shows visually how the collocation schemes differ for a specific number of collocation points.

Figure 5.28 shows the errors, $\mathcal{E}$, when these polynomials were used as the collocation scheme for the unit cylinder problem, over a range of wavelengths. It is clear that none of the above collocation schemes is effective at improving the accuracy
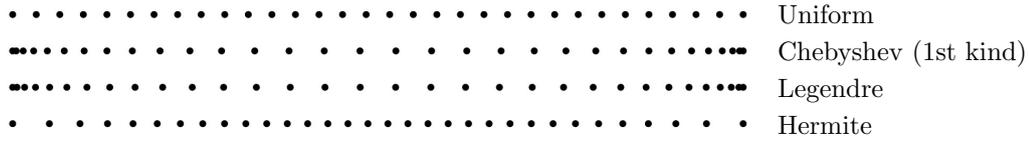
Figure 5.27: Uniform, Chebyshev, Legendre and Hermite collocation points in $[-1, 1]$ for 32 collocation points.

of the solution. The uniform spacing provides a greater accuracy. Compared to the Chebyshev and Legendre schemes (clustering collocation towards the elements ends), the uniform spacing provided an accuracy benefit between one and four orders of magnitude in most cases. Indeed, the best alternative scheme to uniformly spaced collocation points was that based on the Hermite roots.

Other polynomials including Gegenbauer and Bessel functions have been trialled but the resulting errors associated with these follow similar trends to the other polynomials, or the errors obtained are worse than the cases presented here. Hence, they serve only to saturate the point being made. They perform no better than any of the cases displayed here.

5.9.2   Clustering about the Fock domain

Consider a cylinder approximated by four, equal-length elements. If one element faces the impinging wave, it is said to be in the illuminated zone; the element on the opposite side of the cylinder is in the shadow zone. The remaining two elements, that lie between the illuminated and shadow zone, are said to be in the Fock domain.

For asymptotically high wavenumbers, the wave potential in the illuminated zone approaches $2\phi^{\mathrm{inc}}$; the wave potential in the shadow zone can be considered to be 0. The Fock domain is, therefore, a transition region between these two zones; here, there is grazing incidence of the impinging plane wave and high gradients of potential that can lead to difficulties in the numerical modelling of the domain.

If there are P collocation points per element, a collocation point can be removed from the illuminated zone and from the shadow zone and added to the Fock domains. Then the $P - 1$ collocation points in the illuminated and shadow zones can be collocated uniformly; similarly, the $P + 1$ collocation points in the Fock domains can be collocated uniformly.

Figure 5.29 shows the errors for simulations, over a range of wavenumbers, when adding or removing points to or from the Fock domain. Moving a small number of points appears to make little difference, though some simulations do perform better; this rare occurrence can be attributed to the small fluctuations in error found when different CHIEF points are used. If a larger number of points are moved, the accuracy of solutions is clearly worse than with uniform collocation point spacing.
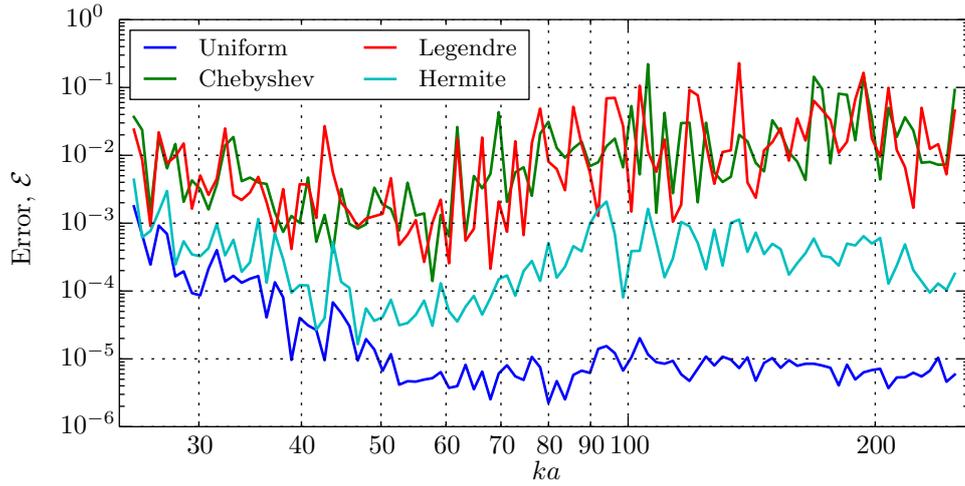
(a) Two elements
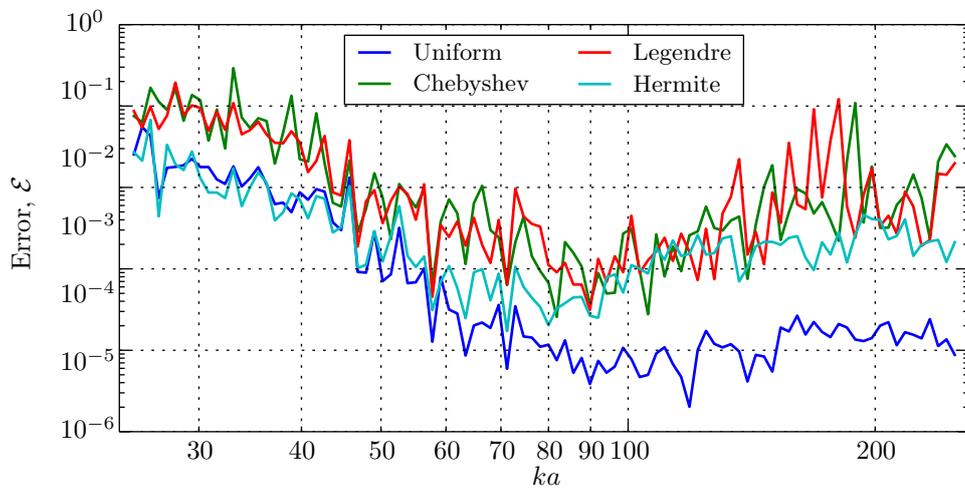
(b) Five elements

Figure 5.28: Comparison of collocation strategies based on polynomial roots.
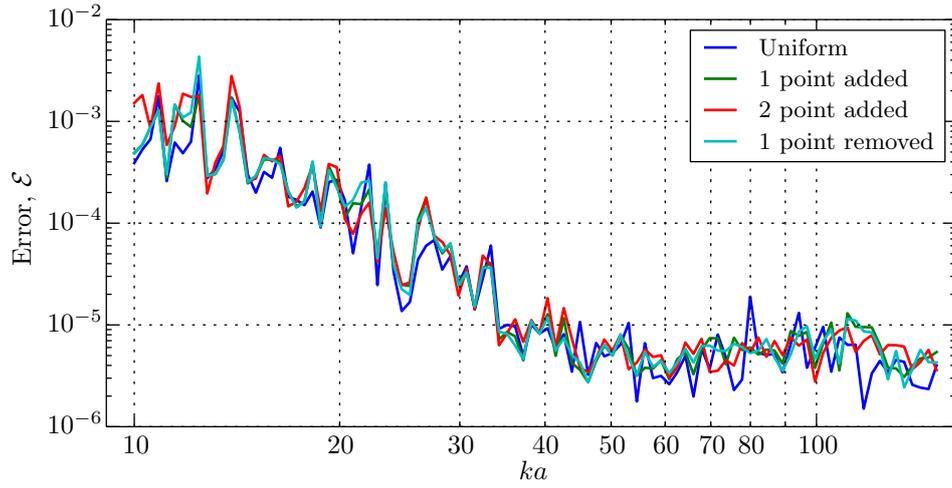
(a) Small clustering
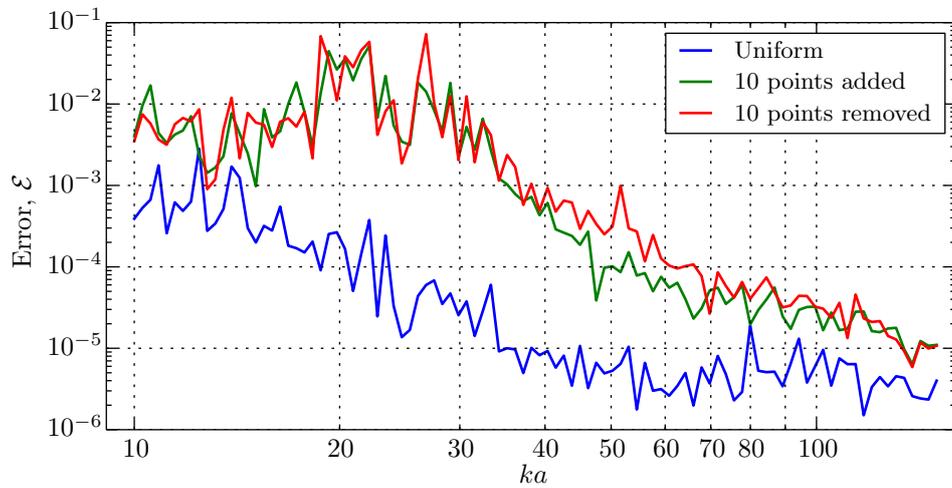
(b) Large clustering

Figure 5.29: Comparison of collocation strategies with consideration of Fock domain.

5.9.3   Randomly perturbed spacing

In order to determine whether differently spaced collocation points, other than the structured schemes tested, could provide a benefit to PU-BEM simulations, a scheme was developed to take uniformly spaced collocation points and move them slightly by a random perturbation. Thus, the location of each collocation point, ξ_i, is now expressed

$$\xi_i = \xi_i^{\text{uniform}} + \rho\sigma_i, \qquad (5.29)$$

where $\sigma_i \in (-1, 1)$ is a random number generated for each collocation point and ρ is a constant.

Two approaches are used with the randomly perturbed spacing. One approach is to fix ρ in all cases regardless of wavenumber; the second approach is to vary ρ based on the spacing between uniform collocation points (which varies according to M). Figure 5.30 shows the effect of each approach: setting $\rho = 0.05$ and setting ρ to be equal to the distance between uniform collocation points. 10 simulations were run for each wavenumber; the average of the 5 most accurate solutions was used to calculate $\mathcal{E}$.

Examining Figure 5.30 it is clear that uniform spacing provides the greatest accuracy. This becomes more important as the wavenumber increases and, therefore, there are more collocation points.

5.10   Conclusions

Using a collocation PU-BEM for wave scattering simulations, errors are found to be at a maximum at the element ends. This is exacerbated by a lack of continuity at the element ends, associated with Lagrangian shape functions. It has been shown that a novel set of shape functions, based of trigonometric functions, increase the continuity at the element ends and, thereby, improve the approximation of potential in such problems. It should be noted that these accuracy gains are not replicable for conventional BEM schemes, i.e. trigonometric shape functions do not improve upon piecewise quadratic approximations unless a plane wave enriched basis is used.

For geometries with geometry blends, the PU-BEM is susceptible to somewhat increased errors at points where different segments blend together.

The choice of collocating the boundary integral equation at equally spaced points around the boundary of the scatterer has been shown to be the most effective approach to collocation.
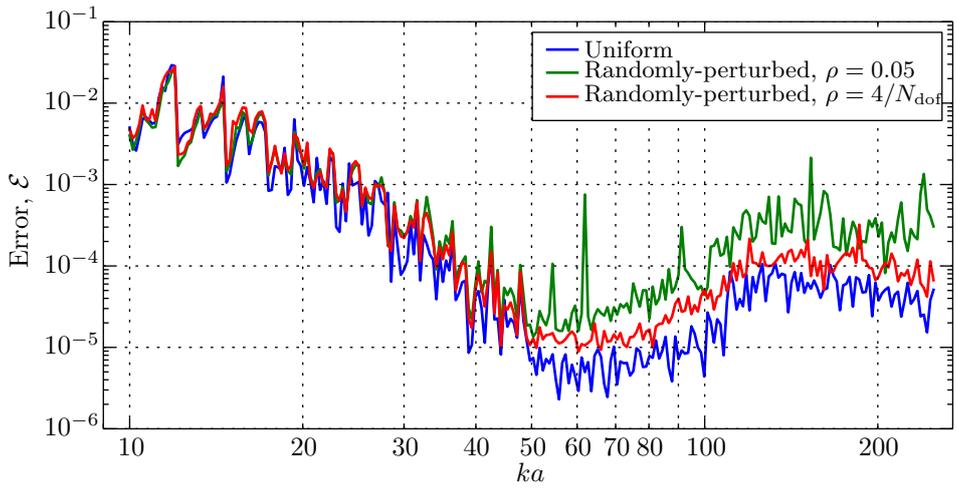
(a) Two elements; space between uniform points is $4/N_{\mathrm{dof}}$
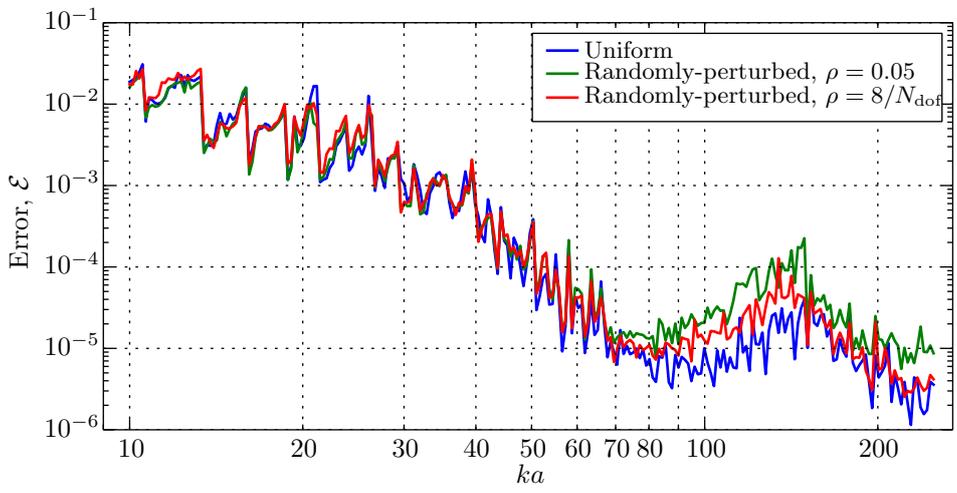
(b) Four elements; space between uniform points is $8/N_{\mathrm{dof}}$

Figure 5.30: Comparison of errors of PU-BEM simulations using uniform collocation scheme and PU-BEM simulations using randomly perturbed collocation schemes.

6

PU-BEM for three-dimensional problems

6.1 Considerations for 3D BEM

This section contains background work on the PU-BEM in 3D, much of which is covered in [97]. The novel aspect of this chapter is the introduction of a new technique, based on a physical analogy of charged particles held in equilibrium, used to generate equally spaced points on a unit sphere. The existing literature on the subject is discussed in §6.2; while the new technique and its application to PU-BEM is discussed in §6.3 onwards.

Many components of the derivation in Chapter 3 are applicable to BEM problems in both two and three dimensions. However, the numerical implementation described in §3.4 is predominantly applicable only to two-dimensional problems. For three-dimensional problems, one has to consider: the different Green's function and the nature of its singularity; the new types of elements used to discretise the boundary; in the case of PU-BEM, how to evaluate the highly oscillatory integrals. In addition to this, one has to consider how to choose the plane wave directions for the enrichment of the basis functions in PU-BEM.

6.1.1 Regularisation

BEM simulations of acoustic wave scattering begin with (3.23), repeated here:

$$c(\mathbf{p})\phi(\mathbf{p}) + \int_{\Gamma} \left[\frac{\partial G(\mathbf{p}, \mathbf{q})}{\partial n(\mathbf{q})} - \alpha(\mathbf{q})G(\mathbf{p}, \mathbf{q}) \right] \phi(\mathbf{q}) \mathrm{d}\Gamma(\mathbf{q}) =$$
$$\int_{\Gamma} \beta(\mathbf{q})G(\mathbf{p}, \mathbf{q}) \mathrm{d}\Gamma(\mathbf{q}) + \phi^{\mathrm{inc}}(\mathbf{p}). \quad (3.23)$$

Before discretising this equation, one should first consider the different types of fundamental solution used for three-dimensional Helmholtz problems. Unlike in 2D, the derivative Green's function, $\partial G/\partial n$, is not regular but is $\mathcal{O}(1/r)$ or weakly-singular. The same is true for the Green's function, G. While coordinate transformations exist—and one of these is discussed in §6.1.3—it is worth considering the use of a

regularisation scheme.

Several regularisation schemes exist that remove the singularity of the derivative Green's function. The regularised BIE described below, developed by Liu [80], makes use of the derivative Green's function for the Laplace equation:

$$\frac{\partial \bar{G}(\mathbf{p}, \mathbf{q})}{\partial n} = -\frac{1}{4\pi r^2} \frac{\partial r}{\partial n}. \tag{6.1}$$

Liu's regularisation is derived from the ability to express the jump term $c(\mathbf{p})$ as:

$$c(\mathbf{p}) = \gamma - \int_{\Gamma} \frac{\partial \bar{G}(\mathbf{p}, \mathbf{q})}{\partial n(\mathbf{q})} d\Gamma(\mathbf{q}), \quad \forall \mathbf{p} \in \Gamma, \tag{6.2}$$

where $\gamma = 1$ for infinite domains and $\gamma = 0$ for finite domains. The jump term (6.2) can be substituted into (3.23) to obtain the regularised BIE (RBIE):

$$\gamma \phi(\mathbf{p}) + \int_{\Gamma} \left[\frac{\partial G(\mathbf{p}, \mathbf{q})}{\partial n(\mathbf{q})} - \alpha(\mathbf{q}) G(\mathbf{p}, \mathbf{q}) \right] \phi(\mathbf{q}) d\Gamma(\mathbf{q}) - \int_{\Gamma} \frac{\partial \bar{G}(\mathbf{p}, \mathbf{q})}{\partial n(\mathbf{q})} \phi(\mathbf{p}) d\Gamma(\mathbf{q})$$
$$= \int_{\Gamma} \beta(\mathbf{q}) G(\mathbf{p}, \mathbf{q}) d\Gamma(\mathbf{q}) + \phi^{\text{inc}}(\mathbf{p}). \tag{6.3}$$

While this is the form of the equation used in the current and later chapters, it is not immediately clear how this regularisation scheme works. Therefore, it can be useful to express (6.3) in a slightly different form, adding and subtracting a Laplace derivative Green's function term:

$$\gamma \phi(\mathbf{p}) + \int_{\Gamma} \left[\frac{\partial G(\mathbf{p}, \mathbf{q})}{\partial n(\mathbf{q})} - \alpha(\mathbf{q}) G(\mathbf{p}, \mathbf{q}) - \frac{\partial \bar{G}(\mathbf{p}, \mathbf{q})}{\partial n(\mathbf{q})} \right] \phi(\mathbf{q}) d\Gamma(\mathbf{q})$$
$$+ \int_{\Gamma} \frac{\partial \bar{G}(\mathbf{p}, \mathbf{q})}{\partial n(\mathbf{q})} [\phi(\mathbf{q}) - \phi(\mathbf{p})] d\Gamma(\mathbf{q}) = \int_{\Gamma} \beta(\mathbf{q}) G(\mathbf{p}, \mathbf{q}) d\Gamma(\mathbf{q}) + \phi^{\text{inc}}(\mathbf{p}). \tag{6.4}$$

In the first integral of (6.4), one can see that the Laplace derivative Green's function is subtracted from the Helmholtz derivative Green's function. These functions have the same nature of singularity and so the Laplace derivative Green's function is effectively removing that singularity from the integral; this is demonstrated in Figure C.8 of the appendices.

The second integral of (6.4) also differs from that in (6.3). The Laplace derivative Green's function multiplied by $\phi(\mathbf{q})$ is now added back into the equation. While the Green's function is singular in nature, $[\phi(\mathbf{q}) - \phi(\mathbf{p})]$ has a regularising effect as it approaches zero as $\mathbf{q}$ approaches $\mathbf{p}$ (the point of singularity). The Green's function is $\mathcal{O}(1/r)$ and the regularising term is $\mathcal{O}(r)$; hence, the product of the two terms is $\mathcal{O}(1)$ (regular).

For problems of perfectly reflecting scatterers, this regularisation scheme is more effective than the Telles coordinate transformation in §6.1.3 (see Appendix C). However, for other boundary conditions, the final integral remains unchanged and is weakly singular; the effectiveness of this regularisation on such problems has not

been shown in any literature.

6.1.2   Discretisation of the boundary

The boundary, Γ, is again discretised into E non-overlapping elements, Γ_e. However, due to the increase in dimension from 2D to 3D, these elements have a new mapping based on a two-dimensional local coordinate:

$$\Gamma_e = \{\mathbf{F}_e(\xi_1, \xi_2) : \xi_1, \xi_2 \in [-1, 1]\}. \tag{6.5}$$

The geometry of Γ_e is approximated in the same fashion as two-dimensional elements:

$$x(\xi) = \sum_{j=1}^{J} N_j(\xi) x_j, \tag{6.6}$$

$$y(\xi) = \sum_{j=1}^{J} N_j(\xi) y_j, \tag{6.7}$$

$$z(\xi) = \sum_{j=1}^{J} N_j(\xi) z_j, \tag{6.8}$$

where there are J nodes and shape functions on an element. Assuming isoparametric elements, the potential over an element is also approximated as above, where instead of geometry nodes there are ϕ_j. A diagrammatical representation of a quadratic three-dimensional boundary element can be seen in Figure 6.1; its associated shape functions are:

$$N_1(\xi_1, \xi_2) = \frac{1}{4}\xi_1\xi_2(1 - \xi_1)(1 - \xi_2), \tag{6.9}$$

$$N_2(\xi_1, \xi_2) = -\frac{1}{2}\xi_2(1 - \xi_1)(1 + \xi_1)(1 - \xi_2), \tag{6.10}$$

$$N_3(\xi_1, \xi_2) = -\frac{1}{4}\xi_1\xi_2(1 + \xi_1)(1 - \xi_2), \tag{6.11}$$

$$N_4(\xi_1, \xi_2) = \frac{1}{2}\xi_1(1 - \xi_1)(1 - \xi_2)(1 + \xi_2), \tag{6.12}$$

$$N_5(\xi_1, \xi_2) = \frac{1}{4}\xi_1\xi_2(1 + \xi_1)(1 + \xi_2), \tag{6.13}$$

$$N_6(\xi_1, \xi_2) = \frac{1}{2}\xi_2(1 - \xi_1)(1 + \xi_1)(1 + \xi_2), \tag{6.14}$$

$$N_7(\xi_1, \xi_2) = -\frac{1}{4}\xi_1\xi_2(1 - \xi_1)(1 + \xi_2), \tag{6.15}$$

$$N_8(\xi_1, \xi_2) = -\frac{1}{2}\xi_1(1 - \xi_1)(1 - \xi_2)(1 + \xi_2), \tag{6.16}$$

$$N_9(\xi_1, \xi_2) = (1 - \xi_1)(1 + \xi_1)(1 - \xi_2)(1 + \xi_2). \tag{6.17}$$
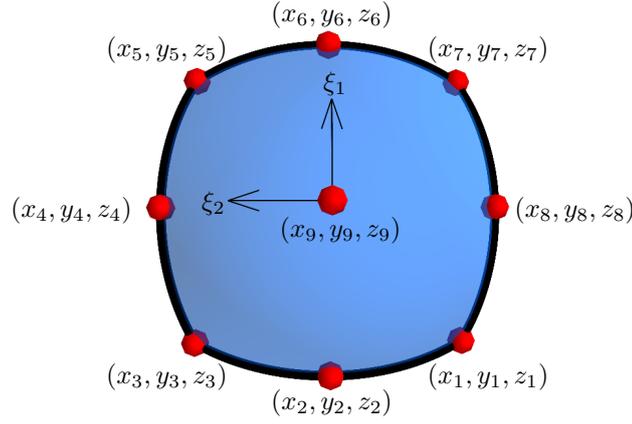
Figure 6.1: A three-dimensional, continuous, quadratic, boundary element.

After discretisation, (6.3) is rewritten

$$\left[\gamma - \sum_{e=1}^{E} L^e\right]\phi(\mathbf{p}) + \sum_{e=1}^{E}\sum_{j=1}^{J} H_j^e \phi_j^e = \sum_{e=1}^{E} K^e + \phi^{\text{inc}}(\mathbf{p}), \tag{6.18}$$

where

$$H_j^e = \int_{-1}^{1}\int_{-1}^{1}\left[\frac{\partial G(\mathbf{p},\mathbf{q}_\xi)}{\partial n(\mathbf{q}_\xi)} - \alpha(\mathbf{q}_\xi)G(\mathbf{p},\mathbf{q}_\xi)\right]N_j^e(\xi_1,\xi_2)|J_{\mathbf{F}_e}|\mathrm{d}\xi_1\mathrm{d}\xi_2, \tag{6.19}$$

$$L^e = \int_{-1}^{1}\int_{-1}^{1}\frac{\partial \bar{G}(\mathbf{p},\mathbf{q}_\xi)}{\partial n(\mathbf{q}_\xi)}|J_{\mathbf{F}_e}|\mathrm{d}\xi_1\mathrm{d}\xi_2, \tag{6.20}$$

$$K^e = \int_{-1}^{1}\int_{-1}^{1}\beta(\mathbf{q}_\xi)G(\mathbf{p},\mathbf{q}_\xi)|J_{\mathbf{F}_e}|\mathrm{d}\xi_1\mathrm{d}\xi_2, \tag{6.21}$$

$\mathbf{q}_\xi \equiv \mathbf{q}(\xi_1,\xi_2)$ and $|J_{\mathbf{F}_e}|$ is the Jacobian of transformation of the mapping in (6.5). Using an appropriate integration scheme and, if required, coordinate transformation, (6.18) can be collocated at all the element nodes in order to find the unknown values of ϕ_j^e.

The evaluation of the normal n begins, again, with the tangential vectors in the local coordinate directions, $\mathbf{m}_1$ and $\mathbf{m}_2$:

$$\begin{aligned}
\mathbf{m}_1 &= \frac{\partial x(\xi_1,\xi_2)}{\partial \xi_1}\hat{\mathbf{x}} + \frac{\partial y(\xi_1,\xi_2)}{\partial \xi_1}\hat{\mathbf{y}} + \frac{\partial z(\xi_1,\xi_2)}{\partial \xi_1}\hat{\mathbf{z}}, \\
\mathbf{m}_2 &= \frac{\partial x(\xi_1,\xi_2)}{\partial \xi_2}\hat{\mathbf{x}} + \frac{\partial y(\xi_1,\xi_2)}{\partial \xi_2}\hat{\mathbf{y}} + \frac{\partial z(\xi_1,\xi_2)}{\partial \xi_2}\hat{\mathbf{z}},
\end{aligned} \tag{6.22}$$

where $\hat{\mathbf{x}}$, $\hat{\mathbf{y}}$ and $\hat{\mathbf{z}}$ are the unit vectors in, respectively, the x, y and z directions. The

normal vector, $\mathbf{n}$, is equal to the cross product of $\mathbf{m}_1$ and $\mathbf{m}_2$:

$$\mathbf{n} = \mathbf{m}_1 \times \mathbf{m}_2 = \begin{vmatrix} \hat{\mathbf{x}} & \hat{\mathbf{y}} & \hat{\mathbf{z}} \\ \dfrac{\partial x(\xi_1, \xi_2)}{\partial \xi_1} & \dfrac{\partial y(\xi_1, \xi_2)}{\partial \xi_1} & \dfrac{\partial z(\xi_1, \xi_2)}{\partial \xi_1} \\ \dfrac{\partial x(\xi_1, \xi_2)}{\partial \xi_2} & \dfrac{\partial y(\xi_1, \xi_2)}{\partial \xi_2} & \dfrac{\partial z(\xi_1, \xi_2)}{\partial \xi_2} \end{vmatrix} \tag{6.23}$$

$$= n_x \hat{\mathbf{x}} + n_y \hat{\mathbf{y}} + n_z \hat{\mathbf{z}}.$$

Individually, the outward pointing normal components are:

$$\begin{aligned} n_x &= \frac{\partial y(\xi_1, \xi_2)}{\partial \xi_1} \frac{\partial z(\xi_1, \xi_2)}{\partial \xi_2} - \frac{\partial z(\xi_1, \xi_2)}{\partial \xi_1} \frac{\partial y(\xi_1, \xi_2)}{\partial \xi_2}, \\ n_y &= \frac{\partial z(\xi_1, \xi_2)}{\partial \xi_1} \frac{\partial x(\xi_1, \xi_2)}{\partial \xi_2} - \frac{\partial x(\xi_1, \xi_2)}{\partial \xi_1} \frac{\partial z(\xi_1, \xi_2)}{\partial \xi_2}, \\ n_z &= \frac{\partial x(\xi_1, \xi_2)}{\partial \xi_1} \frac{\partial y(\xi_1, \xi_2)}{\partial \xi_2} - \frac{\partial y(\xi_1, \xi_2)}{\partial \xi_1} \frac{\partial x(\xi_1, \xi_2)}{\partial \xi_2}, \end{aligned} \tag{6.24}$$

from which the unit normal vector components can be easily determined by dividing (6.24) by the magnitude of the normal vector

$$|\mathbf{n}| = \sqrt{n_x^2 + n_y^2 + n_z^2}, \tag{6.25}$$

which is equal to the Jacobian of transformation:

$$|J_{\mathbf{F}_e}| = \frac{\mathrm{d}\Gamma}{\mathrm{d}(\xi_1, \xi_2)} = \sqrt{n_x^2 + n_y^2 + n_z^2}. \tag{6.26}$$

6.1.3   Coordinate transformation

If the RBIE is used and the scatterer of the problem is perfectly reflecting, $\alpha(\mathbf{q}) = \beta(\mathbf{q}) = 0 \ \forall \mathbf{q}$, then (6.18) can be collocated without any consideration of singularities. For all other boundary conditions, the weakly singular nature of $G(\mathbf{p}, \mathbf{q})$ must be considered.

One way of removing the singularity at the collocation point $\mathbf{p}$ is to use a co-ordinate transformation such as that developed by Rêgo Silva *et al.* [102]. In this scheme, rectangular elements are split into four triangles that meet at the collocation point (see Figure 6.2); each of these triangular cells is then integrated using a new local polar coordinate system. The transformation is only applied when the collocation point lies on the element being integrated; a standard quadrature can be used otherwise.

When using the transformation, the integrals of (6.18) are rewritten as

$$L^e = \sum_{t=1}^{T} \int_{\theta_1}^{\theta_2} \int_0^{F(\theta)} \frac{\partial \bar{G}(\mathbf{p}, \mathbf{q}_\xi)}{\partial n(\mathbf{q}_\xi)} |J_{\mathbf{F}_e}| \rho \, \mathrm{d}\rho \, \mathrm{d}\theta, \tag{6.27}$$
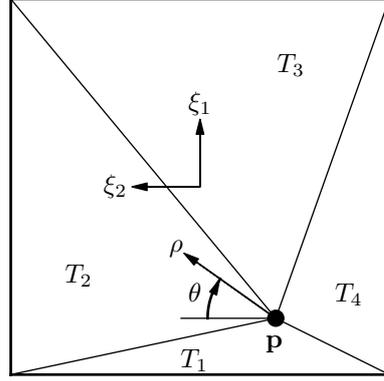
Figure 6.2: Rectangular element subdivided into triangles for Telles transformation.

$$K^e = \sum_{t=1}^{T} \int_{\theta_1}^{\theta_2} \int_0^{F(\theta)} \beta(\mathbf{q}_\xi) G(\mathbf{p}, \mathbf{q}_\xi) |J_{\mathbf{F}_e}| \, \rho \, d\rho \, d\theta, \tag{6.28}$$

$$H_j^e = \sum_{t=1}^{4} \int_{\theta_1}^{\theta_2} \int_0^{F(\theta)} \left[\frac{\partial G(\mathbf{p}, \mathbf{q}_\xi)}{\partial n(\mathbf{q}_\xi)} - \alpha(\mathbf{q}_\xi) G(\mathbf{p}, \mathbf{q}_\xi) \right] N_j(\xi_1, \xi_2) |J_{\mathbf{F}_e}| \, \rho \, d\rho \, d\theta, \tag{6.29}$$

where θ_1 and θ_2 are the minimum and maximum angles of each triangular cell, $F(\theta)$ is the maximum possible value of ρ for the value of θ being evaluated—this varies over the integral but is trivial to determine. The value of ρ acts as the Jacobian of the transformation; it reduces the singularity as it is $\mathcal{O}(r)$, approaching zero as the evaluation points get closer to the singularity, i.e. as $r \to 0$.

6.1.4 PU enrichment in 3D

The plane wave enrichment for PU-BEM is applied in 3D in much the same way as it is in 2D. The nodal potentials ϕ_j^e are expressed as a summation of plane waves, just as in (4.1):

$$\phi^e(\mathbf{q}(\xi)) = \sum_{j=1}^{J} N_j^e(\xi) \sum_{m=1}^{M} A_{jm}^e \exp\left(ik\mathbf{d}_{jm}^e \cdot \mathbf{q}\right), \tag{6.30}$$

where there are M plane waves in each expansion with prescribed directions of propagation $\mathbf{d}_{jm}^e \in \mathbb{R}^3$ and unknown amplitudes, $A_{jm}^e \in \mathbb{C}$.

Substitution of (6.30) into (6.18) yields

$$\left[\gamma - \sum_{e=1}^{E} L^e \right] \phi(\mathbf{p}) + \sum_{e=1}^{E} \sum_{j=1}^{J} H_{jm}^e A_{jm}^e = \sum_{e=1}^{E} K^e + \phi^{\mathrm{inc}}(\mathbf{p}), \tag{6.31}$$

where L^e and K^e are the same as in (6.20) and (6.21) respectively; H_{jm}^e is defined

as

$$H_{jm}^e = \int_{-1}^{1} \int_{-1}^{1} \left[\frac{\partial G(\mathbf{p}, \mathbf{q}_\xi)}{\partial n(\mathbf{q}_\xi)} - \alpha(\mathbf{q}_\xi) G(\mathbf{p}, \mathbf{q}_\xi) \right] N_j^e(\xi_1, \xi_2) \exp\left(i k \mathbf{d}_{jm}^e \cdot \mathbf{q}_\xi \right) |J_{\mathbf{F}_e}| \mathrm{d}\xi_1 \mathrm{d}\xi_2,$$
(6.32)

and $\phi(\mathbf{p})$ must be discretised similarly to (6.30):

$$\phi(\mathbf{p}_\xi) = \sum_{j=1}^{J} N_j^{e(\mathbf{p})}(\xi) \sum_{m=1}^{M} A_{jm}^{e(\mathbf{p})} \exp\left(i k \mathbf{d}_{jm}^{e(\mathbf{p})} \cdot \mathbf{p}_\xi \right),$$
(6.33)

where $\phi(\mathbf{p}_\xi) = \phi(\xi)$ and $e(\mathbf{p})$ is the element on which the collocation point $\mathbf{p}$ lies. (6.31) is the discretised BIE for 3D PU-BEM can be collocated to solve the Helmholtz equation.

The choice of $\mathbf{d}_{jm}^e$ is not as trivial as in two-dimensions where uniform points about the unit-circle are chosen. Instead, it is now desirable to have uniform points about the unit-sphere. This task may, at first, appear trivial but soon two things become apparent: first, that it is not as simple as choosing uniform points on a spherical coordinate system—these points become clustered towards the poles of the unit-sphere; second, there are an infinite number of solutions to the problem for $M > 2$.

Thus, a different approach is required to find these uniform points. In other PU work [76, 97], a discretised cube method has been used; this is described in §6.3.1. This method has been successful in producing accurate results with PUFEM and PU-BEM but it is restricted to certain values of M. Other existing methods to find these points are discussed in §6.2 while a novel method, developed by the author, is presented and numerical results provided from §6.3 onwards.

6.1.5   Integration cells

As with 2D PU-BEM simulations, 3D PU-BEM elements can span many wavelengths in size. To capture the oscillating function over these elements, each element is split into a set of integration cells, similar to how 2D PU-BEM elements were in §5.4.

Figure 6.3 shows a diagram of how an element is divided into integration cells. If it assumed that each element is square in shape, the number of integration cells is chosen so that the sides of those integration cells are no longer than $\lambda/4$ in length (to prevent aliasing); thus, the number of integration cells, N_{cells}, on an element is expressed as:

$$N_{\text{cells}} = \left\lceil \left(\frac{2k\sqrt{A_e}}{\pi} \right) \right\rceil^2,$$
(6.34)

where $\lceil \cdot \rceil$ denotes the ceiling function* and A_e is the area of the element.

---

*$\lceil x \rceil = \min\{n \in \mathbb{Z} \,|\, n \geq x\}$
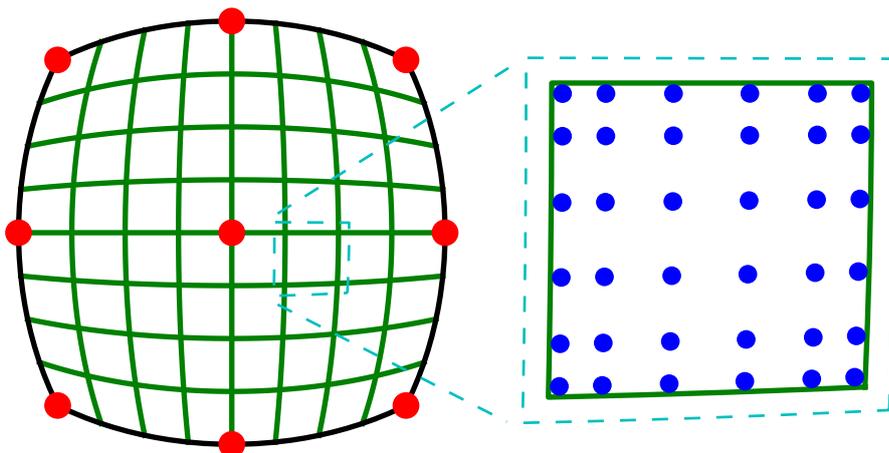
Figure 6.3: 3D boundary element divided into integration cells.

6.1.6   Efficiency measure: τ

The efficiency of BEM simulations can be measured in terms of τ again: the number of degrees of freedom per wavelength of the problem. This is defined as:

$$\tau = \sqrt{\frac{N_{\mathrm{dof}}}{A_\Gamma/\lambda^2}}, \tag{6.35}$$

or

$$\tau = \frac{2\pi}{k}\sqrt{\frac{N_{\mathrm{dof}}}{A_\Gamma}}, \tag{6.36}$$

where A_Γ is the surface area of the scatterer.

6.2 N points on a sphere in literature

Researchers from a diverse set of fields have studied the problem of finding a uniform set of points on a sphere. In Monte Carlo approaches, the desire is to produce a set of points that is statistically uniform; that is, a suitable χ^2 test shows no significant deviation from the uniform distribution. Possibly the simplest method to achieve a statistically uniform distribution of points on the unit-sphere was first devised for the unit-circle by von Neumann [129] and extended by Cook [34] for spheres of three dimensions and higher. A sample $\mathbf{x}$ is taken from the uniform distribution on $[-1, 1]^n$, where n is the number of dimensions being considered. The sample is rejected if its Euclidean norm, $\|\mathbf{x}\|$, is greater than 1 and accepted if $\|\mathbf{x}\| \leq 1$. Sampling continues until the desired number of points is obtained. The points are then normalised so that they are placed on the surface of the sphere. This method is adequate for circles and three-dimensional spheres. However, as n increases, the size of the space $\|\mathbf{x}\| > 1$ becomes much larger than the space $\|\mathbf{x}\| \leq 1$; this means the ratio of rejected to accepted points increases rapidly and most of the computational

burden is on generating points that will be discarded.

A similar method, presented by Muller [92], uses sample points taken from the normal distribution. This is possible as the multivariate normal distribution is radially symmetric. Given a suitable normal distribution, this method has a lower ratio of rejected to accepted points compared to taking points from the uniform distribution. A family of methods, using the beta distribution, were developed for higher dimensional spheres [54, 85, 115, 124, 133]. The relationship between these efficient methods was presented by Harman and Vladimir [52].

In mathematics, the 'uniform spacing' of points ordinarily refers to points that fit the statistical, uniform distribution. Conversely, in the physical sciences, 'uniform spacing' of points refers to making the distance or angle between adjacent points equal by maximising or minimising some criterion. One such example of this is the Thomson Problem: determining the minimum energy configuration of N electrons on the surface of a sphere. This is often associated with the Tammes problem in which N points are arranged on the surface of a sphere so that the minimum distance between them is maximised. Erber and Hockney [43] presented equilibrium configurations of charges on a sphere for $2 \leq N \leq 65$. Glasser and Every [48] extended these calculations to $N \leq 101$. Morris *et al.* [90] developed a genetic algorithm that searches for the steepest-decent in energy; with this algorithm, configurations were extended to $N \leq 200$. Saff and Kuijlaars [108] considered configurations of $N \to \infty$, stating that the general pattern of optimal configuration was the same for all values of N.

In the study of meteorology, spherical grids can be used to model the atmosphere. Kurihara [72] stated that a homogeneous density of grid points on a globe is desirable, presenting a new grid system that was almost homogeneous. Sahr *et al.* [109] later reviewed methods of so-called geodesic discrete global grid systems in which the globe, modelled as an oblate spheroid, is divided in to cells; some of these approaches examined ways of making these cells of equal area. It can be desirable to find uniformly spaced points on other surfaces: in operational research, Rubinstein [107] and Smith [120] considered generating random vectors uniformly on the surface of complex, multidimensional surfaces.

6.3 Generating uniform points on a sphere

6.3.1 Discretised cube boundary method

While in two dimensions, the uniform spacing of directions around the unit circle is a trivial problem, the move to three dimensions presents a greater difficulty, since it is not generally possible, and certainly not intuitive, to define a uniform division of the 4π solid angle. There are also some trivial cases relating to the vertices and/or faces of the platonic solids. However, in order to take full advantage of the plane wave basis methods in wave modelling, considerably larger numbers of directions
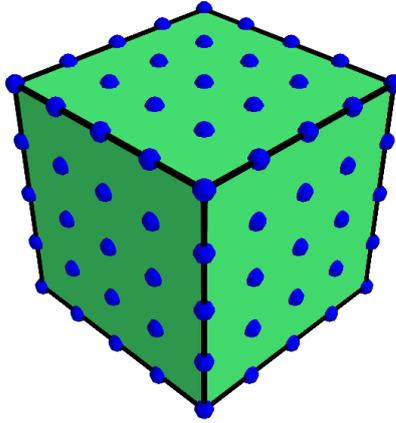
Figure 6.4: Uniform boundary meshing of a cube.

are desirable.

A simple method has been used by PU-BEM and PUFEM authors to date [76,97]; this involves a uniform boundary meshing of a cube, such as the 5×5 case shown in Figure 6.4. A reasonably well spaced set of directions is defined by the vectors joining the centre of the cube to each 'node' on the cube's boundary. For the application in question, the accuracy of wave propagation solutions does not seem to be sensitive to the moderately small non-uniformity of spacing, and so this approach has been satisfactory. However, the method is limited to a few special cases of M for which a boundary-meshed cube is available, specifically $M = 6p^2 + 2$ (where $p \in \mathbb{Z}^+$), allowing $M = 8, 26, 56, 98, \ldots$. This imposes a significant limitation on the computational efficiency since, if one considers the variable τ in enriched simulations, it is likely that one requires a value that lies in between those contained in this set to optimise performance.

The new method described herein overcomes this limitation and, moreover, provides a greater uniformity of spacing compared to the discretised cube boundary method.

6.3.2 Coulomb force method

Consider a sphere of unit radius and of surface S on which lie particles at locations described by vectors $\mathbf{u}_i$, $i = 1, 2, \ldots, M$. Let these particles each have unit mass and unit electrical charge so that they repel each other with Coulomb forces varying with $1/|\mathbf{r}|^2$ where $r = \mathbf{u}_i - \mathbf{u}_j$. In a suitably damped system, the particles will find a static equilibrium state in which they occupy quasi-uniform spacing. We use a simple explicit time-stepping scheme, but require no stiffness term since the particles are free to float on S.

Starting from a random set of vectors $\mathbf{u}_i^0$, the superscript denoting the time at

which a quantity acts, the resultant Coulomb force vector $\mathbf{F}_i$ at time t is given by

$$\mathbf{F}_i^t = A \sum_{j=1}^{M} \frac{(1 - \delta_{ij})\mathbf{r}}{|\mathbf{r}|^3}, \tag{6.37}$$

where A is a scalar multiplier and δ_{ij} is the Kronecker delta. This will be oriented away from S, and so we define vector $\mathbf{f}_i$ as the projection of $\mathbf{F}_i$ on S which, since $\mathbf{u}_i$ are unit vectors, is given by

$$\mathbf{f}_i^t = (\mathbf{F}_i^t \times \mathbf{u}_i^t) \times \mathbf{u}_i^t. \tag{6.38}$$

The acceleration, $\ddot{\mathbf{u}}_i$, of each particle is

$$\ddot{\mathbf{u}}_i^t = \mathbf{f}_i^t - c\dot{\mathbf{u}}_i^t, \tag{6.39}$$

where c is an equivalent viscous damping coefficient and $\dot{\mathbf{u}}_i$ is the velocity of the particle. The velocity and position at the subsequent time, $t + \Delta t$, are given by

$$\dot{\mathbf{u}}_i^{t+\Delta t} = \dot{\mathbf{u}}_i^t + \ddot{\mathbf{u}}_i^t \Delta t, \tag{6.40}$$

$$\hat{\mathbf{u}}_i^{t+\Delta t} = \mathbf{u}_i^t + \dot{\mathbf{u}}_i^t \Delta t, \tag{6.41}$$

$$\mathbf{u}_i^{t+\Delta t} = \frac{\hat{\mathbf{u}}_i^{t+\Delta t}}{\left|\hat{\mathbf{u}}_i^{t+\Delta t}\right|}, \tag{6.42}$$

where (6.42) is used to normalise the position vectors to relocate the particles back onto S. Equations (6.37) to (6.42) are repeated in a time-stepping scheme to convergence.

An appropriate measure of the performance of the method is the minimum angle, ρ, between any two vectors $\mathbf{u}_i$ and $\mathbf{u}_j$, i.e.

$$\rho = \min \left(\cos^{-1} \frac{\mathbf{u}_i \cdot \mathbf{u}_j}{|\mathbf{u}_i||\mathbf{u}_j|} \right) \quad i = 1, \ldots, M; \; j = 1, \ldots, M; \; i \neq j. \tag{6.43}$$

An effective method will maximise ρ for an arbitrary M.

A study of repeated runs having the same M shows that the converged values of $\mathbf{u}_i$ are different for each run. This is expected because of the random initial $\mathbf{u}_i^0$ and the freely floating nature of the particles. However, they differ only in the local coordinate system in which the system is viewed; i.e. the values of ρ are the same for the same M.

It remains to determine suitable values of the parameters A, c and Δt. If the damping c is too low, the particles may exhibit large oscillatory behaviour and require more time steps to reach an equilibrium position, if they indeed converge at all. Similarly, if c is too high, a large number of times steps (or a large scalar A) will be required to reach an equilibrium position.
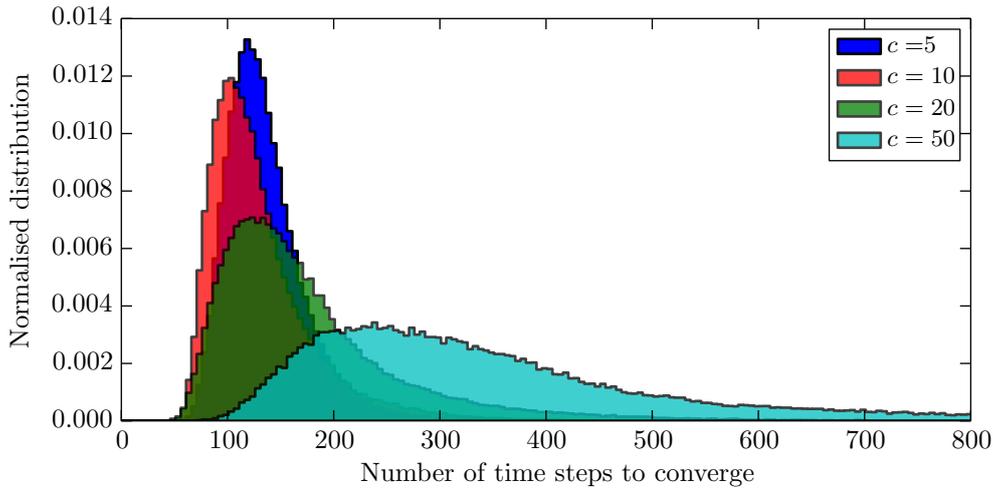
Figure 6.5: Histogram showing distributions of the number of iterations taken for a solution to converge to within 1% of a fully-converged solution for $M = 50$.

Numerical tests show $A = 100$ and $\Delta t = 0.01$ provide for convergence for $M < 100$. The determination of a suitable damping c may be found by considering the statistical distribution of the number of iterations required to reach a value within 1% of the converged minimum angle ρ_M; i.e. the number of iterations required to reach a value of ρ such that $|\rho_M - \rho| < 0.01\rho_M$. As an illustrative example, Figure 6.5 shows distributions of convergence rates for the case of $M = 50$ for four values of damping: $c = 5, 10, 20, 50$. Similar figures can be produced for other values of M.

Distributions such as those in Figure 6.5 can be approximated by log-normal distributions. For damping values $c = 1, 5, 10, 15$ and a range of M, suitably-sized samples were obtained from which the mean, μ, and variance, σ, of each distribution's natural logarithm were calculated using the maximum likelihood method. The values of μ are shown in Figure 6.6. From this figure, it is clear that $c = 1$ requires, on average, more time steps to converge to a 1% solution, $|\rho_M - \rho| < 0.01\rho_M$, than higher values of c; this is due to the large oscillations of the particles with low damping. The distributions at higher values of c have similar means, μ, at low values of M. However, simulations with damping values $c = 10$ and $c = 15$ both become slow to converge as M increases towards 140; indeed, none of the calculations with $c = 15$ for $M > 120$ converged within 1000 time steps.

Figure 6.6 only gives an idea of the mean number of time steps required to obtain a 1% solution. A low variance is also desirable. Individual values of σ are not simple to interpret. Instead, the cumulative distribution function can be used to predict the likelihood that a simulation will have converged to a 1% solution in a given number of time steps. Figures 6.7a and 6.7b show this likelihood for 300 and 500 time steps respectively. For simulations of $M < 80$, 300 time steps and a damping value of $c = 5$ converge in the vast majority of cases; the minimum likelihood of converging to a 1% solution is 99.1% ($M = 5$). The other values of damping considered here provide a less certain performance. For simulations of $M \geq 80$, a damping value of
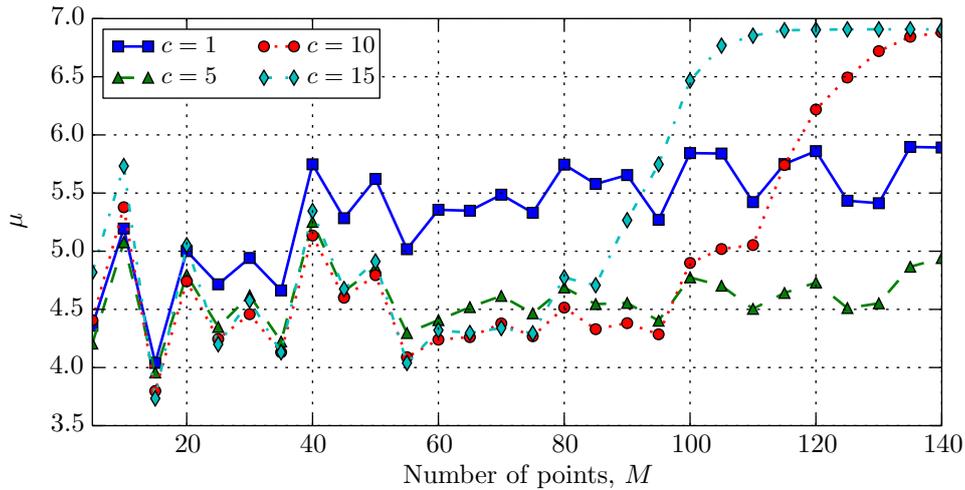
Figure 6.6: Natural logarithm means, μ, of distributions similar to Figure 6.5. (Sample sizes: 1000)

$c = 5$ is also suitable but 500 time steps are recommended; the minimum likelihood of a 1% solution drops to 93.6% ($M = 140$). It should be noted that the solutions outside 1% still exhibit a greater ρ than the discretised cube boundary method.

From the analysis above, the author adopted $c = 5$ with $A = 100$ and $\Delta t = 0.01$; they use 300 time steps for simulations of $M < 80$ and 500 time steps for simulations of $80 \leq M \leq 140$. For $M > 140$, the method exhibits instability using the above parameters and a reduced time step of 0.001 is recommended.

In some applications it may be desirable to bias the directions in one direction or another. In the partition-of-unity finite element formulation for wave diffraction analysis, for example, there may be knowledge of the dominant wave direction. This may come from our physical understanding of the nature of the problem, e.g. scattered waves becoming radial at a large distance from the scatterer, or as the product of some adaptive strategy.

Such a biasing can be achieved by including an external point charge at a desired location. This should have a negative charge such that it attracts the particles on the surface of the sphere (methods using a positive repulsive charge diametrically opposite to the desired concentration do not produce as good a clustering). The point charge needs to be placed off the sphere so that it produces the desired effect without danger of producing very large attractive forces should one of the particles become almost coincident with the external charge. Typically a charge of approximately half the combined charges of the other particles, and located at a radius of 1.5, produces a reasonable concentration, though this value can be varied as required to achieve any arbitrary degree of clustering.

It is found that the introduction of an external charge greatly reduces the robustness of the method and the equilibrium can be difficult to achieve, particularly for high M. In order to counteract this instability, it is recommended that the reduced time step of 0.001 be adopted for all M if trying to obtain a set of biased points.
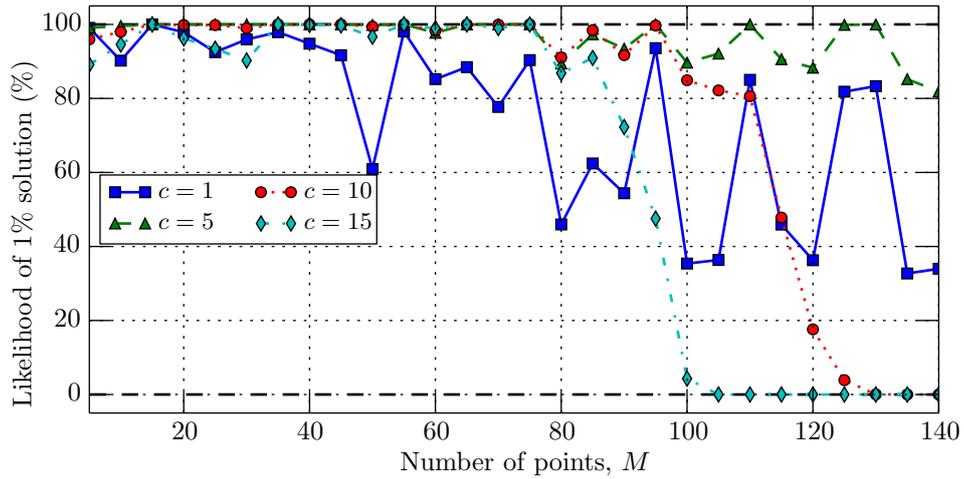
(a) 300 time steps
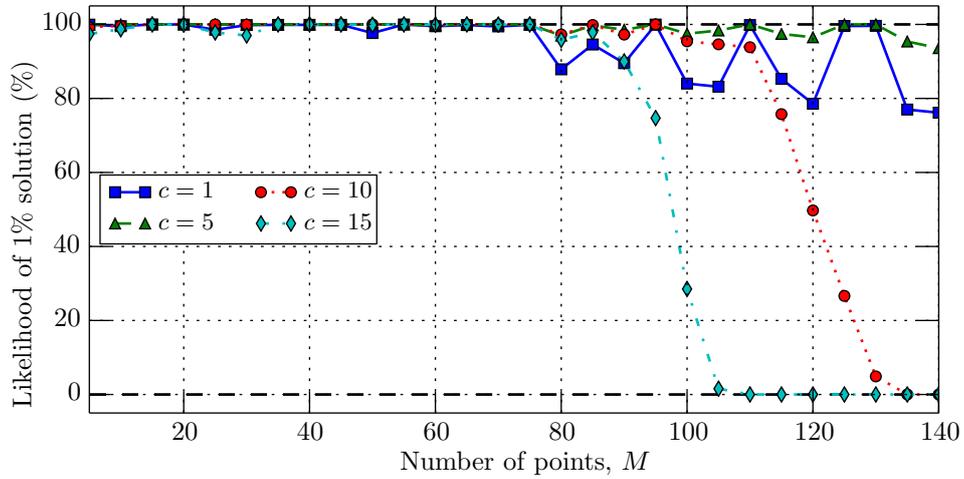
(b) 500 time steps

Figure 6.7: Likelihood of 1% solution, $|\rho_M - \rho| < 0.01\rho_M$, within a given number of time steps, calculated using the cumulative distribution function.

(a) Discretised cube boundary solution   **(b)** Coulomb force solution
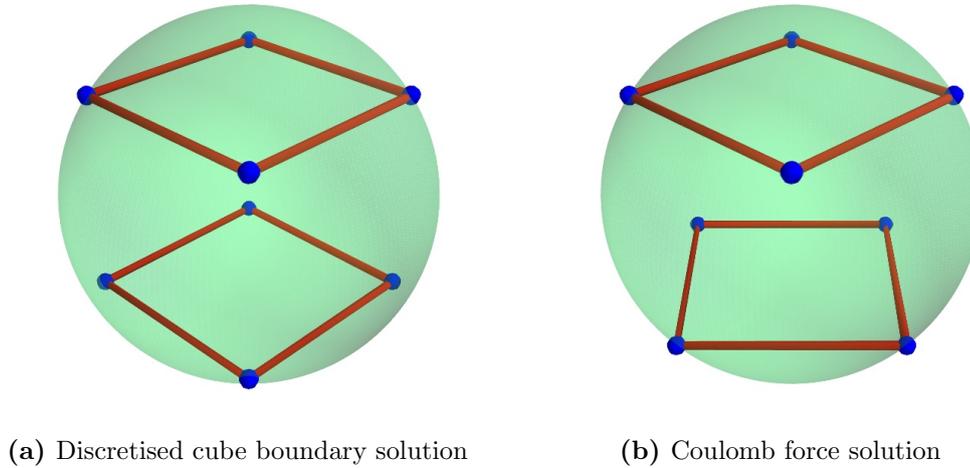
Figure 6.8: Converged solutions, $M = 8$.

6.4   Example points distributions

Figure 6.8a shows a solution for the case $M = 8$ as determined by the discretised cube boundary method; lines have been added to help show how these are the vertices of a cube. Figure 6.8b shows the same case but determined by the Coulomb force method; the lines added show that this appears like two faces of a cube that are rotated 45° from each other.

This is an interesting case as both methods produce an equally spaced distribution of points with an equal minimum distance between points—approximately $2/\sqrt{3}$. However, the equilibrium states exhibit slightly different values of ρ. For the discretised cube boundary, the minimum angle between points is $\rho = 70.5°$; this is lower than that for Coulomb force solution which exhibits $\rho = 71.7°$.

If the solution of the discretised cube method is used as the initial vectors for the Coulomb force method, the system will converge immediately to that configuration ($\rho = 70.5°$). For any other initial vectors, the system will converge to $\rho = 71.7°$. The authors conclude that the latter solution is a lower potential energy state to which random systems will converge. This is made possibly more interesting when one considers that the discretised cube method solution corresponds to the vertices of a platonic solid—the cube in this case. Intuition might suggest that the vertices of such solids correspond with low energy states; however, the results above is a counterexample to this hypothesis.

The improvement in ρ is found consistently for the different M that can be obtained by the discretised cube boundary method. These are summarised in Table 6.1.

Figure 6.9 shows the solution for the case $M = 152$ determined by both methods. The points in Figure 6.9a appear to be uniformly spaced in portions of the sphere; however, it is clearly more densely populated with points towards the top-right of

Table 6.1: Comparison of values of ρ from discretised cube boundary solutions and converged Coulomb force solutions.

p	M	ρ (cube)	ρ (Coulomb)
1	8	70.5°	71.7°
2	26	35.3°	38.8°
3	56	22.0°	26.7°
4	98	15.8°	20.7°
5	152	12.3°	16.3°
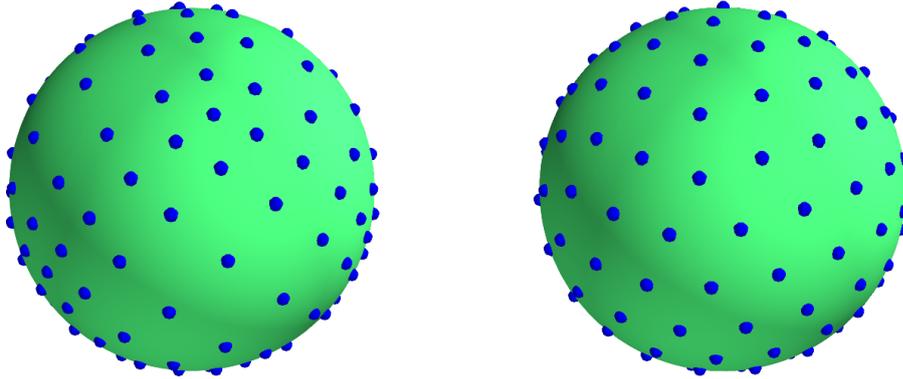
(a) Discretised cube boundary solution

(b) Coulomb force solution

Figure 6.9: Converged solutions, $M = 152$.

the sphere than the bottom. Conversely, the points in Figure 6.9b appear to be uniformly spaced over the entire sphere.

Figure 6.10 displays the same solutions as Figure 6.9 but projected on a planar azimuth-inclination space. Despite the distortion from projecting a sphere onto a square graph, the differences are clear. Considering a central latitudinal strip, Figure 6.10a shows clear irregularities in the spacing of points while Figure 6.10b shows a more uniform spacing.

Finally, Figure 6.11 shows the converged solution for a case in which clustering of particles is required. Arbitrarily, the case of $M = 71$ is considered, with an external charge located at a radius of 1.5. The points are clearly clustered towards one point on the sphere. This point can be prescribed by fixing the position of the external charge.

6.5   Scattering by a unit sphere

The following numerical results are from simulations of a plane wave impinging a unit-radius, perfectly scattering sphere. This problem has an analytical solution, expressed in (2.26). A visual representation of the real part of the potential over the surface of the sphere can be seen in Figure 6.12.

Simulations are run using a collocation PU-BEM employing the CHIEF method

(a) Discretised cube boundary solution   **(b)** Coulomb force solution
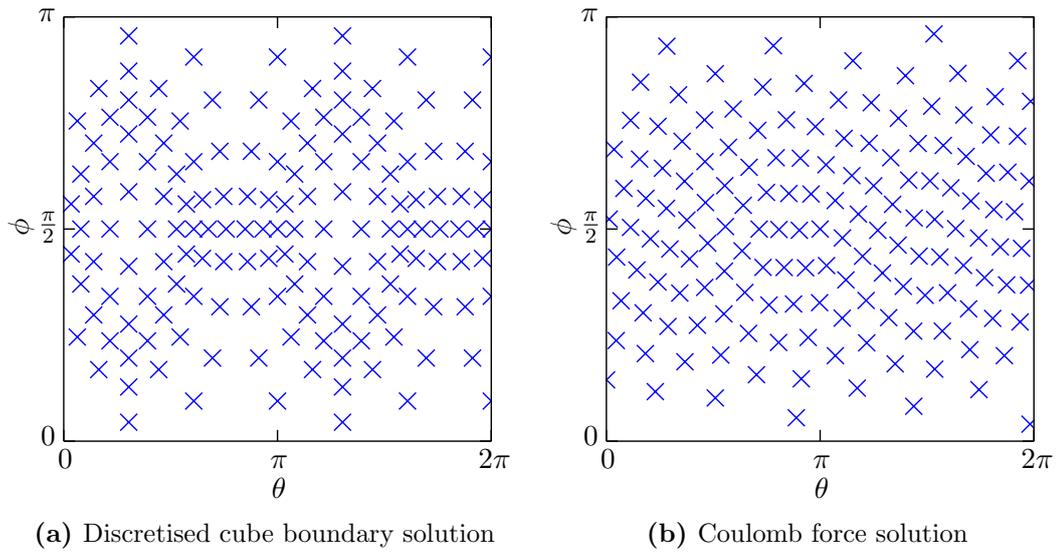
Figure 6.10: $M = 152$ solutions, represented using spherical coordinates of points: θ azimuth, ϕ inclination.
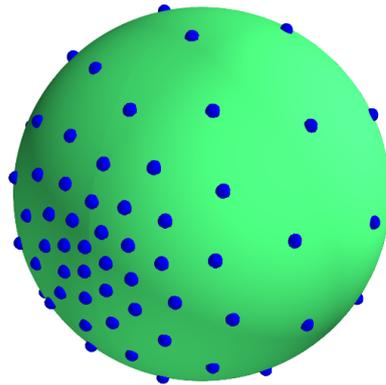
Figure 6.11: Particle clustering, $M = 71$.
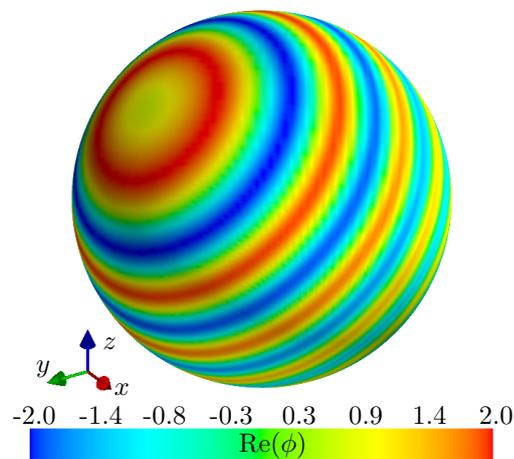
Figure 6.12: Scattering by a sphere at $k = 20$. Isovalues of the real-part of acoustic potential are shown.
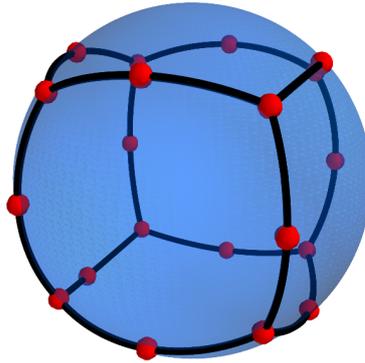
Figure 6.13: Representation of the sphere mesh: black lines represent element edges; small red spheres represent nodal points.

to overcome any nonuniqueness. In order to remove any integration error, matrix entries are calculated using a 50×50 Gauss quadrature with each element subdivided into integration cells with sides no longer than $\lambda/4$ to prevent aliasing. The linear system of equations is solved using SVD. τ for 3D problems is more complicated to work out than for 2D problems, with the square of the surface area of a scatterer being used to represent the length in one coordinate direction. For the problem of the unit sphere:

$$\tau = \sqrt{\frac{\pi N_{\mathrm{dof}}}{k^2}}. \tag{6.44}$$

The sphere is discretised into 6 quadratical, 8-noded elements. Analytical geometry points can be obtained by using a cube-to-sphere mapping: consider a cube with coordinates $\bar{x}, \bar{y}, \bar{z} \in [-1, 1]$; any point $(\bar{x}, \bar{y}, \bar{z})$ on the surface on the cube—i.e. at least one of $\bar{x}, \bar{y}, \bar{z}$ must be equal to 1 or -1—can be mapped to a point (x, y, z) on the surface of the unit-radius sphere with the mapping

$$
\begin{aligned}
x &= \bar{x}\sqrt{1 - \frac{\bar{y}^2}{2} - \frac{\bar{z}^2}{2} + \frac{\bar{y}^2\bar{z}^2}{3}}, \\
y &= \bar{y}\sqrt{1 - \frac{\bar{x}^2}{2} - \frac{\bar{z}^2}{2} + \frac{\bar{x}^2\bar{z}^2}{3}}, \\
z &= \bar{z}\sqrt{1 - \frac{\bar{x}^2}{2} - \frac{\bar{y}^2}{2} + \frac{\bar{x}^2\bar{y}^2}{3}}.
\end{aligned}
\tag{6.45}
$$

The meshed sphere can be seen in Figure 6.13.

In order to make direct comparisons between the new Coulomb force method and the discretised cube boundary method of choosing plane wave directions, the case of $M = 8$ is considered. The inclusion of the incident plane wave direction in the partition-of-unity expansion has been found beneficial in two dimensions [96]. The authors also found it improved the accuracy of simulations in three dimensions. To include this wave direction with the Coulomb force method, one charge can be fixed in the time stepping scheme (as described in the previous section). With the discretised cube boundary method, a rotation must be applied to the solution unless

a point is already coincident with the incident plane wave direction.

Figure 6.14a shows the errors, $\mathcal{E}$, of PU-BEM simulations using these methods. Though the results at some wavenumbers appear to favour the Coulomb force method, the results show no clear distinction in accuracy between the two. As the total number of degrees of freedom, N_{dof}, used in all the simulations is 80, the value of τ decreases as ka increases; this causes the errors of the simulations to increase gradually as ka increases. In order to achieve more accurate simulations, refinement by either increasing the number of elements/nodes and/or plane waves in the expansion is required.

Figure 6.14b shows the condition numbers of the BEM system matrices of each simulation. The conditioning of the system matrix improves as the value of τ decreases. Figure 6.14b does not show a significant difference between the discretised cube boundary and Coulomb force methods.

While the previous example shows that the Coulomb force method does not improve the accuracy of PU-BEM simulations given a value of M that can be obtained with discretised cube boundary method, the principal advantage of the new method is in the ability to choose an arbitrary M. For example, if it is established, from (6.44), that $M = 30$ would provide a prescribed error, using the discretised cube boundary method to choose wave directions of the PU-BEM enrichments results in running a simulation with $M = 56$ (the lowest available). The computational operations required for PU-BEM system matrices are of $\mathcal{O}(N_{\text{dof}}{}^2)$ for building and $\mathcal{O}(N_{\text{dof}}{}^3)$ for solving. This would increase the total number of operations (and therefore time for simulation) significantly for each enriched node using the higher M. As the number of elements in the mesh increases, so does the computational expense of using the extra plane waves. It is, therefore, extremely desirable to have the flexibility which is offered by the new approach to choose the exact number of plane waves desired.

Figure 6.15a displays the N_{dof} required in order to obtain an error of "engineering precision", which the authors define as $\mathcal{E} \sim 1\%$. The figure shows the large discrete increases in M, and therefore N_{dof}, required when using the discretised cube boundary method. In comparison, much smaller discrete increases in N_{dof} are required when using the Coulomb force method. The curves interpolate at the few coincidental points where the M required to obtain a 1% error is equal to a value that can be obtained using the discretised cube boundary method.

Figure 6.15b shows the value of τ of each simulation in Figure 6.15a. Two trends are noted. First, there is a significant rise in τ when M (and therefore N_{dof}) rises using the discretised cube boundary method. At low wavenumbers, this leads to values of $\tau > 10$ which is higher than that required for an error $\mathcal{E} \sim 1\%$ using the conventional BEM. This also has a negative impact on the conditioning of the PU-BEM system matrix which becomes susceptible to errors in the solution so requires a more robust solver. Secondly, the overall trend is that the τ required
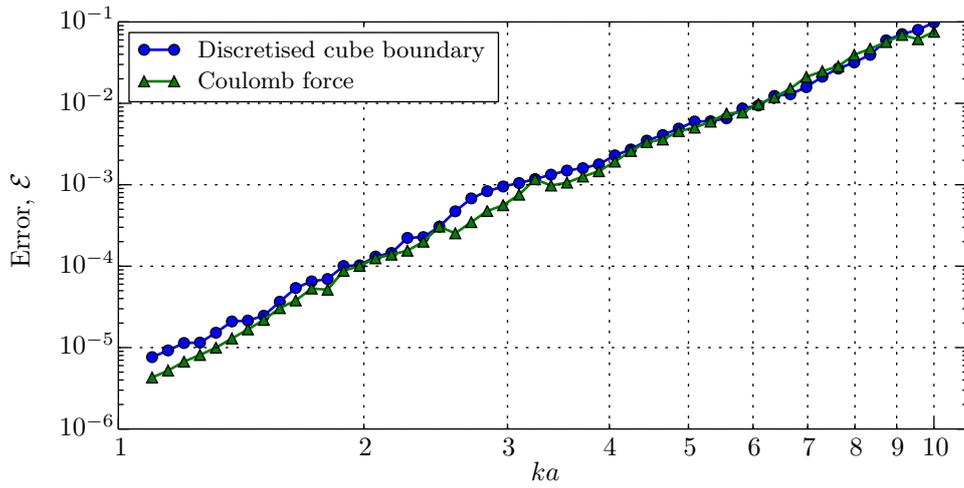
(a) Simulation errors
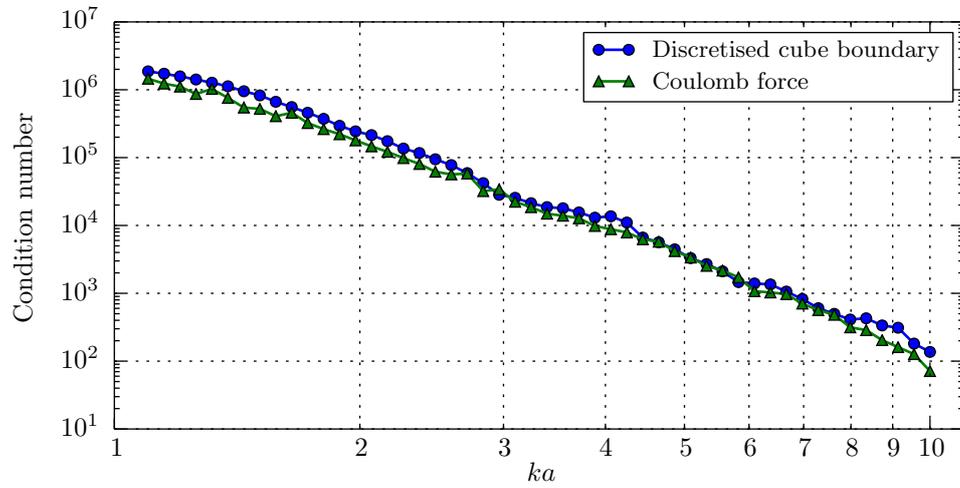
(b) Condition numbers

Figure 6.14: Comparison of PU-BEM simulations using different methods to choose $M = 8$ wave direction in the enrichment.
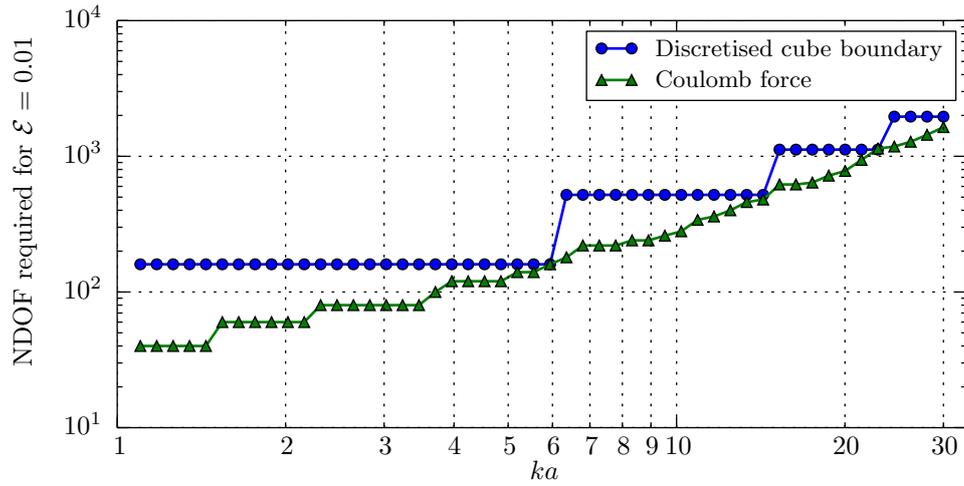
(a) Number of degrees of freedom required to obtain 1% error
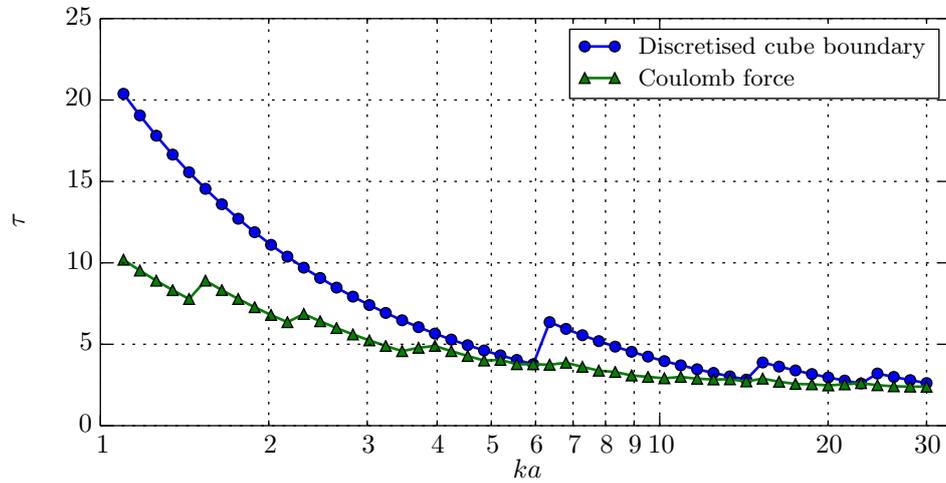
(b) τ required to obtain 1% error

Figure 6.15: Comparison of requirements of PU-BEM simulations of sphere problem to obtain 1% error using different methods wave directions in the enrichment.

to obtain an error $\mathcal{E} \sim 1\%$ falls as ka increases. For $ka = 30$, a value $\tau \approx 2.4$ (1640 degrees of freedom) was required for the PU-BEM simulation using the Coulomb force method; in comparison, a conventional BEM simulation with $\tau \approx 10$ would require approximately 28,640 degrees of freedom.

Figure 6.16a is similar to Figure 6.15a but shows the N_{dof} required but for a smaller error: $\mathcal{E} \sim 0.1\%$. The same pattern as Figure 6.15a is observed, demonstrating the principal advantage of the Coulomb force method: the ability to choose an arbitrary M.

As discussed above, N_{dof} has a direct impact on the runtime of a simulation, due to the operations required to build and solve the PU-BEM system. It should be noted that in a direct comparison of runtimes between the Coulomb force method and discretised cube method, the former takes significantly longer due to the time-
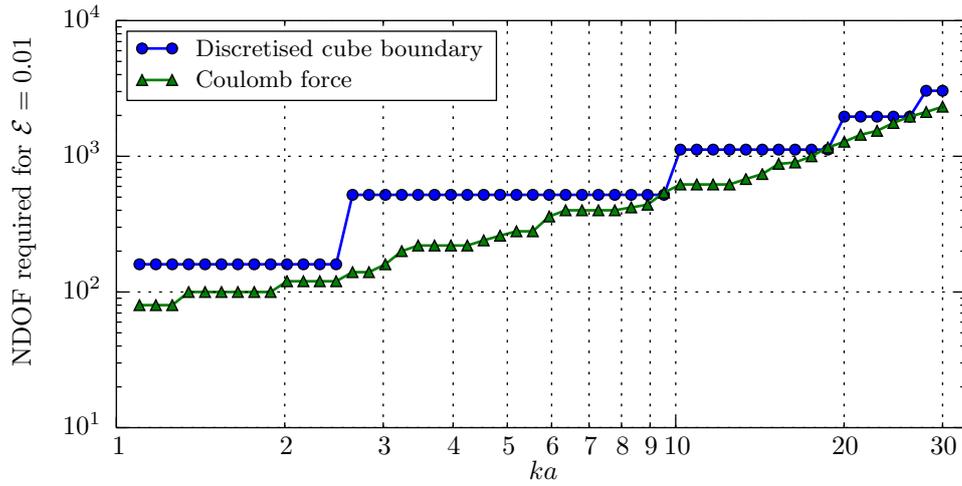
(a) Number of degrees of freedom required to obtain 0.1% error
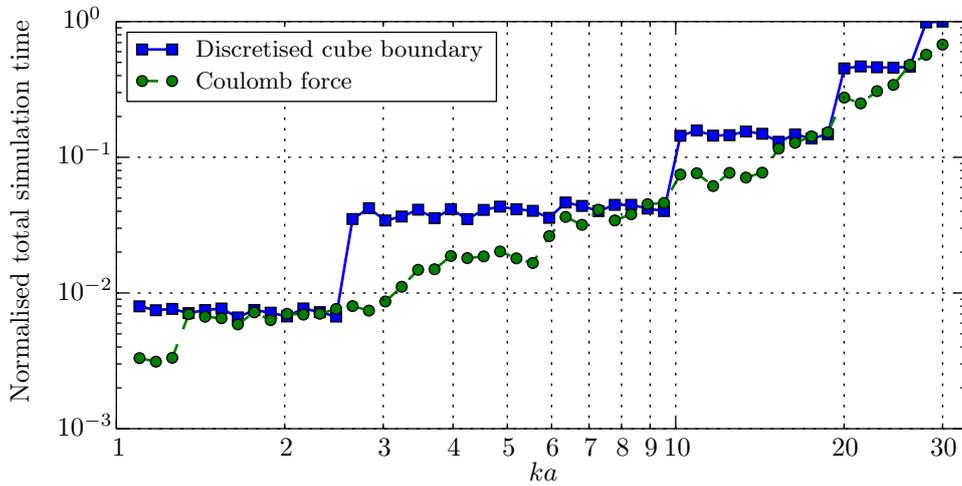
(b) Total simulation runtime of simulations in (a)

Figure 6.16: Comparison of requirements of PU-BEM simulations of sphere problem to obtain 1% error using different methods wave directions in the enrichment.

stepping nature of the scheme. Despite this, the process of finding plane wave directions still constitutes less than 0.1% of the total runtime of all the PU-BEM simulations in this work (for $M < 100$, the Coulomb force method runtime was < 1 second). Figure 6.16b plots the normalised total runtimes of the simulations in Figure 6.16a. With similar steps in the curves, the two figures show a strong correlation; Figure 6.16b demonstrates that the extra runtime required to use the Coulomb force method is insignificant over the period of the entire simulation.

6.6 Conclusions

This chapter has presented a new method for producing evenly spaced distributions of arbitrary numbers of points on a spherical surface. Although this has widespread

application in science and engineering, the motivation is the efficient solution of partition-of-unity finite and boundary element problems in 3D wave scattering.

The method is a simple one, based on the use of an explicit time stepping scheme to converge to a static equilibrium state for a set of charged particles on a spherical surface. Extensions to other geometries are straightforward. Recommendations are made for values of key parameters such as time step and damping.

The method repeatably and accurately reproduces well-known equilibrium states analogous to the platonic solids, and gives improved distributions in comparison with a discretised cube boundary method. The greatest advantage over this latter method, though, lies in the fact that arbitrary numbers of points may be evenly spaced.

The method has been extended by introducing an external charge to give rise to clustering of the directions towards a desired orientation.

Finally, numerical results of PU-BEM wave scattering simulations have been given. These results demonstrate the advantage and flexibility of choosing an arbitrary number of plane waves in a partition-of-unity expansion.

7

Isogeometric analysis and NURBS

7.1 Introduction

In previous PU-BEM work (Chapters 5 and 6 and [97–99]), it has been found that having an analytical geometry is very beneficial. If either the collocation or integration points are not located on the analytical surface, the approximation error increases rapidly as the element sizes increase.

It should be noted that it is possible to get accurate solutions without the analytical geometry. However, the elements are required to be much smaller than with an analytical geometry. Effectively, using an approximate geometry relinquishes most of the advantages of using the enrichment.

Table 7.1 compares PU-BEM simulations of the cylinder problem described in §5.5 using analytical and approximated geometries. It clearly demonstrates the impact of using an analytical geometry. Although the accuracy obtained by the PU-BEM simulation using 20 approximated elements is far greater than the accuracy that would be obtained by a conventional BEM with the same number of degrees of freedom, it is still substantially less accurate than the solution obtained with an analytical geometry.

It is clear from Table 7.1 that there is significant benefit to be derived from using the analytical geometry with a PU enriched BEM. Unfortunately, Lagrangian shape functions do not provide this for many geometries. For the simulations in Chapters 5 and 6, the scatterers were simple enough that analytical geometries were available.

Table 7.1: Comparison of errors of PU-BEM simulations of the cylinder problem ($k = 50$) using analytical or approximated geometry.

Analyical geometry (2 elements)			Approximated geometry (2 elements)			Approximated geometry (20 elements)		
M	τ	Error, $\mathcal{E}$	M	τ	Error, $\mathcal{E}$	M	τ	Error, $\mathcal{E}$
38	3.04	3.15×10^{-6}	38	3.04	8.60×10^{-1}	4	3.20	7.28×10^{-2}
50	4.00	7.22×10^{-7}	50	4.00	8.58×10^{-1}	5	4.00	2.70×10^{-2}

This may not be feasible for more complicated scatterers.

An alternative way of providing the exact geometry to a PU enriched BEM simulation is desirable. This is the motivation for exploring the use of isogeometric analysis in the BEM.

7.2 Isogeometric Analysis

Creating a suitable mesh can be a significantly complicated and time-consuming stage of numerical analysis. Techniques that improve mesh quality or reduce the time required to make a suitable mesh are of interest to both the academic and industrial communities. To this end, Hughes *et al.* [56] presented isogeometric analysis (IGA): the concept of using the basis functions that describe a geometry in computer-aided design (CAD) to construct exact geometries for numerical analysis.

While most numerical analysis software makes use of Lagrangian shape functions to describe the geometry and unknown fields of a problem, Hughes *et al.* showed that using *non-uniform rational B-splines* (NURBS) as the basis for analysis provided accuracy benefits over the former approach. IGA should also reduce the difficulties of creating and refining a mesh; this is particularly apparent for large, complex geometries. Most IGA papers have considered the use of NURBS; however, more recently, other basis functions have been investigated such as T-splines [6].

[56] and much of the early research in the isogeometric field applied IGA in the context of the finite element analysis. Applications include structural vibrations [37], fluid-structure interaction [5] and electromagnetics [19]. IGA has also been coupled with existing enriched FEM approaches such as XFEM: De Luycker *et al.* [40] presented such a combination for problems in fracture mechanics.

A potential pitfall for IGA finite elements is that the functions used in CAD only describe the boundary of geometries. Much of the focus of IGA has, therefore, been on developing complicated preprocessing stages from which a solid can be created from the CAD geometry. A much simpler option is to utilise boundary elements.

The NURBS that are ubiquitous in CAD software only describe the boundary of the geometries being modelled. The BEM only requires the boundary of a geometry to be meshed. Hence, IGA and BEM would appear to be a natural combination. It may even be possible to fully integrate the two technologies so that no manual meshing is required at all. This would be of particular interest in industry when conducting preliminary design studies.

While IGA may be a relatively new term, the concept of using splines in BEM is not. In 1990, Cabral *et al.* [21, 22] presented a BEM formulation using B-splines for problems governed by Laplace's equation. An isoparametric formulation was used and it was concluded that these functions were well-suited to solved BEM problems.

More recently, research under the name of isogeometric BEM is increasing rapidly: Politis *et al.* [101] presented an isogeometric BEM for problems of potential flow;

Kang and Qian [66] have presented an isogeometric boundary integral method for shape optimization; Simpson *et al.* [116, 117] applied the approach to elastostatic analysis, coining the term IGABEM; Takahashi and Matsumoto [123] applied the fast multipole method to IGABEM for the Laplace equation; Scott *et al.* [112] employed T-splines for elastostatic problems; Belibassakisa *et al.* [8] presented an isogeometric BEM method for the ship wave resistance problem; and Heltai *et al.* [53] solved Stokes flow problems in 3D with IGABEM.

Some research has already been conducted in the field of isogeometric boundary elements for acoustic problems by Simpson *et al.* [118]; however, an enriched approach has not yet been presented by any other author.

The following sections introduce B-spline and NURBS curves and surfaces and the Bézier elements they can be decomposed into. They are intended only as a brief introduction to the topic and to introduce the nomenclature used in this thesis. This nomenclature differs from other texts and journal papers. A more thorough introduction to the topic of NURBS can be found in [100] and [106]. Chapters 8 and 9 will introduce the use of NURBS in boundary element simulations of acoustic scattering problems.

7.3   B-splines

B-splines and NURBS curves are interpolations of the form:

$$\mathbf{F}(\xi) = \sum_{j=0}^{J} f_j(\xi)\mathbf{P}_j, \tag{7.1}$$

where $\mathbf{F}$ is the function being represented, $\mathbf{P}_j$ are control points—bold here as they could be position vectors—and $\{f_j(\xi), j = 0, \ldots, J\}$ are piecewise polynomial basis functions, on the local coordinate ξ. In this sense, there is little difference between a B-spline representation and a Lagrangian representation. It is the forming of the basis functions and the nature of the control points that distinguish B-splines from Lagrangian curves.

7.3.1   B-spline basis functions

Computation of a set of basis functions first requires a specification of a knot vector and the degree. Let $\Xi = \{\xi_0, \ldots, \xi_s\}$ be a nondecreasing sequence of real numbers, i.e. $\xi_j \leq \xi_{j+1}$ for $j = 0, \ldots, s - 1$. The ξ_j are called knots and Ξ is called the knot vector. There are $s + 1$ knots in a knot vector. The knot vector is the fundamental description of the basis functions of a B-spline.

The jth B-spline basis function of pth-degree is denoted by $N_{j,p}(\xi)$ and is defined

Figure 7.1: Triangular table demonstrating the recursive nature of B-spline basis functions.

$$N_{0,0}$$
$$N_{0,1}$$
$$N_{1,0} \qquad N_{0,2}$$
$$N_{1,1} \qquad N_{0,3}$$
$$N_{2,0} \qquad N_{1,2}$$
$$N_{2,1} \qquad N_{1,3}$$
$$N_{3,0} \qquad N_{2,2}$$
$$N_{3,1}$$
$$N_{4,0}$$
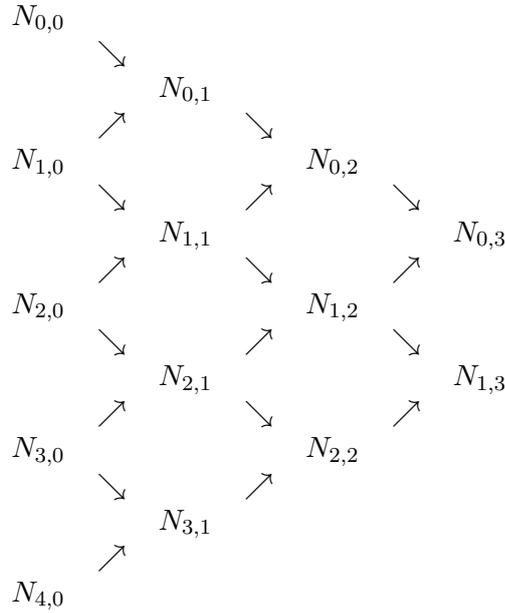
as, for $p = 0$,

$$N_{j,0}(\xi) = \begin{cases} 1 & \text{if } \xi_j \leq \xi \leq \xi_{j+1} \\ 0 & \text{otherwise,} \end{cases} \qquad (7.2)$$

and, for $p \in \mathbb{Z}^+$,

$$N_{j,p}(\xi) = \frac{\xi - \xi_j}{\xi_{j+p} - \xi_j} N_{j,p-1}(\xi) + \frac{\xi_{j+p+1} - \xi}{\xi_{j+p+1} - \xi_{j+1}} N_{j+1,p-1}(\xi). \qquad (7.3)$$

Note, (7.3) can lead to the quotient $\frac{0}{0}$; this is evaluated as zero.

$N_{j,0}(\xi)$ is a step function, equal to one on the half-open interval $\xi \in [\xi_j, \xi_{j+1})$ and zero everywhere else. This half-open interval is called the jth knot span. For $p > 0$, $N_{j,p}(\xi)$ is a linear combination of two $(p - 1)$-degree basis functions; i.e. B-spline basis functions are recursive in nature. The computation of basis functions is diagrammatically represented in Figure 7.1. This triangular table shows which basis functions are required to make higher degree basis functions.

If there are $s+1$ knots in a knot vector, there are s zeroth-degree basis functions $N_{j,0}$, $s-1$ first degree functions $N_{j,1}$, and so forth: in general, there are $s - p$ pth-degree functions, $N_{j,p}$. An alternative way of stating this is: for $s + 1$ knots and degree p, there are $J + 1$ basis functions where $J = s - p - 1$.

Figure 7.2 shows a set of B-spline basis functions and the effect of varying a single knot. Notice that only three second-degree basis functions are affected by this change in knot. Note also, in any knot span $[\xi_j, \xi_{j+1})$ there are, at most, $p+1$ nonzero basis functions: $N_{j-p,p}(\xi), \ldots, N_{j,p}(\xi)$. This can be confirmed by considering Figure 7.1 again. Knowledge of this can avoid the unnecessary computation of null basis functions for a given value of ξ. It is also known that B-spline basis functions have
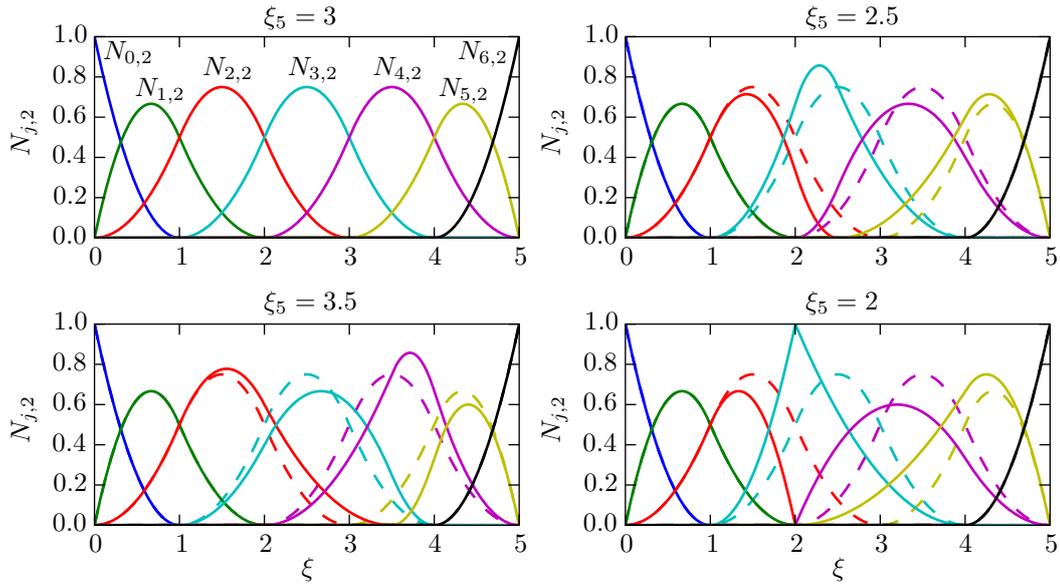
Figure 7.2: Second-degree basis functions, $N_{j,2}$, of the knot vector $\Xi=\{0, 0, 0, 1, 2, \xi_5, 4, 5, 5, 5\}$. Each plot uses a different value of ξ_5.

the partition of unity property; i.e. $\sum N_{j,p}(\xi) = 1$ for $\xi \in [\xi_0, \xi_s]$.

The first derivative of $N_{j,p}$ is given by

$$N'_{j,p}(\xi) = \frac{p}{\xi_{j+p} - \xi_j} N_{j,p-1}(\xi) - \frac{p}{\xi_{j+p+1} - \xi_{j+1}} N_{j+1,p-1}(\xi). \qquad (7.4)$$

A more general formula for the kth derivative is

$$N^{(k)}_{j,p}(\xi) = p \left(\frac{N^{(k-1)}_{j,p-1}(\xi)}{\xi_{j+p} - \xi_j} - \frac{N^{(k-1)}_{j+1,p-1}(\xi)}{\xi_{j+p+1} - \xi_{j+1}} \right). \qquad (7.5)$$

7.3.2   B-spline curves

A pth-degree B-spline curve is defined by

$$\mathbf{C}(\xi) = \sum_{j=0}^{J} N_{j,p}(\xi)\mathbf{P}_j, \quad \xi \in [a, b], \qquad (7.6)$$

where $\mathbf{P}_j$ are the control points, and $N_{j,p}(\xi)$ are the pth-degree B-spline functions defined on the knot vector

$$\Xi = \{\underbrace{a,\ldots,a}_{p+1}, \xi_{p+1}, \ldots, \xi_{s-p+1}, \underbrace{b,\ldots,b}_{p+1}\},$$

with $s + 1$ knots. For the remainder of this thesis, the assumption is made that $a = 0$ and $b = 1$, such that $\xi \in [0, 1]$ on any B-spline, NURBS or Bézier curve.

Figure 7.3 shows basis functions and sections of the B-spline curve corresponding to the individual knot spans; the alternating solid/dashed segments correspond to
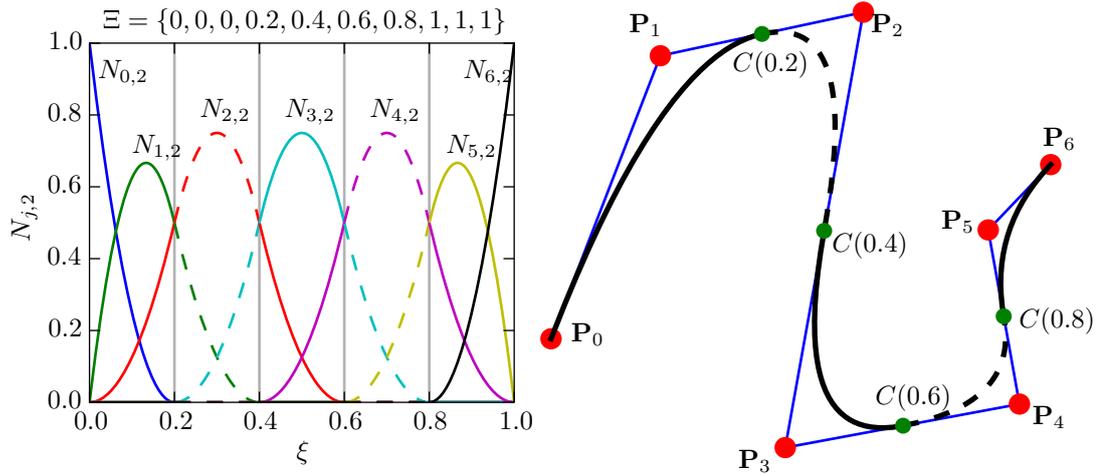
Figure 7.3: Quadratic B-spline basis functions and B-spline curve. The blue line represents the control polygon, mapped by the control points (red dots). The green dots show the parts of the curve where $\xi = 0.2, 0.4, 0.6, 0.8$.

the different knot spans defining the curve. One immediate observation is that this curve only interpolates the control points at the end points. While it is possible to select knot vectors that will interpolate more control points, it is an important property to note. It means that control points are not the same as nodes in Lagrangian representations.

Some texts use the term *multiplicity* to mean to number of times a knot is repeated within Ξ. If a knot, ξ, is repeated k times then $N_{j,p}(\xi)$ is least $p - k$ times continuously differentiable. B-spline basis functions are infinitely differentiable elsewhere. A B-spline curve inherits this property; thus, $\mathbf{C}(\xi)$ is infinitely differentiable between knots and s, at least, $p - k$ times continuously differentiable at a knot of multiplicity k.

B-splines can be modified by changing the knot vector or moving control points. The blue line in Figure 7.3, known as the *control polygon*, represents a piecewise linear approximation of the curve approximated with the control points. The approximation is improved by knots and control points (h-refinement) or degree elevation (p-refinement).

$\mathbf{C}^{(k)}(\xi)$, the kth derivative of $\mathbf{C}(\xi)$, can be computed using the kth derivatives of the basis functions (see (7.4) and (7.5)):

$$\mathbf{C}^{(k)}(\xi) = \sum_{j=0}^{J} N_{j,p}^{(k)}(\xi)\mathbf{P}_j. \tag{7.7}$$

7.4   NURBS

A pth-degree NURBS curve is defined by

$$\mathbf{C}(\xi) = \frac{\sum\limits_{j=0}^{J} N_{j,p}(\xi)w_j\mathbf{P}_j}{\sum\limits_{j=0}^{J} N_{j,p}(\xi)w_j}, \tag{7.8}$$

where $\mathbf{P}_j$ are the control points (forming a control polygon), $w_j > 0$ are weights, and $N_{j,p}(\xi)$ are pth-degree B-spline basis functions defined on a knot vector Ξ. Again, it is assumed that $\xi \in [0,1]$.

If one defines

$$R_{j,p}(\xi) = \frac{N_{j,p}(\xi)w_j}{\sum\limits_{i=0}^{J} N_{i,p}(\xi)w_i}, \tag{7.9}$$

then equation (7.8) can be rewritten in the form

$$\mathbf{C}(\xi) = \sum_{j=0}^{J} R_{j,p}(\xi)\mathbf{P}_j. \tag{7.10}$$

The $R_{j,p}(\xi)$ are the piecewise rational basis functions on $\xi \in [0,1]$. They have many similar properties to B-spline functions, e.g. partition of unity. Indeed, if all $w_j = \alpha$ and $\alpha \neq 0$ then $R_{j,p}(\xi) = N_{j,p}(\xi)$ for all j. Thus, B-splines can be considered a special case of NURBS.

The important difference between NURBS and B-splines is the use of the variable weights, w_j. This is demonstrated in Figure 7.4 where a single weight in a quadratic NURBS curve is being varied to alter a curve. Note that varying w_1 only modifies the curve in the interval $\xi \in [0, \frac{2}{3}]$; this property is known as *local approximation* and becomes useful when decomposing NURBS curves (§7.4.2) into their piecewise components. Generally, if w_j increases, $\mathbf{C}(\xi)$ moves closer to $\mathbf{P}_j$. For a fixed ξ, a straight line can be drawn through $\mathbf{C}(\xi)$ for $0 \leq w_j \leq \infty$; this is demonstrated in Figure 7.4 by the green line at $\xi = 3/20$.

Derivative NURBS curves can be calculated using the following formulae:

$$\mathbf{C}^{(k)}(\xi) = \sum_{j=0}^{J} R_{j,p}^{(k)}(\xi)\mathbf{P}_j, \tag{7.11}$$

where

$$R_{j,p}'(\xi) = w_j\frac{W(\xi)N_{j,p}'(\xi) - W'(\xi)N_{j,p}(\xi)}{W(\xi)^2}, \tag{7.12}$$

$$W^{(k)}(\xi) = \sum_{j=0}^{J} N_{j,p}^{(k)}(\xi)w_j, \tag{7.13}$$
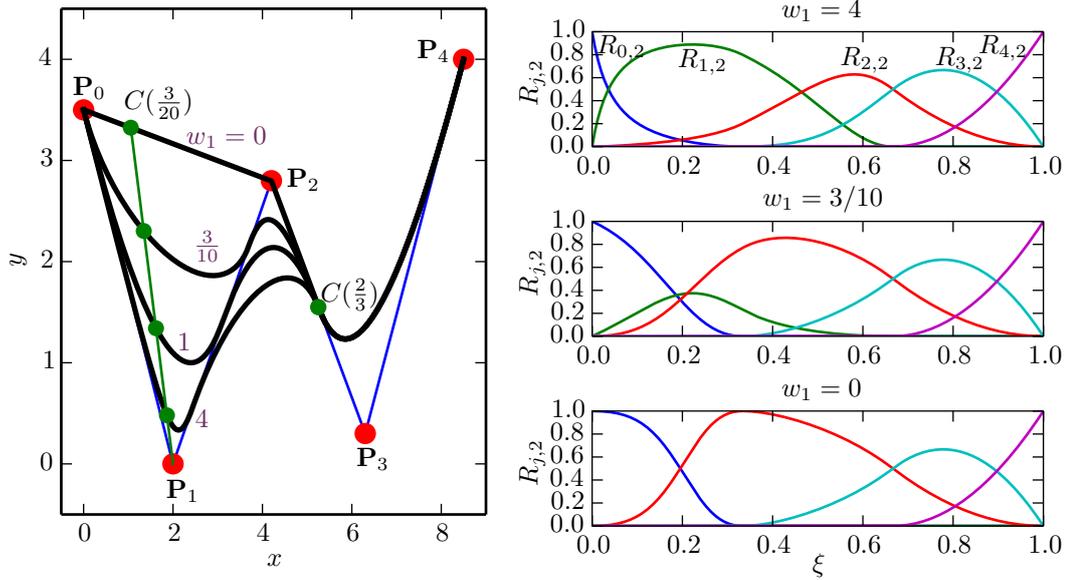
Figure 7.4: Quadratic NURBS curve, $\Xi = \{0, 0, 0, \frac{1}{3}, \frac{2}{3}, 1, 1, 1\}$, with varying w_1; all other $w_i = 1$.

and, for higher derivatives,

$$R_{j,p}^{(k)}(\xi) = \frac{w_j N_{j,p}^{(k)}(\xi) - \sum_{i=1}^{k} \binom{k}{i} W^{(i)}(\xi) R_{j,p}^{(k-i)}(\xi)}{W(\xi)}, \tag{7.14}$$

where

$$\binom{k}{i} = \frac{k!}{i!(k-i)!}. \tag{7.15}$$

7.4.1   Homogeneous coordinates

An efficient method of representing NURBS curves is with *homogeneous coordinates*. Control points are considered to have an extra dimension; i.e. 2D control points are three-dimensional vectors. Let H be a perspective map

$$\mathbf{P}_j = H\{\mathbf{P}_j^w\} = H\{(X_j, Y_j, W_j)\} = \left(\frac{X_j}{W_j}, \frac{Y_j}{W_j}\right) = (x_j, y_j). \tag{7.16}$$

Multiplying the two-dimensional x_j and y_j coordinates by their respective weight w_i and creating $\mathbf{P}_j^w = (x_j w_j, y_j w_j, w_j)$ circumvents the calculation of rational basis functions as non-rational B-spline basis functions can be used on these three-dimensional control points before being mapped into Euclidean two-dimensional points. Explicitly:

$$\mathbf{C}(\xi) = H\{\mathbf{C}^w(\xi)\} = H\left\{\sum_{j=0}^{J} N_{j,p}(\xi)\mathbf{P}_i^w\right\}. \tag{7.17}$$

The above also works similarly, mapping 3D control points into a four-dimensional vector.

Implementing homogeneous coordinates, and therefore using only non-rational basis functions, could reduce the computational burden of using NURBS as simpler basis functions are required. This effect will be greater when the derivatives of an interpolation are required. The technique was not implemented for the work within this thesis, however, but should be considered when taking the work further.

7.4.2   NURBS curve decomposition

NURBS curves can, in fact, be presented by a set of piecewise, rational Bézier curves. NURBS are simply an efficient way of storing such a curve for CAD purposes as they reduce the number of control points and basis functions.

For numerical analysis, however, using Bézier curves (or patches in 3D) is preferable for two reasons: firstly, the concept of knot vectors and knot spans does not translate easily into existing numerical methods, while 'elements' are easily understood; secondly, the basis functions of Bézier elements—so-called *Bernstein polynomials*—are much faster to compute as they are defined over the entire element—rather than having to compute knot spans—and they are not recursive.

Bézier control points are obtained by refining (inserting knots into) the knot vector until each interior knot has multiplicity p. Piegl and Tiller [100] discuss knot insertion thoroughly and provides sample code for efficient algorithms[*].

Bézier curves of pth degree are defined by

$$\mathbf{C}(\xi) = \sum_{j=0}^{p} B_{j,p}(\xi)\mathbf{P}_j, \quad \xi \in [0,1], \tag{7.18}$$

where $\mathbf{P}_j$ are control points and $B_{j,p}$ are their respective Bernstein polynomials given by

$$B_{j,p}(\xi) = \frac{p!}{j!(p-j)!}\xi^j(1-\xi)^{p-i}. \tag{7.19}$$

The derivative of a Bernstein polynomial is defined as

$$B'_{j,p} = p(B_{j-1,p-1}(\xi) - B_{j,p-1}(\xi)), \tag{7.20}$$

where

$$B_{-1,p-1}(\xi) \equiv B_{p,p-1}(\xi)) = 0. \tag{7.21}$$

Rational Bézier curves and their derivatives are calculated in the same way as NURBS: (7.9) can be used substituting $N_{j,p}$ for $B_{j,p}$.

---

[*]N.B. In the edition of Piegl and Tiller [100] used in this work, a number of errors were found. In particular, the algorithms concerning surface knot refinement and decomposition (`A5.5` and `A5.7`) contain missing lines and repeated variable names respectively.

(a) Lagrangian   **(b)** B-spline   **(c)** NURBS
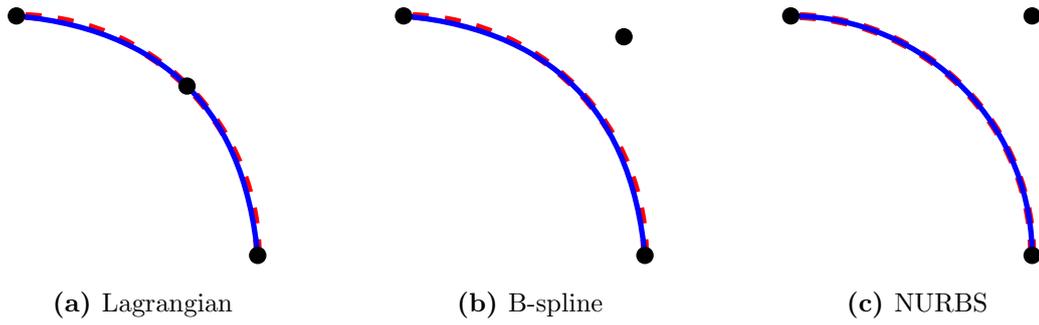
Figure 7.5: Representation of a circular arc using difference basis functions; the red dashed line is an analytical arc.

7.5   Example: circular arc

As stated at the start of this chapter, it is extremely beneficial to have an exact geometry when using an enriched boundary element formulation. This is not always available if using Lagrangian shape functions or non-rational B-splines. An example of this is one of the few geometries for which there is an analytical solution to the Helmholtz equation: the scattering by an infinite cylinder.

An analytical circular arc is available to a BEM code if using polar coordinates; however, with most geometries involving a combination of geometries components, a Cartesian coordinate system is usually used.

Figure 7.5 shows a circular arc modelled by quadratic Lagrangian, B-spline and NURBS basis functions. They all appear to be good approximations; however, only one of the blue curves lies exactly on the dashed analytical curve: the NURBS representation provides the exact arc. The arcs used here are large so that the error can be seen by eye. In practice, much smaller Lagrangian arcs would be used; nevertheless, the error still exists.

7.6   NURBS surfaces

A B-spline surface is a bidirectional net of control points, two knot vectors, and the product of the corresponding univariate B-spline basis on each control point:

$$\mathbf{S}(\xi_1, \xi_2) = \sum_{i=0}^{I} \sum_{j=0}^{J} N_{i,p}(\xi_1) N_{j,q}(\xi_2) \mathbf{P}_{i,j}, \quad \xi_1, \xi_2 \in [0,1], \tag{7.22}$$

with

$$\Xi_1 = \{\underbrace{0, \ldots, 0}_{p+1}, \xi_{1,p+1}, \ldots, \xi_{1,r-p+1}, \underbrace{1, \ldots, 1}_{p+1}\},$$

$$\Xi_2 = \{\underbrace{0, \ldots, 0}_{q+1}, \xi_{2,q+1}, \ldots, \xi_{2,s-q+1}, \underbrace{1, \ldots, 1}_{q+1}\}.$$

Ξ_1 has $r + 1$ knots, Ξ_2 has $s + 1$ knots. Also,

$$r = I + p + 1 \quad \text{and} \quad s = J + q + 1. \tag{7.23}$$

Derivatives of B-spline surfaces are calculated in the form

$$\frac{\partial^{k+l}}{\partial^k \xi_1 \partial^l \xi_2} \mathbf{S}(\xi_1, \xi_2) = \sum_{i=0}^{I} \sum_{j=0}^{J} N_{i,p}^{(k)}(\xi_1) N_{j,q}^{(l)}(\xi_2) \mathbf{P}_{i,j}. \tag{7.24}$$

NURBS surfaces extend from B-spline surfaces similar to the way NURBS curves do from B-spline curves. The definition initially takes the form

$$\mathbf{S}(\xi_1, \xi_2) = \frac{\sum_{i=0}^{I} \sum_{j=0}^{J} N_{i,p}(\xi_1) N_{j,q}(\xi_2) w_{i,j} \mathbf{P}_{i,j}}{\sum_{i=0}^{I} \sum_{j=0}^{J} N_{i,p}(\xi_1) N_{j,q}(\xi_2) w_{i,j}}, \quad \xi_1, \xi_2 \in [0, 1]. \tag{7.25}$$

As before, piecewise rational basis functions can be introduced:

$$R_{i,j}(\xi_1, \xi_2) = \frac{N_{i,p}(\xi_1) N_{j,q}(\xi_2) w_{i,j}}{\sum_{k=0}^{I} \sum_{l=0}^{J} N_{k,p}(\xi_1) N_{l,q}(\xi_2) w_{k,l}}, \tag{7.26}$$

so that (7.25) can be rewritten as

$$\mathbf{S}(\xi_1, \xi_2) = \sum_{i=0}^{I} \sum_{j=0}^{J} R_{i,j}(\xi_1, \xi_2) \mathbf{P}_{i,j}. \tag{7.27}$$

As explained in §7.4.1, NURBS surfaces can be expressed using homogeneous coordinates. Further, the surfaces can be decomposed into their constituent Bézier patches which are easy to implement into existing 3D BEM codes and whose basis functions are computationally less expensive.

7.6.1 Decomposition

NURBS surfaces can be decomposed into an array of Bézier patches in much the same way as curves could. The process is too long to mention in these pages but is explained fully in [100] along with pseudo-code that can be used.

The resulting Bézier patches/elements of pth degrees are defined by

$$\mathbf{S}(\xi_1, \xi_2) = \sum_{i=0}^{p} \sum_{j=0}^{p} B_{i,p}(\xi_1) B_{j,q}(\xi_2) \mathbf{P}_{i,j}, \quad \xi_1, \xi_2 \in [0, 1]. \tag{7.28}$$

Rational basis functions are formed as in (7.26).

8

2D IGABEM and XIBEM

8.1   Formulation of XIBEM for the Helmholtz equation

As explained in §7.4.2, NURBS curves can be decomposed into rational Bézier elements. Some implementations, however, use the original NURBS curves. For the examples in this thesis, there is no discernible difference in the meshes of either form: the control points are the same and the basis functions take the same form. For more complex meshes, it is possible that decomposing NURBS or T-spline meshes into rational Bézier elements creates more degrees of freedom. It is not possible to say whether this is a negative artefact of mesh decomposition or whether those new control points are actually beneficial. This is an investigation for the future.

For reasons of computational ease and for easy integration into the conventional BEM and PU-BEM of the previous work, rational Bézier elements were used for the simulations in this chapter and in Chapter 9. The derivations herein will consider both the case of using a NURBS mesh directly and using its decomposition.

8.1.1   IGABEM

A suitable equation to start with is (3.23), repeated here for convenience,

$$c(\mathbf{p})\phi(\mathbf{p}) + \int_{\Gamma} \left[\frac{\partial G(\mathbf{p},\mathbf{q})}{\partial n(\mathbf{q})} - \alpha(\mathbf{q})G(\mathbf{p},\mathbf{q}) \right] \phi(\mathbf{q})\mathrm{d}\Gamma(\mathbf{q}) =$$
$$\int_{\Gamma} \beta(\mathbf{q})G(\mathbf{p},\mathbf{q})\mathrm{d}\Gamma(\mathbf{q}) + \phi^{\mathrm{inc}}(\mathbf{p}). \quad (3.23)$$

In the classical, collocation BEM, Γ would now be discretised into elements on which the geometry and ϕ are approximated with polynomial, isoparametric elements. Here, instead of piecewise polynomial elements, it is assumed that the scatterer can be expressed as a NURBS curve.

The relationship described in (7.10) provides an analytical geometry given by the mapping

$$\Gamma = \{\mathbf{F}(\xi) : \xi \in [0,1)\}, \quad (8.1)$$

where $\mathbf{F} : \mathbb{R} \to \mathbb{R}^2$ is a NURBS curve of order p and with knot vector Ξ. The

variation of potential over Γ can now be formally expressed in terms of the NURBS interpolation,

$$\phi(\mathbf{q}_\xi) = \sum_{j=0}^{J} R_{j,p}(\xi)\phi_j, \tag{8.2}$$

where $\mathbf{q}_\xi \equiv \mathbf{q}(\xi)$ is used to make the integral equations clearer, and ϕ_j are unknown "control potentials" associated with each of the $J+1$ NURBS basis functions, $R_{j,p}$. Substitution of (8.2) into (3.23) gives the IGABEM boundary integral equation,

$$c(\mathbf{p})\phi(\mathbf{p}) + \sum_{j=0}^{J} \int_0^1 \left[\frac{\partial G(\mathbf{p}, \mathbf{q}_\xi)}{\partial n(\mathbf{q}_\xi)} - \alpha(\mathbf{q}_\xi)G(\mathbf{p}, \mathbf{q}_\xi) \right] R_{j,p}(\xi)|J_\mathbf{F}|\phi_j \mathrm{d}\xi =$$

$$\int_0^1 \beta(\mathbf{q}_\xi)G(\mathbf{p}, \mathbf{q}_\xi)|J_\mathbf{F}|\mathrm{d}\xi + \phi^{\mathrm{inc}}(\mathbf{p}), \quad (8.3)$$

where $|J_\mathbf{F}|$ is the Jacobian of the mapping in (8.1) and $\phi(\mathbf{p})$ is discretised as:

$$\phi(\mathbf{p}_\xi) = \sum_{j=0}^{J} R_{j,p}(\xi)\phi_j, \tag{8.4}$$

where $\mathbf{p}_\xi = \mathbf{p}(\xi)$.

To find the unknown potentials on Γ, (8.3) is collocated at a sufficient number of points on the boundary to yield a system of linear equations that can be solved in a conventional fashion with the integrals being evaluated with appropriate quadrature. In the conventional BEM, the collocation points are placed on nodal points. This is not possible in IGABEM because geometry control points can lie off the boundary. Instead, the Greville abscissae [50, 64] are used, denoted by $\hat{\xi}_g$ and calculated using the NURBS knot vector:

$$\hat{\xi}_g = \frac{\xi_{g+1} + \xi_{g+2} + \cdots + \xi_{g+p-1}}{p}, \quad g = 1, 2, \ldots, J. \tag{8.5}$$

Although there are $J+1$ NURBS basis functions and control points, the Greville abscissae provide only J collocation points. However, the first and last geometry control points of a boundary will be coincident (for closed curves); thus, the first and last NURBS basis functions are combined and the control potentials are also combined as one degree of freedom. This is similar to shared nodes between continuous polynomial elements.

8.1.2 IGABEM with decomposed mesh

Using a decomposed NURBS mesh, the equations are similar except now it is said that there are E non-overlapping rational Bézier elements Γ_e and the analytical geometry is given by

$$\Gamma_e = \{\mathbf{F}_e(\xi) : \xi \in [0, 1)\}, \quad e = 1, \ldots, E, \tag{8.6}$$

where the $\mathbf{F}_e : \mathbb{R} \rightarrow \mathbb{R}^2$ are rational Bézier curves of order p; the variation of potential over each element is,

$$\phi^e(\mathbf{q}_\xi) = \sum_{j=0}^{p} R_{j,p}^e(\xi)\phi_j^e. \tag{8.7}$$

Finally, the IGABEM boundary integral equation becomes

$$c(\mathbf{p})\phi(\mathbf{p}) + \sum_{e=1}^{E}\sum_{j=0}^{p}\int_0^1\left[\frac{\partial G(\mathbf{p},\mathbf{q}_\xi)}{\partial n(\mathbf{q}_\xi)} - \alpha(\mathbf{q}_\xi)G(\mathbf{p},\mathbf{q}_\xi)\right]R_{j,p}^e(\xi)|J_{\mathbf{F}_e}|\phi_j^e\mathrm{d}\xi =$$

$$\sum_{e=1}^{E}\int_0^1\beta(\mathbf{q}_\xi)G(\mathbf{p},\mathbf{q}_\xi)|J_{\mathbf{F}_e}|\mathrm{d}\xi + \phi^{\mathrm{inc}}(\mathbf{p}), \quad (8.8)$$

where $|J_{\mathbf{F}_e}|$ is the Jacobian of the mapping in (8.6) and $\phi(\mathbf{p})$ is discretised as:

$$\phi^{e(\mathbf{p})}(\mathbf{p}_\xi) = \sum_{j=0}^{J} R_{j,p}^{e(\mathbf{p})}(\xi)\phi_j^{e(\mathbf{p})}, \tag{8.9}$$

where $e(\mathbf{p})$ is the element on which the collocation point $\mathbf{p}$ lies.

At this point, it is important to note that Bézier decomposition creates inherently C^0 elements because the process (described in §7.4.2) enforces every interior knot to have multiplicity p. For complex geometries, this will almost certainly lead to C^0 continuity in places where the original NURBS curve had higher continuity between knot spans. Thus, this effectively makes the approach described here a subset of what is anticipated when researchers consider IGA. However, for the problems in this chapter, this has little affect on the XIBEM meshes which are already C^0 continuous at these points and so have identical rational Bézier functions to NURBS functions. For refined IGABEM meshes, however, there will be a decreased continuity where single knots have been inserted to create more knot spans / elements.

Collocation with (8.8) is simpler as no Greville abscissae need to be calculated. Instead, p collocation points are placed on each element, equally spaced in the local coordinate; collocation points at shared control points are not repeated. This has the added benefit that equal spacing in the parametric space automatically clusters collocation points, and therefore provides extra information, in regions of high curvature.

8.1.3 XIBEM

The extended IGABEM introduces a linear, partition-of-unity expansion of plane waves on each NURBS basis function such that (8.2) is reformulated,

$$\phi(\mathbf{q}_\xi) = \sum_{j=0}^{J} R_{j,p}(\xi)\sum_{m=1}^{M} A_{jm}\exp(ik\mathbf{d}_{jm}\cdot\mathbf{q}_\xi), \quad |\mathbf{d}_{jm}| = 1, \tag{8.10}$$

where there are M plane waves in each expansion with prescribed directions of propagation, $\mathbf{d}_{jm} \in \mathbb{R}^2$, and unknown amplitudes, $A_{jm} \in \mathbb{C}$.

The substitution of (8.10) into (8.3) yields

$$c(\mathbf{p})\phi(\mathbf{p}) + \sum_{j=0}^{J}\sum_{m=1}^{M} H_{jm}A_{jm} = \int_0^1 \beta(\mathbf{q}_\xi)G(\mathbf{p},\mathbf{q}_\xi)|J_{\mathbf{F}}|\mathrm{d}\xi + \phi^{\mathrm{inc}}(\mathbf{p}), \qquad (8.11)$$

where

$$H_{jm} = \int_0^1 \left[\frac{\partial G(\mathbf{p},\mathbf{q}_\xi)}{\partial n(\mathbf{q}_\xi)} - \alpha(\mathbf{q}_\xi)G(\mathbf{p},\mathbf{q}_\xi)\right] R_{j,p}(\xi)\exp(ik\mathbf{d}_{jm}\cdot\mathbf{q}_\xi)|J_{\mathbf{F}}|\mathrm{d}\xi, \qquad (8.12)$$

and $\phi(\mathbf{p})$ is discretised in a similar fashion to (8.10):

$$\phi(\mathbf{p}_\xi) = \sum_{j=0}^{J} R_{j,p}(\xi)\sum_{m=1}^{M} A_{jm}\exp(ik\mathbf{d}_{jm}\cdot\mathbf{p}_\xi). \qquad (8.13)$$

(8.11) is the discretised form of the BIE for XIBEM which can be collocated in order to solve (2.5).

The Greville abscissae no longer provide a sufficient number of collocation points. To obtain the required number of collocation points, JM points can be placed uniformly on $\xi \in [0,1)$. An alternative scheme is to uniformly place M collocation points between each knot span; that is to place collocation points between distinct values of ξ_i. In this thesis, XIBEM was applied to a decomposed mesh so it is not possible to say which of these schemes would be most effective.

8.1.4 XIBEM with decomposed mesh

Using rational Bézier elements, XIBEM starts to look similar to the PU-BEM. The potential on each rational Bézier basis function is expanded

$$\phi_j^e(\mathbf{q}_\xi) = \sum_{m=1}^{M} A_{jm}^e\exp(ik\mathbf{d}_{jm}^e\cdot\mathbf{q}_\xi), \quad \left|\mathbf{d}_{jm}^e\right| = 1, \qquad (8.14)$$

and the substitution of (8.14) into (8.8) yields

$$c(\mathbf{p})\phi(\mathbf{p}) + \sum_{e=1}^{E}\sum_{j=0}^{p}\sum_{m=1}^{M} H_{jm}^e A_{jm}^e = \sum_{e=1}^{E} Q^e + \phi^{\mathrm{inc}}(\mathbf{p}), \qquad (8.15)$$

where

$$H_{jm}^e = \int_0^1 \left[\frac{\partial G(\mathbf{p},\mathbf{q}_\xi)}{\partial n(\mathbf{q}_\xi)} - \alpha(\mathbf{q}_\xi)G(\mathbf{p},\mathbf{q}_\xi)\right] R_{j,p}^e(\xi)\exp(ik\mathbf{d}_{jm}^e\cdot\mathbf{q}_\xi)|J_{\mathbf{F}_e}|\mathrm{d}\xi, \qquad (8.16)$$

$$Q^e = \int_0^1 \beta(\mathbf{q}_\xi)G(\mathbf{p},\mathbf{q}_\xi)|J_{\mathbf{F}_e}|\mathrm{d}\xi, \qquad (8.17)$$

and $\phi(\mathbf{p})$ is discretised as

$$\phi_j^{e(\mathbf{p})}(\mathbf{p}_\xi) = \sum_{m=1}^{M} A_{jm}^{e(\mathbf{p})} \exp(ik\mathbf{d}_{jm}^{e(\mathbf{p})} \cdot \mathbf{p}_\xi). \qquad (8.18)$$

where $e(\mathbf{p})$ is the element on which the collocation point $\mathbf{p}$ lies.

This form of XIBEM is used in the numerical examples to follow. The equation is collocated by placing pM collocation points uniformly over each rational Bézier element. Again, collocation points at the end of elements are not repeated.

8.1.5 Choice of enriching wave and integration

The parameter τ is used again is this work, defined as the number of degrees of freedom per wavelength on Γ. More explicitly, the total number of degrees of freedom $N_{\text{dof}} = JM$ is equal to τ multiplied by the number of wavelengths needed to describe Γ; for the XIBEM with a decomposed mesh, $N_{\text{dof}} = EpM$, assuming the order, p, is the same for all elements.

To obtain a desired τ, one is free to increase J or p through knot refinement—inserting knots into the knot vector and creating new control points—and/or increase M by including more plane waves in each basis. For multiple scatterers of different sizes, M can be set globally or locally. It has been found that keeping elements or knot spans similar in length and using a global value of M provides better conditioning than varying M; however, good solutions can be obtained using either approach and a more thorough investigation of the effect of varying M is required. In the PU-BEM, it has been found that increasing M and using fewer elements—but keeping τ constant—provides a greater accuracy of approximation; different types of refinement constitute another topic that should be explored in XIBEM. The plane wave directions in the enrichment are defined uniformly about the unit circle, as described in (4.7).

It should be recalled that for wave problems the Green's function is oscillatory and that all integrations need to be evaluated using a sufficient number of points to capture that oscillation, even in the far field. Thus, for XIBEM simulations, the scheme described in §5.4 is used with integration cells of $\lambda/4$ and a sixth-order Gauss quadrature giving an average integration point spacing of $\lambda/24$. For IGABEM simulations, a sixth-order quadrature is used over each element which is no greater than $2\lambda/\tau$ in length (i.e. the length depends on the τ defined), giving an average integration point spacing of $\lambda/3\tau$.

8.2 Notes on numerical results

The XIBEM can be used to solve acoustic wave scattering problems involving single or multiple scatterers; examples of both types of simulation are included in this
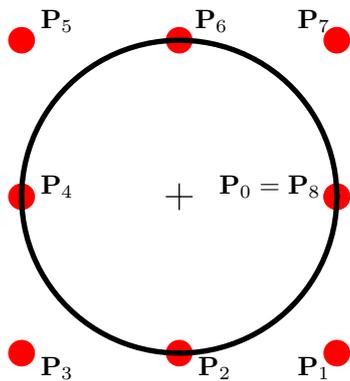
Figure 8.1: Unit-radius circle NURBS curve.
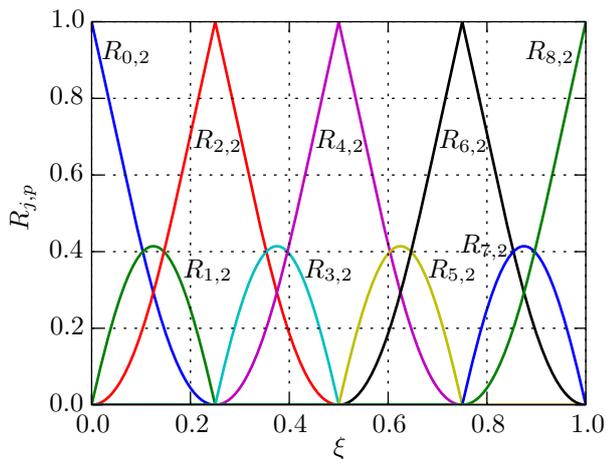
Figure 8.2: NURBS basis functions for unit-circle of degree $p = 2$ shown in Figure 8.1.

chapter. The boundary condition used in all simulations is that of a perfectly reflecting scatter: $\alpha(\mathbf{q}) = \beta(\mathbf{q}) = 0 \; \forall \mathbf{q}$. The CHIEF method [111], as described in §3.4.6, is used to overcome the nonuniqueness problem. All the linear systems of equations are solved using SVD, regardless of their conditioning. The errors, $\mathcal{E}$, are evaluated in a relative L^2-norm sense—as described in (B.1)—using 1000 equally spaced points around each scatterer in the problem.

In this chapter, four types of simulation are referred to: *conventional BEM* implies a piecewise, polynomial BEM using continuous, isoparametric, quadratic elements; *IGABEM* implies an isogeometric BEM using rational Bézier elements, derived from a decomposed NURBS mesh, to describe the geometry and potential function of the scatterer (i.e. it is isogeometric *and* isoparametric); *XIBEM* refers to the extended IGABEM where the rational Bézier basis functions approximating the potential over the boundary are enriched with a linear combination of plane waves; finally, *PU-BEM* refers to a partition-of-unity BEM like that in Chapter 5.

8.3 Scattering by a unit cylinder

Consider a cylinder of radius $a = 1$, centred at the origin. The cylinder is impinged by an incident plane wave of amplitude $A^{\text{inc}} = 1$, and which propagates in the direction $\mathbf{d}^{\text{inc}} = (1, 0)$—angle of incidence $\theta^{\text{inc}} = 0$ radians. This problem has an analytical solution which is described in §2.4.

The isogeometric mesh of a cylinder used in this work consists of a square of nine control points, as shown in Figure 8.1, and NURBS basis functions of degree $p = 2$, displayed in Figure 8.2. When decomposed into rational Bézier elements, the NURBS curve is split at $\xi = \frac{1}{4}, \frac{1}{2}, \frac{3}{4}$. This results in four rational Bézier elements with identical rational Bézier basis functions, as seen in Figures 8.3 and 8.4.

Initially, a comparison between the conventional BEM and the IGABEM is
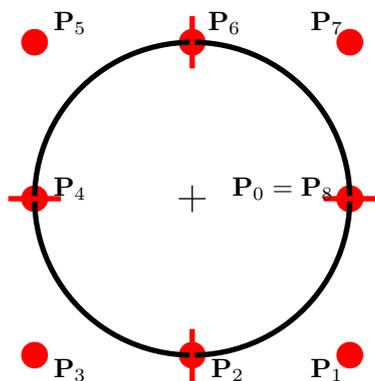
Figure 8.3: NURBS-based unit-radius circle decomposed into four rational Bézier elements.
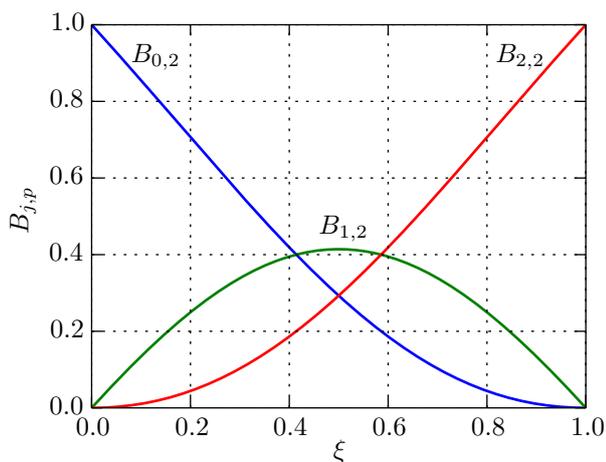
Figure 8.4: Rational Bézier basis functions, of degree $p = 2$, associated with each element in Figure 8.3.

sought. The quality of simulation solution over a range of ka is investigated. As ka increases, degrees of freedom are added to maintain that the number of degrees of freedom per wavelength of the problem, $\tau \approx 10$. In the conventional BEM, the number of elements E must increase as $\tau = 2E/ka$. This is simply achieved by defining E elements of uniform size describing the circumference of the circle. In the IGABEM case, $\tau = J/ka$, so more NURBS basis functions are required before decomposition into rational Bézier elements; this is achieved through knot refinement. In this work, the inserted knots are equally spaced, on the local coordinate, between existing knots. Due to the integer nature of the additions of degrees of freedom, τ cannot be guaranteed to be exactly 10 for all simulations.

The integrals in the conventional BEM are evaluated using six-point quadrature over each element, similar to IGABEM. Higher order integration quadrature has been tested on both types of simulation; however, it was found that the results using the scheme above were similarly accurate, so the errors presented here are mainly due to the discretisation.

Figure 8.5 shows the errors, $\mathcal{E}$, of the simulations using these two methods. The integer nature of addition of elements or knots, to maintain $\tau \approx 10$, causes the sawtooth effect observed at lower values of ka. IGABEM clearly provides a greater accuracy of approximation; this improvement in accuracy is approximately one order of magnitude for $ka > 10$. The greater accuracy is due to the integration points being mapped to the analytical surface of the cylinder by the rational Bézier functions; the polynomial functions of the conventional BEM provide only an approximation to the geometry—though an analytical geometry could be used in some cases. These same functions approximate the wave potential over the boundary and so greater accuracy is also obtained here.

To draw a comparison between IGABEM and XIBEM simulations, first a study
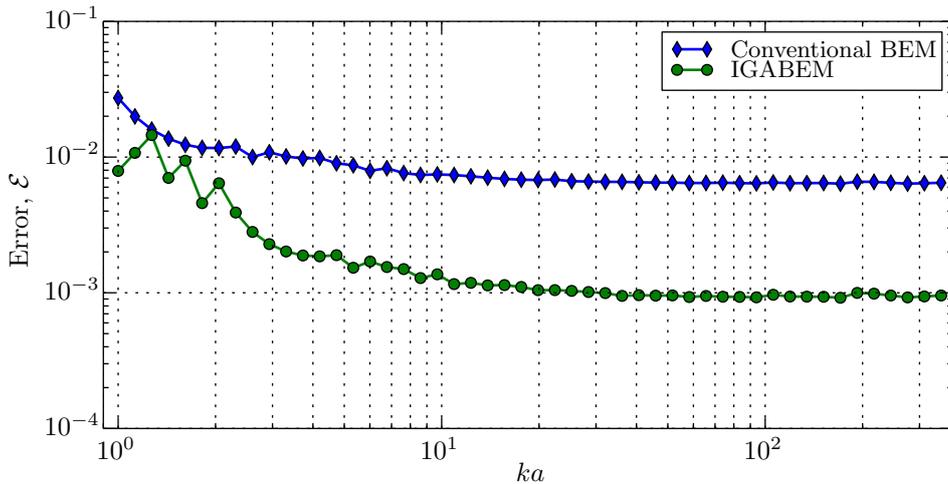
Figure 8.5: Comparison of accuracy of conventional BEM and IGABEM simulations for the hard cylinder problem.

of simulation accuracy with respect to the variable τ is conducted. For XIBEM simulations, the original mesh can be used with no knot refinement. Instead, the number of plane waves, M, in the expansion on each rational Bézier function can be varied; by including the same number of waves in each expansion, $\tau = EpM/ka$. Figure 8.6a shows the accuracy of IGABEM and XIBEM simulations of the cylinder problem for a fixed $ka = 48$ and varying τ. The accuracy of IGABEM simulations increases with increasing τ; for $\sim 1\%$ accuracy, $\tau \approx 5$ is required. At lower values of τ, the accuracy of XIBEM simulations increase with increasing τ with $\sim 1\%$ accuracy being obtainable for $\tau \approx 2.5$. However, once $\tau > 6$, the accuracy of the method appears to be at a maximum.

The cause of this plateau in accuracy can be explained by examining the condition number of the system matrices. The inclusion of the highly oscillatory plane waves in the XIBEM simulations deteriorates the conditioning of the system matrix. Figure 8.6b shows the condition number of the simulations in Figure 8.6a. It appears that the condition number of the XIBEM system matrices also reaches a plateau for $\tau > 6$; however, it is observable that this maximum is approximately 10^{16} which is a computational limit of the SVD routine used in this work. Conversely, the conditioning of the IGABEM simulations appears to be consistent and significantly better than that of the XIBEM simulations. PUM researchers of wave problems commonly report conditioning problems; however, as shown here, the use of a truncated SVD to solve the linear system handles the ill-conditioning well so that solutions of a high accuracy can be gained. As M becomes considerably larger than used in this study, the level of ill-conditioning could increase to a level at which SVD cannot obtain a reasonable solution. However, if J is increased and M decreased, the conditioning of the system can be controlled.

A further comparison of IGABEM and XIBEM simulations is performed, now for varying ka. τ is now approximately fixed: $\tau \approx 10$ for IGABEM simulations;
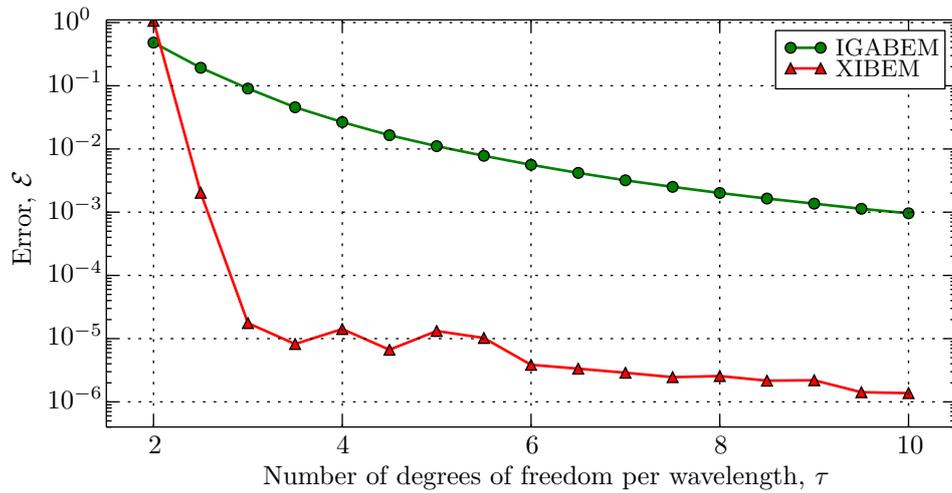
(a) Simulation errors
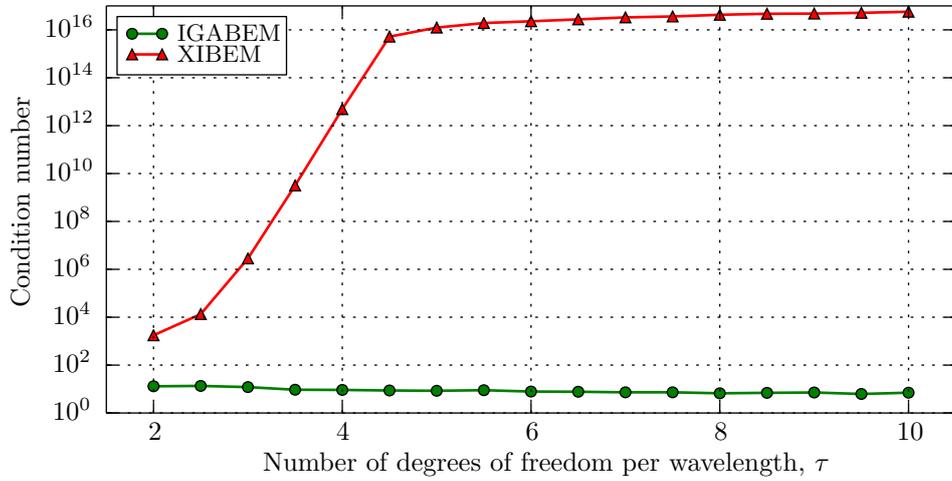
(b) System matrix condition numbers

Figure 8.6: Comparison of IGABEM and XIBEM simulations of cylinder problem with $ka = 48$.

$\tau \approx 3$ for XIBEM simulations. The reader is reminded that this means the XIBEM simulations are computed using only 30% of the number of degrees of freedom used in the IGABEM simulations; the resulting system matrices are less than 10% of the size. Figure 8.7a shows the errors, $\mathcal{E}$, of the IGABEM and XIBEM simulation for $30 \leq ka \leq 500$. As ka increases, the error in the XIBEM approximations decreases rapidly reaching a minimum of approximately 10^{-6}. The IGABEM simulations provide a consistent approximation with an error of approximately 10^{-3}.

Figure 8.7b shows the condition numbers of the system matrices of the simulations in Figure 8.7a. As in the case of varying τ, the conditioning of the IGABEM system matrices is stable, with a condition number $< 10^2$. The increasing ka, and therefore increasing M, leads to degraded conditioning of the XIBEM system matrices. Again, they reach a computational maximum $\sim 10^{16}$; this point on the ka axis corresponds approximately with maximum accuracy obtained in Figure 8.7a. In terms of the reduction of errors, the system solver routine appears to be the limiting factor of the XIBEM simulations; however, SVD is clearly still capable of recovering approximations with an error of $\sim 10^{-6}$ even when the system is very poorly conditioned.

Finally, the XIBEM is compared to the partition-of-unity enriched PU-BEM. PU-BEM simulations are run using continuous quadratic elements and also using trigonometric elements as presented in Chapter 5. The errors, $\mathcal{E}$, of the XIBEM and PU-BEM simulations can be seen in Figure 8.8a, with the corresponding matrix condition numbers in Figure 8.8b. The accuracy of the simulations over the range of ka studied are similar. No method can be said to be significantly more accurate than another. It should be noted, however, that the PU-BEM simulations do not use the quadratic or trigonometric shape functions to locate integration or collocation points. These points are carefully placed on the analytical surface of the scatterer; failure to do so results in unsuccessful simulations with errors $> 100\%$ (though more accurate results can be achieved by using more than four elements). Therefore, the XIBEM simulations hold a significant advantage over the PU-BEM in that the integration and collocation points are automatically mapped to the analytical surface.

8.4 Scattering by multiple scatterers

A second numerical example is included to demonstrate the ability of these boundary element simulations to approximate solutions to problems of multiple scatterers and with internal reflections. The geometry includes a unit-cylinder as described in Section 8.3, but now centred at (2,0). A capsule is defined as two semi-circular arcs centred at (1,0) and (-1,0) and rotating through $\pi/2 > \theta > -\pi/2$ and $3\pi/2 > \theta > \pi/2$ respectively; these arcs are joined by straight line segments of length 2. The geometry includes two of these capsules, rotated $\pm\pi/4$ about the origin and translated through (-1,2) and (-1,-2) respectively. The NURBS representation of a

(a) Errors of simulations
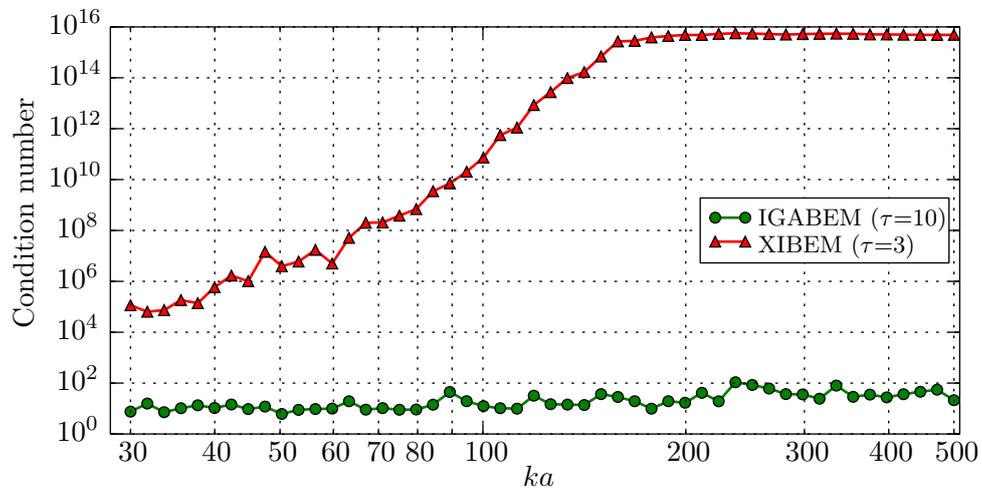
(b) System matrix condition numbers

Figure 8.7: Comparison of IGABEM and XIBEM simulations of cylinder problem over a spectrum with fixed τ.
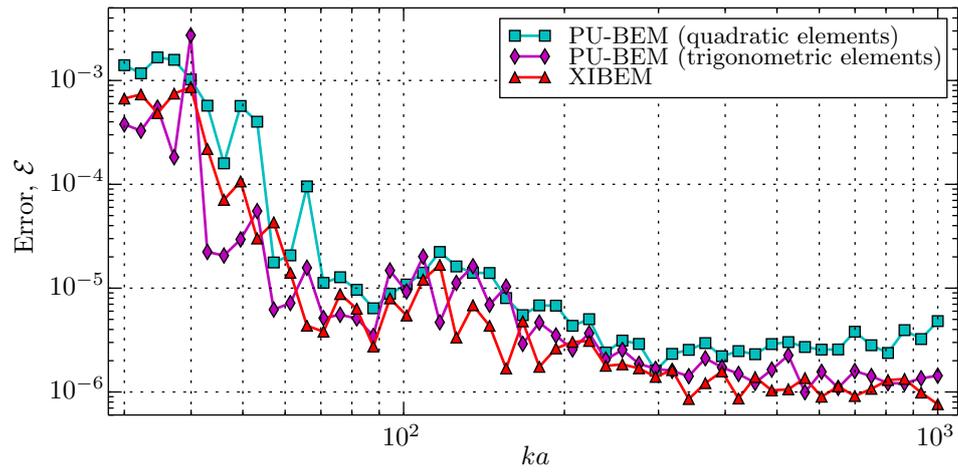
(a) Simulation errors
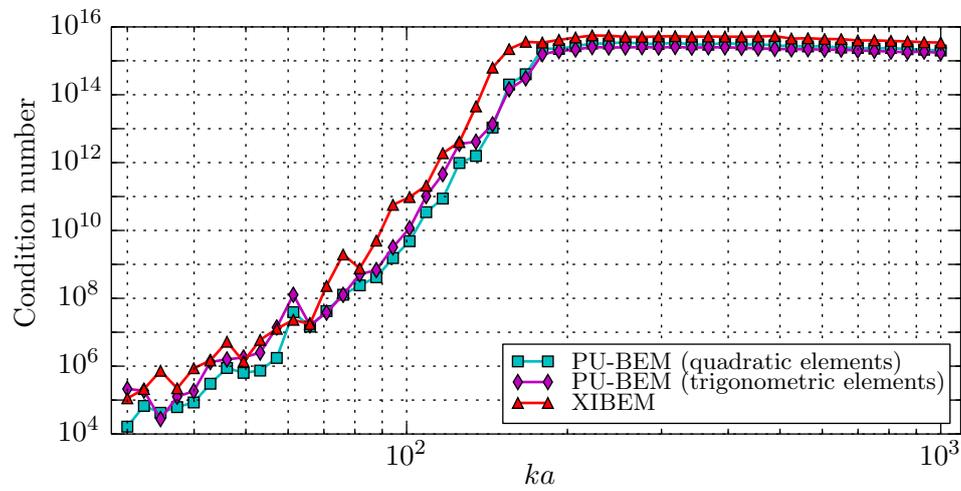
(b) System matrix condition numbers

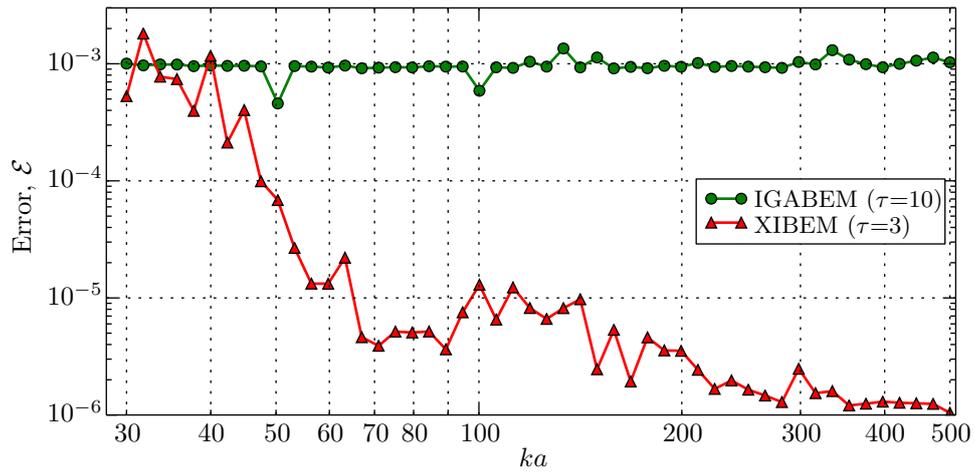**Figure 8.8:** Comparison of XIBEM and PU-BEM simulations of cylinder problem over a spectrum with a fixed τ.
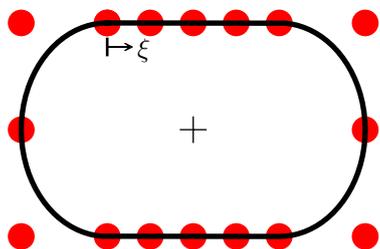
Figure 8.9: NURBS representation of capsule.
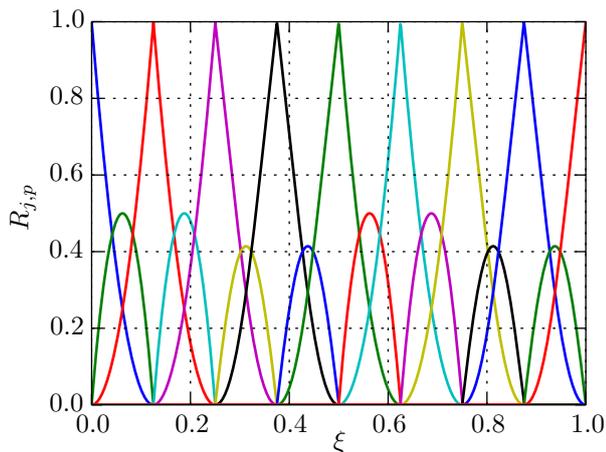
Figure 8.10: NURBS basis functions associated with Figure 8.9.

capsule can been seen in Figure 8.9 with the associated basis functions in Figure 8.10. Note the effect of varying weights on the basis functions; the heights of some of the basis functions vary between straight line segments and arc segments.

Figure 8.11 displays the multi-scatterer geometry and illustrates the absolute value of the total potential, with an incident wave propagating with incidence angle $\theta^{\mathrm{inc}} = 3\pi/4$. No analytical solution for this problem is available; instead, a converged MFS approximation is used as a reference solution when calculating the errors, $\mathcal{E}$.

Figure 8.12 displays the errors of conventional BEM, IGABEM and XIBEM simulations of the multi-scatterer problem. For each simulation type, the number of degrees of freedom per wavelength, τ, is noted in the figure legend; it can be seen that XIBEM results are obtained using three times fewer degrees of freedom than used by the other simulations. The IGABEM approximations are clearly more accurate than those of the conventional BEM; furthermore, the XIBEM approximations have smaller errors than both.

For this problem, condition numbers for conventional BEM simulations and IGA-BEM simulations are similar, in the range $28 \leq \kappa \leq 215$. These are well conditioned in comparison with XIBEM simulations which have a consistent condition number $\kappa \sim 10^{16}$. Unlike the case of the single cylinder problem, the XIBEM system matrices are ill-conditioned for lower values, as well as higher values, of ka. This is because the number of plane waves, M, in the expansion on each NURBS basis function varies between the cylinder and capsule scatterers. Regardless of the ill-conditioned system matrices of the XIBEM simulations, the SVD of these can provide approximations more accurate than the IGABEM by over an order of magnitude.

Finally, Figure 8.13 compares the accuracy of XIBEM simulations with PU-BEM simulations. With the exception of problems for $ka < 20$, the accuracy of XIBEM and PU-BEM simulations are indistinguishable in this form; nor does the examination of the numerical values provide any significant indication that one method
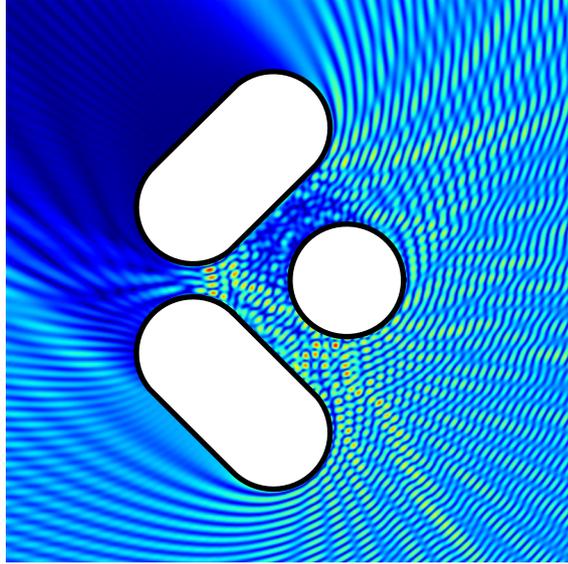
Figure 8.11: A plot of $|\phi|$ illustrating of the internal reflections and scattering caused by the multi-scatterer geometry: $ka = 25$, $\theta^{\mathrm{I}} = 3\pi/4$.
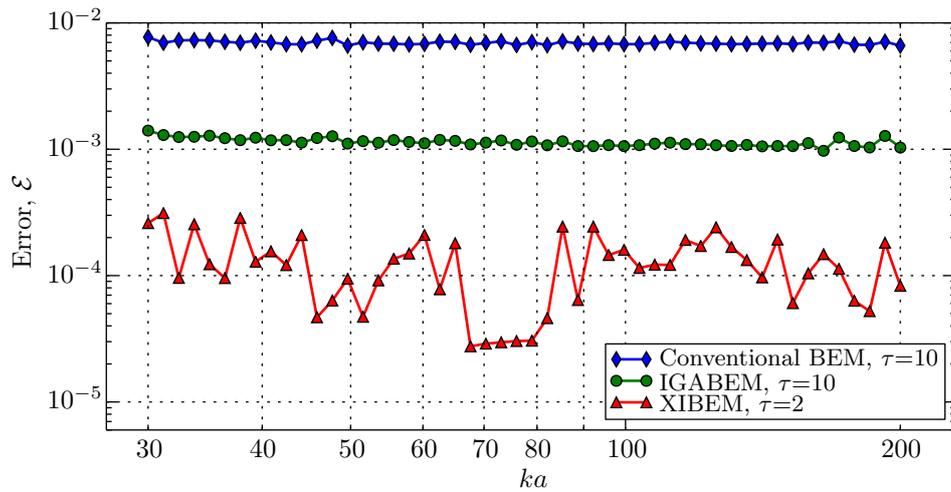
Figure 8.12: Comparison of accuracy of conventional BEM, IGABEM and XIBEM simulations, for the multi-scatterer problem, for fixed τ and varying ka.
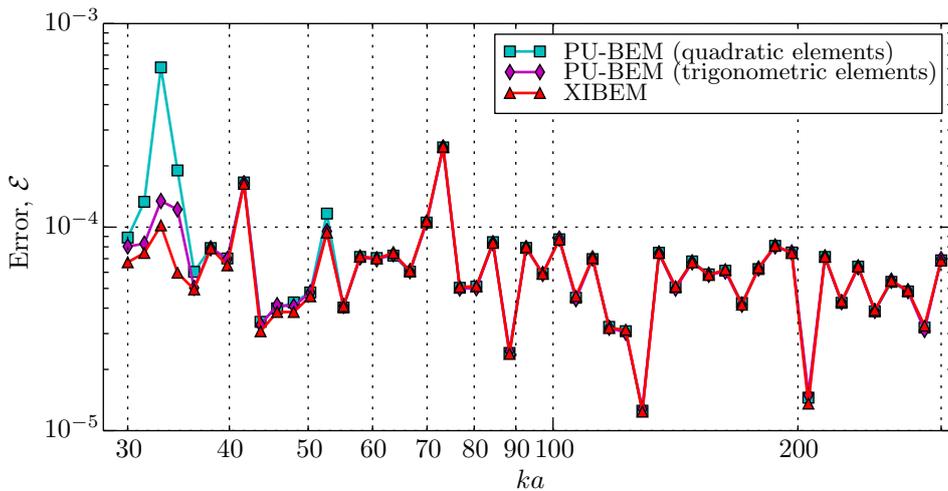
Figure 8.13: Comparison of accuracy of XIBEM and PU-BEM simulations, for the multi-scatterer problem, for fixed $\tau = 3$ and varying ka.

provides consistently more accurate solutions than another. Nearly all of the increased accuracy of this method is found in the plane wave expansion; these findings are similar to those found in Chapter 5. It should be noted again, however, that the collocation and integration points have to be placed on the analytical surface of the scatterer which is inherent in the XIBEM formulation but requires prudence with the PU-BEM formulation.

8.4.1 Run time

The recursive nature of the NURBS basis functions makes them more computationally expensive to compute than Lagrangian functions; however, efficient algorithms [100] can reduce this overhead. One alternative, Bézier decomposition, has been used for the XIBEM simulations here. Another alternative method, Bézier extraction [13], exploits this relationship between NURBS and rational Bézier curves without the need to explicitly decompose the original NURBS curve(s).

The evaluation of the highly oscillatory plane waves in the XIBEM enrichment is also more expensive than evaluating a basis with only nodal values of potential and shape functions; however, this computational expense comes with the benefit of significantly smaller system matrices, reducing system building and solving times. Normalised run times for some approximations by the conventional BEM, IGABEM and XIBEM can be seen in Table 8.1. Simulations times are used only as an indicator; without doubt, more efficient implementations of all three methods are possible. Similar to Table 5.1, the system build and system solve times in in Table 8.1 are not normalised with the same value to avoid readers making unfair comparisons between the matrix assembly (executed by the author's Python script) and matrix solving (executed by optimised libraries).

It can be seen that the improved accuracy of the IGABEM simulations comes at the expense of using the more computationally expensive NURBS basis functions.

Table 8.1: Comparison of simulation times for approximations to the multiple scatterer problem by conventional BEM, IGABEM, and XIBEM. Times are normalised with respect to the longest time of that column.

	Degrees of freedom	System build (normalised)	System solve (normalised)	L^2 error, $\mathcal{E}$
$ka = 30$, BEM	1600	0.0128	0.0076	7.7×10^{-3}
$ka = 30$, IGABEM	1600	0.0417	0.0128	1.4×10^{-3}
$ka = 30$, XIBEM	480	0.0046	0.0008	2.6×10^{-4}
$ka = 70$, BEM	3580	0.0637	0.0902	6.9×10^{-3}
$ka = 70$, IGABEM	3580	0.1622	0.1467	1.1×10^{-3}
$ka = 70$, XIBEM	1075	0.0200	0.0198	2.9×10^{-5}
$ka = 150$, BEM	7600	0.5719	0.8364	6.8×10^{-3}
$ka = 150$, IGABEM	7600	1.0000	1.0000	1.1×10^{-3}
$ka = 150$, XIBEM	2280	0.0854	0.0907	6.1×10^{-5}

The system matrices can take more than twice as long to evaluate than the conventional BEM. The solving of system matrices also takes longer for the IGABEM. The XIBEM simulations take considerably less time to run. This is expected as the system matrices contain 91% fewer entries than those of the conventional BEM and IGABEM simulations. However, the more complicated integration of the XIBEM basis functions could have reduced this time saving during matrix assembly stage of the simulations if more efficient integration schemes were used for the conventional BEM and IGABEM simulations. Overall, it is clear that XIBEM simulations take less time than both conventional BEM and IGABEM simulations, while providing more accurate solutions.

8.5   Conclusions

This chapter has presented two formulations of isogeometric boundary element methods for two-dimensional Helmholtz problems.

In the first formulation, the IGABEM, the geometries of a problem and the approximation of the potential function over the boundary of acoustic scatterers are described by NURBS basis functions. The analytical geometry, provided by NURBS basis functions, used in the integration of the boundary integrals, and the NURBS-approximated function on the scatterer boundary, lead to reduced errors compared to a conventional BEM scheme.

In the second formulation, the XIBEM, the IGABEM has been extended by the use of a plane wave basis to express the wave potential. The superior accuracy of this approach has been demonstrated for problems of single and multiple scatterers with smooth boundaries. These superior accuracies are achieved despite a significant reduction in the degrees of freedom required for a given problem; for an accuracy of $\sim 1\%$, three-times fewer degrees of freedom are required for XIBEM simulations than for conventional BEM or IGABEM simulations. This reduction in system size means that simulations take less time and, for a fixed computational memory

resource, problems of shorter wavelengths are possible. This extends the effective bandwidth for which the isogeometric boundary element approach is valid.

Though small, the system matrices from XIBEM simulations are generally ill-conditioned. It has been shown that SVD is an effective solver for these type of matrices; indeed, the authors found no limit to the scheme other than the available computer memory.

Errors for XIBEM and PU-BEM were compared and found to be similar. However, empirically it has been found there is a requirement, with the partition-of-unity enrichment, for collocation and integration points to be placed on the analytical surface of a scatterer. For PU-BEM simulations, this creates significant difficulties for more complex geometries as these points cannot be recovered from the Lagrangian shape functions. The NURBS basis functions used in XIBEM simulations provide the analytical geometry inherently and, thus, any geometry from CAD software can be analysed with little or no need for meshing. This is a significant benefit of the XIBEM over PU-BEM simulations.

9

<hr>

3D XIBEM

9.1 Formulation of 3D XIBEM for the Helmholtz equation

As with Chapter 8, the derivation of XIBEM begins with the isogeometric, isoparametric IGABEM; the enrichment is applied to this, thus obtaining the XIBEM. For both the IGABEM and XIBEM, a decomposed NURBS mesh will be used. There are two reasons for this: first, it is easy to implement Bézier element into existing code; second, a similar process referred to as *Bézier extraction* is used in IGABEM papers using T-splines [112, 118]. Thus, the following work is comparable to these papers.

A comparison of the accuracy and efficiency of IGABEM and XIBEM simulations using NURBS and their Bézier compositions is an interesting prospect, particularly for geometries where the decomposition procedure creates new control points.

9.1.1 IGABEM

The starting point for deriving the IGABEM and XIBEM is the regularised BIE of (6.3), repeated here

$$\gamma\phi(\mathbf{p}) + \int_{\Gamma}\left[\frac{\partial G(\mathbf{p},\mathbf{q})}{\partial n(\mathbf{q})} - \alpha(\mathbf{q})G(\mathbf{p},\mathbf{q})\right]\phi(\mathbf{q})\mathrm{d}\Gamma(\mathbf{q}) - \int_{\Gamma}\frac{\partial \bar{G}(\mathbf{p},\mathbf{q})}{\partial n(\mathbf{q})}\phi(\mathbf{p})\mathrm{d}\Gamma(\mathbf{q})$$
$$= \int_{\Gamma}\beta(\mathbf{q})G(\mathbf{p},\mathbf{q})\mathrm{d}\Gamma(\mathbf{q}) + \phi^{\mathrm{inc}}(\mathbf{p}). \quad (6.3)$$

Discretisation

It is assumed that the scatterer boundary can be expressed as a single NURBS or T-spline surface, Γ. This surface is then decomposed into E non-overlapping rational Bézier patches of order p as described in §7.6.1. The analytical geometry on each element is given by

$$\Gamma_e = \{\mathbf{F}_e(\xi_1, \xi_2) : \xi_1, \xi_2 \in [0, 1)\}, \quad (9.1)$$

where $\mathbf{F}_e : \mathbb{R}^2 \to \mathbb{R}^3$. The variation of potential over Γ_e is also formally expressed in terms of the rational Bézier functions,

$$\phi^e(\mathbf{q}_\xi) = \sum_{i=0}^{p} \sum_{j=0}^{p} R_{ij}^e(\xi_1, \xi_2) \phi_{ij}^e, \tag{9.2}$$

where $\mathbf{q}_\xi \equiv \mathbf{q}(\xi_1, \xi_2)$, the patch consists of a $(p+1) \times (p+1)$ grid of control potentials, ϕ_{ij}^e, and R_{ij}^e are their associated rational Bézier functions. The R_{ij}^e are the same as are used for the geometry representation. Patches which share geometry control points also share control potentials. The discretisation of the boundary and substitution of (9.2) into (6.3) gives the 3D IGABEM boundary integral equation,

$$\left[\gamma - \sum_{e=1}^{E} L^e \right] \phi(\mathbf{p}) + \sum_{e=1}^{E} \sum_{i=0}^{p} \sum_{j=0}^{p} H_{ij}^e \phi_{ij}^e = \sum_{e=1}^{E} K^e + \phi^{\text{inc}}(\mathbf{p}), \tag{9.3}$$

where

$$H_{ij}^e = \int_0^1 \int_0^1 \left[\frac{\partial G(\mathbf{p}, \mathbf{q}_\xi)}{\partial n} - \alpha(\mathbf{q}_\xi) G(\mathbf{p}, \mathbf{q}_\xi) \right] R_{ij}^e(\xi_1, \xi_2) |J_{\mathbf{F}_e}| \, \mathrm{d}\xi_1 \mathrm{d}\xi_2, \tag{9.4}$$

$$L^e = \int_0^1 \int_0^1 \frac{\partial \bar{G}(\mathbf{p}, \mathbf{q}_\xi)}{\partial n} \phi(\mathbf{p}) |J_{\mathbf{F}_e}| \, \mathrm{d}\xi_1 \mathrm{d}\xi_2, \tag{9.5}$$

$$K^e = \int_0^1 \int_0^1 \beta(\mathbf{q}_\xi) G(\mathbf{p}, \mathbf{q}_\xi) |J_{\mathbf{F}_e}| \mathrm{d}\xi_1 \mathrm{d}\xi_2, \tag{9.6}$$

where $|J_{\mathbf{F}_e}|$ is the Jacobian of the mapping in (9.1). $\phi(\mathbf{p})$ is also expanded as

$$\phi^{e(\mathbf{p})}(\mathbf{q}_\xi) = \sum_{i=0}^{p} \sum_{j=0}^{p} R_{ij}^{e(\mathbf{p})}(\xi_1, \xi_2) \phi_{ij}^{e(\mathbf{p})}, \tag{9.7}$$

where $\mathbf{p}_\xi = \mathbf{p}(\xi_1, \xi_2)$.

The reader is reminded of the comments made in the penultimate paragraph of §8.1.2. Bézier decomposed meshes are inherently C^0 whereas the original NURBS surfaces can have greater continuity at knot intervals. Unlike Chapter 8 however, the XIBEM meshes are not already C^0 continuous and so both IGABEM and XIBEM simulations are both using an approach that would be considered a subset of what is anticipated when researchers talk of IGA. Decomposed meshes are used because they are quick to implement into existing BEM codes.

Collocation

To find the unknown potentials on Γ, (9.3) is collocated at a sufficient number of points on the boundary to yield a system of linear equations that can be solved in a conventional fashion. In the conventional BEM, collocation points are placed on element nodes. This is not possible in IGABEM as geometry control points can, and

often do, lie away from the boundary. Working with the rational Bézier patches, a $(p+1) \times (p+1)$ grid of points equally spaced in the local (ξ_1, ξ_2) coordinate can be used.

9.1.2 XIBEM

To form the extended isogeometric BEM, the linear, partition-of-unity expansion of plane waves is introduced to express ϕ_{ij}^e on each basis function such that (9.2) is reformulated,

$$\phi^e(\mathbf{q}_\xi) = \sum_{i=0}^p \sum_{j=0}^p R_{i,j}^e(\xi_1, \xi_2) \sum_{m=1}^M A_{ijm}^e \exp\left(\iota k \mathbf{d}_{ijm}^e \cdot \mathbf{q}_\xi\right), \quad \left|\mathbf{d}_{ijm}^e\right| = 1, \qquad (9.8)$$

where there are M plane waves in each expansion with prescribed directions of propagation, $\mathbf{d}_{ijm}^e \in \mathbb{R}^3$, and unknown amplitudes, $A_{ijm}^e \in \mathbb{C}$. Note that ι is used to expressed the imaginary number to avoid confusion with the subscript i.

Substitution of (9.8) into (9.3) yields

$$\left[\gamma - \sum_{e=1}^E L^e\right] \phi(\mathbf{p}) + \sum_{e=1}^E \sum_{i=0}^p \sum_{j=0}^p \sum_{m=1}^M H_{ijm}^e A_{ijm}^e = \sum_{e=1}^E K^e + \phi^{\text{inc}}(\mathbf{p}), \qquad (9.9)$$

where L^e and K^e can be expressed the same way as in (9.5) and (9.6) respectively, and

$$H_{ijm}^e = \int_0^1 \int_0^1 \left[\frac{\partial G(\mathbf{p}, \mathbf{q}_\xi)}{\partial n} - \frac{\partial \bar{G}(\mathbf{p}, \mathbf{q}_\xi)}{\partial n}\right] R_{ij}^e(\xi_1, \xi_2) \exp\left(\iota k \mathbf{d}_{ijm}^e \cdot \mathbf{q}_\xi\right) |J_{\mathbf{F}_e}| \, \mathrm{d}\xi_1 \mathrm{d}\xi_2,$$
$$(9.10)$$

This is the discretised form of the BIE for 3D XIBEM which can be collocated in order to solve the Helmholtz equation (2.5). Note that $\phi(\mathbf{p})$ can be expressed in a similar fashion to (9.8):

$$\phi(\mathbf{p}_\xi) = \sum_{i=0}^p \sum_{j=0}^p R_{i,j}^{e(\mathbf{p})}(\xi_1, \xi_2) \sum_{m=1}^M A_{ijm}^{e(\mathbf{p})} \exp\left(\iota k \mathbf{d}_{ijm}^{e(\mathbf{p})} \cdot \mathbf{p}_\xi\right), \qquad (9.11)$$

where $e(\mathbf{p})$ is the element on which the collocation point $\mathbf{p}$ lies.

Collocation

The inclusion of plane waves on each rational Bézier function means that the number of degrees of freedom on each element is greater than the number of control points; thus, a $(p+1) \times (p+1)$ grid of collocation points is no longer sufficient. Instead, a $Z \times Z$ grid of collocation points equally spaced in the local (ξ_1, ξ_2) coordinate system is used on each element, such that the number of collocation points is equal or greater to the number of degrees of freedom on that element; i.e $Z^2 \geq (p+1)(p+1)M$ (assuming a global M). The scheme can lead to creating an overdetermined system matrix;

however, this scheme provides an equal spacing of points in the local coordinate and is much simpler to implement than a scheme that carefully collocates $M(p+1)^2$ points.

9.1.3 Integration and solution

For conventional BEM and IGABEM simulations in the numerical examples to follow, a 10×10 Gauss quadrature is used on each element. For the large elements used in XIBEM, the scheme described in §6.1.5 is used; elements are divided to ensure an average integration point spacing of $\lambda/40$—that is 10 Gauss points over cells with sides $\lambda/4$.

To find the potential on Γ, (9.3) or (9.9) is evaluated at the set of collocation points. This yields a system of linear equations,

$$\left[[\gamma - \mathbf{L}]\mathbf{C} + \mathbf{H} \right] \left\{ \phi \right\} = \left\{ \mathbf{K} + \phi^{\mathrm{inc}} \right\}, \tag{9.12}$$

where $\mathbf{L}$ is a diagonal matrix containing the integrals from (9.5); the matrix $\mathbf{C}$ results from interpolations of $\phi(\mathbf{p})$; the matrix $\mathbf{H}$ is fully populated with integrals from (9.4) or (9.10); the vector $\mathbf{K}$ contains the integrals from (9.6); the vector ϕ^{inc} contains the incident wave potentials at the collocation points; finally, the unknown vector ϕ corresponds to the unknown potentials ϕ^e_{ij} or amplitudes A^e_{ijm}, depending on whether the simulation is IGABEM or XIBEM.

The system in (9.12) is solved using SVD. Though this is not necessary in all cases—the conditioning of some matrices is suitable for a QR decomposition—SVD provides a highly accurate solution from the BEM equations, thus demonstrating the efficacy of the method.

In this chapter, three types of BEM simulation are referred to: *conventional BEM* implies a piecewise, polynomial BEM using continuous, isoparametric, quadratic elements; *IGABEM* implies an isogeometric BEM using the rational Bézier functions of a decomposed NURBS surface to describe the geometry and potential function over the scatterer; *XIBEM* refers to the extended isogeometric BEM, like the IGABEM, except the rational Bézier functions used to describe the potential are enriched with a linear combination of plane waves.

9.2 Unit sphere

The first test problem considered is that of a plane wave impinging a perfectly reflecting sphere. This problem is chosen because an analytical solution, (2.26), exists. The sphere has radius $a = 1$; the incident wave is of unit-amplitude and propagates in the direction $\mathbf{d}^{\mathrm{inc}} = (1, 0, 0)$.

For the conventional BEM mesh, the cube-to-sphere mapping described in §6.5 is used. A sphere meshed using this mapping can be seen in Figure 9.1a. To refine
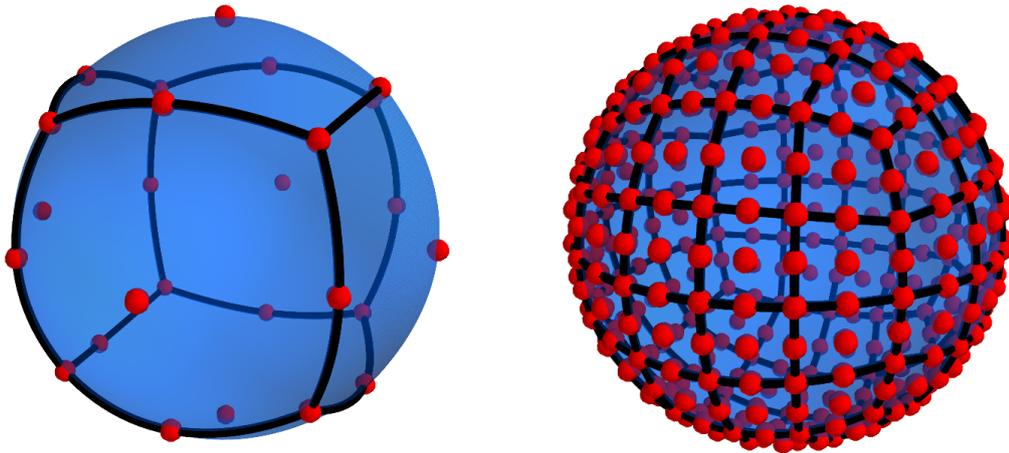
(a) Initial cube-to-sphere mesh with six elements

(b) *h*-refined mesh; each face has been split into sixteen elements

Figure 9.1: Representations of the conventional BEM sphere mesh.

this mesh, each element is simply split into a square number $(4, 9, 16, \ldots)$ of smaller elements; a refined meshed is seen in Figure 9.1b.

The initial IGABEM and XIBEM meshes are created by rotating a semi-circular arc about a central axis—in this case, the z-axis is used. The initial mesh can be seen in Figure 9.2a, with the control points that lie off the surface of the sphere clearly visible. Figure 9.2a is the final mesh for XIBEM; the rational Bézier functions of each geometry element can simply be enriched. For IGABEM, refinements can be made through knot insertion; this is similar to how the elements are split for the conventional BEM. The refined mesh can be seen in Figure 9.2b. From visual examination, the refined IGABEM mesh is not as regular as the mesh in Figure 9.1b. Despite this, it will be shown that the exact geometry used for integration and the rational Bézier functions used to approximate the potential over the surface of the scatterer provide an equally accurate solution.

Another immediate difference that is apparent between the conventional BEM meshes and this isogeometric mesh is the shape of the elements: the mesh in Figure 9.2a has seemingly triangular elements. The elements are, in fact, quadrilateral; the three points along one edge are simply coincident. In this case, these points are the north and south pole of the sphere. For the purposes of functional approximation, these coincident control points are considered a single degree of freedom. The effect of these poles and this type of element becomes apparent in Figure 9.2b: the local coordinate system is only uniform in the longitudinal directions; the Euclidean length in the latitudinal coordinate direction decreases towards the poles.

At these poles, although the normal n is well defined in principal, it cannot be calculated because the necessary tangents are not well defined. This is not a problem with the formulation used in this thesis as no integration points are placed there; however, assuming collocation points are placed there, the Burton-Miller formulation requires derivatives at this point and so manual adjustments are required for analysis
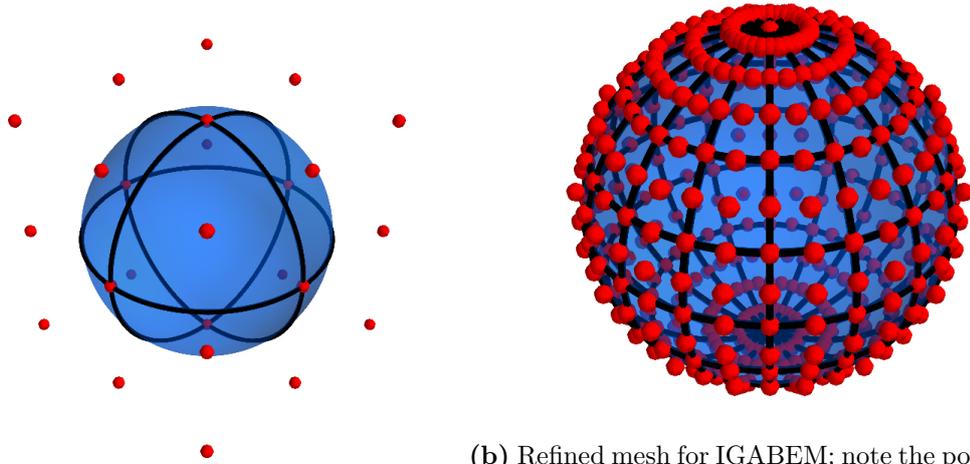
(b) Refined mesh for IGABEM; note the pole
(a) Initial mesh for IGABEM and XIBEM   at the top and bottom

Figure 9.2: Representations of NURBS-based meshes.

[118]. This makes the use of CHIEF points rather than the Burton-Miller formulation more desirable when using isogeometric meshes for acoustic scattering analysis.

Using the $Z \times Z$ collocation grid, described in the formulation, will give multiple collocation points at the poles. As only one of these equations can be used—the rest providing no additional information—there will be an insufficient number of collocation points. Therefore, if coincident collocation points are detected, a $(Z + 1) \times (Z + 1)$ grid can be used (to ensure an adequate number of equations) with the coincident collocation points replaced by a single collocation point.

9.2.1 CHIEF

Thus far, no demonstration has been given to show that the use of CHIEF successfully overcomes the non-uniqueness problem. For a sphere of radius a, the eigenfrequencies at which this nonuniqueness occurs are $ka = n\pi$ where $n \in \mathbb{Z}^+$. To demonstrate the effect of CHIEF points, two sets of XIBEM simulations were run over a range of wavenumbers using 50 plane waves in the basis enrichment; one set of simulations used only collocation points on the surface of the scatterer while the other set added five CHIEF collocation points (an arbitrary but small number). The error of each simulation was evaluated using (B.1) and (2.26). The results can be seen in Figure 9.3. The results verify that the XIBEM formulation with CHIEF is stable at the irregular frequencies while simulations without CHIEF are clearly unstable at those frequencies.

9.2.2 Determining τ required

As discussed in earlier chapters, the number of degrees of freedom N_{dof} used in a BEM simulation has a direct and significant impact on the runtime of that simulation. It is, therefore, desirable to use as few degrees of freedom as possible whilst not
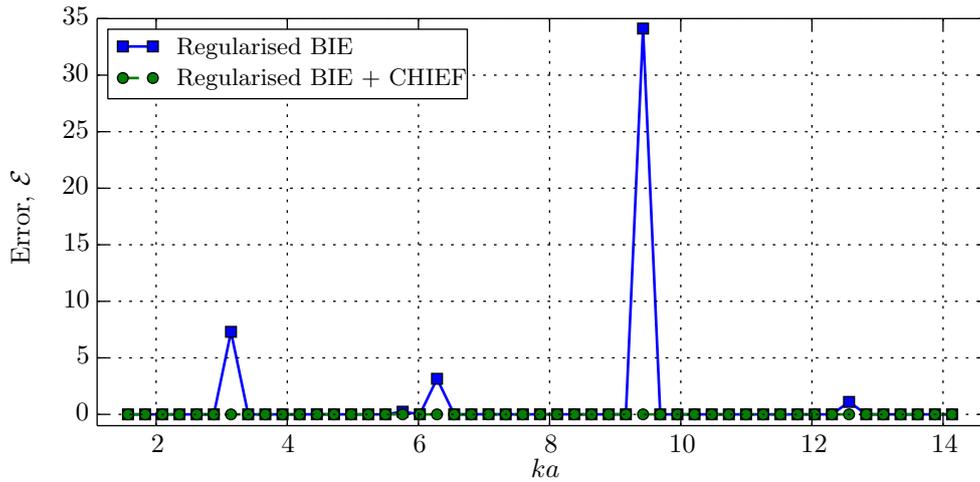
Figure 9.3: Comparison of L_2 errors $\mathcal{E}$ of XIBEM simulations of the unit sphere problem with $M = 50$.

compromising on solution accuracy. The reader is reminded that, in this work, τ is the measure of computational efficiency in terms of degrees of freedom. It is defined as the number of degrees of freedom used in each coordinate direction divided by the wavelengths in the problem. For the unit sphere, this is can be explicitly expressed as

$$\tau = \sqrt{\frac{\pi N_{\text{dof}}}{k^2}}. \tag{9.13}$$

It is desirable to use a method that requires a low value of τ relative to other methods—assuming a similar level of accuracy.

Simulations of the unit-sphere problem were run over a spectrum. Starting with the coarsest mesh and adding more degrees of freedom through h-refinement (for conventional BEM or IGABEM) or adding plane waves into the enriched basis (XIBEM). Simulations were stopped when the error of that simulation was $< 1\%$. Figure 9.4a shows the N_{dof} that was required for a solution of accuracy $\mathcal{E} < 1\%$. Figure 9.4b shows the values of τ calculated using (9.13) and the data from Figure 9.4a.

It is prudent to note that the simulations are confined to the meshes defined at the start of §9.2 and shown in Figures 9.1 and 9.2. Due to the way the refinements are being made, there are significant jumps in N_{dof} at each refinement level. Table 9.1 notes the first few of these iterations for the conventional BEM and IGABEM meshes. The XIBEM mesh consists of the 26 rational Bézier functions of the first IGABEM mesh with the plane wave enrichments; the N_{dof} of the XIBEM mesh is simply then $26M$ i.e. $N_{\text{dof}} = 26, 52, 78, \ldots$.

Taking the above into consideration, the results for low ka in Figures 9.4a and 9.4b do not show the minimum N_{dof} and τ required for any conventional BEM/IGABEM/XIBEM simulation of this problem, but rather those of simulations using the meshes defined in this section. This explains the plateaus seen in
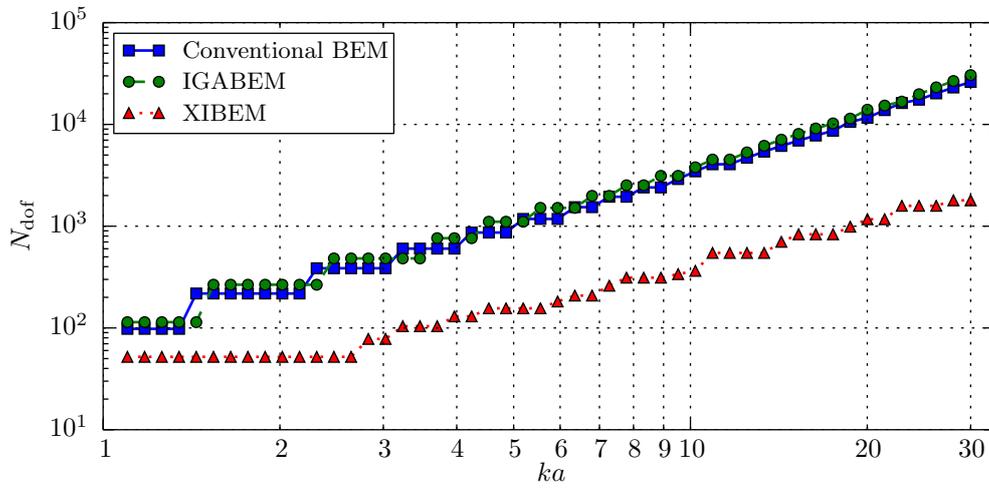
(a) Number of degrees of freedom required to obtain 1% error
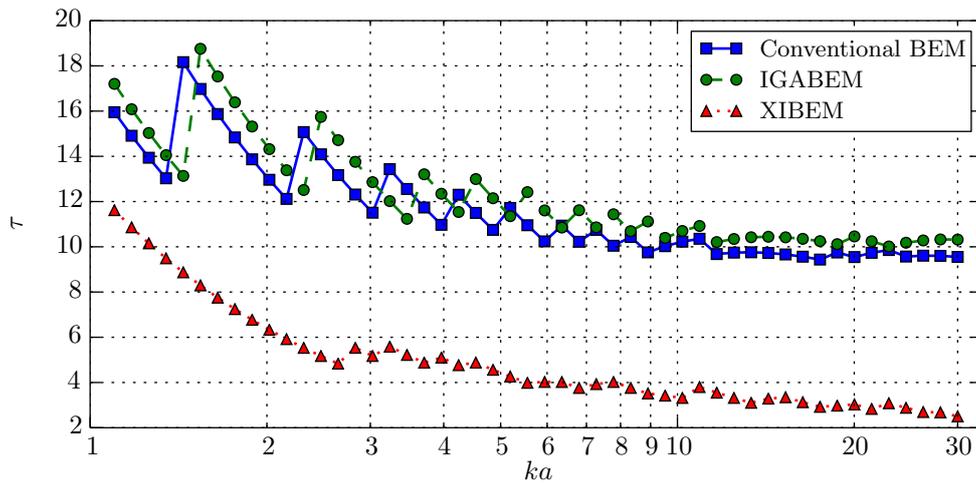
(b) τ required to obtain 1% error

Figure 9.4: Comparison of refinement required to obtain 1% error with conventional BEM, IGABEM and XIBEM simulations over a range of wavenumbers.

Table 9.1: Conventional BEM and IGABEM mesh data for the scattering sphere problem

	Conventional BEM					IGABEM				
Refinement level	0	1	2	3	4	0	1	2	3	4
E	6	24	54	96	150	8	32	72	128	200
N_{dof}	26	98	21	386	602	26	114	266	482	762
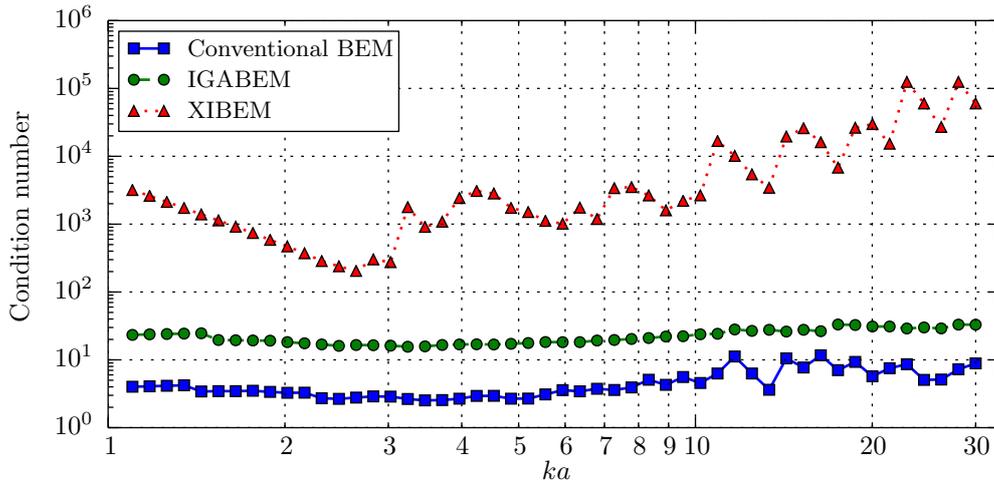
Figure 9.5: Conditioning of system matrices of simulations in Figure 9.4a.

the plots of Figure 9.4a and helps to understand the seemingly high values of τ seen for low ka in Figure 9.4b. The steps in τ seen in the latter figure correspond to the step changes in N_{dof}.

Despite the above, there is a clear trend seen in Figure 9.4b: XIBEM simulations require fewer degrees of freedom than both conventional BEM and IGABEM simulations. As ka increases, conventional BEM and IGABEM simulations appear to need $\tau \approx 10$ for a 1% error while XIBEM simulations require $\tau \approx 3.5$.

Finally for this set of simulations, the condition numbers of the system matrices can be seen in Figure 9.5. In previous two-dimensional work (Chapters 5 and 8 and [99]), it was observed that the approximation basis enrichment had a strong detrimental effect on the conditioning of the system matrices: condition numbers $> 10^{16}$ were recorded. Despite these high condition numbers, solving these systems with SVD still provided very accurate solutions. In Figure 9.5 higher condition numbers are observed for XIBEM again; however, the conditioning in this three-dimensional problem is far better than seen in the equivalent two-dimensional problem. This is possibly due to the enrichment functions—the plane waves—diverging from each other more rapidly in three dimensions instead of two.

As the condition numbers are lower, more efficient solvers could potentially be used. However, the majority of the runtimes of simulations are dominated by the integration and building of the system matrices. This took at least 97% of the total runtime of all XIBEM simulations (it took 99% on average).

9.2.3 Medium wavelength problems

While the previous results show the comparative performance of XIBEM against conventional BEM and IGABEM schemes, the main interest of the work lies in solving problems of shorter wavelengths. By reducing the N_{dof} required to solve a certain problem to a given accuracy, this extends the spectrum for which accurate

results can be obtained with a fixed computational resource. The conventional BEM and IGABEM problems in Figures 9.4 and 9.5 were the largest that could be solved on the conventional desktop PC used for this work, with the largest system matrix being $10,686 \times 10,586$ (approximately 1.8 GB of memory with complex double precision).

The results in Figure 9.4b suggest that XIBEM simulations require $\tau \approx 3.5$ to obtain approximately a 1% error for problems approaching medium wavelengths. This is slightly higher than in the previous work where $\tau \approx 3$ has been used. This is potentially due to the mesh consisting of elements with collapsed poles. These elements are adequate for defining geometry, particularly for use in CAD. They have not been designed specifically for numerical analysis, however, so it is unsurprising to find that their performance might not match that of the regular elements used in §6.5.

Simulations are run over the spectrum $ka \in [20, 60]$, adjusting M such that $\tau \approx 3$. The errors of these simulations can be seen in Figure 9.6a and the condition numbers in Figure 9.6b. For $ka = 60$, the number of plane waves was $M = 396$ and the system matrix was $10,396 \times 10,296$ in size. Using a τ slightly lower than the 3.5 suggested in §9.2.2, it is not surprising to find that some of the simulations have an error of $> 1\%$. Towards the higher wavenumbers, the errors appear to be reducing slightly. It would be interesting to see if this trend continues; however, this is not possible with the current code on the current hardware. Either more memory or the use of an iterative solver would be required.

9.2.4   Off-surface wave potential

The results displayed so far relate to the total potential on the surface of the scatterer. However, engineers are equally, if not more, interested in the wave potential off the scatterer. It is found that the errors in BEM approximations of potential off the surface of a scatterer are lower than those found on the surface. This is due to the smoothing effect of the integration in the BIE; on the surface of a scatterer, the potential is simply found through the basis functions on each element. Table 9.2 displays some errors of IGABEM and XIBEM simulations on and off the surface of the unit sphere. The far-field errors were calculated by evaluating the potential at points on the surface of an imaginary sphere of radius $a = 5$. The increase in accuracy when evaluating potentials off-surface is clear.

Figures 9.7 and 9.8 are plots of absolute total potential off the surface of the sphere obtained from an XIBEM simulation.

9.3   Torus

The final problem to be examined in this thesis is that of a scattering torus. Simulations are run for the cases of an impinging wave propagating in the direction
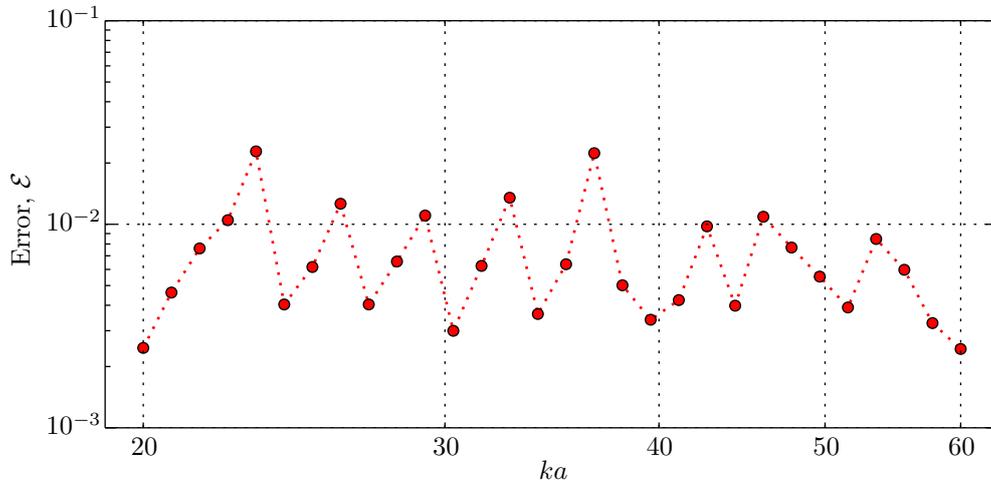
(a) L_2 errors, $\mathcal{E}$
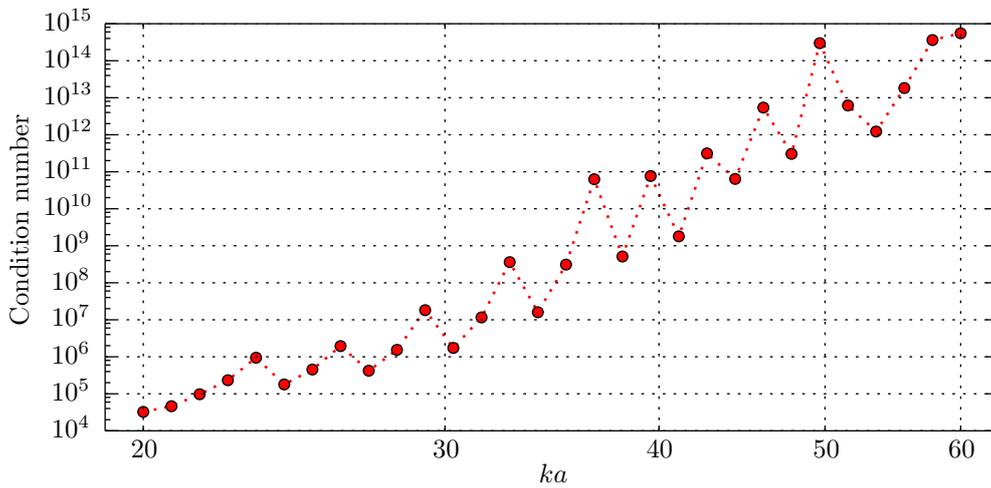
(b) Condition numbers of system matrices

Figure 9.6: XIBEM simulations of medium wavelength simulations of unit-sphere problem.

Table 9.2: Difference between L^2 errors evaluated on the surface of the spherical scatterer and in the far field.

		IGABEM			XIBEM	
	N_{dof}	L^2 surface	L^2 far-field	N_{dof}	L^2 surface	L^2 far-field
$ka = 3$	482	7.0×10^{-3}	1.4×10^{-4}	78	6.9×10^{-3}	1.7×10^{-4}
$ka = 7.75$	1986	1.1×10^{-2}	3.7×10^{-4}	260	1.5×10^{-2}	1.3×10^{-3}
$ka = 20$	13946	9.2×10^{-3}	9.5×10^{-4}	1170	5.0×10^{-3}	7.8×10^{-4}
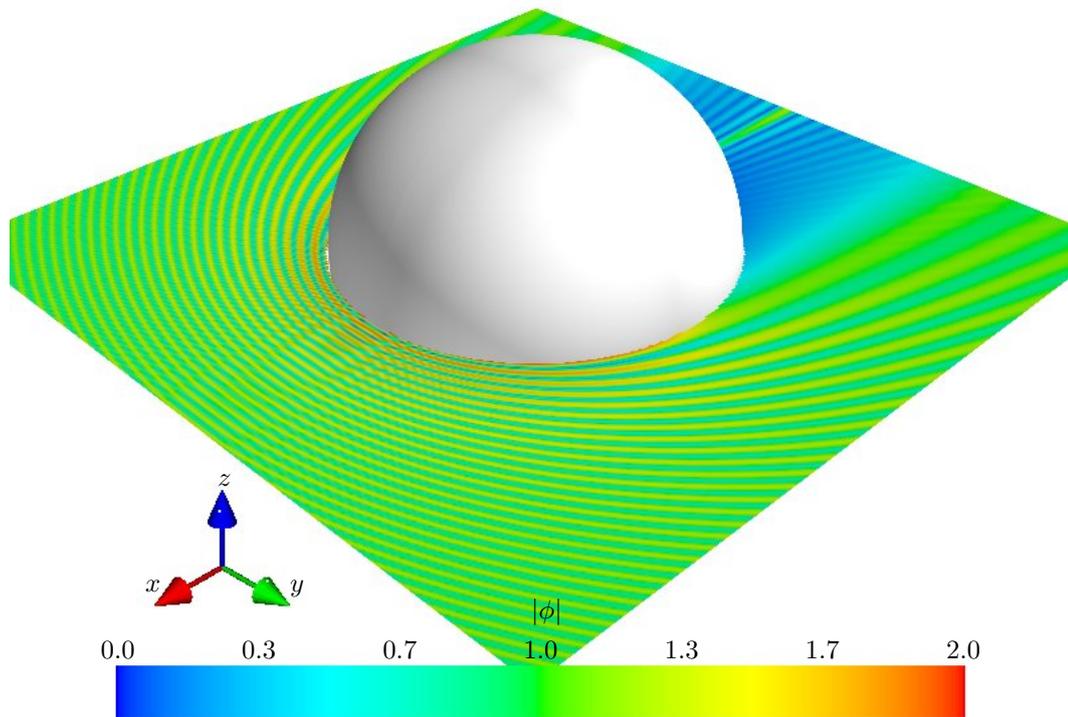
Figure 9.7: Total scattered wave in the unit-sphere problem; $z = 0$ plane; ka=60.
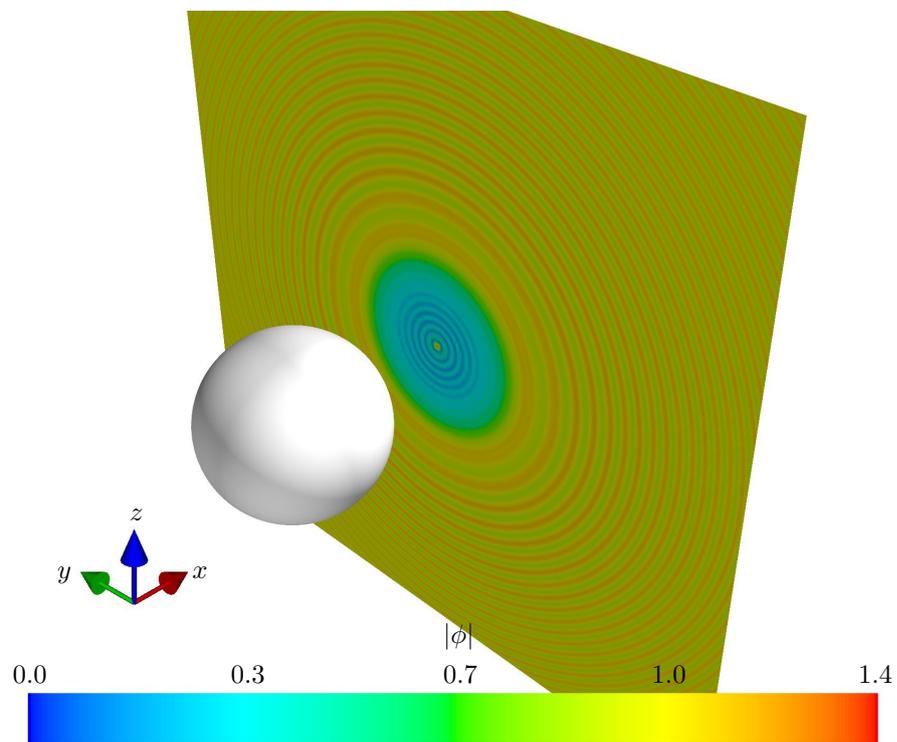
Figure 9.8: Total scattered wave in the unit-sphere problem; $x = 2$ plane; ka=60.

(a) Slice of geometry at $y = 0$ **(b)** View along the z-axis
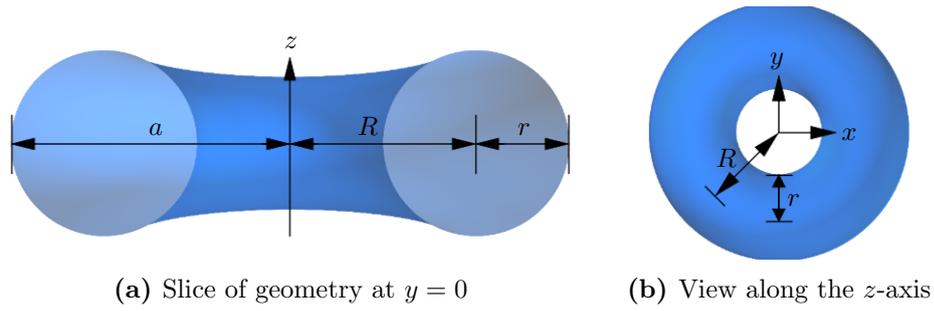
Figure 9.9: Torus geometry. The torus appears to be slender in the middle in (a) due to the perspective used.

(a) Isometric view **(b)** View along the z-axis
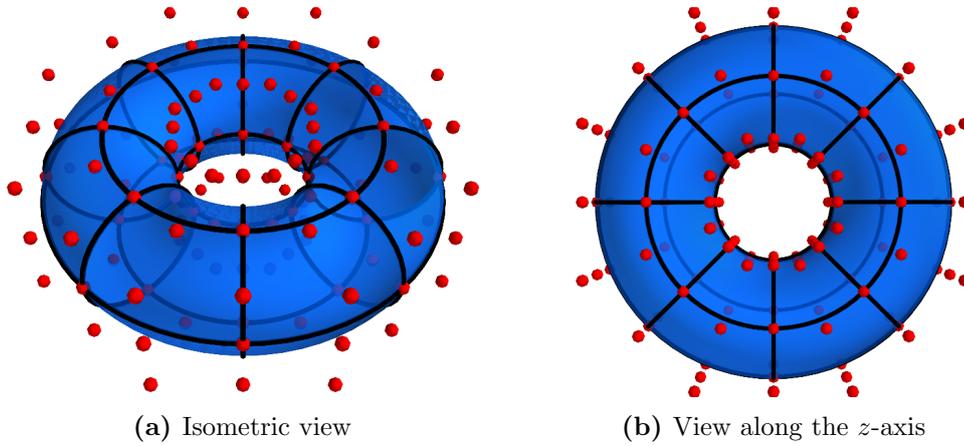
Figure 9.10: Torus mesh.

$\mathbf{d}^{\text{inc}} = \left(\frac{3}{5}, 0, -\frac{4}{5}\right)$. The torus specified here is a ring torus with major radius $R = 1$ and minor radius $r = 0.5$. The geometry of the torus is shown in in Figure 9.9.

The isogeometric representation of the torus is shown in Figure 9.10. It consists of 32 elements and 128 control points. Unlike the sphere, the isogeometric representation of a torus does not have any polar singularities. The surface area of a torus is $4\pi^2 Rr$, so this torus has a surface area of $2\pi^2$; the parameter τ for this geometry is therefore defined as

$$\tau = \frac{2\pi}{k}\sqrt{\frac{N_{\text{dof}}}{A_\Gamma}} = \sqrt{\frac{2N_{\text{dof}}}{k^2}}. \tag{9.14}$$

Two cases are considered: the first is $ka = 30$; the second is $ka = 45$.* There is no analytical solution for this problem and so a converged MFS solution is used to evaluate the errors in the approximation. With a conventional BEM, these simulations would require $20,000$ and $45,000$ degrees of freedom respectively; the latter of these two would then require a 32 GB matrix to be stored and inverted. For this reason, only XIBEM and PU-BEM simulations of this problem are run. The PU-BEM solution is possible due to the torus geometry having the analytical parametric

---

*Note that $a = R + r = 1.5$.

Table 9.3: Initial tabulated results of simulations of torus problem with $ka = 30$.

				XIBEM		PU-BEM
M	N_{dof}	τ	κ	$L^2(\Gamma)$ error	κ	$L^2(\Gamma)$ error
13	1,664	2.88	3.7×10^3	6.35%	2.8×10^3	9.42%
16	2,048	3.20	6.3×10^3	2.36%	5.5×10^3	1.53%
19	2,432	3.49	3.2×10^4	1.01%	3.1×10^4	1.46%
22	2,816	3.75	4.0×10^5	1.86%	3.8×10^5	1.69%
25	3,200	4.00	2.1×10^5	0.18%	2.6×10^5	0.22%

representation:

$$x = \big(R + r\cos(\theta_2)\big)\cos(\theta_1), \tag{9.15}$$

$$y = \big(R + r\cos(\theta_2)\big)\sin(\theta_1), \tag{9.16}$$

$$z = r\sin(\theta_2), \tag{9.17}$$

where $\theta_1, \theta_2 \in [0, 2\pi)$. The PU-BEM mesh has the same element boundaries as the XIBEM mesh so that the results are comparable.

Initial tabulated results of XIBEM and PU-BEM simulations can be found in Table 9.3. The L^2-errors were evaluated by comparing the potential at 2,592 points, equally spaced over the local coordinate of each element on the torus. The table shows that XIBEM and PU-BEM accuracies are comparable, with neither method providing consistently more accurate approximations. However, it should be noted again that the PU-BEM simulations are only possible because of the available parametric equations in (9.15)–(9.17); without these equations, PU-BEM would not provide the saving in degrees of freedom that the XIBEM does.

It is interesting to see that the errors in Table 9.3 do not decrease uniformly: in particular, there is a significant reduction in errors between the first two rows and the last two rows. The reason for these reductions is the large increase in the number of collocation points being used. For the $M = 13$ simulations, 2,048 collocation points are used; for the $M = 16, 19, 22$, simulations, 3,200 collocation points are used; for the $M = 25$ simulations, 4,608 collocation points are used. Clearly, the number of collocation points has an impact on the solution accuracy. This is not something that was observed for the sphere problem as there was already an excess of collocation points from the $(Z + 1) \times (Z + 1)$ grid.

Table 9.4 shows some errors and condition numbers of XIBEM simulations of the torus problem using different numbers of collocation points, N_{coll}. These are displayed along with the fraction of collocation points to degrees of freedom. As the number of collocation points used increases, the error decreases. This effect is significant for $N_{\text{coll}}/N_{\text{dof}} < 1.5$; it appears less significant for greater values. The effect can also be noted in the condition numbers of the system that fall as the system becomes increasingly over-defined.

As the collocation scheme used in this 3D work is fixed to a square grid of points,

Table 9.4: Comparison of errors and system condition number of XIBEM simulations of torus problem ($ka = 30$) with varying numbers of collocation points.

	$M = 19$				$M = 22$		
N_{coll}	$\dfrac{N_{\text{coll}}}{N_{\text{dof}}}$	κ	L^2 error	N_{coll}	$\dfrac{N_{\text{coll}}}{N_{\text{dof}}}$	κ	L^2 error
2,592	1.07	2.5×10^5	3.33%	3,200	1.14	3.8×10^5	1.33%
3,200	1.32	3.4×10^4	1.09%	3,872	1.38	8.0×10^4	0.49%
3,872	1.59	1.8×10^4	0.66%	4,608	1.64	5.2×10^4	0.32%
4,608	1.89	1.4×10^4	0.43%	5,408	1.92	4.4×10^4	0.18%
5,408	2.22	1.4×10^4	0.47%	6,272	2.23	4.1×10^4	0.16%

Table 9.5: Initial tabulated results of XIBEM simulations of torus problem with $ka = 45$.

					XIBEM		PU-BEM	
M	N_{dof}	N_{coll}	$\dfrac{N_{\text{coll}}}{N_{\text{dof}}}$	τ	κ	L^2 error	κ	L^2 error
28	3,584	5,408	1.51	2.82	1.0×10^4	3.66%	8.2×10^3	3.15%
34	4,352	6,272	1.44	3.11	5.0×10^4	1.13%	4.9×10^4	1.51%
41	5,248	8,192	1.56	3.41	2.4×10^5	0.28%	2.6×10^5	0.39%
49	6,272	9,248	1.47	3.73	2.3×10^6	0.15%	2.7×10^6	0.27%
57	7,296	11,552	1.58	4.03	1.4×10^7	0.06%	1.5×10^7	0.09%

it is not possible to determine with any certainty what fraction of $N_{\text{coll}}/N_{\text{dof}}$ is ideal. Indeed, it could be the case that this fraction is not constant. It is also possible that a rectangular grid could be more suitable given that the elements of the outermost of the torus appear rectangular; this type of grid would also give more control of the number of collocation points used.

XIBEM and PU-BEM simulations were also run of the torus problem with a shorter wavelength: $ka = 45$. The results of the simulations can be seen in Table 9.5. Care was taken so that at least 1.4 times as many collocation points were used as degrees of freedom. By doing this, the errors continue to decrease as τ is increased; this is more like the behaviour expected of both the PU-BEM and XIBEM and observed in the previous chapters of this thesis.

Four of the five simulations in Table 9.5 show XIBEM to give a more accurate approximations than PU-BEM. However, the values are similar and four simulations is not enough to claim a statistical significance. The condition numbers of both approaches are similar too, showing that the plane wave enrichment is the main cause of ill conditioning. None of the condition numbers is significantly large; however, they are greater than those found for $ka = 30$.

Although it cannot be said that XIBEM is performing better than PU-BEM here, it should be reiterated that this is a special case for which PU-BEM is easily implemented. While it may be possible to provide an analytical geometry to PU-BEM for a more complex problem, this is much easier with XIBEM as the geometry functions can be imported directly from a CAD model.

Using more collocation points reduces the benefits that the PU-BEM and XIBEM

have over conventional BEM simulations in that the total number of matrix entries increases. However, the benefit of the reduction in N_{dof} is still significant. Consider the case of $ka = 45$ using a conventional BEM simulation. For a 1% error, this would require $\tau \approx 10$ or 45,000 degrees of freedom; this gives a matrix system with over 2 billion complex coefficients. Conversely, considering the case of $\tau = 3.41$ in Table 9.5, the matrix system has just less than 43 million entries. This is almost a 98% reduction in matrix entries, a significant figure.

Figures 9.11 to 9.15 show some plots of potential on the torus surface. Figures 9.16 and 9.17 are plots of scattering off the torus surface; Figure 9.16, in particular, shows the internal reflections created within the torus. The figures show the short wavelength of the problem being solved. These images were only possible because the XIBEM scheme required so few degrees of freedom.

9.4   Conclusions

Decomposed NURBS meshes have been used to represent the geometries of three-dimensional scatterers. The functions that describe these geometries, multiplied by families of plane waves, have been used to approximate the potential over the surface of said scatterers. Using this discretisation in a direct collocation BEM approach, the so-called extended isogeometric boundary element method, has given accurate approximations.

Compared to the PU-BEM, the XIBEM performs similarly with neither method appearing significantly more accurate. However, the XIBEM has an analytical geometry provided by the same functions used in approximation of the field variable. The problems explored in this chapter were both special cases for which there is an easy analytical geometry representation for PU-BEM.

IGABEM has not been shown to be more accurate than the conventional BEM when using the same number of degrees of freedom. Meshing may be easier with an isogeometric mesh but the basis functions take longer to evaluate and so it is undesirable to use unless there is an accuracy benefit also.

Conversely, the XIBEM requires far fewer degrees of freedom to achieve engineering accuracy for the same problem. Although the XIBEM requires a surplus of collocation points to obtain the greatest accuracy, the overall reduction in matrix size is significant, approaching 98%.

XIBEM still requires a more efficient integration scheme to compete with the acceleration methods than can be applied to conventional BEM and IGABEM. The nature of the optimal collocation scheme is still be understood also. Despite this, XIBEM is clearly a method that has significant potential and is deserving of more research.

0.0   0.4   0.9   1.3   1.7   2.1   2.6   3.0
$|\phi|$
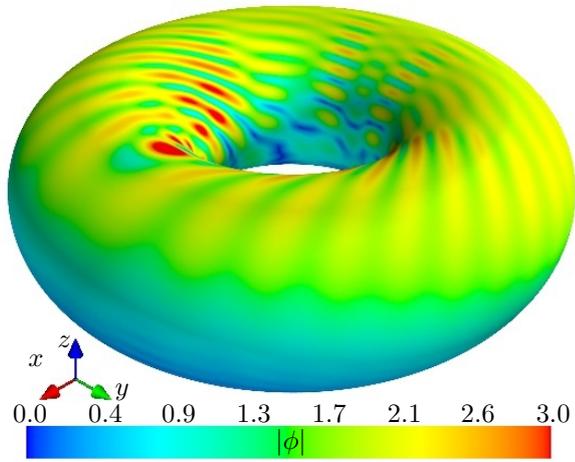
Figure 9.11: Isometric view of absolute total field on the torus; ka=45.

0.0   0.4   0.9   1.3   1.7   2.1   2.6   3.0
$|\phi|$
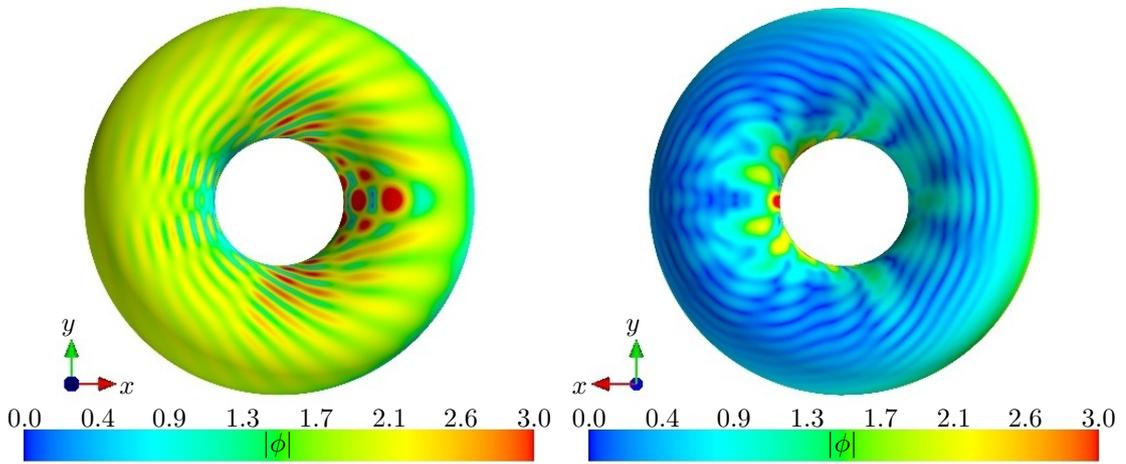
Figure 9.12: $-z$ (top down) view of absolute total field on the torus; ka=45.

0.0   0.4   0.9   1.3   1.7   2.1   2.6   3.0
$|\phi|$

Figure 9.13: $+z$ (bottom up) view of absolute total field on the torus; ka=45.

−3.5   −2.5   −1.5   −0.5   0.5   1.5   2.5   3.5
$Re(\phi)$
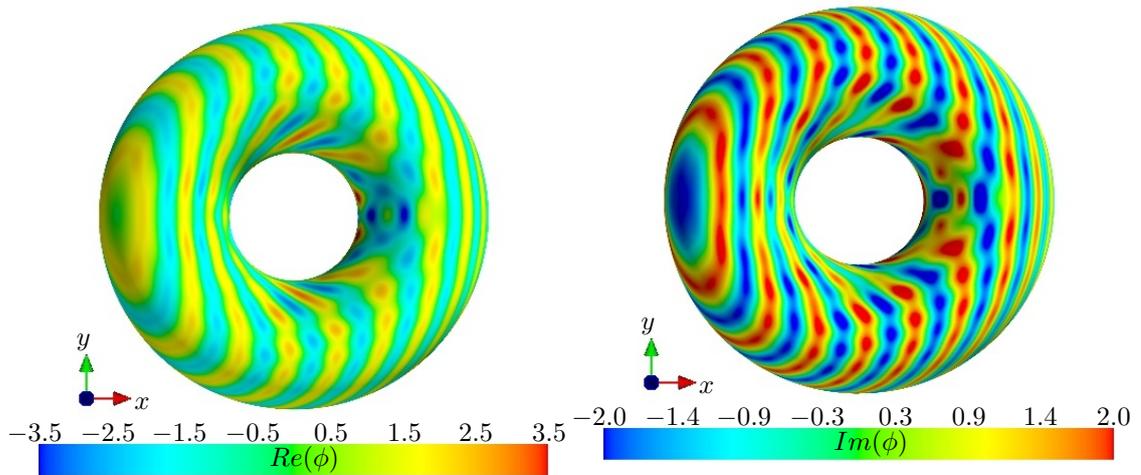
Figure 9.14: $-z$ (top down) view of real part of the total field on the torus; ka=45.

−2.0   −1.4   −0.9   −0.3   0.3   0.9   1.4   2.0
$Im(\phi)$

Figure 9.15: $-z$ (top down) view of imaginary part of the total field on the torus; ka=45.
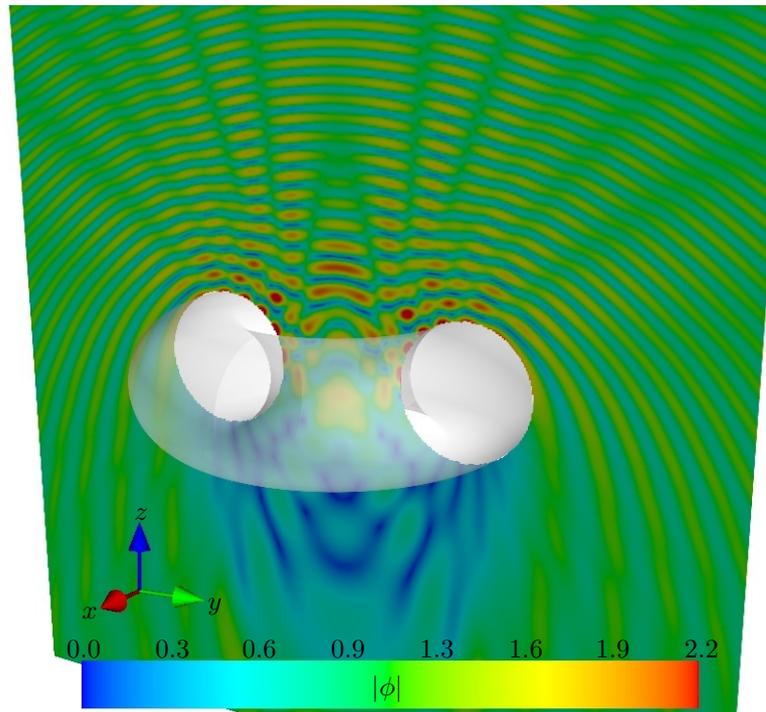
Figure 9.16: $x = 0$ plane of absolute value of total field of the torus problem; ka=45.
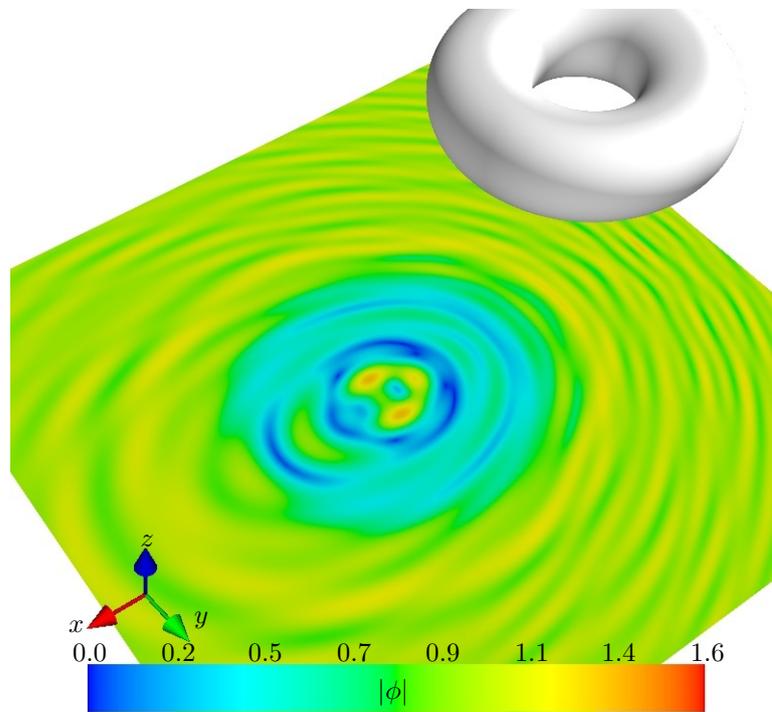
Figure 9.17: Absolute value of total acoustic field of the torus problem shown at $z = -3$; ka=45.

10

Conclusions and future work

10.1 Conclusions

This thesis has explored different basis functions for use in partition of unity boundary element simulations (PU-BEM) of problems governed by the Helmholtz equation. Results cover a spectrum of frequencies but a particular area of interest is medium-wavelength problems.

Trigonometric shape functions were designed for use in two-dimensional simulations. These were developed in order to reduce the errors in approximation of potential found on continuous PU-BEM elements. The maximum of these errors were previously found to be at the ends of such elements. The C^0 nature of these elements was proposed to be the cause. The novel trigonometric shape functions provided C^∞ in the basis function which, indeed, reduced the errors previously experienced on PU-BEM elements, although they were not found to be beneficial in conventional BEM simulations.

A small study of collocation strategies for PU-BEM simulations was performed. Collocation at roots of polynomials were trialled, as were schemes with clustered or randomly perturbed points. It was found that uniformly spaced collocation points provided the most accurate solutions. One potential shortcoming of this work was that it was not possible to say whether this approach provides more accurate solutions because points are uniform in the local coordinate system or in the global geometry.

Although the increased continuity of trigonometric shape functions did improve the accuracy of PU-BEM simulations, the improvement was not as significant as expected. Thus, the focus of the work changed to finding an effective way of providing a partition-of-unity enriched BEM simulation with an exact geometry. PU-BEM simulations derive significant accuracy benefits from having collocation and integration points placed on the analytical surface of the scatterer in a problem. If the analytical description of a scatterer is used, much larger elements can be used for the approximation of the field variable (acoustic potential in this case). As using analytical geometries has great accuracy benefits for PU-BEM, only a small number of geometries have been used in simulations thus far.

Non-uniform rational B-splines (NURBS) are used to describe geometries in CAD software. This geometry representation can be used in numerical analysis. These basis functions can also be used to approximate acoustic potential over the surface of a scatterer. This combination, often referred to with the acronym IGABEM, is a topic being researched by a significant number of groups currently.

This thesis has presented a pioneering approach to enrich the functional approximation functions of IGABEM, in a partition of unity sense, with linear combinations of plane waves. This approach—coined within these pages as the extended isogeometric boundary element method (XIBEM)—incorporates the benefits of an enriched basis with the benefits of using an analytical geometry in the evaluation of boundary integrals.

Though only simple 2D and 3D geometries have been considered so far, the new approach already shows significant potential as higher accuracy is obtainable with fewer degrees of freedom used. Fewer degrees of freedom leads to fewer equations and smaller matrix systems to solve. This allows problems of smaller wavelength to be solved with a fixed computational resource than was possible with conventional BEM or IGABEM simulations. These benefits come at the expense of more complicated integration, though there is no reason to suggest that efficient integration schemes cannot be developed. The linear system of equations used to solve XIBEM simulations is also ill-conditioned and so a robust solver is required—here singular value decomposition (SVD) is used.

XIBEM provides the foundation of what could be a fully integrated CAD/BEM, design and numerical analysis tool. Such a tool would be of great interest to design engineers in a range of industries, particularly concerning conceptual design. While validation of analysis using an alternative method may be desired, the ability to switch between a design geometry and a numerical analysis in the early stages of a design process could lead to faster and more efficient development.

10.2 Recommendations for future work

Most research projects produce more questions than answers and the work in this thesis is no different. The following are some ideas for future research in the area of enriched boundary elements. The ideas have been split into short and long projects.

10.2.1 Short projects

Uniform collocation by geometry or local coordinate

The work in §5.9 showed that a uniform collocation scheme was optimal for 2D PU-BEM simulations. However, the nature of the geometry was such that these collocation points were placed uniformly in the local coordinate system and globally. Geometries in which the local coordinate system is non-uniform or geometries with

varying element lengths should be trialled. Simulations using uniform collocation by local coordinate and uniform over the global boundary Γ should be tested.

Number of collocation points required for PU-BEM and XIBEM

In §9.3 it was noted that the PU-BEM and XIBEM simulations required more collocation points than degrees of freedom in order to maximise the accuracy of each method. This was not observed during the 2D studies; however, many CHIEF points were used in that earlier work (up to 20% extra equations) and so these provide the extra equations to the system matrix. A study could be carried out for 2D simulations to determine if there is an optimal fraction for $N_{\mathrm{coll}}/N_{\mathrm{dof}}$ and whether equations are best added through surface collocation or CHIEF.

Global or local τ

Throughout this thesis, elements of similar size have been used and M has been a global variable. The variable τ has been calculated as a global variable also. It is, however, possible to calculate τ as a local variable or element. Variable M has been tested before but this appears to have a detrimental effect on matrix conditioning. However, it is possible that some geometries could have great variation in element size. In such cases, it may be more beneficial to have a variable M and τ rather than a global τ. This may be of benefit as less degrees of freedom may be used. A study should be conducted on such a geometry: an extended capsule may be an ideal 2D case.

Different partition of unity enriching functions

Some authors have had success using Bessel functions as the enrichment in a basis. A few unsuccessful attempts to do this with PU-BEM have been made; however, no attempts have been published. A thorough study of different enriching functions could be performed, with the intention of showing that plane waves are the ideal enriching function for PU-BEM and XIBEM simulation of Helmholtz wave scattering problems.

Trigonometric shape functions for 3D boundary elements

The work of Chapter 5 has not been extended to three-dimensional problems. It should be possible to develop a 4-, 8- or 9-noded two-dimensional boundary element which uses trigonometric shape functions. Such an element may have similar benefits to 3D PU-BEM simulations as to 2D PU-BEM simulations.

Study of effective wavelength of PU-BEM and XIBEM basis functions

In §9.2.2 it was stated that integration takes, on average, 99% of the simulation time. Studies that reduce the number of integration points required are of significant
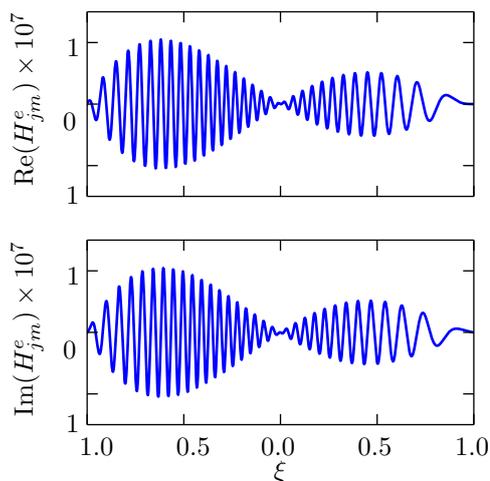
Figure 10.1: Example of H_{jm}^e over an enriched element in a PU-BEM simulation with a shorter effective wavelength; $k = 50$.
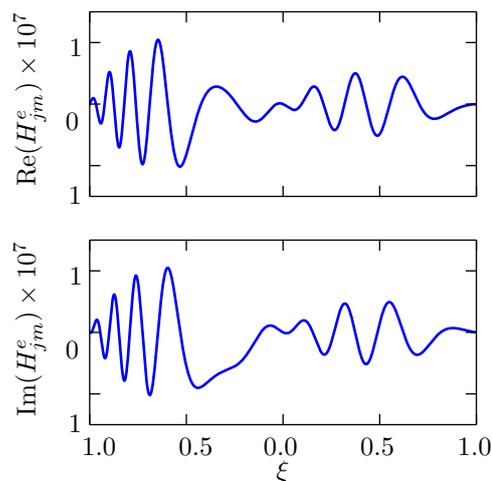
Figure 10.2: Another example of H_{jm}^e over an enriched element in a PU-BEM simulation with a longer effective wavelength; $k = 50$.

benefit to PU-BEM and XIBEM research. A small study of one-dimensional integrals could be performed to determine the nature of the different 2D PU-BEM and XIBEM basis functions in an enrichment. Figure 5.9 showed the nature of one such basis function. Figures 10.1 and 10.2 below show two more such examples which look quite different. They are plots of the same shape function but multiplied by different waves in the enrichment. There is clearly a need to understand the nature of these basis functions further; doing this may lead to a new efficient form of integration for them.

10.2.2   Long projects

XIBEM: Collocation vs. Galerkin

There is no published comparison of enriched boundary element formulations using the collocation and Galerkin approaches to solve for unknowns. Typically, it is suggested that collocation is faster while Galerkin is more stable. It could be a valuable exercise to establish exactly what the advantages and disadvantages of each method is with numerical data to back up these claims. Perhaps one method is better than another or perhaps it is simply a case of choosing the right approach for each problem to be solved.

NURBS vs. Bézier decomposition vs. Bézier extraction

In this work, the use of NURBS or Bézier decomposition has been somewhat arbitrary. Notably, however, the NURBS-based IGABEM in 2D outperformed conventional BEM simulations whereas the Bézier decomposition IGABEM in 3D did not. There is no immediately obvious explanation for this with the exception of the Greville abcissae that are used only in the NURBS-based IGABEM.

A thorough investigation of IGABEM and XIBEM using different forms of the same mesh is vital. Bézier decomposition and Bézier extraction are used as a means of reducing simulation time; however, it may be done at the expense of significant accuracy.

Convergence and simulation times should be compared. This would be particularly interesting for meshes where the Bézier decomposition introduces new control points that do not exist for the NURBS representation. Whether these are of benefit to XIBEM simulations or not is important.

Homogeneous coordinates, discussed in §7.4.1, could also be considered. Use of these could reduce the time required to generate the NURBS or Bézier interpolation functions.

Mixed elements for geometry basis

NURBS and their decompositions have been shown to be suitable tools for representing geometry in CAD software and their functions can be used for numerical analysis. Over the past few decades, isoparametric representation has become the standard approach for numerical analysis. However, there is, currently, no practical proof that NURBS and their decompositions are ideal functions with which to approximate field variables such as acoustic potential. In particular, the case of a sphere—with its collapsed elements at the poles—seems like a counter-intuitive way of representing such functions. An isogeometric approach could be developed that uses NURBS to provide the analytical geometry for collocation and integration while more conventional functions are used to approximate potential.

Efficient integration of XIBEM elements

It is no secret that the most time consuming and computationally expensive task in all BEM simulations is integration. Some schemes have been developed that reduce this computational burden for conventional BEM simulations; some of these schemes could and have been easily converted for use in IGABEM simulations.

One potential limiting factor with XIBEM simulations is lack of efficient integration schemes. Within this thesis, the approach used leads to accurate evaluation of integrals but it is not quick. In particular, no attention was paid to the effective wavelength of an integral—it was discussed in §4.2.3 that the wavelength of an enriched function changes $\bar{\lambda} \in [0, 2\lambda]$.

It would be a very interesting mathematical project to devise a more efficient version of the current scheme used. Supplementary to this, existing techniques for rapid integration of oscillatory functions should be explored.

PU-BEM/XIBEM for Maxwell's equations

While the applications for solving wave scattering problems in acoustics are vast, the applications for electromagnetic wave scattering are even greater. The formulation for solving Maxwell's equations is more complicated as field variables are vectors rather than scalars. The BEM is already an established tool for electromagnetic analysis and so an enriched form of the PU-BEM or XIBEM would be of great interest to both academic and industrial communities.

XIBEM large-scale problems

PU-BEM and XIBEM can clearly reduce the number of degrees of freedom required to obtain a reasonable approximation to a wave scattering problem. The benefits of this are clear for the small problems considered to date. As problems grow in scale, however, various techniques such as the fast multipole method (FMM) and adaptive cross approximation (ACA) can increase the solution speed of conventional BEM approximations.

Proof of the benefits of enriched boundary elements is required for a large-scale problem. It must be shown than either FMM and ACA do not overcome the benefits of PU-BEM and XIBEM. Else, an acceleration technique must be developed for large-scale PU-BEM and XIBEM simulations that makes the technique faster and more accurate than accelerated conventional BEM schemes.

Experimental validation

This project idea could be easily combined with the project above: 'XIBEM large-scale problems'.

Engineering and mathematical papers on numerical methods often focus on problems with analytical solutions or demonstrate convergence to prove efficacy. The work in this thesis is no different. Theoretical problems are ultimately only of interest to academics, however. An experiment could be set up and numerical tools used to predict the acoustic potential. Validation of a numerical method through experimentation would interest a wider community. If it could be shown that XIBEM simulations are faster and more accurate than other BEM (and finite element) simulations—including real-life problems—the impact could push boundary elements to the forefront of numerical analysis research.

References

[1] ABBOUD, T., NÉDÉLEC, J. C., AND ZHOU, B. Improvement of the integral equation method for high frequency problems. In *Third International Conference on Mathematical and Numerical Aspects of Wave Propagation* (Philadelphia, USA, 1995), SIAM Proceedings Series, SIAM, pp. 178–187.

[2] ANAND, A., BOUBENDIR, Y., ECEVIT, F., AND REITICH, F. Analysis of multiple scattering iterations for high-frequency scattering problems. II: The three-dimensional scalar case. *Numerische Mathematik 114*, 3 (2009), 373–427.

[3] BABUŠKA, I., AND MELENK, J. The partition of unity method. *International Journal for Numerical Methods in Engineering 40*, 4 (1997), 727–758.

[4] BANAUGH, R. P., AND GOLDSMITH, W. Diffraction of steady acoustic waves by surfaces of arbitrary shape. *Journal of the Acoustical Society of America 35*, 10 (1963), 1590–1601.

[5] BAZILEVS, Y., CALO, V., HUGHES, T. J. R., AND ZHANG, Y. Isogeometric fluid-structure interaction: theory, algorithms, and computations. *Computational Mechanics 43*, 1 (2008), 3–37.

[6] BAZILEVS, Y., CALO, V. M., COTTRELL, J. A., EVANS, J. A., HUGHES, T. J. R., LIPTON, S., SCOTT, M. A., AND SEDERBERG, T. W. Isogeometric analysis using T-splines. *Computer Methods in Applied Mechanics and Engineering 199*, 58 (2010), 229–263.

[7] BECKER, A. A. *The Boundary Element Method in Engineering: A Complete Course*. McGraw-Hill, Maidenhead, UK, 1992.

[8] BELIBASSAKISA, K. A., GEROSTATHISB, T. P., KOSTASB, K. V., POLITIS, C. G., KAKLISA, P. D., GINNISA, A. I., AND FEURERA, C. A BEM-isogeometric method for the ship wave-resistance problem. *Ocean Engineering 60* (2013), 53–67.

[9] BENTHIEN, W., AND SCHENCK, A. Nonexistence and nonuniqueness problems associated with integral equation methods in acoustics. *Computers & Structures 65*, 3 (1997), 295–305.

[10] BÉRIOT, H., PERREY-DEBAIN, E., BEN TAHAR, M., AND VAYSSADE, C. Plane wave basis in Galerkin BEM for bidimensional wave scattering. *Engineering Analysis with Boundary Elements 34*, 2 (2010), 130–143.

[11] BETTESS, P. Short-wave scattering: problems and techniques. *Philosophical Transactions of the Royal Society of London, Series A 362*, 1816 (2004), 421–443.

[12] BETTESS, P., LAGHROUCHE, O., AND PERREY-DEBAIN (EDS.), E. Short–wave scattering [Theme issue]. *Philosophical Transactions of the Royal Society of London, Series A 362*, 1816 (2004), 417–696.

[13] BORDEN, M. J., SCOTT, M. A., EVANS, J. A., AND HUGHES, T. J. R. Isogeometric finite element data structures based on Bézier extraction of NURBS. *International Journal for Numerical Methods in Engineering 87* (2011), 15–47.

[14] BOWMAN, J. J., SENIOR, B. A., AND USLENGHI, P. L. E. *Electromagnetic and Acoustic Scattering by Simple Shapes*. Hemisphere, New York, USA, 1987.

[15] BREBBIA, C. A. *The Boundary Element Method for Engineers*. Pentech Press, London, UK, 1978.

[16] BREBBIA, C. A., AND DOMINGUEZ, J. Boundary element methods for potential problems. *Applied Mathematical Modelling 1*, 7 (1977), 372–378.

[17] BREBBIA, C. A., AND DOMINGUEZ, J. *Boundary Elements: An Introductory Course*. Computational Mechanics Publications, Southampton, UK, 1989.

[18] BRUNO, O. P., GEUZAINE, C. A., MONRO, J. A., AND REITICH, F. Prescribed error tolerances within fixed computational times for scattering problems of arbitrarily high frequency: the convex case. *Philosophical Transactions of the Royal Society of London, Series A 362*, 1816 (2004), 629–645.

[19] BUFFA, A., SANGALLI, G., AND VÁZQUEZ, R. Isogeometric analysis in electromagnetics: B-splines approximation. *Computer Methods in Applied Mechanics and Engineering 199*, 1720 (2010), 1143–1152.

[20] BURTON, A. J., AND MILLER, G. F. The application of integral equation methods to the numerical solution of some exterior boundary-value problems. *Proceedings of the Royal Society of London. Series A, Mathematical and Physical Sciences 323*, 1553 (1971), 201–210.

[21] CABRAL, J. J. S. P., WROBEL, L. C., AND BREBBIA, C. A. A BEM formulation using B-splines: I-uniform blending functions. *Engineering Analysis with Boundary Elements 7*, 3 (1990), 136–144.

[22] CABRAL, J. J. S. P., WROBEL, L. C., AND BREBBIA, C. A. A BEM formulation using B-splines: II-multiple knots and non-uniform blending functions. *Engineering Analysis with Boundary Elements 8*, 1 (1991), 51–55.

[23] CAMP, C. V., AND GIPSON, G. S. Overhauser elements in boundary element analysis. *Mathematical and Computer Modelling 15* (1991), 59–69.

[24] CANNELL, D. M., AND LORD, N. J. George Green, mathematician and physicist 1793-1841. *The Mathematical Gazette 77*, 478 (1993), 26–51.

[25] CESSENAT, O., AND DESPRÉS, B. Application of an ultra weak variational formulation of elliptic pdes to the two-dimensional Helmholtz problem. *SIAM Journal of Numerical Analysis 35*, 1 (1998), 255–299.

[26] CESSENAT, O., AND DESPRÉS, B. Using plane waves as base functions for solving time harmonic equations with the ultra weak variational formulation. *Journal of Computational Acoustics 11*, 2 (2003), 227–238.

[27] CHANDLER-WILDE, S., AND LANGDON, S. A Galerkin boundary element method for high frequency scattering by convex polygons. *SIAM Journal of Numerical Analysis 45*, 2 (2007), 610–640.

[28] CHANDLER-WILDE, S. N., GRAHAM, I. G., LANGDON, S., AND SPENCE, E. A. Numerical-asymptotic boundary integral methods in high-frequency scattering. *Acta Numerica 21* (2012), 89–305.

[29] CHEN, I. L., CHEN, J. T., AND LIANG, M. T. Analytical study and numerical experiments for radiation and scattering problems using the chief method. *Journal of Sound and Vibration 248*, 5 (2001), 809–828.

[30] CHEN, L. H., AND SCHWEIKERT, D. G. Sound radiation from an arbitrary body. *Journal of the Acoustical Society of America 35*, 10 (1963), 1626–1632.

[31] CHENEY, W., AND KINCAID, D. *Numerical Mathematics and Computing*, 6th ed. Thomson Brooks/Cole, Belmont, CA, USA, 2008.

[32] CHERTOCK, G. Sound radiation from vibrating surfaces. *Journal of the Acoustical Society of America 36*, 7 (1964), 1305–1313.

[33] CISKOWSKI, R. D., AND BREBBIA, C. A. *Boundary Element Methods in Acoustics*. Computational Mechanics Publications, Southampton, UK, 1991.

[34] COOK, J. M. Rational formulae for the production of a spherically symmetric probability distribution. *Mathematics of Computation 11* (1957), 81–82.

[35] COPLEY, L. G. Integral equation method for radiation from vibrating bodies. *Journal of the Acoustical Society of America 41*, 4 (1967), 807–816.

[36] COPLEY, L. G. Fundmental results concerning integral representations in acoustic radiation. *Journal of the Acoustical Society of America 44*, 1 (1968), 28–32.

[37] COTTRELL, J. A., REALI, A., BAZILEVS, Y., AND HUGHES, T. J. R. Isogeometric analysis of structural vibrations. *Computer Methods in Applied Mechanics and Engineering 195*, 4143 (2006), 5257–5296.

[38] CRUSE, T. A., AND WILSON, R. B. Advanced applications of boundary-integral equation methods. *Nuclear Engineering and Design 46*, 1 (1978), 223–234.

[39] DE LA BOURDONNAYE, A. A microlocal discretization method and its utilization for a scattering problem. *Comptes Rendus de l'Académie des Sciences - Série I 318*, 4 (1994), 385–388.

[40] DE LUYCKER, E., BENSON, D. J., BELYTSCHKO, T., BAZILEVS, Y., AND HSU, M. C. X-FEM in isogeometric analysis for linear fracture mechanics. *International Journal for Numerical Methods in Engineering 87*, 6 (2011), 541–565.

[41] DIWAN, G. C., TREVELYAN, J., AND COATES, G. A comparison of techniques for overcoming non-uniqueness of boundary integral equations for the collocation partition of unity method in two-dimensional acoustic scattering. *International Journal for Numerical Methods in Engineering 96*, 10 (2013), 645–664.

[42] DOMÍNGUEZ, V., GRAHAM, I. G., AND SMYSHLYAEV, V. P. A hybrid numerical-asymptotic boundary integral method for high-frequency acoustic scattering. *Numerische Mathematik 106* (2007), 471–510.

[43] ERBER, T., AND HOCKNEY, G. M. Equilibrium configurations of n equal charges on a sphere. *Journal of Physics A: Mathematical and General 24*, 23 (1991), L1369–L1377.

[44] FARHAT, C., HARARI, I., AND FRANCA, L. P. The discontinuous enrichment method. *Computer Methods in Applied Mechanics and Engineering 190*, 48 (2001), 6455–6479.

[45] FARHAT, C., HARARI, I., AND HETMANIUK, U. A discontinuous Galerkin method with Lagrange multipliers for the solution of Helmholtz problems in the mid-frequency regime. *Computer Methods in Applied Mechanics and Engineering 192*, 11-12 (2003), 1389–1419.

[46] FREDHOLM, I. Sur une classe d'équations fonctionnelles. *Acta Mathematica 27*, 1 (1903), 365–390.

[47] FRIEDMAN, M. B., AND SHAW, R. Diffraction of pulse by cylindrical obstacles of arbitrary cross section. *Journal of Applied Mechanics 29* (1962), 40–46.

[48] GLASSER, L., AND EVERY, A. G. Energies and spacings of point charges on a sphere. *Journal of Physics A: Mathematical and General 25*, 9 (1992), 2473–2482.

[49] GRAY, L. J., AND SANSOUCIE, C. A Hermite interpolation algorithm for hypersingular boundary integrals. *International Journal for Numerical Methods in Engineering 36* (1993), 2357–2367.

[50] GREVILLE, T. Numerical procedures for interpolation by spline functions. *Journal of the Society for Industrial and Applied Mathematics Series B Numerical Analysis 1*, 1 (1964), 53–68.

[51] GUIGGIANI, M., G, K., RIZZO, F. J., AND RUDOLPHI, T. J. A general algorithm for the numerical solution of hypersingular boundary integral equations. *Journal of Applied Mechanics 59*, 3 (1992), 604–614.

[52] HARMAN, R., AND VLADIMIR, L. On decompositional algorithms for uniform sampling from n-spheres and n-balls. *Journal of Multivariate Analysis 101*, 10 (2010), 2297–2304.

[53] HELTAI, L., ARROYO, M., AND DESIMONE, A. Nonsingular isogeometric boundary element method for Stokes flows in 3D. *Computer Methods in Applied Mechanics and Engineering 268* (2014), 514–539.

[54] HICKS, J. S., AND WHEELING, R. F. An efficient method for generating uniformly distributed points on the surface of an n-dimensional sphere. *Communications of the ACM 2*, 4 (1959), 17–19.

[55] HONNOR, M. E., TREVELYAN, J., AND HUYBRECHS, D. Numerical evaluation of the two-dimensional partition of unity boundary integrals for Helmholtz problems. *Journal of Computational and Applied Mathematics 234*, 6 (2010), 1656–1662.

[56] HUGHES, T. J. R., COTTRELL, J. A., AND BAZILEVS, Y. Isogeometric analysis: CAD, finite elements, NURBS, exact geometry and mesh refinement. *Computer Methods in Applied Mechanics and Engineering 194*, 3941 (2005), 4135–4195.

[57] HUTTUNEN, T., MONK, P., AND KAIPIO, J. P. Computational aspects of the ultra-weak variational formulation. *Journal of Computational Physics 182*, 1 (2002), 27–46.

[58] Ihlenburg, F., Babuska, I., and Sauter, S. Reliability of finite element methods for the numerical computation of waves. *Advances in Engineering Software 28*, 7 (1997), 417–424.

[59] Irons, B. M. Engineering applications of numerical integration in stiffness methods. *AIAA Journal 4*, 11 (1966), 2035–2037.

[60] Jaswon, M. A. Integral equation methods in potential theory. i. *Proceedings of the Royal Society of London. Series A, Mathematical and Physical Sciences 275*, 1360 (1963), 23–32.

[61] Jaswon, M. A., and Ponter, A. R. An integral equation solution of the torsion problem. *Proceedings of the Royal Society of London. Series A, Mathematical and Physical Sciences 273*, 1353 (1963), 237–246.

[62] Jaswon, M. A., and Symm, G. T. *Integral Equation Methods in Potential Theory and Elastostatics*. Academic Press, London, UK, 1977.

[63] Jeans, R., and Mathews, I. C. The wave superposition method as a robust technique for computing acoustic fields. *Journal of the Acoustical Society of America 92*, 2 (1992), 1156–1166.

[64] Johnson, R. W. Higher order B-spline collocation at the Greville abscissae. *Applied Numerical Mathematics 52*, 1 (2005), 63–75.

[65] Jones, D. S. *Acoustic and Electromagnetic Waves*. Clarendon Press, Oxford, UK, 1986.

[66] Kang, L., and Qian, X. Isogeometric analysis and shape optimization via boundary integral. *Computer-Aided Design 43*, 11 (2011), 1427–1437.

[67] Kim, T., Dominguez, V., Graham, I. G., and Smyshlyaev, V. P. Recent progress on hybrid numerical-asymptotic method for high-frequency scattering problems. In *7th UK Conference on Boundary Integral Methods (UKBIM7)* (Nottingham, UK, July 2007).

[68] Kirkup, S. M. *The Boundary Element Method in Acoustics: A Development in Fortran*. Integrated Sound Software, Hebden Bridge, UK, 1998.

[69] Kondapalli, P. S., Shippy, D. J., and Fairweather, G. Analysis of acoustic scattering in fluids and solids by the method of fundamental solutions. *Journal of the Acoustical Society of America 91*, 4 (1992), 1844–1854.

[70] Koopmann, G. H., Song, L., and Fahnline, J. B. A method for computing acoustic fields based on the principle of wave superposition. *Journal of the Acoustical Society of America 86*, 6 (1989), 2433–2438.

[71] Kovalevsky, L., Ladevèze, P., Riou, H., and Bonnet, M. The variational theory of complex rays for three-dimensional Helmholtz problems. *Journal of Computational Acoustics 20*, 4 (2012), 1250021.

[72] Kurihara, Y. Numerical integration of the primitive equations on a spherical grid. *Monthly Weather Review 93*, 7 (1965), 399–415.

[73] Lachat, J. C., and Watson, J. O. Effective numerical treatment of boundary integral equations: a formulation for three-dimensional elastostatics. *International Journal for Numerical Methods in Engineering 10*, 5 (1976), 991–1005.

[74] Ladevèze, P., Arnaud, L., Rouch, P., and Blanzé, C. The variational theory of complex rays for the calculation of medium-frequency vibrations. *Engineering Computations 18*, 1/2 (2001), 193–214.

[75] Laghrouche, O., Bettess, P., and Astley, R. J. Modelling of short wave diffraction problems using approximating systems of plane waves. *International Journal for Numerical Methods in Engineering 54*, 10 (2002), 1501–1533.

[76] Laghrouche, O., Bettess, P., Perrey-Debain, E., and Trevelyan, J. Wave interpolation finite elements for Helmholtz problems with jumps in the wave speed. *Computer Methods in Applied Mechanics and Engineering 194*, 2-5 (2005), 367–381.

[77] Langdon, S., and Chandler-Wilde, S. N. A wavenumber independent boundary element method for an acoustic scattering problem. *SIAM Journal of Numerical Analysis 43*, 6 (2006), 2450–2477.

[78] Li, S., and Huang, Q. An improved form of the hypersingular boundary integral equation for exterior acoustic problems. *Engineering Analysis with Boundary Elements 34*, 3 (2010), 189–195.

[79] Linton, C. M., and Evans, D. V. The interaction of waves with arrays of vertical circular cylinders. *Journal of Fluid Mechanics 215* (1990), 549–569.

[80] Liu, Y. *Fast Multipole Boundary Element Method: Theory and Applications in Engineering*. Cambridge University Press, Cambridge, UK, 2009.

[81] Liu, Y., and Rizzo, F. J. *Boundary Elements XIII*. Springer Netherlands, 1991, ch. Application of Overhauser C^1 Continuous Boundary Elements to Hypersingular BIE for 3-D Acoustic Wave Problems, pp. 957–966.

[82] Liu, Y., and Rizzo, F. J. Scattering of elastic waves from thin shapes in three dimensions using the composite boundary integral equation formulation. *Journal of the Acoustical Society of America 102*, 2 (1997), 926–932.

[83] LUOSTARI, T., HUTTUNEN, T., AND MONK, P. The ultra weak variational formulation using Bessel basis functions. *Communications in Computational Physics 11*, 2 (2012), 400–414.

[84] LUOSTARI, T., HUTTUNEN, T., AND MONK, P. Error estimates for the ultra weak variational formulation in linear elasticity. *ESAIM: Mathematical Modelling and Numerical Analysis 47*, 1 (2013), 183–211.

[85] MARSAGLIA, G. Choosing a point from the surface of a sphere. *The Annals of Mathematical Statistics 43*, 2 (1972), 645–646.

[86] MASSIMI, P., TEZAUR, R., AND FARHAT, C. A discontinuous enrichment method for three-dimensional multiscale harmonic wave propagation problems in multi-fluid and fluid-solid media. *International Journal for Numerical Methods in Engineering 76*, 3 (2008), 400–425.

[87] MELENK, J. M., AND BABUŠKA, I. The partition of unity finite element method: Basic theory and applications. *Computer Methods in Applied Mechanics and Engineering 139*, 1-4 (1996), 289–314.

[88] MELENK, J. M., AND BABUŠKA, I. Approximation with harmonic and generalized harmonic polynomials in the partition of unity method. *Computer Assisted Mechanics and Engineering Sciences 4*, 3/4 (1997), 607–632.

[89] MOHSEN, A., AND HESHAM, M. An efficient method for solving the nonuniqueness problem in acoustic scattering. *Communications in Numerical Methods in Engineering 22*, 11 (2006), 1067–1076.

[90] MORRIS, J. R., DEAVEN, D. M., AND HO, K. M. Genetic-algorithm energy minimization for point charges on a sphere. *Physical Review B: Condensed Matter and Materials Physics 53*, 4 (1996), R1740–R1743.

[91] MORSE, P. M., AND FESHBACH, H. *Methods of Theoretical Physics: Part II.* McGraw-Hill, 1953.

[92] MULLER, M. E. A note on a method for generating points uniformly on n-dimensional spheres. *Communications of the ACM 2*, 4 (1959), 19–20.

[93] NAIR, N. V., AND SHANKER, B. Generalized method of moments: a novel discretization technique for integral equations. *IEEE Transactions on Antennas and Propagation 59*, 6 (2011), 2280–2293.

[94] NAIR, N. V., SHANKER, B., AND KEMPEL, L. Generalized method of moments: a boundary integral framework for adaptive analysis of acoustic scattering. *Journal of the Acoustical Society of America 132*, 3 (2012), 1261–1270.

[95] ORTIZ, J. C., WALTERS, H. G., GIPSON, G. S., AND BREWER III, J. A. *Mathematical and Computational Aspects.* Boundary Elements IX. Springer Berlin Heidelberg, 1987, ch. Development of Overhauser Splines as Boundary Elements, pp. 401–407.

[96] PEAKE, M. J., TREVELYAN, J., AND COATES, G. Extended isogeometric boundary element method (XIBEM) for two-dimensional Helmholtz problems. *Computer Methods in Applied Mechanics and Engineering 259* (2013), 93–102.

[97] PERREY-DEBAIN, E., LAGHROUCHE, O., BETTESS, P., AND TREVELYAN, J. Plane-wave basis finite elements and boundary elements for three-dimensional wave scattering. *Philosophical Transactions of the Royal Society of London, Series A 362*, 1816 (2004), 561–577.

[98] PERREY-DEBAIN, E., TREVELYAN, J., AND BETTESS, P. New special wave boundary elements for short wave problems. *Communications in Numerical Methods in Engineering 18*, 4 (2002), 259–268.

[99] PERREY-DEBAIN, E., TREVELYAN, J., AND BETTESS, P. Plane wave interpolation in direct collocation boundary element method for radiation and wave scattering: numerical aspects and applications. *Journal of Sound and Vibration 261*, 5 (2003), 839–858.

[100] PIEGL, L., AND TILLER, W. *The NURBS book*, 2nd ed. Springer-Verlag, 1997.

[101] POLITIS, C., GINNIS, A. I., KAKLIS, P. D., BELIBASSAKIS, K., AND FEURER, C. An isogeometric BEM for exterior potential-flow problems in the plane. In *2009 SIAM/ACM Joint Conference on Geometric and Physical Modeling* (New York, NY, USA, 2009), SPM '09, ACM, pp. 349–354.

[102] RÊGO SILVA, J. J., WROBEL, L. C., AND TELLES, J. C. F. A new family of continuous/discontinuous three-dimensional boundary elements with application to acoustic wave propagation. *International Journal for Numerical Methods in Engineering 36*, 10 (1993), 1661–1679.

[103] RIOU, H., LADEVÈZE, P., AND KOVALEVSKY, L. The variational theory of complex rays: an answer to the resolution of mid-frequency 3D engineering problems. *Journal of Sound and Vibration 332*, 8 (2013), 1947–1960.

[104] RIZZO, F. J. An integral equation approach to boundary value problems of classical elastostatics. *Quarterly of Applied Mathematics 25*, 1 (1967), 83–95.

[105] RJASANOW, S., AND WEGGLER, L. ACA accelerated high order BEM for Maxwell problems. *Computational Mechanics 51*, 4 (2013), 431–441.

[106] ROGERS, D. F. *An introduction to NURBS: with historical perspective.* Morgan Kaufmann, London, UK, 2001.

[107] RUBINSTEIN, R. Y. Generating random vectors uniformly distributed inside and on the surface of different regions. *European Journal of Operational Research 10*, 2 (1982), 205–209.

[108] SAFF, E. B., AND KUIJLAARS, A. B. J. Distributing many points on a sphere. *The Mathematical Intelligencer 19*, 1 (1997), 5–11.

[109] SAHR, K., WHITE, D., AND KIMERLING, A. J. Geodesic discrete global grid systems. *Cartography and Geographic Information Science 30*, 2 (2003), 121–134.

[110] SATO, M., YOSHIOKA, S., TSUKUI, K., AND YUUKI, R. Accurate numerical integration of singular kernels in the two-dimensional boundary element method. In *Boundary Elements X*, C. Brebbia, Ed. Springer, Berlin, Germany, 1988, pp. 279–296.

[111] SCHENCK, H. A. Improved integral formulation for acoustic radiation problems. *Journal of the Acoustical Society of America 44*, 1 (1968), 41–58.

[112] SCOTT, M. A., SIMPSON, R. N., EVANS, J. A., LIPTON, S., BORDAS, S. P. A., HUGHES, T. J. R., AND SEDERBERG, T. W. Isogeometric boundary element analysis using unstructured T-splines. *Computer Methods in Applied Mechanics and Engineering 254* (2013), 197–221.

[113] SEYBERT, A. F., AND RENGARAJAN, T. K. The use of CHIEF to obtain unique solutions for acoustic radiation using boundary integral equations. *Journal of the Acoustical Society of America 81*, 5 (1987), 1299–1306.

[114] SEYBERT, A. F., SOENARKO, B., RIZZO, F. J., AND SHIPPY, D. J. An advanced computational method for radiation and scattering of acoustic waves in three dimensions. *Journal of the Acoustical Society of America 77*, 2 (1985), 362–368.

[115] SIBUYA, M. A method for generating uniformly distributed points on n-dimensional spheres. *Annals of the Institute of Statistical Mathematics 14*, 1 (1962), 81–85.

[116] SIMPSON, R. N., BORDAS, S. P. A., LIAN, H., AND TREVELYAN, J. An isogeometric boundary element method for elastostatic analysis: 2D implementation aspects. *Computers & Structures 118* (2013), 2–12.

[117] SIMPSON, R. N., BORDAS, S. P. A., TREVELYAN, J., AND RABCZUK, T. A two-dimensional isogeometric boundary element method for elastostatic analysis. *Computer Methods in Applied Mechanics and Engineering 209-212* (2012), 87–100.

[118] SIMPSON, R. N., SCOTT, M. A., TAUS, M., THOMAS, D. C., AND LIAN, H. Acoustic isogeometric boundary element analysis. *Computer Methods in Applied Mechanics and Engineering 269* (2014), 265–290.

[119] SINGH, K. M., AND TANAKA, M. On non-linear transformations for accurate numerical evaluation of weakly singular boundary integrals. *International Journal for Numerical Methods in Engineering 50*, 8 (2001), 2007–2030.

[120] SMITH, R. L. Efficient Monte Carlo procedures for generating points uniformly distributed over bounded regions. *Operations Research 32*, 6 (1984), 1296–1308.

[121] STEPHAN, E. P., MAISCHAK, M., AND LEYDECKER, F. An *hp*-adaptive finite element/boundary element coupling method for electromagnetic problems. *Computational Mechanics 39*, 5 (2007), 673–680.

[122] SYMM, G. T. Integral equation methods in potential theory. ii. *Proceedings of the Royal Society of London. Series A, Mathematical and Physical Sciences 275*, 1360 (1963), 33–46.

[123] TAKAHASHI, T., AND MATSUMOTO, T. An application of fast multipole method to isogeometric boundary element method for Laplace equation in two dimensions. *Engineering Analysis with Boundary Elements 36*, 12 (2012), 1766–1775.

[124] TASHIRO, Y. On methods for generating uniform random points on the surface of a sphere. *Annals of the Institute of Statistical Mathematics 29*, 1 (1977), 295–300.

[125] TELLES, J. C. F. A self-adaptive co-ordinate transformation for efficient numerical evaluation of general boundary element intergrals. *International Journal for Numerical Methods in Engineering 24*, 5 (1987), 959–973.

[126] TELLES, J. C. F., AND OLIVEIRA, R. F. Third degree polynomial transformation for boundary element integrals: further improvements. *Engineering Analysis with Boundary Elements 13*, 2 (1994), 135–141.

[127] TREVELYAN, J. *Boundary Elements for Engineers: Theory and Applications.* Computational Mechanics Publications, Southampton, UK, 1994.

[128] TREVELYAN, J., AND COATES, G. On adaptive definition of plane wave basis for wave boundary elements in acoustic scattering: the 2D case. *Computer Modeling in Engineering & Sciences 55*, 2 (2010), 147–168.

[129] VON NEUMANN, J. Various techniques used in connection with random digits. *Journal of Research of the National Bureau of Standards 12* (1951), 36–38.

[130] WATSON, J. O. *Developments in Boundary Element Methods - 4*. Elsevier Applied Science, 1986, ch. Hermitian cubic and singular elements for plane strain.

[131] WILTON, D. T., MATHEWS, I. C., AND JEANS, R. A. A clarification of nonexistence problems with the superposition method. *Journal of the Acoustical Society of America 94*, 3 (1993), 1676–1680.

[132] WROBEL, L. C. *The Boundary Element Method, Vol. I: Applications in Thermo-fluids and Acoustics*. John Wiley & Sons, Ltd., Chichester, UK, 2002.

[133] YANG, Z., PANG, W. K., HOU, S. H., AND LEUNG, P. K. On a combination method of VDR and patchwork for generating uniform random points on a unit sphere. *Journal of Multivariate Analysis 95*, 1 (2005), 23–36.

[134] ZIENKIEWICZ, O. C. Achievements and some unsolved problems of the finite element method. *International Journal for Numerical Methods in Engineering 47*, 1-3 (2000), 9–28.

A

Bessel functions

Bessel functions, of order p, are linearly independent solutions of Bessel's equation:

$$x^2 \frac{\mathrm{d}^2 y}{\mathrm{d}x^2} + x \frac{\mathrm{d}y}{\mathrm{d}x} + (x^2 - p^2)y = 0, \quad p \geq 0, x > 0. \tag{A.1}$$

They are sometimes called cylindrical functions because they arise naturally from physical problems stated in cylindrical coordinates.

There are two classes of solution: *Bessel functions of the first kind*, $J_p(x)$, and *Bessel functions of the second kind*, $Y_p(x)$. They are similar to sines and cosines: for large values of x, $J_p(x)$ is approximate to a cosine and $Y_p(x)$ is approximate to a sine. Both of these are shifted by a phase that depends on p and they are dampened by $1/\sqrt{x}$. More explicitly, as x goes to infinity,

$$J_p(x) \sim \sqrt{\frac{2}{\pi x}} \cos\left(x - \frac{1}{2}p\pi - \frac{\pi}{4}\right), \tag{A.2}$$

$$Y_p(x) \sim \sqrt{\frac{2}{\pi x}} \sin\left(x - \frac{1}{2}p\pi - \frac{\pi}{4}\right). \tag{A.3}$$

These approximations hold as long as $|\arg(x)| < \pi$ and the error for each approximation is $\mathcal{O}(1/|x|)$. These relationships are demonstrated in Figure A.1.

For small values of x, $J_p(x)$ is approximate to x^p and $Y_p(x)$ is approximate to x^{-p}. More specifically,

$$J_p(x) \sim \frac{x^p}{2^p \Gamma(1+p)}, \tag{A.4}$$

$$Y_p(x) \sim -\frac{2^p \Gamma(p)}{\pi x^p}, \tag{A.5}$$

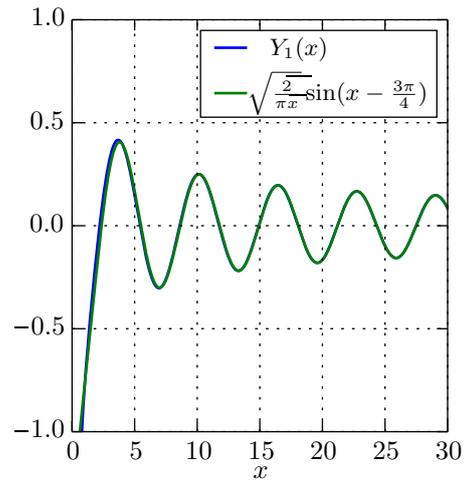where $\Gamma(x)$ is the gamma function:

$$\Gamma(x) = \int_0^\infty e^{-t} t^{x-1} \, \mathrm{d}t, \quad x > 0. \tag{A.6}$$

The relationships in (A.2)–(A.5) can be visualised using a couple of plots. First, consider J_2 and J_6. For large values of x, both J_2 and J_6 behave like cosines and their phases are $5\pi/4$ and $13\pi/4$ respectively. As the difference in phases is 2π, the two
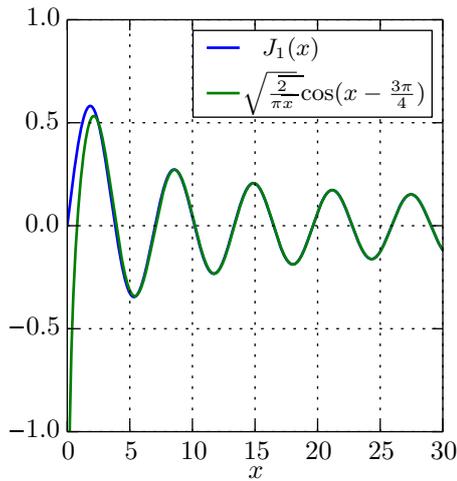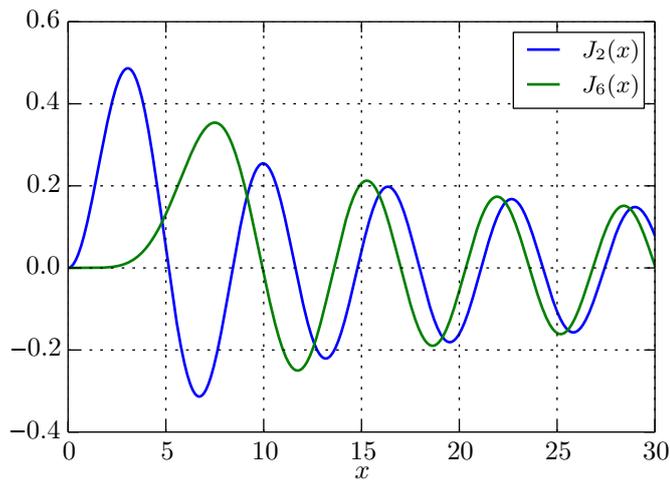
(a) Bessel function of the first kind and cosine approximation

(b) Bessel function of the second kind and cosine approximation

Figure A.1: Bessel functions compared to cosine and sine plots.

Figure A.2: Bessel functions of the first kind, order two and six.

functions should be nearly in phase. For small values of x, J_2 should be approximate to x^2 whereas J_6 should be approximate to x^6; so for J_2 should look steep and J_6 flat when compared to each other for small values of x. These observations can be seen in Figure A.2.

Now consider J_1 and Y_1. For large values of x, these should be approximately $\pi/4$ out of phase, just like sine and cosine. For small values of x, J_1 is proportional to x while Y_1 is proportional to $-x$; so, while both graphs will be increasing for small values of x, Y_1 will be much steeper at first as it originates at $-\infty$. These observations can be seen in Figure A.3.
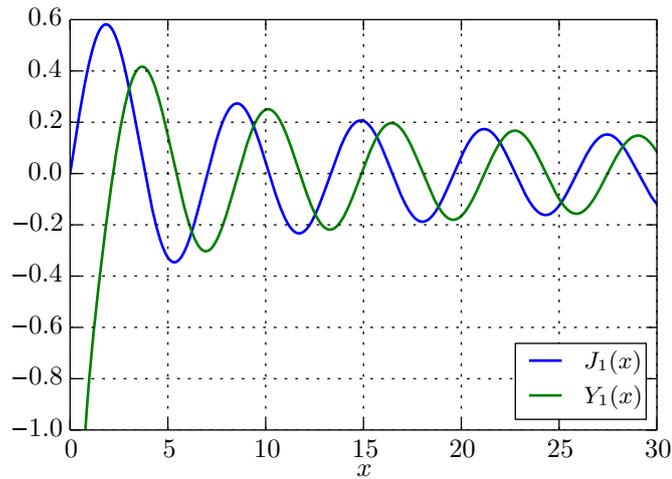
Figure A.3: Bessel functions of the first kind and second kind, order one.

A.1   Definition of Bessel function of the first kind: $J_p(x)$

$$J_p(x) = \sum_{k=0}^{\infty} \frac{(-1)^k (x/2)^{2k+p}}{k!\Gamma(k+p+1)}, \quad p \geq 0 \tag{A.7}$$

In the special cases when $p = n$,

$$J_p(x) = \sum_{k=0}^{\infty} \frac{(-1)^k (x/2)^{2k+n}}{k!(k+n)!}, \quad J_{-n}(x) = (-1)^n J_n(x). \tag{A.8}$$

A.2   Definition of Bessel function of the second kind: $Y_p(x)$

$$Y_p(x) = \frac{(\cos p\pi) J_p(x) - J_{-p}(x)}{\sin px} \tag{A.9}$$

When $p = n$, the right-hand side of (A.9) reaches the indeterminate $0/0$. By application of L'Hôpital's rule, it can be shown that for $p = 0$,

$$Y_p(x) = \frac{2}{\pi} J_0(x) \left(\log \frac{x}{2} + \gamma \right) - \frac{2}{\pi} \sum_{k=0}^{\infty} \frac{(-1)^k (x/2)^{2k}}{(k!)^2} \left(1 + \frac{1}{2} + \ldots + \frac{1}{k} \right), \quad x > 0, \tag{A.10}$$

where γ is Euler's constant:

$$\gamma = \int_0^{\infty} e^{-t} \log t \, \mathrm{d}t = 0.577215\ldots. \tag{A.11}$$

For $n = 1, 2, 3 \dots$,

$$Y_n(x) = \frac{2}{\pi} J_n(x) \log \frac{x}{2} - \frac{1}{\pi} \sum_{k=0}^{\infty} \frac{(n-k-1)!}{k!} \left(\frac{x}{2}\right)^{2k-n}$$

$$- \frac{1}{\pi} \sum_{k=0}^{\infty} \frac{(-1)^k (x/2)^{2k+n}}{k!(k+n)!} \left[\Psi(k+n+1) + \Psi(k+1) \right], \quad x > 0,$$

$$\text{(A.12)}$$

where Ψ is the digamma or psi function:

$$\Psi(x) = -\gamma + \sum_{n=0}^{\infty} \left(\frac{1}{n+1} - \frac{1}{n+x} \right). \tag{A.13}$$

A.3 Identities

The following equations from Jones [65] are useful identities that shows how Bessel functions of different orders are related:

$$z \left[J_{\nu-1}(z) + J_{\nu+1}(z) \right] = 2\nu J_\nu(z), \tag{A.14}$$

$$J_{\nu-1}(z) - J_{\nu+1}(z) = 2J_\nu'(z), \tag{A.15}$$

$$z J_\nu'(z) + \nu J_\nu(z) = z J_{\nu-1}(z), \tag{A.16}$$

$$z J_\nu'(z) - \nu J_\nu(z) = -z J_{\nu+1}(z). \tag{A.17}$$

A.4 Hankel Functions

A Hankel function—sometime called a Bessel function of the third kind—is a linear combination of Bessel functions of the first and second kind.

$$H_p^{(1)}(x) = J_p(x) + iY_p(x), \tag{A.18}$$

$$H_p^{(2)}(x) = J_p(x) - iY_p(x). \tag{A.19}$$

(A.18) and (A.19) are *Hankel functions of the first* and *second kind* respectively. They are prominent in wave propagation and are analogous to $e^{ix} = \cos(x) + i\sin(x)$ because of J_p and Y_p's close resemblance of cosine and sine.

B

Measurement of errors

The majority of errors in this thesis are evaluated in a L^2-norm sense:

$$\mathcal{E}_{L^2} = \frac{\left\| \boldsymbol{\Phi} - \boldsymbol{\Phi}^{\text{ref}} \right\|_{L^2}}{\left\| \boldsymbol{\Phi}^{\text{ref}} \right\|_{L^2}}, \tag{B.1}$$

where $\boldsymbol{\Phi}$ is a vector containing potentials, evaluated using a computational method; the vector $\boldsymbol{\Phi}^{\text{ref}}$ contains reference potentials evaluated using an analytical or converged solution. The L^2-norm of a function $\phi(x)$ is

$$\left\| \phi(x) \right\|_{L^2} = \sqrt{\int |\phi(x)|^2 \, \mathrm{d}x}, \tag{B.2}$$

where $|\cdot|$ denotes the complex modulus. Typically, the L^2-norms in this thesis are taken over the surface of the scatterer. Instead of evaluating the integral using quadrature points, they are evaluated in a trapezium rule sense. Using equally spaced points over the scatterer, to fill the vectors $\boldsymbol{\Phi}$ and $\boldsymbol{\Phi}^{\text{ref}}$, the norm becomes

$$\left\| \phi(x) \right\|_{L^2} = \sqrt{\frac{h}{2} \sum_{k=1}^{n} \left[|\phi(x_{k+1})|^2 + |\phi(x_k)|^2 \right]}, \tag{B.3}$$

where h is the geometrical length between points and n is the total number of points—or the length of the vectors $\boldsymbol{\Phi}$ and $\boldsymbol{\Phi}^{\text{ref}}$.

C

Order of singularity of integrals in the BEM for acoustics

C.1 Introduction

Reading different papers and books on the BEM for Helmholtz problems can lead to some confusion regarding the singular nature of the integrals involved. This is caused by two things: firstly, the nature of the integrals of the BIE differ depending on whether one is considering two-dimensional problems or three-dimensional problems; secondly, authors sometimes refer to order of singularity of the "derivative Green's function" which changes depending on whether it is with respect to r or n.

C.2 Definitions

Two formulations of the BIE for acoustics problems have been considered. The first is the conventional BIE (CBIE):

$$c(\mathbf{p})\phi(\mathbf{p}) + \int_\Gamma \frac{\partial G(\mathbf{p},\mathbf{q})}{\partial n}\phi(\mathbf{q})\,\mathrm{d}\Gamma(\mathbf{q}) = \int_\Gamma G(\mathbf{p},\mathbf{q})\frac{\partial \phi(\mathbf{q})}{\partial n}\,\mathrm{d}\Gamma(\mathbf{q}), \qquad \text{(C.1)}$$

where ϕ is the wave potential and $\partial\phi/\partial n$ is its derivative within respect to the outward-point unit normal, n. The Green's functions $G(\mathbf{p},\mathbf{q})$ and $\partial G(\mathbf{p},\mathbf{q})/\partial n$ are defined in 2D as:

$$G(\mathbf{p},\mathbf{q}) = \frac{i}{4}H_0^{(1)}(kr) \quad \text{in 2D}, \qquad \text{(C.2)}$$

$$\frac{\partial G(\mathbf{p},\mathbf{q})}{\partial n} = \frac{ik}{4}H_1^{(1)}(kr)\frac{\partial r}{\partial n} \quad \text{in 2D}, \qquad \text{(C.3)}$$

where $H_0^{(1)}$ is a Hankel function of the first kind of order zero, $H_1^{(1)}$ is a Hankel function of the first kind of order one, and r is the Euclidean distance between $\mathbf{p}$ and $\mathbf{q}$. In 3D:

$$G(\mathbf{p},\mathbf{q}) = \frac{1}{4\pi r}e^{ikr} \quad \text{in 3D}, \qquad \text{(C.4)}$$

$$\frac{\partial G(\mathbf{p},\mathbf{q})}{\partial n} = \frac{ikr-1}{4\pi r^2}e^{ikr}\frac{\partial r}{\partial n} \quad \text{in 3D}, \qquad \text{(C.5)}$$
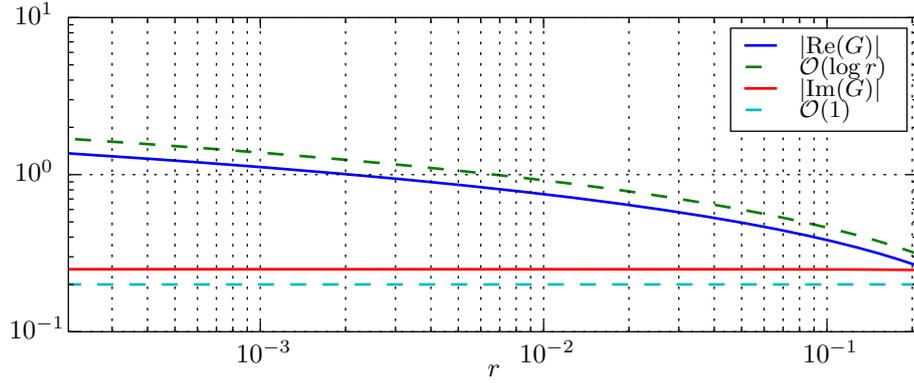
Figure C.1: 2D $G(\mathbf{p}, \mathbf{q})$ kernel.

The second formulation is the regularised BIE (RBIE) from [80]:

$$\gamma \phi(\mathbf{p}) + \int_\Gamma \left[\frac{\partial G(\mathbf{p}, \mathbf{q})}{\partial n} - \frac{\partial \bar{G}(\mathbf{p}, \mathbf{q})}{\partial n} \right] \phi(\mathbf{q}) \, d\Gamma(\mathbf{y}) +$$

$$\int_\Gamma \frac{\partial \bar{G}(\mathbf{p}, \mathbf{q})}{\partial n} [\phi(\mathbf{q}) - \phi(\mathbf{p})] \, d\Gamma(\mathbf{q}) = \int_\Gamma G(\mathbf{p}, \mathbf{q}) \, d\Gamma(\mathbf{q}), \quad \text{(C.6)}$$

where $\gamma = 1$ for infinite domains ($\gamma = 0$ for finite domains) and $\partial \bar{G}(\mathbf{p}, \mathbf{q})/\partial n$ is the derivative of the Green's function for the Laplace equation and is defined as

$$\frac{\partial \bar{G}(\mathbf{p}, \mathbf{q})}{\partial n} = -\frac{1}{2\pi r} \frac{\partial r}{\partial n} \quad \text{in 2D,} \tag{C.7}$$

$$\frac{\partial \bar{G}(\mathbf{p}, \mathbf{q})}{\partial n} = -\frac{1}{4\pi r^2} \frac{\partial r}{\partial n} \quad \text{in 3D.} \tag{C.8}$$

C.3 Two-dimensional problems

The numerical results in this section were evaluated along a 2D element on which a collocation point lies at one end. Exact details of the element are omitted as only the nature of the kernels is of importance. The results are displayed on logarithmic axes to clearly show the order of the singularity in each case.

First, the $G(\mathbf{p}, \mathbf{q})$ kernel is examined. Figure C.1 shows both the real and imaginery part of the kernel. It is the real part that approaches infinity and is $\mathcal{O}(\log r)$. In 2D, this is considered weakly singular. This means that $G(r) \to \infty$ faster than $r \to 0$ and so standard quadrature is not efficient at—or capable of in some cases—obtaining the correct result. A coordinate transformation may improve the accuracy of standard quadrature with this integral.

Now the $\partial G(\mathbf{p}, \mathbf{q})/\partial n$ kernel of the CBIE is considered. First Figure C.2 shows the nature of $\partial G/\partial r$. Again it is the real part that approaches infinity as r decreaes. It is strongly singular: $\mathcal{O}(1/r)$. Importantly though, the $\partial r/\partial n$ component of $\partial G(\mathbf{p}, \mathbf{q})/\partial n$ is $\mathcal{O}(r)$ and so the singularity will be removed. As evidence of this,
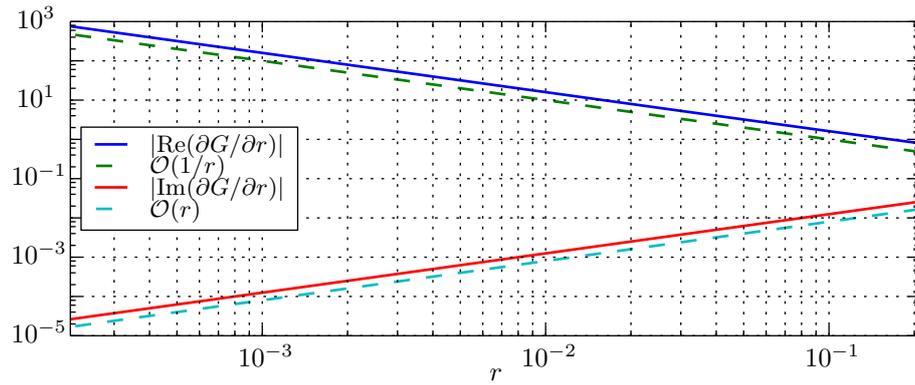
Figure C.2: 2D $\partial G(\mathbf{p}, \mathbf{q})/\partial r$ kernel.
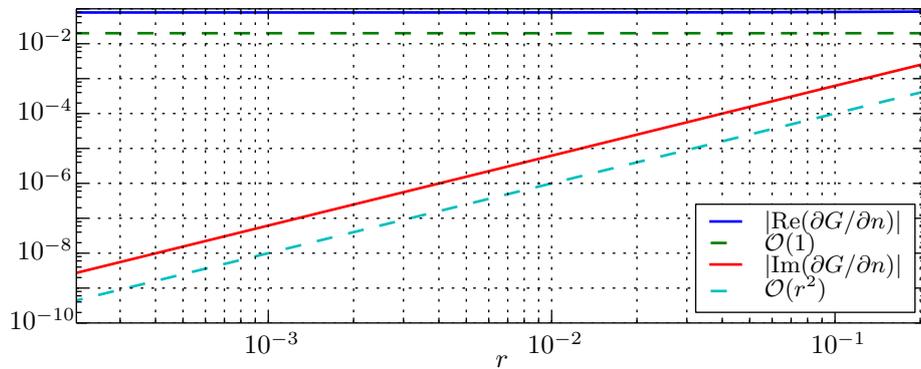

Figure C.3: 2D $\partial G(\mathbf{p}, \mathbf{q})/\partial n$ kernel.

Figure C.3 shows the nature of $\partial G(\mathbf{p}, \mathbf{q})/\partial n$. The real part is now $\mathcal{O}(1)$ which is regular and can be evaluated using standard quadrature.

Given that $\partial G(\mathbf{p}, \mathbf{q})/\partial n$ kernel is regular and $G(\mathbf{p}, \mathbf{q})$ appears in both the CBIE and RBIE, there is no need to employ the regularisation scheme for two-dimensional problems. The CBIE can be used for 2D Helmholtz problems along with a suitable integration scheme for the $G(\mathbf{p}, \mathbf{q})$ kernel.

C.4   Three-dimensional problems

In this section, the results were evaluated over a 3D quadrilateral serendipity element. Again, the details are omitted here except for that the collocation point is at the corner $(\xi_1, \xi_2) = (-1, 1)$ and the $\mathbf{q}$ points are taken along the edge $(\xi_1, 1)$ for $\xi_1 \in (-1, 1]$.

Again, the $G(\mathbf{p}, \mathbf{q})$ kernel is considered first, shown in Figure C.4. The kernel is $\mathcal{O}(1/r)$. This is different order than the two-dimensional case; however, in three-dimensional problems, $\mathcal{O}(1/r)$ is considered weakly singular.

Considering now the derivative Green's function, we can first consider the CBIE kernel. Figure C.5 displays the nature of the Green's derivative without the $\partial r/\partial n$ component, i.e. $\partial G/\partial r$. The derivative is $\mathcal{O}(1/r^2)$ or strongly singular. The full
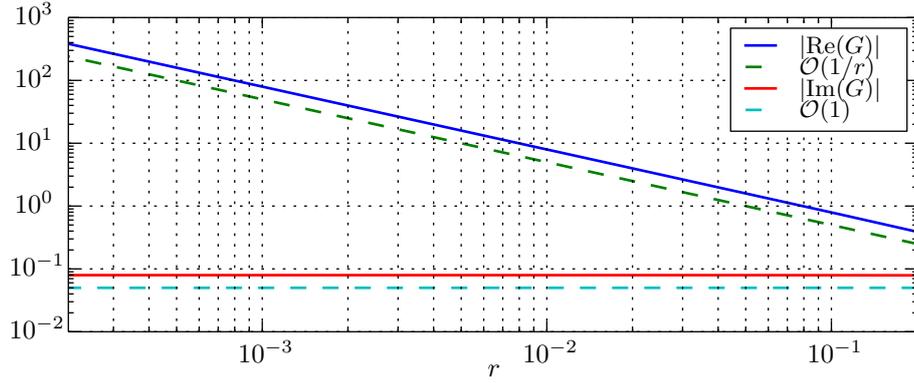
Figure C.4: 3D $G(\mathbf{p}, \mathbf{q})$ kernel.
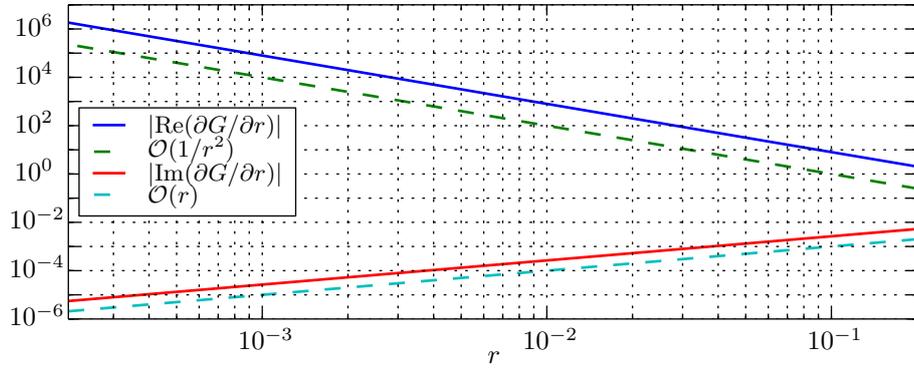
Figure C.5: 3D $\partial G(\mathbf{p}, \mathbf{q})/\partial r$ kernel.

Green's derivative, $\partial G(\mathbf{p}, \mathbf{q})/\partial n$, is $\mathcal{O}(1/r)$ (see Figure C.6). This means that $\partial G(\mathbf{p}, \mathbf{q})/\partial n$ is also weakly singular. This differs from the 2D case where $\partial G(\mathbf{p}, \mathbf{q})/\partial n$ is regular. So while a coordinate transform or other special integral scheme is not required for this integral in 2D, it is required in 3D.

Now the RBIE is considered. First, the function $\partial \bar{G}(\mathbf{p}, \mathbf{q})/\partial n$, which is to be subtracted from the Green's function derivative, is considered. Unlike the complex Helmholtz Green's functions, the Laplace Green's function (also known as the static kernel as it can be obtained with the Helmholtz kernel and $k = 0$) is a real. Figure C.7 displays $\partial \bar{G}(\mathbf{p}, \mathbf{q})/\partial n$ (complete with $\partial r/\partial n$ component) and shows that it is $\mathcal{O}(1/r)$.

This function is integrated independently in (C.6). However, it is part of a product with $[\phi(\mathbf{q}) - \phi(\mathbf{p})]$ which is $\mathcal{O}(r)$. The combination of these to functions results in a regular function that can be evaluated with conventional quadrature.

The regularised Green's derivative kernel, $\partial G(\mathbf{p}, \mathbf{q})/\partial n - \partial \bar{G}(\mathbf{p}, \mathbf{q})/\partial n$, is shown in Figure C.8. Immediately it is seen that the singular component has been effectively removed because the real part of the function is $\mathcal{O}(r)$. This can be easily, and accurately, integrated with standard quadrature.

The RBIE is, therefore, a useful formulation for 3D problem (particularly for the hard scatterer problems studied in this thesis). However, as the $G(\mathbf{p}, \mathbf{q})$ kernel
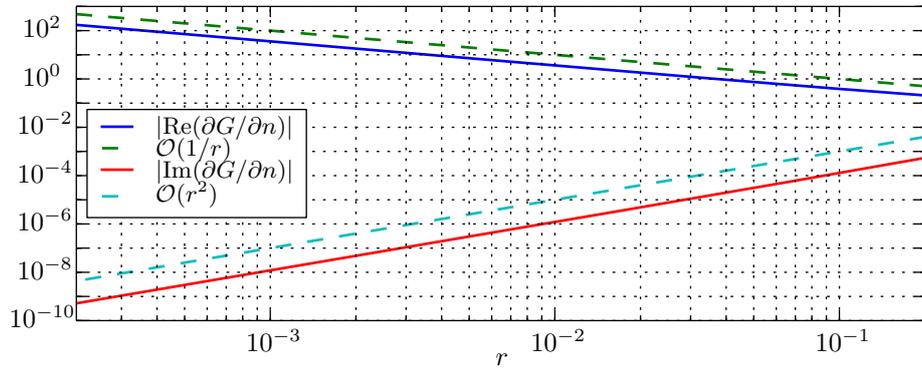
Figure C.6: 3D $\partial G(\mathbf{p}, \mathbf{q})/\partial n$ kernel.
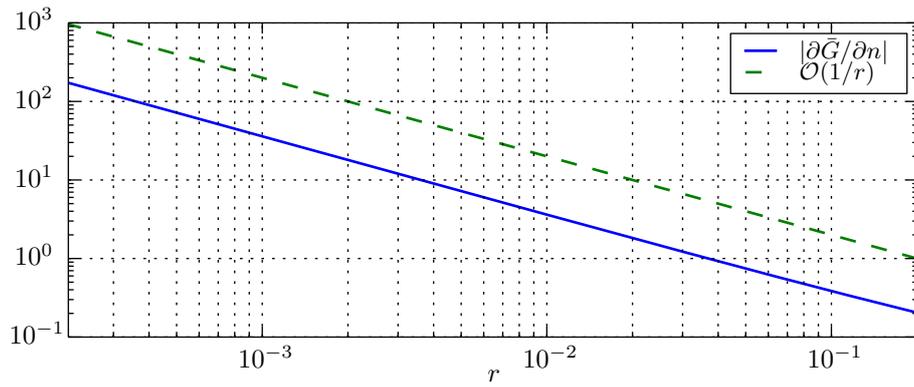

Figure C.7: 3D $\partial \bar{G}(\mathbf{p}, \mathbf{q})/\partial n$ kernel.
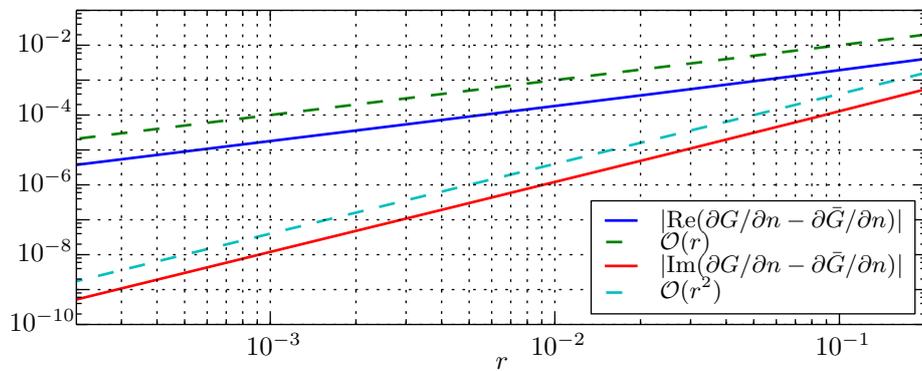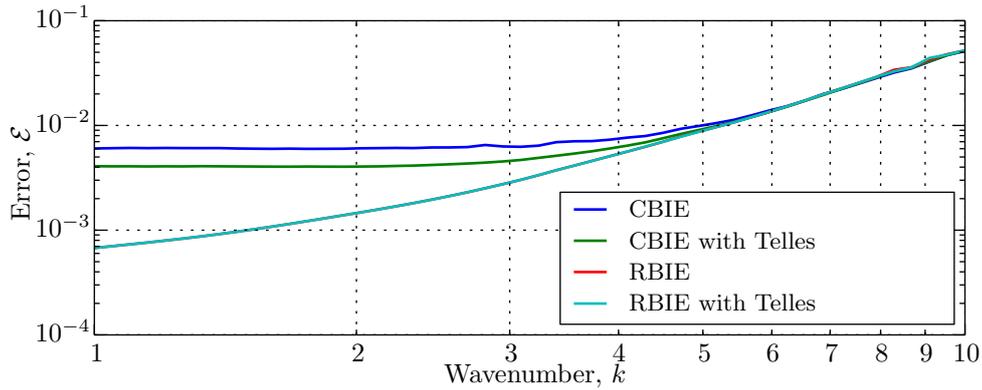

Figure C.8: 3D $\partial G(\mathbf{p}, \mathbf{q})/\partial n - \partial \bar{G}(\mathbf{p}, \mathbf{q})/\partial n$ kernel.

Figure C.9: Conventional polynomial simulation of a plane wave impinging a unit-radius sphere.

is still $\mathcal{O}(1/r)$, it does not completely remove the requirement or special integration schemes entirely if a boundary condition other than the hard scatterer is being considered.

C.5 Three-dimensional numerical example

Figure C.9 displays the L^2-errors of conventional, polynomial BEM simulations of a plane wave impinging a unit-sphere. A 10×10 Gauss quadrature was used to integrate over each element. The results support the findings of the previous section. CBIE simulations benefit from a coordinate transformation (the Telles scheme described in §6.1.3 is used here) to reduce the singularity at collocation points. However, such a scheme is of no benefit to RBIE simulations (the lines representing RBIE lie on top of each other).

It is also notable that the RBIE simulations obtained more accurate results even when the CBIE simulations used the Telles scheme. This may be because the regular integrals are inherently more accurate or it may be that the Telles scheme is not effective enough at removing the singularities.

In conclusion, the RBIE is beneficial for 3D BEM simulations, even if the $G(\mathbf{p}, \mathbf{q})$ kernel is to be evaluated. It is not, however, of benefit to 2D simulations.

C.6 Summary

From the small study here, the following is found:

- in 2D, $G(\mathbf{p}, \mathbf{p})$ is weakly singular: $\mathcal{O}(\log r)$;

- in 2D, $\partial G(\mathbf{p}, \mathbf{p})/\partial n$ is regular: $\mathcal{O}(1)$;

- in 3D, $G(\mathbf{p}, \mathbf{p})$ is weakly singular: $\mathcal{O}(1/r)$;

- in 3D, $\partial G(\mathbf{p}, \mathbf{p})/\partial n$ is weakly singular: $\mathcal{O}(1/r)$;

- a coordinate transformation, such as that of Telles, produces more accurate evaluations of the integrals containing $\partial G(\mathbf{p}, \mathbf{p})/\partial n$ in 3D simulations using the CBIE. However, simulations take longer to run as the quadrature must be transformed for each singular integral;

- the RBIE of [80] makes the derivative kernel regular: $\mathcal{O}(r)$. This removes the need for a coordinate transformation;

- 3D BEM results obtained using the RBIE are more accurate than those obtained using the CBIE.

D

Method of Fundamental Solutions

This appendix presents a simple method of fundamental solutions (MFS) derivation for 2D Helmholtz simulations followed by adaptations for 3D simulations.

D.1 MFS in 2D

First, the potential ϕ, is expressed as the sum of the incident, ϕ^{inc}, and scattered, ϕ^{scat}, potential:

$$\phi(\mathbf{x}) = \phi^{\mathrm{inc}}(\mathbf{x}) + \phi^{\mathrm{scat}}(\mathbf{x}), \quad \mathbf{x} \in \Omega, \tag{D.1}$$

where $\Omega \in \mathcal{R}^2$ is the domain with boundary $\partial\Omega$. The aim of MFS is to solve the Helmholtz equation for the scattered potential:

$$\nabla^2 \phi^{\mathrm{scat}}(\mathbf{x}) + k^2 \phi^{\mathrm{scat}}(\mathbf{x}) = 0, \quad \mathbf{x} \in \Omega. \tag{D.2}$$

This example, like the rest of this thesis, will use the sound-hard boundary condition:

$$\frac{\partial \phi^{\mathrm{scat}}(\mathbf{x})}{\partial n} = -\frac{\partial \phi^{\mathrm{inc}}(\mathbf{x})}{\partial n}, \quad \mathbf{x} \in \partial\Omega. \tag{D.3}$$

Now the scattered potential can be expressed as a linear combination of fundamental solutions centered on a set on a set of m points—termed singular points—that lie outside the approximation domain (i.e. inside the scatterer):

$$\phi^{\mathrm{scat}}(\mathbf{x}) = \sum_{\alpha=1}^{m} A_\alpha \frac{i}{4} H_0^{(1)}\big(k r_\alpha(\mathbf{x})\big), \quad \mathbf{x} \in \Omega, \tag{D.4}$$

where $r_\alpha(\mathbf{x})$ is the Euclidean distance from a singular point to $\mathbf{x}$ and A_α is the strength of the source at the singular point.

At any point, $\mathbf{x}_\beta \in \partial\Omega$, (D.4) can be differentiated:

$$\frac{\phi^{\mathrm{scat}}(\mathbf{x})}{\partial n} = \sum_{\alpha=1}^{m} A_\alpha \frac{ik}{4} H_1^{(1)}\big(k r_\alpha(\mathbf{x}_\beta)\big) \frac{\partial r_\alpha(\mathbf{x}_\beta)}{\partial n}, \quad \mathbf{x}_\beta \in \partial\Omega, \tag{D.5}$$

The MFS process now continues by taking a number of sample points around the boundary, $\mathbf{x}_\beta$ for $\beta = 1, \ldots, p$. For a solution p must at least be equal to m; however, it is usual to use $p > m$.

At each point, the error in approximating the boundary condition using the expansion can be expressed. The error is minimised over the p sampling points in a least squares sense; i.e. S is minimised where

$$S := \sum_{\beta=1}^{p} \left[\frac{\partial \phi^{\text{inc}}(\mathbf{x}_\beta)}{\partial n} - \sum_{\alpha=1}^{m} A_\alpha T_{\alpha\beta} \right]^2 \qquad (\text{D.6})$$

and

$$T_{\alpha\beta} = \frac{ik}{4} H_1^{(1)}\big(kr_\alpha(\mathbf{x}_\beta)\big) \frac{\partial r_\alpha(\mathbf{x}_\beta)}{\partial n}. \qquad (\text{D.7})$$

The least squares procedure ends up with a $\mathbf{Ax} = \mathbf{b}$ matrix expression. Here it is exemplified for the case of $m = 4$:

$$\begin{bmatrix} \sum_{\beta=1}^{p} T_{1\beta}^2 & \sum_{\beta=1}^{p} T_{1\beta}T_{2\beta} & \sum_{\beta=1}^{p} T_{1\beta}T_{3\beta} & \sum_{\beta=1}^{p} T_{1\beta}T_{4\beta} \\ \sum_{\beta=1}^{p} T_{2\beta}T_{1\beta} & \sum_{\beta=1}^{p} T_{2\beta}^2 & \sum_{\beta=1}^{p} T_{2\beta}T_{3\beta} & \sum_{\beta=1}^{p} T_{2\beta}T_{4\beta} \\ \sum_{\beta=1}^{p} T_{3\beta}T_{1\beta} & \sum_{\beta=1}^{p} T_{3\beta}T_{2\beta} & \sum_{\beta=1}^{p} T_{3\beta}^2 & \sum_{\beta=1}^{p} T_{3\beta}T_{4\beta} \\ \sum_{\beta=1}^{p} T_{4\beta}T_{1\beta} & \sum_{\beta=1}^{p} T_{4\beta}T_{2\beta} & \sum_{\beta=1}^{p} T_{4\beta}T_{3\beta} & \sum_{\beta=1}^{p} T_{4\beta}^2 \end{bmatrix} \begin{Bmatrix} A_1 \\ A_2 \\ A_3 \\ A_4 \end{Bmatrix} = \begin{Bmatrix} \sum_{\beta=1}^{p} T_{1\beta} \frac{\partial \phi^{\text{inc}}(\mathbf{x}_\beta)}{\partial n} \\ \sum_{\beta=1}^{p} T_{2\beta} \frac{\partial \phi^{\text{inc}}(\mathbf{x}_\beta)}{\partial n} \\ \sum_{\beta=1}^{p} T_{3\beta} \frac{\partial \phi^{\text{inc}}(\mathbf{x}_\beta)}{\partial n} \\ \sum_{\beta=1}^{p} T_{4\beta} \frac{\partial \phi^{\text{inc}}(\mathbf{x}_\beta)}{\partial n} \end{Bmatrix}.$$
$$(\text{D.8})$$

The coefficients A_α can be found by solving (D.8). These can then be substituted into (D.4) to find the scattered potential or, alternatively, the full potential at a point $\mathbf{x}$ can be expressed as

$$\phi(\mathbf{x}) = \sum_{\alpha=1}^{m} A_\alpha \frac{i}{4} H_0^{(1)}\big(kr_\alpha(\mathbf{x})\big) + \phi^{\text{inc}}(\mathbf{x}), \quad \mathbf{x} \in \Omega. \qquad (\text{D.9})$$

A sufficient number of m is required to find a solution. The value of m required can be found by studying convergence. In this work, it has been found that MFS can provide solutions of engineering accuracy if 3 degrees of freedom per wavelength are used. However, this rule changes based on where the source points are placed. Some MFS solution techniques include the position of the source points as a variable. For the work in this thesis, trial and error was used to find stable and converged solutions.

D.2   MFS in 3D

Much of the MFS procedure for three-dimensional problems is the same except that the fundamental solutions changes. Equations (D.4) onwards change. The scattered

potential is expressed

$$\phi^{\text{scat}}(\mathbf{x}) = \sum_{\alpha=1}^{m} A_\alpha \frac{\exp\left(ikr_\alpha(\mathbf{x})\right)}{4\pi r_\alpha(\mathbf{x})}, \quad \mathbf{x} \in \Omega, \tag{D.10}$$

which differentiated at $\mathbf{x}_\beta \in \partial\Omega$ is

$$\frac{\partial\phi^{\text{scat}}(\mathbf{x}_\beta)}{\partial n} = \sum_{\alpha=1}^{m} A_\alpha \frac{\exp\left(ikr_\alpha(\mathbf{x}_\beta)\right)}{4\pi r_\alpha(\mathbf{x}_\beta)^2} \left(ikr_\alpha(\mathbf{x}_\beta) - 1\right) \frac{\partial r_\alpha(\mathbf{x}_\beta)}{\partial n}, \quad \mathbf{x} \in \partial\Omega. \tag{D.11}$$

The errors S is rewritten

$$S := \sum_{\beta=1}^{p} \left[\frac{\partial\phi^{\text{inc}}(\mathbf{x}_\beta)}{\partial n} + \sum_{\alpha=1}^{m} A_\alpha T_{\alpha\beta} \right]^2, \tag{D.12}$$

where

$$T_{\alpha\beta} = \frac{\exp\left(ikr_\alpha(\mathbf{x}_\beta)\right)}{4\pi r_\alpha(\mathbf{x}_\beta)^2} \left(ikr_\alpha(\mathbf{x}_\beta) - 1\right) \frac{\partial r_\alpha(\mathbf{x}_\beta)}{\partial n}, \tag{D.13}$$

and the matrix system takes a slight different form:

$$\begin{bmatrix} \sum_{\beta=1}^{p} T_{1\beta}^2 & \sum_{\beta=1}^{p} T_{1\beta}T_{2\beta} & \sum_{\beta=1}^{p} T_{1\beta}T_{3\beta} & \sum_{\beta=1}^{p} T_{1\beta}T_{4\beta} \\ \sum_{\beta=1}^{p} T_{2\beta}T_{1\beta} & \sum_{\beta=1}^{p} T_{2\beta}^2 & \sum_{\beta=1}^{p} T_{2\beta}T_{3\beta} & \sum_{\beta=1}^{p} T_{2\beta}T_{4\beta} \\ \sum_{\beta=1}^{p} T_{3\beta}T_{1\beta} & \sum_{\beta=1}^{p} T_{3\beta}T_{2\beta} & \sum_{\beta=1}^{p} T_{3\beta}^2 & \sum_{\beta=1}^{p} T_{3\beta}T_{4\beta} \\ \sum_{\beta=1}^{p} T_{4\beta}T_{1\beta} & \sum_{\beta=1}^{p} T_{4\beta}T_{2\beta} & \sum_{\beta=1}^{p} T_{4\beta}T_{3\beta} & \sum_{\beta=1}^{p} T_{4\beta}^2 \end{bmatrix} \begin{Bmatrix} A_1 \\ A_2 \\ A_3 \\ A_4 \end{Bmatrix} = \begin{Bmatrix} -\sum_{\beta=1}^{p} T_{1\beta} \frac{\partial\phi^{\text{inc}}(\mathbf{x}_\beta)}{\partial n} \\ -\sum_{\beta=1}^{p} T_{2\beta} \frac{\partial\phi^{\text{inc}}(\mathbf{x}_\beta)}{\partial n} \\ -\sum_{\beta=1}^{p} T_{3\beta} \frac{\partial\phi^{\text{inc}}(\mathbf{x}_\beta)}{\partial n} \\ -\sum_{\beta=1}^{p} T_{4\beta} \frac{\partial\phi^{\text{inc}}(\mathbf{x}_\beta)}{\partial n} \end{Bmatrix}. \tag{D.14}$$

(D.14) can be solved to find the A_α which can then substituted into (D.10) to find the scatterer potential or, for the total potential,

$$\phi(\mathbf{x}) = \sum_{\alpha=1}^{m} A_\alpha \frac{\exp\left(ikr_\alpha(\mathbf{x}_\beta)\right)}{4\pi r_\alpha(\mathbf{x})} + \phi^{\text{inc}}(\mathbf{x}), \quad \mathbf{x} \in \Omega. \tag{D.15}$$